



**HAL**  
open science

# Structures et propriétés électroniques de monocouches organiques auto-assemblées caractérisées par STM et XPS

Jérémy Hieulle

► **To cite this version:**

Jérémy Hieulle. Structures et propriétés électroniques de monocouches organiques auto-assemblées caractérisées par STM et XPS. Physique [physics]. École polytechnique, 2014. Français. NNT : . tel-01291387

**HAL Id: tel-01291387**

**<https://pastel.hal.science/tel-01291387>**

Submitted on 21 Mar 2016

**HAL** is a multi-disciplinary open access archive for the deposit and dissemination of scientific research documents, whether they are published or not. The documents may come from teaching and research institutions in France or abroad, or from public or private research centers.

L'archive ouverte pluridisciplinaire **HAL**, est destinée au dépôt et à la diffusion de documents scientifiques de niveau recherche, publiés ou non, émanant des établissements d'enseignement et de recherche français ou étrangers, des laboratoires publics ou privés.

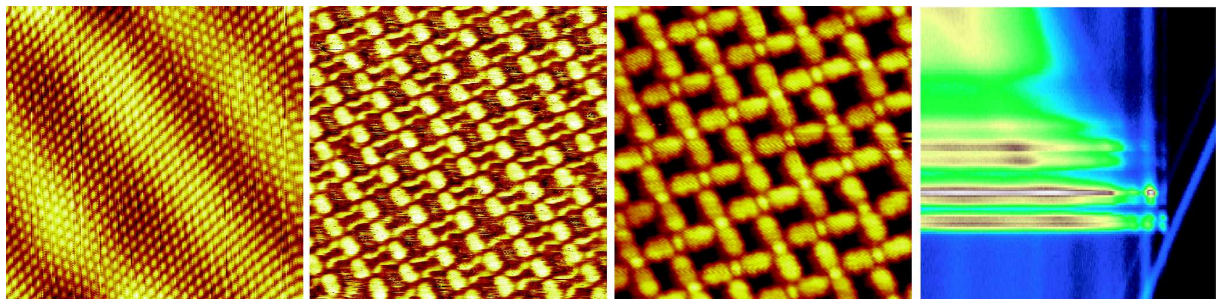


# Structures and Electronic Properties of Organic Self-Assembled Monolayers Characterized by STM and XPS

Jérémy Hieulle

CEA Saclay  
École Polytechnique

PhD. thesis



Gif-sur-Yvette 2014





# Structures and Electronic Properties of Organic Self-Assembled Monolayers Characterized by STM and XPS

Thèse de doctorat  
spécialité: Physique

Présentée par:  
Jérémy Hieulle

Le 26/09/2014

Pour obtenir le grade de:  
Docteur de l'École Polytechnique

## Composition du Jury:

Dr. Emmanuelle LACAZE	CNRS - Université Pierre et Marie Curie	Rapporteur
Dr. Frédéric CHERIOUX	CNRS - Université de Franche-Comté	Rapporteur
Dr. François Ozanam	CNRS - Ecole Polytechnique	Président du Jury
Dr. Costel-Sorin COJOCARU	CNRS - Ecole Polytechnique	Examineur
Dr. Claude HENRY	CNRS - Université Aix-Marseille	Examineur
Dr. Mathieu Silly	Synchrotron SOLEIL	Examineur
Dr. Tristan CREN	CNRS - Université Pierre et Marie Curie	Examineur
Dr. Fabien Silly	CEA - Saclay	Directeur de thèse

# Contents

<b>1</b>	<b>Context and Motivation: Structures and Electronic Properties of Organic Self-Assembled Monolayers</b>	<b>1</b>
1.1	Two-Dimensional Supramolecular Self-Assembly . . . . .	1
1.1.1	The Self-Assembly Process . . . . .	1
1.1.2	Different Types of Molecular Interaction . . . . .	3
1.1.2.1	The Van-der-Waals Interaction . . . . .	3
1.1.2.2	The Covalent Bond . . . . .	5
1.1.2.3	The Metal-Ligand Bond . . . . .	7
1.1.2.4	The Hydrogen Bond . . . . .	8
1.2	How to Control the Organization of Organic Nanoarchitectures . . . . .	10
1.2.1	Influence of External Parameters . . . . .	10
1.2.1.1	Influence of Temperature . . . . .	10
1.2.1.2	Influence of Surface Coverage . . . . .	11
1.2.1.3	Influence of Molecular Substituent . . . . .	12
1.2.1.4	Influence of the Substrate . . . . .	13
1.2.2	Host-Guest Supra-Molecular Networks . . . . .	17
1.3	Electronic Properties of Self-Assembled Molecular Thin Films . . . . .	20
1.3.1	Influence of Molecular Substituents on the Occupancy and Energy Position of the sample's Electronic States . . . . .	20
1.3.2	Determination of the Molecular Adsorption Geometry . . . . .	22
1.3.3	Estimation of the Charge Transfer Time at the Metal-Organic Interface . . . . .	25
<b>2</b>	<b>Experimental Setups</b>	<b>29</b>
2.1	Scanning Tunneling Microscopy . . . . .	29
2.1.1	The Tunneling Effect and Tunneling Current . . . . .	29
2.1.1.1	Simplified Model of the Tunneling Effect . . . . .	29
2.1.1.2	The Tunneling Barrier Shape . . . . .	32
2.1.1.3	The Tunneling Current . . . . .	34
2.1.2	The STM experimental setup . . . . .	37
2.1.2.1	The Piezoelectric Scanner . . . . .	37
2.1.2.2	The Vibration Isolation System . . . . .	39
2.1.2.3	The Ultrahigh Vacuum System . . . . .	40
2.1.2.4	The Evaporation System . . . . .	42
2.2	Photoemission Spectroscopy . . . . .	43

2.2.1	Photoemission Spectroscopy and Related Techniques . . . . .	43
2.2.1.1	Photoemission spectroscopy: basic principle . . . . .	43
2.2.1.2	Photoemission spectroscopy in solid: the three step model . . . . .	44
2.2.1.3	X-ray Photoemission spectroscopy: Core-Level measurements . . . . .	47
2.2.1.4	Near-Edge X-ray Absorption Fine Structure: basic principle . . . . .	50
2.2.1.5	Resonant Photoemission Spectroscopy: basic principle . . . . .	52
2.2.2	The SOLEIL Synchrotron . . . . .	54
2.2.2.1	General Description . . . . .	54
2.2.2.2	The TEMPO Beamline . . . . .	56
<b>3</b>	<b>Structure and Electronic properties of PTCDI films grown on Au(111) surface, investigated by STM and XPS</b> . . . . .	<b>58</b>
3.1	The Au(111) substrate: STM characterization . . . . .	59
3.1.1	The gold single crystal . . . . .	59
3.1.2	The Au(111) herringbone reconstruction . . . . .	60
3.2	Temperature-dependent PTCDI self-assembly on Au(111) substrate . . . . .	61
3.2.1	Tailoring the intermolecular electronic coupling in PTCDI self-assembled monolayer by controlling the substrate temperature . . . . .	61
3.2.2	PTCDI self-assembled architecture formed on Au(111) surface after a post-annealing at 200°C . . . . .	65
3.3	Evolution of the PTCDI core-level spectra with surface coverage . . . . .	66
3.3.1	C1s core-level spectra of PTCDI films . . . . .	67
3.3.2	N1s core-level spectra of PTCDI films . . . . .	68
3.3.3	O1s core-level spectra of PTCDI films . . . . .	70
3.3.4	PTCDI core-level spectra: Comparison with other perylene derivatives . . . . .	71
3.4	Angular NEXAFS spectra of a PTCDI multilayer Film . . . . .	72
3.5	Evolution of the PTCDI NEXAFS and Valence Band spectra with the molecular film thickness . . . . .	74
3.6	Evolution of the PTCDI Resonant Photoemission Spectrum with the molecular film thickness . . . . .	75
<b>4</b>	<b>Self-assembled nanoarchitectures based on NaCl and PTCDI molecules</b> . . . . .	<b>78</b>
4.1	Sodium Chloride: NaCl . . . . .	78
4.1.1	NaCl bulk structure . . . . .	78
4.1.2	NaCl thin film grown on Au(111) surface . . . . .	79
4.2	Tailoring the NaCl-PTCDI bi-molecular nanoarchitectures by controlling the substrate temperature . . . . .	80
4.2.1	NaCl-PTCDI bi-molecular nanoarchitectures formed at room temperature . . . . .	80
4.2.2	NaCl-PTCDI bi-molecular nanoarchitectures formed after a post-annealing at 100°C . . . . .	87

4.2.3	NaCl-PTCDI bi-molecular nanoarchitectures formed after a post-annealing at 150°C . . . . .	89
4.2.4	NaCl-PTCDI bi-molecular nanoarchitectures formed after a post-annealing at 200°C . . . . .	90
<b>5</b>	<b>Self-Assembled Molecular Architectures Investigated by STM</b>	<b>93</b>
5.1	Single-component supramolecular self-assemblies . . . . .	94
5.1.1	Compact Self-Assemblies of Ni(II)-Salen Derivative on HOPG . . . . .	94
5.1.2	DNA bases Self-Assemblies on Au(111) . . . . .	97
5.1.2.1	Guanine Self-Assemblies on Au(111) . . . . .	98
5.1.2.2	Adenine Self-Assemblies on Au(111) . . . . .	100
5.1.3	PTCDA self-assembly on Au(111) . . . . .	101
5.2	Multi-component supramolecular self-assemblies . . . . .	103
5.2.1	Compact PTCDA-Adenine supramolecular self-assemblies . . . . .	103
5.2.2	Compact PTCDI-Adenine supramolecular self-assemblies . . . . .	104
5.2.3	Host-guest supramolecular self-assembly formed by the PTCDI and truncated TAPB molecules . . . . .	107
5.3	Single and multi-component self-assemblies based on 1,3,5-Tris (4-CarboxyPhenyl) Benzene (TCPB) molecule . . . . .	110
5.3.1	Compact networks of TCPB molecules on Au(111) . . . . .	110
5.3.2	Host-guest supramolecular system formed by the TCPB molecules with NaCl on Au(111) . . . . .	114
	<b>General Conclusions</b>	<b>120</b>
	<b>Acknowledgements</b>	<b>122</b>
	<b>Bibliography</b>	<b>124</b>

# Introduction

One of the most important scientific challenges for the next decades is to build and control devices at the nanometer scale. These nanoscale devices promise to have many applications in electronics, physics, biology, chemistry and medicine. For example the nanoscale devices may be used to go further in the miniaturization of electronic compounds. The miniaturization is the privileged way in industry to improve the computer processors efficiency and performances, by increasing the number of transistors per unit area. Another example is the use of nanoscale devices in order to control the medicine delivery at a specific location of the patient's body. This technique promises to increase the efficiency of drugs, and to reduce their side effects by reducing the injected quantity of active substances.

Two different approaches can be used in order to realize the nano-devices, a top-down and a bottom-up approach. The top-down approach is commonly used in industry. It consists in macroscopic techniques like the photolithography, allowing to create integrated circuits by using a concentrate light beam. [1]. However the photolithography method depends strongly on the wavelength of the light beam used. As a consequence the miniaturization of the integrated circuits needs to use light sources, which are more and more efficient and stable. Moreover the construction of transistors with nanometer size, can introduce statistical errors in the binary data processing (0 or 1). These statistical errors are coming from the fact that only few electrons are involved in the interrupter role of the transistors [1].

A judicious manner to create nano-devices is to take advantage of the ability of molecules to self-assemble on surfaces, through the establishment of chemical bonds. This technique is a "bottom-up" approach, using small molecular building blocks in order to create organized architectures. In that case, few molecules can be used to build electronic compounds like transistors and diodes with a size-reduction factor in the order of 100 compared to the presently used compounds [1].

The main advantage of supramolecular self-assembly is to create nano-architectures by using little means, because molecules are organized by themselves [2]. Therefore the self-assembly allows to reduce the production cost of nano-devices, this is particularly interesting for industries in the objective of a future commercialization. However some external parameters must be controlled in order to obtain the desired molecular architecture, as for example the sample's temperature and surface coverage. The supramolecular self-assembly can be tuned by a precise control of the molecular structure. The shape and size of the molecular skeleton, as well as the nature and position of the molecular substituents play a crucial role in the construction of the final molecular architecture.

At the origin of the supramolecular chemistry there is a great advancement in the synthesis of organic molecules, whereby it becomes possible to create molecules with the desired structure and properties [3]. By controlling the molecular structure, it is possible to create molecules forming highly selective interactions at the origin of a self-assembly process. Donald J. Cram, Charles Pedersen and Jean-Marie Lehn received the Nobel prize in chemistry in 1987 for the realization and the use of this kind of molecules in order to create 3D supramolecular architectures. Thenceforward, many research efforts have been done on the realization of self-assembled nano-architectures [4–8].

Scanning Tunneling Microscopy (STM), is the appropriate technique to determine the molecular organization of self-assembled nano-architectures with an atomic resolution. The STM was developed by Gerd Binnig, and Heinrich Rohrer, who received the physics Nobel Prize in 1986 for this innovation. This technique allows to get topographic images of the sample in real space with an atomic resolution, but requires to use a conductive substrate. The conductive surface can have some influence on molecular organization, which must be taken into account in the data interpretations.

Before to get images of the molecular organization, it is needed to deposit the molecules on the conductive surface used. Different techniques of molecular depositions can be used. During my PhD, the molecules were deposited on the surface by evaporation in ultra-high vacuum environment (UHV) from Knudsen-cells. This molecular deposition technique is very reproducible, and allows to prepare samples with a high purity. However with this technique it is really difficult to take images of large molecules like polymers, which are in most cases broken during the evaporation process. In contrast the molecular deposition at the liquid/solid interface is more suitable for the study of large molecules, like polymers [2].

The electronic properties of molecular thin films can be characterized by using surface sensitive techniques, like X-ray Photoemission Spectroscopy. (XPS). The XPS technique was developed by the team of Kai Siegbahn, who received the Physics Nobel Prize in 1981 for this innovation. This technique allows to get chemical information about the atomic species which compose the sample of interest. In fact the binding energies of photo-emitted electrons change with the chemical nature and with the chemical environment of the atomic species involved in the photoemission process [1, 9, 10]. A detailed description of this technique is given in the paragraph 2.2.1.3. Moreover the XPS related techniques, like NEXAFS (Near-Edge X-ray Absorption Fine Structure) and RPES (Resonant Photoemission Spectroscopy), can give information about the molecular adsorption geometry (§2.2.1.4), and charge transfer process occurring at the metal-organic interface (§2.2.1.5), respectively.

During my PhD, I investigated the supramolecular self-assembly of some organic molecules deposited on a clean Au(111) surface by evaporation in UHV. The molecular organization was probed with a VT-STM from Omicron, and the electronic properties of these architectures were probed by using XPS combined with synchrotron radiation facilities. The originality of the work presented here comes from the novel association of molecules used in order to create multi-components nano-architectures. For example the co-deposition of PTCDI<sup>1</sup> with NaCl allows to construct four self-assembled nano-

---

<sup>1</sup>PTCDI: perylene-3,4,9,10-tetracarboxylic diimide.

architectures, depending on the sample temperature (Chapter 4). In addition to that the co-deposition of BAPB<sup>2</sup> molecules with PTCDI allows to create a new porous bimolecular structure (§ 5.2.3). In this PhD thesis I have also shown that a post-annealing of the sample can be used not only to change the structure of a perylene-based film as it is usually expected but also to modify its electronic states. By using X-ray photoemission spectroscopy I showed that a strong modification of the line-shape and energy positions of the electronic states of SAMs is obtained when changing the molecular film thickness. In the same way core-hole-clock spectroscopy shows that the charge transfer dynamics at the PTCDI/Au(111) interface is strongly affected by the film thickness (Chapter 3).

The first chapter gives the state of the art of the researches on supramolecular self-assembly and their electronic properties. The first section of this chapter describes the self-assembly process and some typical intermolecular interactions from which it can originate. The second section gives an overview of the key parameters governing the molecular self-assemblies. The last section gives some examples of the use of XPS (X-ray photoemission spectroscopy) and related techniques to characterize the electronic states of molecular thin films.

The second chapter describes the experimental setups used during my PhD. The first section talk about the scanning tunneling microscope. A simplified model of the tunneling effect and the resulting tunneling current established in a STM junction is given in the first paragraph of this section. The following paragraphs describe the UHV system, the piezoelectric scanner and the vibration isolation system used. The second section of this chapter describes the basic principle of the photoemission spectroscopy and related techniques, like XPS, NEXAFS and RPES. Finally the last paragraph describes the SOLEIL synchrotron facilities and TEMPO beamline used during my PhD.

The third, fourth and fifth chapters expose the experimental results obtained during my PhD. The third chapter is dedicated to the structures and electronic properties of PTCDI thin films. The fourth chapter shows the molecular nanoarchitectures formed by combining NaCl with PTCDI molecules. Finally the fifth chapter gives some experimental results on the key parameters governing the self-assembly of new single-component and multi-components supramolecular nanoarchitectures, and shows how host-guest systems can be used to control the organization of additional species.

---

<sup>2</sup>BAPB: 1,3-Bis(4-AminoPhenyl)Benzene.

# Chapter 1

## Context and Motivation: Structures and Electronic Properties of Organic Self-Assembled Monolayers

In this chapter I will expose the last achievements in the research on supramolecular self-assembly. Firstly I describe the self-assembly mechanism. Secondly I describe different types of intermolecular interaction from which the self-assembly process can originate. Then, I show the interest of using hydrogen bonds to build organic nanoarchitectures. Thirdly I show the influence of the temperature, surface coverage and molecular substituents on the supramolecular organization. Finally I will expose the use of host-guest systems in order to control the assembly of additional molecules which are not organized by themselves on surfaces.

### 1.1 Two-Dimensional Supramolecular Self-Assembly

The control of molecular organization at the nanometer scale is essential in order to develop the new generation of low-cost organic and electronic devices [11]. The molecular architectures can be tailored taking advantage of the self-assembly process. In this way, complex organic nanoarchitectures can be formed through a self-assembly process, by using specific molecular building blocks. Therefore the understanding and the control of the self-assembly process is of prime importance in this field.

#### 1.1.1 The Self-Assembly Process

The self-assembly process originates from a complex balance between molecule-molecule interaction and molecule-substrate interaction. The molecule-molecule interaction consists of a set of attractive and repulsive interactions between the active sites of the molecules, which in some cases leads to the formation of organized architectures. However stronger are the molecule-substrate interactions, harder it is for the molecular active sites to meet together, and then more difficult is the realization of self-assembled structures. In order to overcome this problem, it is helpful to take advantage of the diffusion

process of molecules on the sample's surface. This diffusion process comes from thermal excitation, and involves the meeting of the active sites of the molecules. Finally this results in the formation of intermolecular interactions, which are at the origin of the organized structures [12, 13]. To initiate the diffusion process, the molecules need a mobility energy ( $E_m$ ) higher than the potential barrier created by the surface corrugation (Figure 1.1). To move a molecule from one adsorption site to another site, the

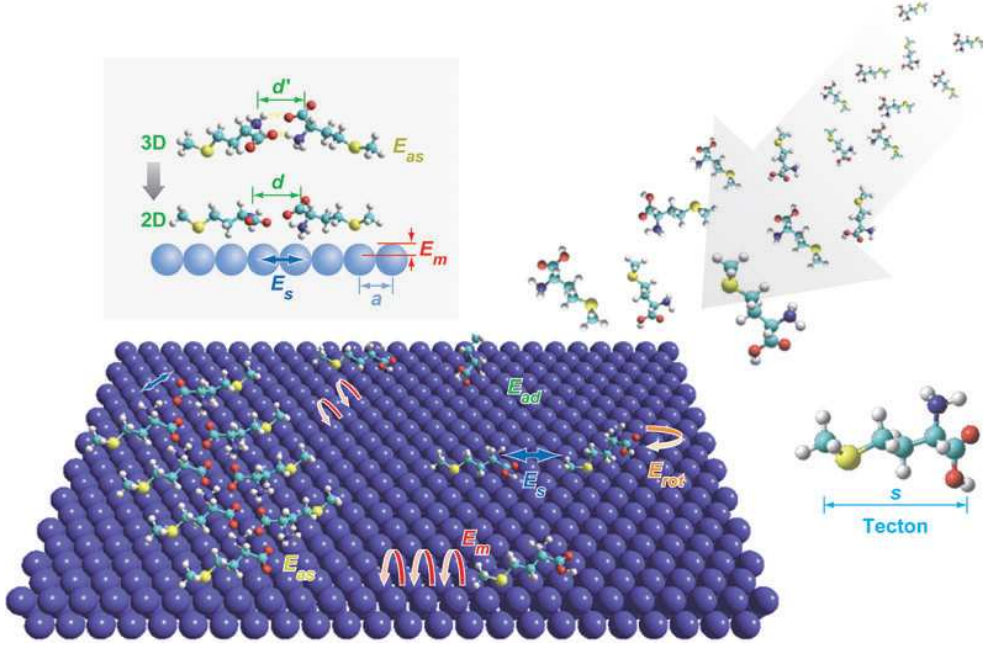


Figure 1.1: The self-assembly process [11].

thermal energy must be higher than the mobility barrier. The thermal excitation of the molecules and their movements are governed by the sample's phonons. These phonons have a frequency between  $10^{12}$  and  $10^{14} s^{-1}$ , coming from network oscillations possessing an amplitude of  $0.1 \text{ \AA}$ . To understand the diffusion process, we can distinguish the two following cases.

- If  $E_m \ll k_B T$ , then the molecules are trapped in their adsorption sites, and they can be considered motionless in some time scale. But if we observed this molecule in a larger time scale, then it is possible to see the jump of this molecule from one adsorption site to another adsorption site. This hazardous jump comes from energetic fluctuations, and can be described by a Markov process<sup>1</sup>. Then the transfer rate of the molecule from one adsorption site to another one, can be written as follows,

$$\Gamma_s = \nu_s \exp[-\beta E_m], \quad (1.1)$$

<sup>1</sup>The Markov process, is a stochastic process describing the future state of the molecule thanks to the unique knowledge of the present state, and not through the knowledge of all previous states. Then  $P(X_{n+1} | X_0, X_1, \dots, X_n) = P(X_{n+1} | X_n)$ , [14].

where  $\nu_s$  corresponds to the sample's phonon frequency, and  $\beta = 1/(k_B T)$  is the Boltzmann factor.

- If  $E_m \simeq k_B T$ , or if  $E_m \gg k_B T$ , then the corrugation of the surface becomes negligible. In this case the diffusion of the molecules at the surface is not restricted to a certain area of the sample, i.e. the molecules can move freely. In that case the expression of the molecular transfer rate obtained in equation 1.1 must be revised. Henceforth the molecular motion at the surface of the sample can be described by the Brownian motion<sup>2</sup>. Then the diffusion coefficient  $D$  can be defined as follows,

$$D = \frac{k_B T}{\gamma m}, \quad (1.2)$$

with  $T$  the temperature,  $\gamma$  the friction coefficient,  $m$  the mass of the molecule, and  $k_B$  the Boltzmann constant.

The equations (1.1) and (1.2), show that temperature is a key parameter controlling the molecular diffusion process. As a consequence the temperature must be controlled in order to initiate the molecular self-assembly process. For example in low-temperature experiments (i.e. below 5K), the molecular self-assembly can be almost inhibited by the low-diffusion process. However in our experiments, the molecules were deposited on samples kept at room temperature. In that case the diffusion process is strong enough for the self-assembly occurs. To summarize the self-assembly process can originate from a thermal diffusion process, which brings together the active sites of molecular building blocks. This implies the formation of intermolecular interactions, from which organized molecular structures can be formed. Therefore the control of the intermolecular interaction is of prime importance in the field of supramolecular chemistry, as described in the next sections.

## 1.1.2 Different Types of Molecular Interaction

To engineer the supramolecular self-assembly, it is helpful to modify the intermolecular interaction by using different types of molecular building blocks. In that way, different kinds of intermolecular interaction can be at the origin of the self-assembly process, like the Van-der-Waals interaction, the covalent bonds, the metal-ligand bonds, and the hydrogen bonds. In the following sections, I will expose some examples of supramolecular self-assemblies built with these different types of interactions. Moreover I will expose the advantages and disadvantages of each type of intermolecular interactions.

### 1.1.2.1 The Van-der-Waals Interaction

The Van-der-Waals interactions are induced by the correlations in the fluctuating polarizations of neighboring particles, which can be perfectly described in quantum dynamics.

---

<sup>2</sup>The Brownian motion is the description of the random motion of a molecule in a solvent. It can also describe the random motion of a molecule diffusing on a solid surface. The Brownian motion doesn't take into account the interactions between molecules, but it considers only the elastic collisions of the molecules.

A simplified description of the Van-der-Waals interactions consists to attribute them to weak dipole-dipole interactions which appear between two neighboring atoms. In fact quantum fluctuations are responsible of a non-symmetric shape of the electron clouds around the atomic cores, inducing the appearance of poor electron areas and rich electron areas creating dipole moments. These dipolar moments imply attractive and repulsive interactions between neighboring atoms depending on their respective signs. An example of supramolecular network built through Van-der-Waals interactions is given by Wende Xiao *et al.* [15], for the 1,3,5-tris(4'-carboxylphenyl)-2,4,6-tris(4'-tert-butylphenyl)-benzene molecules (named **1** in Figure 1.2a) on Au(111) surface. Molecule **1** consists

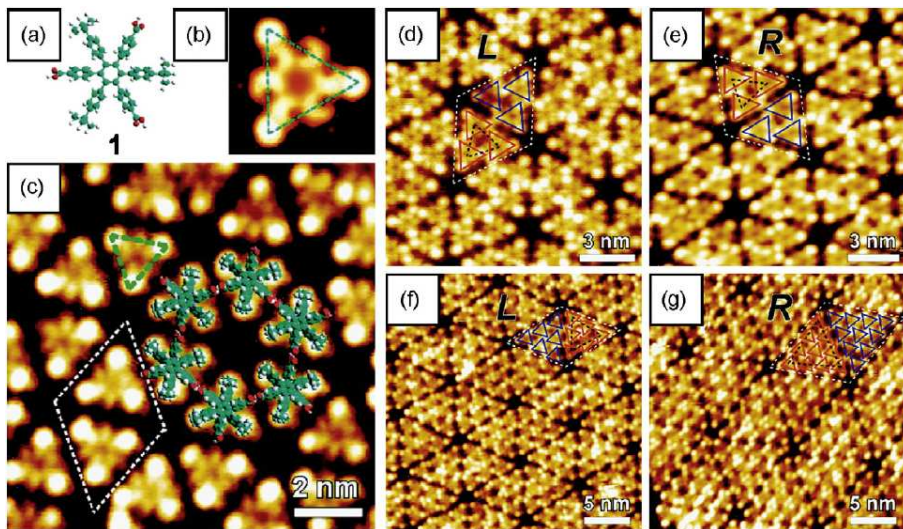


Figure 1.2: (a) Molecular structure of the 1,3,5-tris(4'-carboxylphenyl)-2,4,6-tris(4'-tert-butylphenyl)-benzene (HC) molecule; (b) simulated STM image of the molecule; (c) the honeycomb structure of  $HC_1$  without chirality on Au(111); (d) and (e) L- and R-domains of the  $HC_2$  structure; (f) L-domain of the  $HC_3$  structure; (g) R-domain of the  $HC_4$  structure. Unit cells are indicated by white dashed lines. Individual molecules are highlighted as red and blue triangles (opposite chiral conformations of the molecules) with corners at tertio-butyl positions [15, 16].

of a hexaphenylbenzene core and three alternating tert-butyl and carboxyl end-groups attached to the phenyl rings. The authors have used scanning tunneling microscopy to show that molecules **1** form a series of chiral honeycomb networks on Au(111) surface kept at room temperature (Figures 1.2 c,d,f); denoted  $HC_1$ ,  $HC_2$  and  $HC_3$  respectively. Force field calculations show that these structures are stabilized through Van-der-Waals interactions established between the molecules **1** constituting a half-unit cell. However, the half-unit cells are connected to each other through hydrogen bonds between the carboxylic groups of the molecules **1**. Figure 1.2c, shows the  $HC_1$  network formed when only one molecule **1** constitutes the half-unit cell. Figures 1.2 d,e; show the  $HC_2$  structure, where each unit cell consists of two triangular subunits (half-unit cells). Each half-unit cell is composed of three molecules **1** close-packed via Van-der-Waals interactions. The half-unit cells are connected together via hydrogen bonds between the

carboxyl end-groups of the molecules **1**. The fact that the phenyl rings can rotate around their  $\sigma$ -bond attached to the benzene core, gives two chiral conformations for the adsorption of molecules **1** on Au(111) surface. These two adsorption conformations of the molecules **1** are at the origin of two HC<sub>2</sub> homochiral domains, the left-handed and the right-handed honeycomb structures, denoted as (L) and (R) in the Figures 1.2d, and 1.2e respectively.

In the same way Figure 1.2f, shows the HC<sub>3</sub> network, where each half-unit cell is composed of six molecules **1** close-packed via Van-der-Waals bonds forming a chiral triangle. This chiral subunit is responsible for the formation of two HC<sub>3</sub> homochiral domains, the left-handed (Figure 1.2f), and the right-handed honeycomb structure (not shown here). Figure 1.2g shows the right-handed HC<sub>4</sub> honeycomb structure, which consists of ten molecules **1** connected through Van-der-Waals interactions in each half-unit cells. Finally the HC<sub>2</sub> network can be viewed as an inflation of the HC<sub>1</sub> structure by the addition of two molecules **1** in its half-unit cell. Similarly, the HC<sub>3</sub> network can be viewed as an inflation of the HC<sub>2</sub> structure by the addition of three molecules **1** in its half-unit cell. To conclude, this work shows that it is possible to create organized supramolecular architectures through Van-der-Waals interactions. However the Van-der-Waals interactions are relatively weak (see table 1.1). Therefore, in most cases the supramolecular architectures built through Van-der-Waals forces do not support thermal excitation or external strain produced by the adsorption of additional molecules on the substrate.

### 1.1.2.2 The Covalent Bond

The covalent bond comes from the sharing of the electrons of two atoms. This creates electron pairs which are placed on common energy levels of the two atoms. It means that the electron cloud is delocalized on both atoms. Finally it creates a strong chemical bond between the two atoms. A typical manner to create covalent bonds is to use radicals, which consist of atoms possessing unpaired electrons. Two radicals can react in order to create an electron pair. The formation of radicals can be obtained by thermal or chemical activation. An example of covalently bound supramolecular self-assemblies is given by Leonhard Grill *et al.* [17], for the tetra(4-bromophenyl)porphyrin (Br<sub>4</sub>TPP) molecules grown on the Au(111) surface. Figure 1.3a shows the methodology used by the authors to realize covalently bound molecular architectures. The first step of this method consists to choose small molecular building blocks with reactive end-groups that can form strong covalent bonds at predefined connection points. The second step corresponds to the dissociation of the substituents from the molecular core by heating, in order to create radical groups. The third step consists to use these activated radical groups to construct covalently bound nanostructure through thermal diffusion. In this way the authors used the Br<sub>4</sub>TPP molecules, which are depicted in Figure 1.3b. The Br<sub>4</sub>TPP molecule is composed of bromine groups acting as labile substituent, which can be dissociated in a controlled manner by heating. The Br<sub>4</sub>TPP molecules were deposited on a Au(111) surface kept at room temperature. For an evaporation temperature lower than 550K, the Br<sub>4</sub>TPP molecules remain intact without dissociation of the Br substituent, resulting in the formation of a close-packed structure, Figure 1.3c.

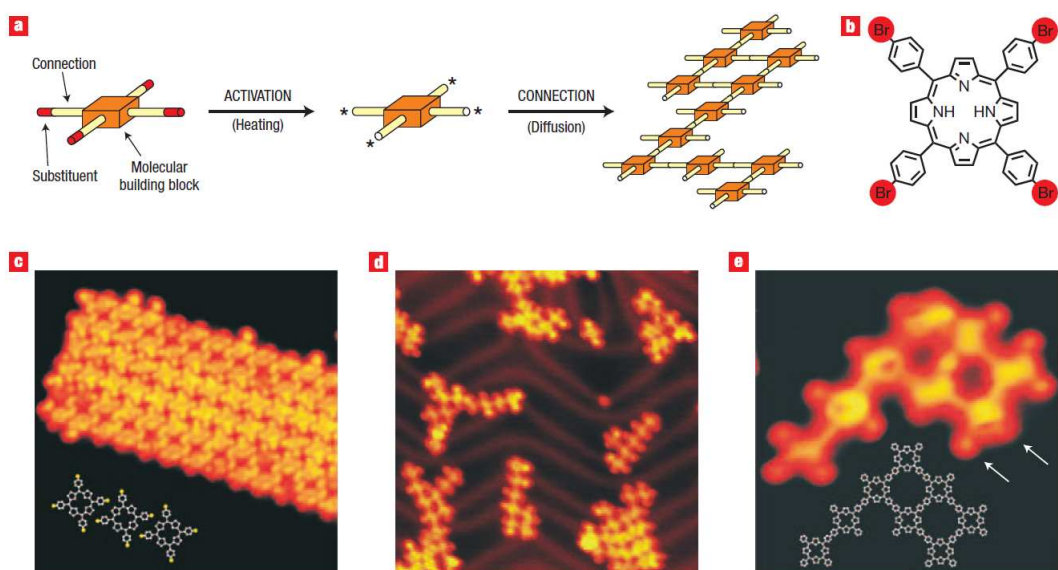


Figure 1.3: Nano-architectures of covalently bound  $\text{Br}_4\text{TPP}$  molecular networks. (a), The concept of the formation of covalently bound networks by connecting activated molecular building blocks. (b), The chemical structure of the  $\text{Br}_4\text{TPP}$  molecule (substituent Br atoms are highlighted in red). (c), STM image ( $20 \times 20 \text{ nm}^2$ ) of a molecular island on Au(111) after deposition at low evaporator temperatures of 550 K prior to being activated. The inset shows the corresponding chemical structure. (d), STM image ( $41 \times 41 \text{ nm}^2$ ) obtained after molecular deposition at elevated temperature (610 K), causing the activation and connection of the molecules to form networks. (e), STM image ( $8.5 \times 8.5 \text{ nm}^2$ ) of a network of eight molecular building blocks. The left and right arrows indicate molecular legs with and without Br atoms, respectively. The chemical structure of the network is given in the inset, [17].

This close-packed structure is formed by minimizing intermolecular distances through molecular diffusion on the surface. In contrast for an evaporation temperature of at least 590K, most of the Bromine atoms are dissociated from the TPP molecular core, resulting in the activation of the phenyl groups by the appearance of radicals. These radicals can react with each other allowing the formation of covalently bound supramolecular architectures through thermal diffusion, Figure 1.3d. Finally the covalently bound nanostructures can adopt various shapes and sizes on the surface. The preferred shape is a one-dimensional structure like a molecular chain, Figure 1.3d. However some small two-dimensional structures are present on the surface, Figure 1.3e. These two-dimensional networks require more than two connection points between the molecules. This means that the two-dimensional structures can be built by using molecules which have lost more than two Bromine substituents. But these two-dimensional networks are in minority, because the evaporation temperature used is not sufficient to dissociate all the Bromine atoms from their molecular cores, as shown in Figure 1.3e. To conclude, controlling the supramolecular self-assembly in order to obtain desired architectures through

strong covalent intermolecular connections is of prime importance, because it enabling efficient electronic transport between the molecules and provides high stability to the networks [17]. However, no extended two-dimensional supramolecular architectures stabilized through covalent bonds have been realized yet. In fact it is difficult to make large networks by repetitive chemical synthesis, as it is shown in the previous example. Moreover, it is also difficult to deposit already formed large covalently bound networks on metallic surfaces, without deterioration of their chemical structures.

### 1.1.2.3 The Metal-Ligand Bond

Another type of bond which can be at the origin of supramolecular self-assembled networks is the Metal-ligand bond [11, 18, 19]. In most cases the Metal-ligand bonds are in character 50% covalent and 50% ionic. This type of bond results from the interaction between one metal atom, and one ligand which can be a molecule, an atom, or an ion. An example of molecular architecture built through Metal-ligand bonds is given by M. Lingenfelder *et al.* [19], Figure 1.4. Figure 1.4 shows the supramolecular self-assembly

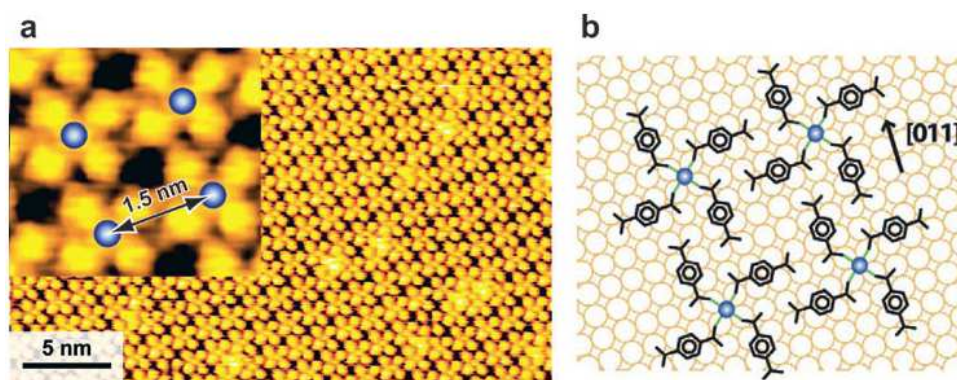


Figure 1.4: (a) High-resolution STM image of the "Clover-leaf" phase, with Fe atoms marked. (b) Geometrical model: each Fe atom (blue spheres) coordinates four 1,4-benzenedicarboxylic acid ligands (TPA molecules), in a square-planar configuration [19].

formed by the TPA<sup>3</sup> molecules and the Fe atoms on a Cu(100) surface. Each Fe atom is bonded to four TPA molecules through Metal-ligand bonds. Finally the molecular network formed possesses a "Clover-leaf" shape. The "Clover-leaf" patterns are linked to each other through O...H-C hydrogen bonds (see §1.1.2.4). The TPA "Clover-leaf" network is obtained by depositing the Fe atoms on top of the molecular film, followed by a post-annealing of the sample at a temperature around 500 K. A close inspection of the high-resolution STM images reveals that TPA molecules in the [Fe(TPA)<sub>4</sub>] complex, are coordinated to the Fe atoms through the "left-hand" oxygen of their carboxylic end-groups (inset of the Figure 1.4a).

To conclude, controlling the supramolecular self-assembly in order to obtain the desired architectures through Metal-ligand connections is of prime importance, because it

<sup>3</sup>TPA: 1,4-benzenedicarboxylic acid.

enabling to form organized nanoarchitectures on surfaces by using little means. However, metallic atoms can form molecular bonds in all directions of the space. So the majority of supramolecular architectures formed through Metal-ligand bonds are three-dimensional structures [19]. Finally the Metal-ligand strength is stronger than the hydrogen bond strength (see table 1.1). This leads to a weaker flexibility in the control of the organization of organic networks based on Metal-ligand bonds compared to organic networks formed through hydrogen bonds (see §1.1.2.4).

#### 1.1.2.4 The Hydrogen Bond

The hydrogen bond is built by dipolar interactions, originating from the electronegativity difference between two neighboring atoms. This type of molecular bonds is ten times weaker than the covalent bonds, but it's really strong compared to the Van-der-Waals bonds (see table 1.1). The hydrogen bond is formed between one positively charged hydrogen atom, and one electronegatively charged atom. The fact that the hydrogen atom has a positive apparent charge, is due to the presence of a second electronegative atom, which is covalently bound to it. Indeed this second electronegative atom attracts the electron cloud of the hydrogen, Figure 1.5. One of the most interesting properties

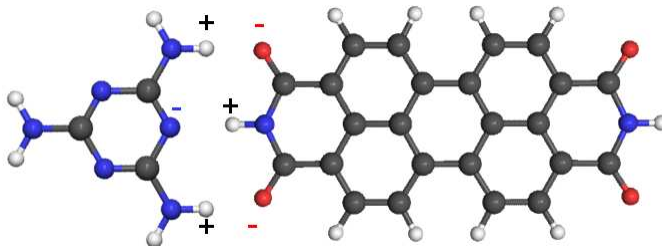


Figure 1.5: Scheme of the hydrogen bonds between a melamine molecule (left), and a PTCDI molecule (right).

of the hydrogen bonds is their directionality. This means that they are established in a precise direction of the space. This direction can correspond with a symmetrical axis of the molecule, allowing the formation of organized supramolecular networks. Many recent researches demonstrate that the hydrogen bonds can be at the origin of a self-assembly process, from which organized supramolecular architectures are formed [20–23].

An example of molecular self-assembly built through hydrogen bonds is given by Greg Pawin *et al.*, for the Anthraquinone molecules deposited on a Cu(111) surface [21]. Figure 1.6a, shows that the Anthraquinone molecules form a honeycomb structure on a Cu(111) surface kept at a temperature between 20 K and 200 K. The honeycomb structure has a pore diameter size of  $\simeq 50$  Å. The sides of each hexagon consist of three parallel Anthraquinone molecules, while the corners of each hexagon consist of three Anthraquinone molecules that form a triangle. Figure 1.6b, shows that the Anthraquinone honeycomb structure is stabilized through  $O \cdots H-C$  hydrogen bonds. This interpretation is confirmed by DFT calculations which provides a  $O \cdots H-C$  molecular distance

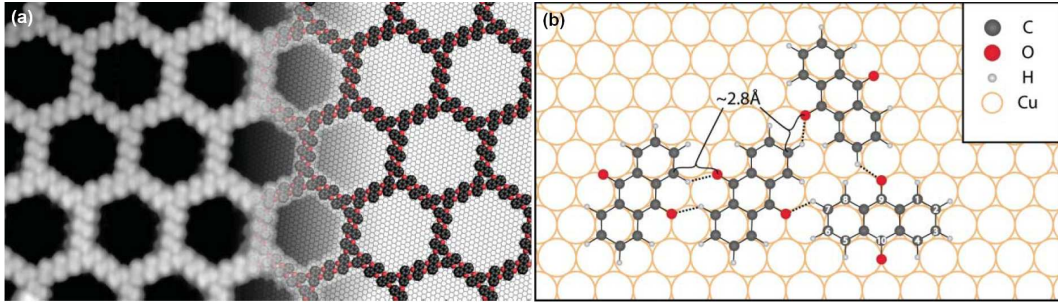


Figure 1.6: (a) **Left:** STM image of the Anthraquinone porous networks formed on Cu(111). Bias  $\simeq 1.3\text{V}$ ; current  $\simeq 73\text{pA}$ ; size,  $26 \times 15\text{nm}^2$ . **Right:** A model of the  $(\sqrt{304} \times \sqrt{304})R23^\circ$  unit cell. Red spheres, oxygen atoms; black spheres, carbon atoms; white spheres, hydrogen atoms; background, copper surface. (b) Scheme of the H-bond networks [21].

equal to  $2.8\text{\AA}$  [21]. The hydrogen bonds allow to build and to tailor the organic network through different external parameters, with a high simplicity compared to other types of bonds. By comparing the energy range of the hydrogen bond with respect to other

	Energy Range	Length	Characteristic
Van-der-Waals bonds	$\simeq 0.02 - 0.1\text{ eV}$	$< 1\text{ nm}$	no selective
Hydrogen bonds	$\simeq 0.05 - 0.7\text{ eV}$	$1.5 - 3.5\text{\AA}$	selective, directional
Metal-Ligand bonds	$\simeq 0.5 - 2\text{ eV}$	$1.5 - 2.5\text{\AA}$	selective, directional
Covalent bonds	$\simeq 1.5 - 5.2\text{ eV}$	$0.74 - 2.28\text{\AA}$	directional

Table 1.1: Comparison between the different types of bonds [11].

types of interactions (see, Table 1.1), it appears that hydrogen bonds are weaker than the covalent bonds and Metal-ligand bonds, but they are stronger than Van-der-Waals interactions. This means that by adjusting the external parameters it is easier to tune the molecular architectures stabilized through hydrogen bonds, compared to molecular architectures built through covalent bonds or metal-ligand bonds. Moreover Table 1.1 shows that the hydrogen bonds and the Metal-ligand bonds are both selective and directional, in contrast to the Van-der-Waals interactions. Selectivity, means that the bond is established between atoms having a specific chemical nature. Therefore the molecular skeleton can be tailored in order to establish hydrogen bonds at a precise position of the molecular core, enabling to create organized architectures in a predictable way. It is the reasons why during my PhD, I have used molecules which are able to form hydrogen bonds, in order to obtain predictable self-assembled architectures which can be easily controlled through the external parameters (see §1.2.1).

## 1.2 How to Control the Organization of Organic Nanoarchitectures

### 1.2.1 Influence of External Parameters

In this section I will expose the influence of some external parameters on the molecular organization. The first paragraph described the influence of temperature. The second paragraph shows the influence of surface coverage. The third paragraph talks about the influence of molecular substituents. The last paragraph shows the influence of the substrate used on the molecular self-assembly.

#### 1.2.1.1 Influence of Temperature

An easy way to tune the molecular organization is to control the sample's temperature [24]. In fact by increasing the sample's temperature, the energy of the system is increased. This energy increased can be used to realize a phase transition from a disordered phase to an ordered phase, or from an organized phase to another one [25–27]. For example F. Silly *et al.* [28], shown that PTCDI<sup>4</sup> and Melamine<sup>5</sup> molecules deposited on Au(111) surface kept at room temperature, can form a closely-packed network called the "Pinwheel" structure, Figure 1.7a. The closely-packed "Pinwheel" structure depicted

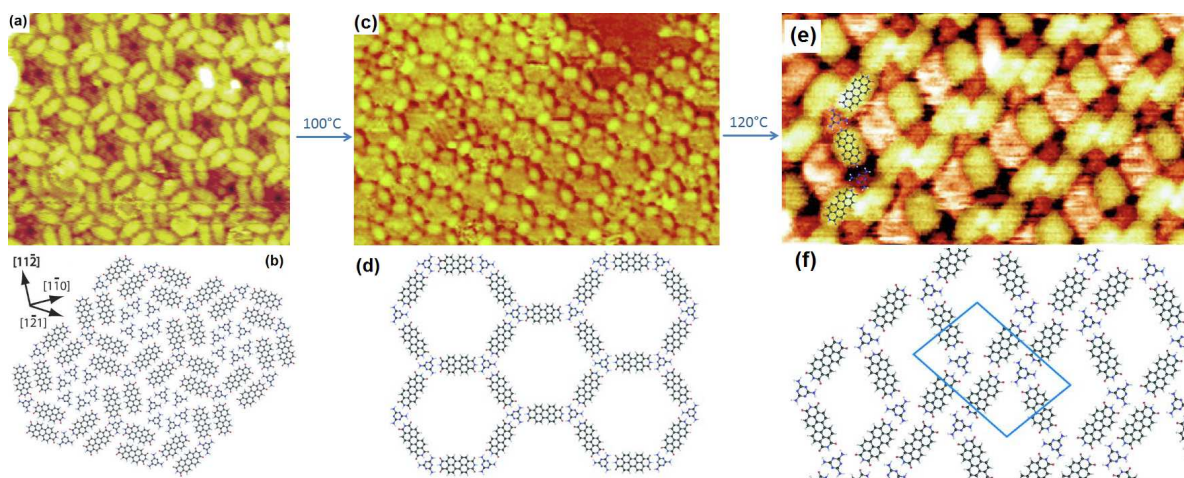


Figure 1.7: (a) STM image of the Pinwheel structure formed at room temperature by the PTCDI and Melamine molecules on Au(111). (b) Scheme of the Pinwheel structure. (c) STM image of the Honeycomb structure formed after a post-annealing of the sample at 100° C. (d) Scheme of the Honeycomb structure. (e) STM image of the Parallelogram phase obtained after a post-annealing at 120° C. (f) Scheme of the Parallelogram structure [28].

in Figures 1.7a,b is formed through the establishment of hydrogen bonds between the

<sup>4</sup>PTCDI: perylene-3,4,9,10-tetracarboxylic diimide.

<sup>5</sup>Melamine: 1,3,5-triazine-2,4,6-triamine.

Melamine and the PTCDI molecules. After a post-annealing of this structure above 100° C, a porous network is formed, Figures 1.7c,e. In the same way after post-annealing the sample at 120° C, a new Parallelogram structure was formed, Figure 1.7e. Therefore the sample's temperature is a key parameter to tailor the supramolecular nanoarchitectures. In fact there is an increase of the kinetic energy of the system with temperature which breaks the molecular bonds and then allows the molecules to diffuse easily at the surface of the sample. The diffusion of molecules allows to bring together their active sites, and involves the formation of new molecular bonds which are at the origin of a change in the molecular organization [25–28].

### 1.2.1.2 Influence of Surface Coverage

Another parameter which can be adjusted to control the supramolecular self-assembly, is the surface coverage [29, 30]. The surface coverage is the ratio between the area of the surface covered by the molecules and the total surface area of the sample. Usually this quantity is expressed in term of monolayer (ML), where 1ML corresponds to a surface totally covered by the molecules. An example of the influence of surface coverage on molecular organization is given by M. Stöhr *et al.* [29] for DPDI<sup>6</sup> molecules adsorbed on Cu(111) surface. Figure 1.8, shows that the DPDI molecules can form three different

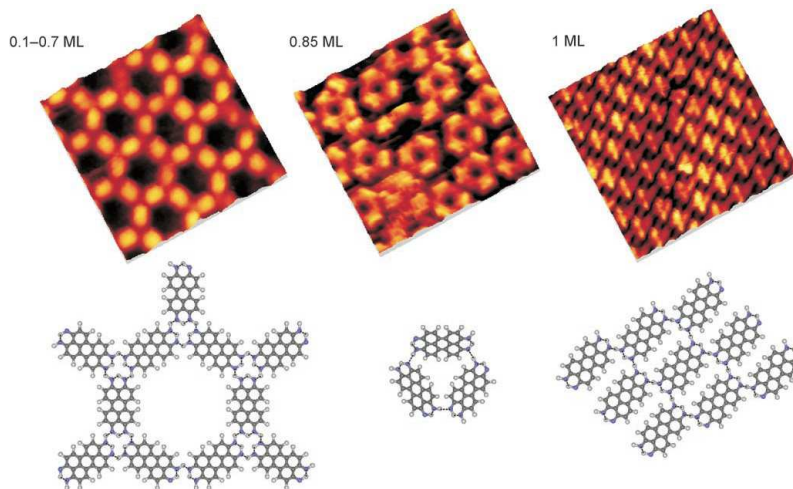


Figure 1.8: STM images and the corresponding chemical structure, of the DPDI molecules on Cu(111) for different surface coverages. At a surface coverage between 0.1 and 0.7ML, the DPDI molecules form a hexagonal structure. At a surface coverage of 0.85ML, DPDI molecules form a trimeric structure. Finally, at a surface coverage of 1ML, DPDI molecules form a close-packed chain structure [29].

molecular networks on Cu(111), depending on the surface coverage [29]. At a surface coverage between 0.1 and 0.7ML a hexagonal network is formed, where a DPDI molecule is placed on each side of a hexagon. In contrast at a surface coverage of 0.85ML, a

<sup>6</sup>DPDI: 4,9-diaminoperylene-quinone-3,10-diimine.

trimeric phase is formed where one DPDI molecule is placed on each side of a triangle. Finally by increasing the surface coverage up to 1ML, a closely-packed network is formed where the DPDI molecules are forming molecular chains. Therefore the surface coverage is a key parameter to control and tailor the supramolecular self-assembly on surfaces. Low surface coverage facilitates the appearance of porous networks; in contrast high surface coverage promotes the formation of compact structures [29].

### 1.2.1.3 Influence of Molecular Substituent

In the same way, the supramolecular self-assembly can be tuned through a precise choice of the molecular substituents used. In fact by changing molecular substituents, a modification of the intermolecular interactions can occur. This modification involves a change in the strengths and lengths of the chemical bonds, which can induce a molecular reorganization. An example of the influence of molecular substituents on the molecular organization is given by Takashi Yokoyama *et al.* [31] for four tertiarybutylphenyl porphyrin derivatives deposited on the inert Au(111) surface kept at room temperature. Cyanophenyl substituents are used to control the molecular organization, because they have a symmetric shape with an asymmetric charge distribution which is particularly adapted to create dipole-dipole interactions between neighboring molecular substituents. The porphyrin derivatives synthesized in the experiment of Takashi Yokoyama *et al.* are based on 5,10,15,20-tetrakis-(3,5-di-tertiarybutylphenyl)porphyrin ( $H_2$ -TBPP) molecule, which has a porphyrin core and four di-tertiarybutylphenyl (tBP) substituents, Figure 1.9a. At low coverage, single  $H_2$ -TBPP molecules are placed at the elbow of the Au(111) surface, Figure 1.9e. The replacement of a tBP substituent of the  $H_2$ -TBPP molecule by a cyanophenyl substituent (Figure 1.9b), leads to a new CTBPP<sup>7</sup> molecule which self-assembled at low coverage on gold surface into triangular clusters, Figure 1.9f. These triangular clusters are composed of three CTBPP molecules which are linked together through C–H···N–C hydrogen bonds between the cyanophenyl substituents, as it is confirmed by DFT calculations, Figure 1.9j. Finally, if a second tBP group is replaced by a cyanophenyl substituent in the  $H_2$ -TBPP molecule, then a new BCTBPP<sup>8</sup> molecule is synthesized with two types of isomers the cis-BCTBPP and trans-BCTBPP, Figures 1.9c,d; respectively. The cis-BCTBPP molecules are self-assembled into a supramolecular tetramer (Figure 1.9g), where the anti-parallel cyanophenyl substituents are linked to each other through the C–H···N–C hydrogen bonds, as it is confirmed by DFT calculations, Figure 1.9k. The trans-BCTBPP molecules are self-assembled in linear chains (Figure 1.9h), which are stabilized through the establishment of C–H···N–C hydrogen bonds between the cyanophenyl substituents, as shown in the Figure 1.9i.

To conclude, the chemical nature of the substituents as well as their positions in the molecular skeleton are crucial to control in a predictable way the supramolecular organization on metallic surfaces.

---

<sup>7</sup>CTBPP: (cyanophenyl)-tris(di-tertiarybutylphenyl)porphyrin.

<sup>8</sup>BCTBPP: bis(cyanophenyl)-bis(di-tertiarybutylphenyl)porphyrin.

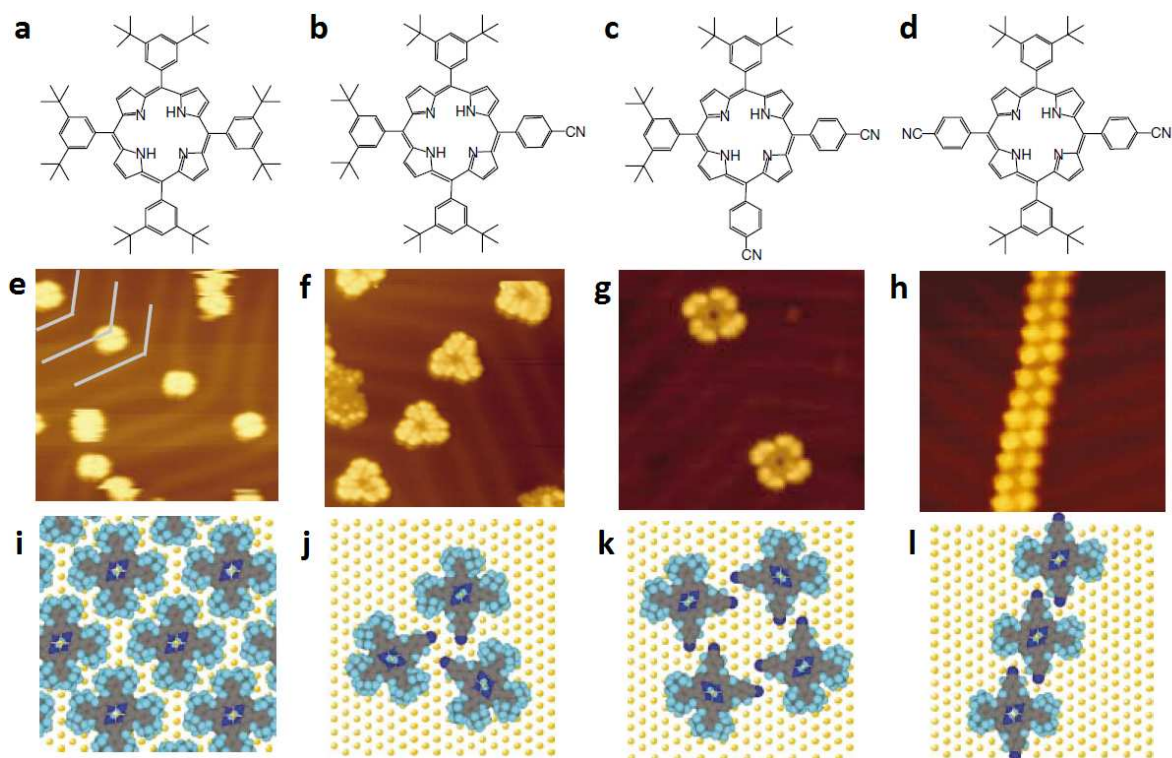


Figure 1.9: Chemical structures of the: **a**,  $H_2$ -TBPP; **b**, CTBPP; **c**, *cis*-BCTBPP; **d**, *trans*-BCTBPP. STM images at 63 K and molecular models of the corresponding supramolecular aggregations obtained on the Au(111) surface: **e**, **i**,  $H_2$ -TBPP island; **f**, **j**, CTBPP trimer; **g**, **k**, *cis*-BCTBPP tetramer; **h**, **l**, *trans*-BCTBPP wire (imaged area,  $20 \times 20 \text{ nm}^2$ ). The STM image of the single  $H_2$ -TBPP molecule consist of two rectangular protrusions surrounded by four lobes, corresponding to the central porphyrin and the tertiarybutyl substituents respectively [31].

#### 1.2.1.4 Influence of the Substrate

Another manner to control the supramolecular self-assembly is to modify the molecule-substrate interactions through a precise choice of the substrate used. For example the relatively strong reactivity of the Cu(111) surface can be used in order to create preferential adsorption sites for the Anthraquinone molecules, leading to the formation of a porous hexagonal network (Figure 1.6) which is not observed on less reactive surfaces [21]. However, strong molecule-substrate interaction makes harder to create organized molecular architectures in a predictable way by only considering the molecular skeleton and molecular substituents used. It is the reason why during my PhD, I preferred to use less reactive substrates like the Au(111) surface.

The Au(111) reconstruction, corresponds to a rearrangement of the atomic packing at the surface in order to minimize the surface energy. The modification of the atomic packing implies an atomic overdensity at the surface. This overdensity involves a uniaxial and uniform contraction of the topmost hexagonal layer in the  $[1\bar{1}0]$  direction

of approximately 4.55%, [32]. The typical fcc packing of the gold bulk is modified at the surface, leading to a rectangular unit-cell with lattice vectors  $22a$  and  $\sqrt{3}a$ , (where  $a = \frac{\sqrt{2}}{2}b$ , with  $b \simeq 4.08\text{\AA}$  the lattice parameter of the gold fcc bulk structure). The superstructure formed by the atomic rearrangement at the surface consists of alternating fcc and hcp packing with in between a transition region which appears bright in the STM images, Figure 1.10c. The fcc domains correspond to the largest dark regions in the STM images, whereas the hcp domains correspond to the dark regions with the smallest sizes. The difference in size between the fcc and hcp domains results from their difference in energy. The Au(111) exhibits a periodic pattern of pairwise parallel corrugation

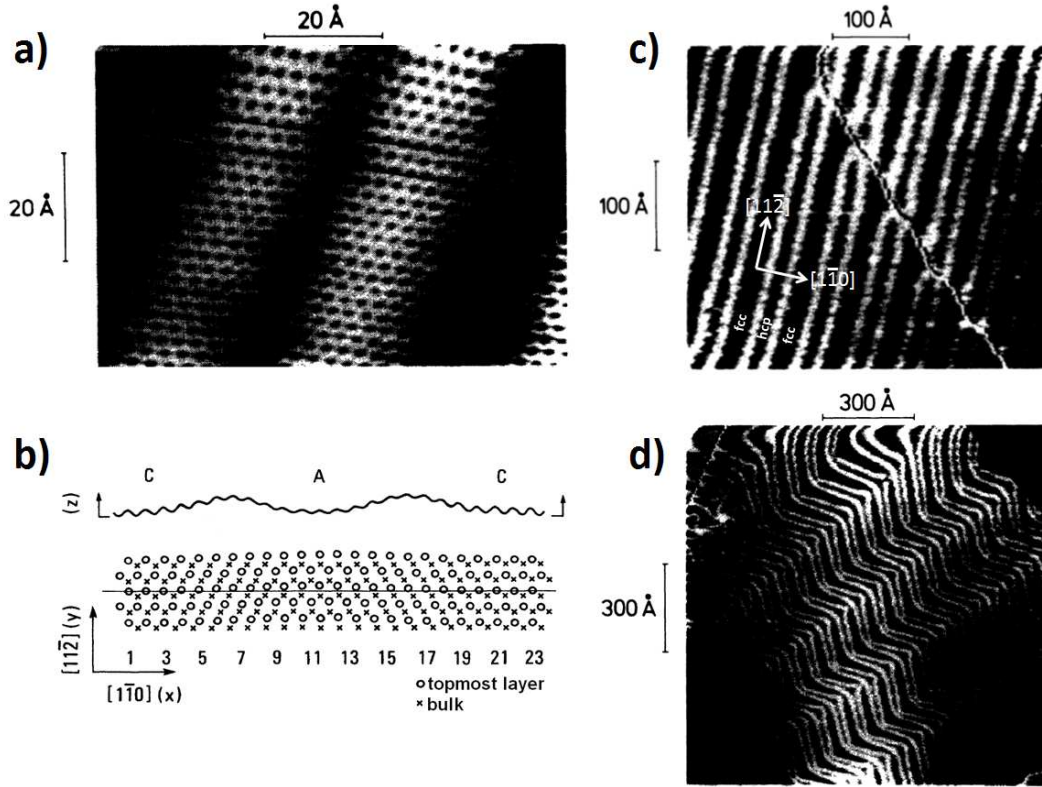


Figure 1.10: STM images of the  $[(22 \pm 1) \times \sqrt{3}]$  Au(111) reconstruction: (a) small-range with atomic resolution,  $8 \times 6 \text{ nm}^2$ ,  $V_s = -69 \text{ mV}$ ,  $I_t = 631 \text{ nA}$ , [32]; (b) Frenkel-Kontorova model for the Au(111) surface reconstruction. The crosses denote the positions of atoms in the second layer, whereas open circles denote the positions of atoms in the reconstructed topmost layer. C and A mark the regions of ABC (fcc) and ABA (hcp) stacking, respectively. The displacement of the atoms from the straight line which has been drawn in the  $[1\bar{1}0]$  direction appear clearly [33–35]; (c) medium range STM image which crossing a step edge ( $45 \times 45 \text{ nm}^2$ ), [32]; (d) wide range STM image  $120 \times 120 \text{ nm}^2$ , [32].

lines, running in the  $[11\bar{2}]$  direction, Figure 1.10c. The distance between neighbor pairs in the  $[1\bar{1}0]$  direction is  $22a = 63\text{\AA}$ , whereas the individual lines within a pair are separated by  $44\text{\AA}$ . The corrugation amplitude of the reconstructed surface is  $0.20 \pm 0.05\text{\AA}$ .

The superstructure unit-cell is rectangular ( $63 \times 4.7 \text{Å}^2$ ), with 24 surface atoms on 23 bulk atoms along the  $[1\bar{1}0]$  contraction direction [32–34], Figure 1.10a. It is possible to notice that this surface contraction could be described by a Frenkel-Kontorova model employing a sine-Gordon potential (Figure 1.10b), which will not be detailed here. An additional long-range periodicity can be observed in the reconstructed topmost layer, consisting of a modification of the corrugation lines direction by  $\pm 120^\circ$ , forming a zigzag pattern which is the so called "Herringbone" reconstruction. The typical distance between two modifications of the corrugation lines direction is  $\simeq 250 \text{Å}$ , but this distance can be affected by surface defects. This zigzag pattern allows to relax the uniaxial  $[1\bar{1}0]$  contraction in all the three surface directions, and thus enables a minimization of the total surface energy.

Another interesting thing is that the Au(111) reconstruction can affect the local reactivity of the substrate, and then can be used to tune the molecular self-organization. F.Silly *et al.* [35], give a perfect example of that, for a PTCDI-melamine thin film grown on Au(111) surface, Figure 1.11. The deposition of the PTCDI and Melamine molecules

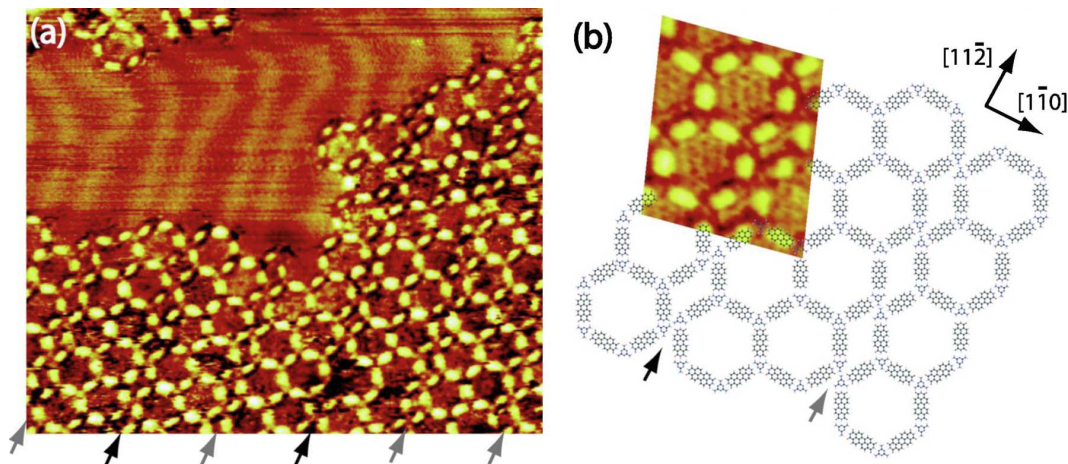


Figure 1.11: a) STM image of the PTCDI-melamine supramolecular honeycomb network formed on Au(111) substrate, taken at room temperature; Tunnelling parameters:  $50 \times 35 \text{nm}^2$ ,  $V_s = -1.5 \text{V}$ ,  $I_t = 0.15 \text{nA}$ . b) Molecular model of the supramolecular network with a superimposed high resolution STM image. The two types of parallelogram rows are indicated by black and gray arrows [35].

on Au(111) surface followed by a post-annealing at  $80^\circ\text{C}$  during 15h, lead to the formation of the supramolecular architecture presented in the Figure 1.11a. This network consists of alternating double-rows of hexagons and single-rows of parallelograms. Each hexagon is composed of six PTCDI and six Melamine molecules, whereas each parallelogram is composed of four PTCDI and six Melamine molecules, as indicated in the Figure 1.11b. The PTCDI molecules appear yellow and the melamine molecules appear brown in the STM images. The molecular architecture is stabilized by the formation of PTCDI-melamine dimers through the establishment of two  $\text{O} \cdots \text{H}$  and one  $\text{N} \cdots \text{H}$  hydrogen bonds, as shown in the Figure 1.11b. By comparing the PTCDI-Melamine

structure and the underlying Au(111)-( $22 \times \sqrt{3}$ ) substrate in Figure 1.11a, it appears that the separation between parallelogram rows matches with the periodicity of the herringbone reconstruction in the  $[1\bar{1}0]$  direction (around 6.3nm). In fact, the parallelogram structures are localized along the  $[11\bar{2}]$  direction in the fcc sites of the gold substrate, while the bright corrugation lines of the Au(111) surface pass through the center of the PTCDI-Melamine hexagons. Moreover, it can be noticed that PTCDI and Melamine molecules form a honeycomb structure entirely composed of hexagons on other substrates, like the Ag terminated Si(111) surface [36]. This shows that the PTCDI-Melamine parallelogram rows are present on the Au(111) surface in order to accommodate the honeycomb supramolecular networks with the periodicity of the underlying herringbone reconstruction in the  $[1\bar{1}0]$  direction, allowing an energy minimization of the system. Finally, this example shows that the Au(111) surface reconstruction can be used to tailor the supramolecular self-assembly of a mixture of PTCDI and Melamine molecules.

Another example of the influence of the Au(111) herringbone reconstruction on molecular organization is given by Takashi Yokoyama *et al.* [31], for a trans-BCTBPP<sup>9</sup> porphyrin derivatives depicted in the Figure 1.12a. The trans-BCTBPP porphyrin

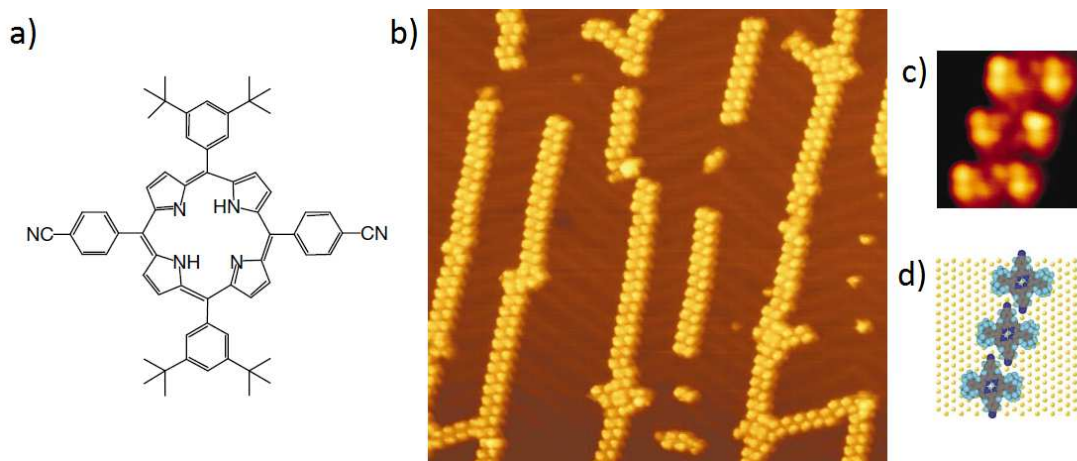


Figure 1.12: a) Chemical structure of the trans-BCTBPP porphyrin, where two cyanophenyl groups were substituted at the trans position. b) STM image at 63 K of trans-BCTBPP wires formed on the Au(111) surface (imaged area,  $70 \times 70\text{nm}^2$ ). The supramolecular wires are extended across the elbows of the herringbone patterns. The observed maximum wire length is above 100nm, depending on the terrace width. c) High-resolution STM image (imaged area,  $5.3 \times 5.3\text{nm}^2$ ) of the trans-BCTBPP wire network. d) The molecular model of the trans-BCTBPP wire structure [31].

molecules were deposited on the Au(111) surface kept at room temperature by sublimation from a Knudsen cell in a UHV environment, while the STM measurements were carried out at 63K. Figure 1.12b shows that the trans-BCTBPP form molecular

<sup>9</sup>The trans-BCTBPP porphyrin is a 5,10,15,20-tetrakis-(3,5-di-tertiarybutylphenyl)porphyrin, where two di-tertiarybutylphenyl substituents are replaced by two cyanophenyl groups at the trans position.

wires with a maximum length of 100nm, depending on the terrace width. These molecular chains are stabilized by the establishment of C–H···N–C hydrogen bonds between the cyanophenyl groups of the molecules, as it can be deduced from the high resolution STM image and DFT calculations in Figures 1.12c,d. Moreover Figure 1.12b, shows that the linear chains formed by the trans-BCTBPP molecules are placed at the elbows of the Au(111) reconstruction. This can be explained by the fact that the herringbone reconstruction changes the local reactivity of the gold surface, favoring the molecular nucleation on the most reactive sites of the substrate (elbows sites). Secondly the authors observed, that some branches are formed in other directions of the substrate due to the threefold symmetry of the Au(111) surface, Figure 1.12b. Finally, these results show that the trans-BCTBPP porphyrin supramolecular assembly can be tuned by using the herringbone reconstruction and by adjusting the terrace width of the Au(111) surface.

To conclude, relatively inert surfaces can be used as the Au(111) in order to minimize molecule-substrate interaction and then to create nanoarchitectures in a predictable way by only considering the molecule-molecule interaction. But in some cases it is needed to take into account the influence of the Au(111)-(22 ×  $\sqrt{3}$ ) herringbone reconstruction on molecular organization. In fact, for defined organic systems the herringbone reconstruction can influence the molecular nucleation and then the self-assembly.

## 1.2.2 Host-Guest Supra-Molecular Networks

A last way to control the self-assembly is to use host-guest supramolecular systems in order to organize molecular entities on surfaces which are not organized by themselves [16,28,37–41]. A beautiful manner to create host-guest supramolecular networks, is to use porous molecular architectures as templates for the adsorption of additional molecular species. In that way the underlying porous molecular network creates preferential adsorption sites for additional molecules, leading to the formation of organized host-guest supramolecular systems. Porous molecular architectures can be built by using single-component or multi-components system. In most cases the energy balance of the system favors the growth of molecular close-packed structures, which are more stable. Therefore, to realize porous molecular architectures it is necessary to choose molecules which can form many molecular-bonds, in order to stabilize the porous structure.

A first example of the use of porous systems to control the organization of additional organic entities on metal surface, is given by Meike Stöhr *et al.* [40] for the dehydrogenated DPDI<sup>10</sup> molecules on Cu (111) surface. Figures 1.13a,b show the hexagonal porous structure formed by thermally dehydrogenate DPDI molecules on Cu(111) surface. The dehydrogenation reaction generates complementary hydrogen-bonds, forming like a donor/acceptor system which is responsible to the growth of the honeycomb network [28]. Figure 1.13c, shows a STM image taken at 77K of the C<sub>60</sub> and ZnOEP<sup>11</sup> complexes subsequently deposited at room temperature on the dehydrogenate DPDI honeycomb structure. Both ZnOEP and C<sub>60</sub> are trapped and statistically distributed in the porous hexagonal structure. The authors have also shown that at room temperature

---

<sup>10</sup>DPDI: 4,9-diaminoperylene-quinone-3,10-diimine.

<sup>11</sup>ZnOEP: Zinc octaethylporphyrin.

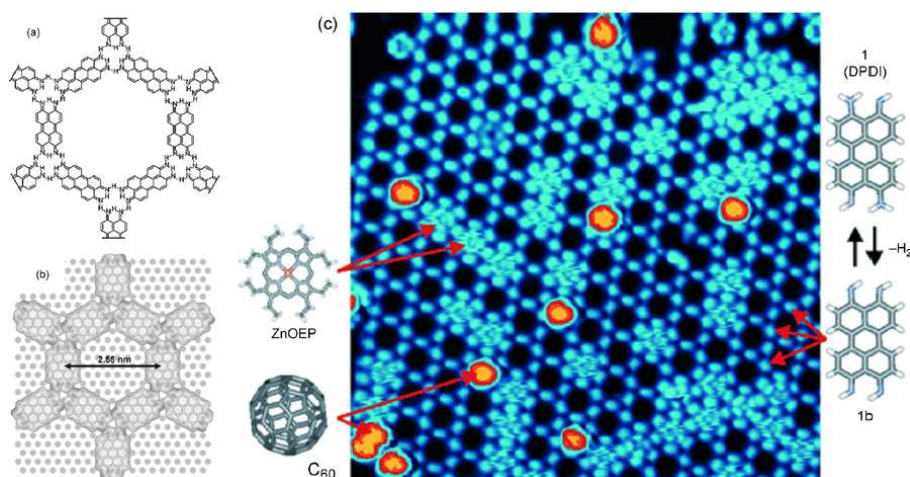


Figure 1.13: (a,b) Chemical structure and self-assembled structure of the dehydrogenated DPDI molecule on Cu (111) surface. (c) STM image of the DPDI hexagonal porous network, hosting ZnOEP and  $C_{60}$  molecules,  $30 \times 30 \text{ nm}^2$  [16, 40].

and in the absence of the DPDI porous network, the  $C_{60}$  molecules can move freely on the Cu(111) surface and form close-packed hexagonal islands (not shown here). In fact, there is the formation of significant attractive Van-der-Waals interactions between the  $C_{60}$  molecules, due to polarization fluctuation waves on these molecules. Nevertheless, when the  $C_{60}$  molecules are trapped in the DPDI porous network, they cannot jump from one pore to another. In contrast to  $C_{60}$ , the ZnOEP molecules don't display any ordered networks outside of the DPDI honeycomb structure. These results show how a porous supramolecular structure can be used to control the organization of different molecular entities on metallic surfaces.

Another example of a host-guest system is given by E. Mena-Osteritz et P. Bäuerle [41], for the complexation of  $C_{60}$  on a Cyclooligothiophene (C[12]T) monolayer templates, at the 1,2,3-trichlorobenzene/HOPG<sup>12</sup> interface. Figure 1.14a, shows the close-packed structure formed by the cyclooligothiophene on HOPG(001). The conjugated  $\pi$ -system of the cyclothiophene rings appears in bright color due to higher tunneling current. The insulating alkyl chains and the interior cavity of the cyclothiophene appear darker in the STM image, due to a lower tunneling current. Semi-empirical calculations show that the cyclooligothiophene molecules are connected to each other through weak Van-der-Waals interactions between the alkyl side chains. Figure 1.14a, shows an isolated  $C_{60}$  molecule (white arrow) adsorbed at the 1,2,3-trichlorobenzene/HOPG interface. Although Figure 1.14c, shows the different adsorption sites of the  $C_{60}$ -Cyclooligothiophene system. There are two main adsorption sites, labeled "C" (cavity), or "R", (rim). The R-type fullerene is imaged as a bright spot with an apparent diameter of 1 nm, whereas the C-type fullerene is imaged as a diffuse spot with an apparent diameter of 1.6 nm. This shows that the C adsorption sites are less stable than the R sites. In the R sites the  $C_{60}$  molecules are really localized, whereas in the C sites the

<sup>12</sup>HOPG: highly ordered pyrolytic graphite.

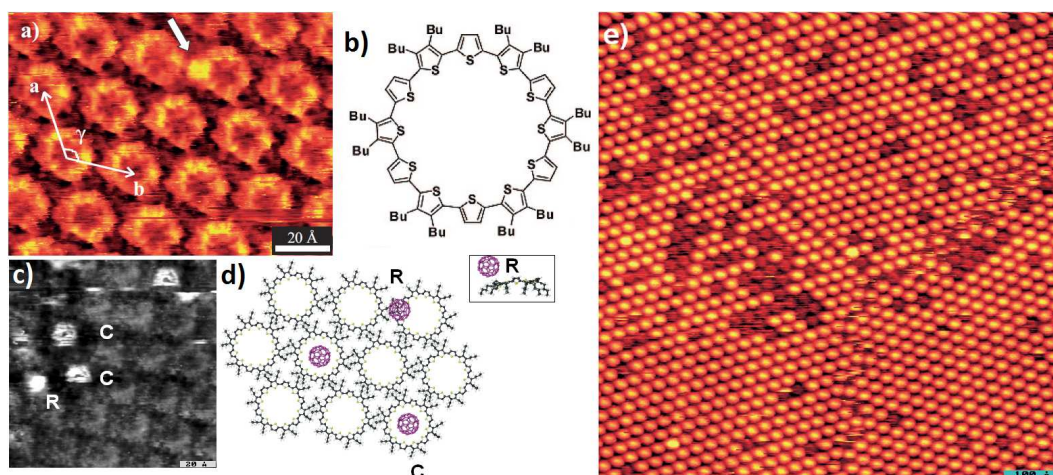


Figure 1.14: a) STM image of a monolayer of C[12]T on HOPG(001), including a C[12]T-C<sub>60</sub> complex (white arrow). Image area: 11.6nm×8.7nm; tunneling conditions: bias voltage  $V_s=-700$  mV, tunneling current  $I_t=44$ pA; b) Scheme of the conjugated macrocycle C[12]T; c) STM image of a monolayer of C[12]T on HOPG and C<sub>60</sub>-fullerenes adsorbed at different sites. Image area: 20nm×20nm; tunneling conditions:  $V_s=-705$ mV,  $I_t=57$ pA. Fullerenes at different adsorption sites are labeled C (cavity) and R (rim). d) Calculated model for the different adsorption sites of the fullerenes on the macrocycle-modified surface (inset, upper right); e) STM image of C[12]T-C<sub>60</sub> complexes, including some non-complexed macrocycles (deep red). Image area: 79nm×79nm; tunneling conditions:  $V_s=-500$ mV,  $I_t=7$ pA, [41].

C<sub>60</sub> molecules can move inside the pores. Moreover the authors have shown that the complexation ratio is 1:1, which means that a second C<sub>60</sub> molecule is never adsorbed on a cyclooligothiophene which has already been complexed. Finally Figure 1.14e, shows that at high coverage the ordered monolayer of cyclooligothiophene acts as a template to epitaxially grow three-dimensional nanoarchitectures with the C<sub>60</sub> molecules [41].

To summarize, the use of porous supramolecular networks to create host-guest systems is a useful tool to organize molecular entities which are not organized by themselves on metal surfaces. It is the reason why I have used these kinds of host-guest systems during my PhD, in order to control the organization of sodium-chloride compound on Au(111) surface (see § 5.3.2). In conclusion, a lot of tools can be used in order to control the supramolecular self-assembly on metal surfaces, like the substrate and molecular substituents used, as well as the sample's temperature, surface coverage and host-guest systems. However the control of the structure of organic self-assembled monolayers is not sufficient by itself to build the new generation of organic compounds. In fact the control of the electronic properties of these self-assembled monolayers is also of prime importance in order to construct useful organic devices. It is the reason why in the following sections I will describe some results from the literature on the characterization of the electronic properties of organic self-assembled monolayers.

## 1.3 Electronic Properties of Self-Assembled Molecular Thin Films

Many surface sensitive techniques can be used to characterize the electronic states of molecular thin films grown on surfaces. For example the X-ray photoemission spectroscopy (XPS) can be used to determine the shape and energy positions of the sample's electronic states (§1.3.1). The Near Edge X-ray Absorption Fine Structure (NEXAFS) spectroscopy can be used to determine the molecular adsorption geometry on substrates (§1.3.2). Finally, the resonant photoemission spectroscopy (RPES) also called the core-hole clock spectroscopy can be used to estimate the charge transfer process occurring at the metal-organic interface (§1.3.3).

### 1.3.1 Influence of Molecular Substituents on the Occupancy and Energy Position of the sample's Electronic States

X-ray photoemission spectroscopy, can be used in order to determine the occupancy and the energy position of the electronic states of a sample of interest. This is of prime importance to get information about the electronic properties of self-assembled monolayers. Moreover XPS, can be used to get chemical information about how the molecular substituents can affect the sample's electronic states. A lot of studies have been performed in order to determine the occupancy and energy position of the electronic states of organic self-assembled structures on surfaces [42–44]. A great example of that is given by Dietrich R.T. Zahn *et al.*, for PTCDA and DiMe-PTCDI<sup>13</sup> deposited onto sulfur-passivated GaAs(001), Figure 1.15. The peak-fit analysis was done by using the

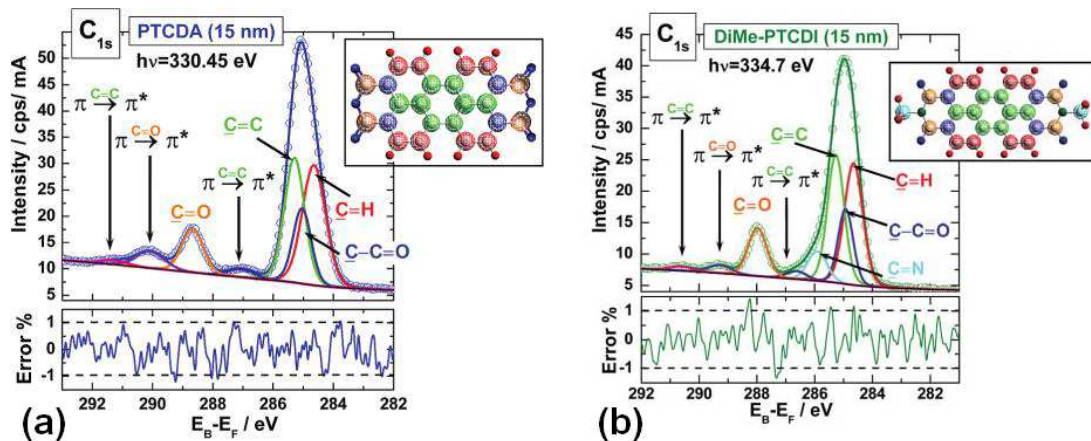


Figure 1.15: Results of the peak fit analysis: (a)  $C_{1s}$  spectrum of a PTCDA thin film. (b)  $C_{1s}$  spectrum of a DiMe-PTCDI thin film [42].

so-called Voigt profile function, which describes the core-level line shape by a convolution

<sup>13</sup>DiMe-PTCDI: N,N'-dimethyl-3,4,9,10-perylene tetracarboxylic diimide.

of Gaussian and Lorentzian contributions. The Lorentzian width ( $W_L$ ) corresponding to the core-hole lifetime, was fixed at 0.075eV during the fitting procedure [42]. In contrast, the authors allowed the Gaussian width ( $W_G$ ) corresponding to the experimental broadening to vary during the fitting procedure. The peak-fit analysis was done with the support of DFT calculations, which will not be shown here. Figure 1.15a shows the results of the peak fit analysis obtained for the  $C_{1s}$  spectrum of a PTCDA thin film. The  $C_{1s}$  spectrum is composed of two main peaks, one at 285.3eV and one at 288.9eV. The first peak at 285.3eV corresponds to the carbon atoms of the aromatic part of the PTCDA molecule. In contrast the peak at 288.9eV corresponds to the carbon atoms of the anhydride part of the PTCDA molecule. The carbon atoms involved in the C=O bonds have a higher binding energy than the carbon atoms placed in the aromatic rings (C=C, C-H, C-C=O). This higher binding energy comes from the higher electronegativity of the oxygen atom compared to carbon and hydrogen atoms [42]. Figure 1.15a, shows also the presence of three small peaks lying at binding energies of 287eV, 290eV, and 291.2eV. These weaker peaks are attributed to multi-electron excitation, i.e. to shake-up<sup>14</sup> process. Finally by comparing the peak areas of each compound, it becomes possible to determine the sample stoichiometry. The authors have done the same fitting procedure for the  $C_{1s}$  spectrum of a DiMe-PTCDI thin film [42], Figure 1.15b. The peak fit analysis shows that the aromatic peak of the  $C_{1s}$  spectrum of DiMe-PTCDI presents an asymmetry at the high binding energy range. This asymmetry can be attributed to carbon atoms involved in the C-N bonds. The other peaks of Figure 1.15b, are identical to those previously observed for PTCDA. However, the binding energies of these peaks and their line-shape vary significantly from PTCDA to DiMe-PTCDI. The C=O peak is shifted by 0.6eV to the lower binding energies for DiMe-PTCDI compared to PTCDA. The replacement of oxygen atoms by amino groups which are less electronegative, allows to reduce the energy splitting between the aromatic parts and the functional group parts of the  $C_{1s}$  spectrum. This example shows that the occupancy and the energy position of the sample's electronic states are strongly affected by the molecular substituents used.

Dietrich R.T. Zahn *et al.* [42], have obtained some information by analyzing the  $O_{1s}$  spectrum of PTCDA and DiMe-PTCDI deposited onto sulfur-passivated GaAs(001), Figure 1.16 The line-shape of the PTCDA and DiMe-PTCDI  $O_{1s}$  spectra was curve fitted by using a Voigt function with a Lorentzian width fixed at 120meV [42]. Figure 1.16a, shows that the  $O_{1s}$  spectrum of a PTCDA thin film is composed of two main peaks at 531.5eV and 533.5eV. These peaks are attributed to the oxygen atoms involved in the O=C and C-O-C bonds respectively. Moreover the fitting procedure reveals that there is an intense shake-up satellite at 533.2eV. In contrast the  $O_{1s}$  spectrum of a DiMe-PTCDI exhibit only one main peak at 531.5eV, corresponding to the oxygen atoms involved in the O=C bond. The signature of the oxygen atoms involved in the C-O-C bonds disappears, due to the replacement of the two central oxygen atoms of PTCDA by two amine groups in DiMe-PTCDI. The  $O_{1s}$  spectrum of DiMe-PTCDI also display a  $\pi - \pi_{C=O}^*$  shake-up peak at 533.2eV. However the intensity of this peak is lower

---

<sup>14</sup>The shake-up process corresponds to the excitation of a supplementary valence electron around the core-hole. The excited electron is promoted from an occupied to an unoccupied energy level. This excitation results in the appearance of intermediate states, corresponding to satellite peaks in the XPS spectrum ( $\pi - \pi^*$  transition).

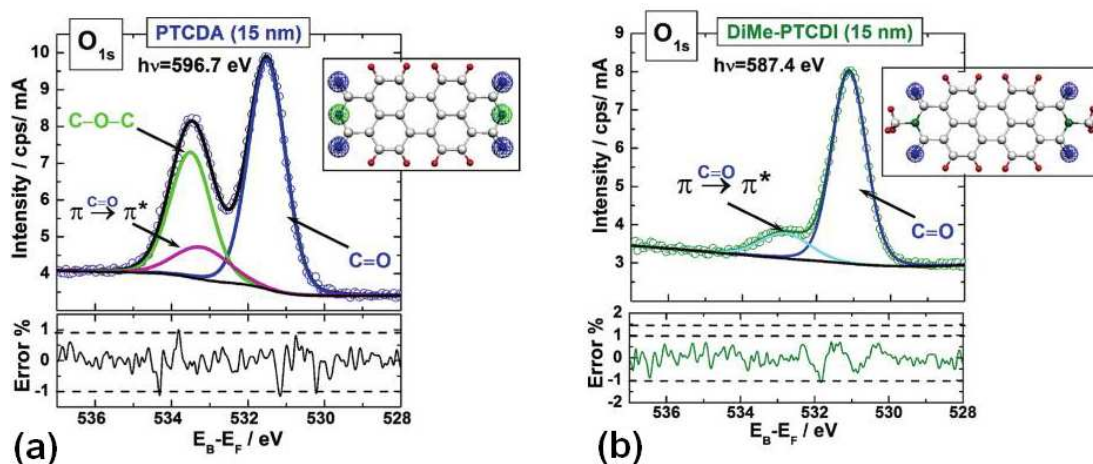


Figure 1.16: Results of the peak fit analysis: (a)  $O_{1s}$  spectrum of a PTCDA thin film. (b)  $O_{1s}$  spectrum of a DiMe-PTCDI thin film [42].

than the  $\pi - \pi_{C=O}^*$  shake-up peak of PTCDA. Moreover the  $\pi - \pi_{C=O}^*$  shake-up process correspond to a charge transfer from the aromatic part to the functional group. This charge transfer is facilitated in the case of PTCDA due to the higher electronegativity of oxygen compared to the amino group of DiMe-PTCDI. Finally, this explains the fact that the  $\pi - \pi_{C=O}^*$  peak intensity is higher for PTCDA, than for DiMe-PTCDI.

To summarize X-ray photoemission spectroscopy is a useful tool in order to obtain chemical information on the molecular film used. In fact, XPS can be performed in order to determine the influence of the molecular substituents used on the occupancy and energy position of the sample's electronic states. In that way it is possible to determine the influence of molecular substituents on the electronic properties of self-assembled thin films. This is of prime importance, in order to develop the new generation of organic devices. In addition to that the determination of the molecular adsorption geometry on metallic surfaces is crucial, because it is directly related to the molecule-substrate and molecule-molecule interactions governing the self-assembly process. It is the reason why in the next section I described how XPS (and related techniques) can be used to determine the adsorption geometry of molecules on surfaces.

### 1.3.2 Determination of the Molecular Adsorption Geometry

Angular dependent NEXAFS (Near-Edge X-ray Absorption Fine Structure) spectroscopy is an appropriated tool to determine the molecular adsorption geometry of planar molecules. Liang Cao *et al.* give a perfect example of the use of Angular dependent NEXAFS spectroscopy to determine the adsorption geometry of PTCDA<sup>15</sup> molecules on the Au(111) surface [45]. Figures 1.17a,b show the results of the NEXAFS spectra obtained for PTCDA at monolayer and multilayer coverages. The NEXAFS spectra were taken for different incident angles ( $\theta$ ) of the X-ray beam. The incident angle  $\theta$

<sup>15</sup>PTCDA: 3,4,9,10-perylene-tetracarboxylic dianhydride.

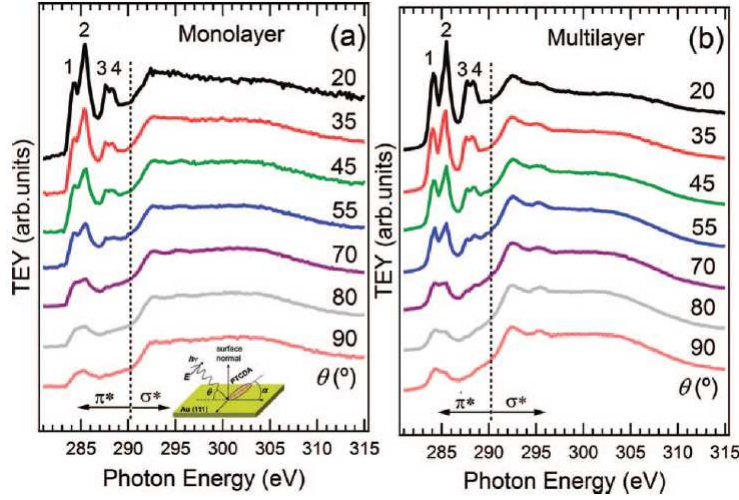


Figure 1.17: Angular dependent NEXAFS spectrum of PTCDA molecules on Au(111) surface taken at the C K-edge: a) for monolayer coverage, b) for multilayer coverage (10ML) [45].

of the X-ray beam, is defined with respect to the substrate surface plane (inset in Figure 1.17a). Figures 1.17a,b show the appearance of sharp resonant peaks below 290eV (labeled 1 to 4), which are attributed to the  $C_{1s} \rightarrow \pi^*$  transitions. However the broad absorption peak observed above 290eV can be assigned to the  $C_{1s} \rightarrow \sigma^*$  transitions. Strong modifications of the peak intensity are observed by changing the incident angle  $\theta$ . The PTCDA monolayer and multilayer spectra, both display a strongest  $\pi^*$  resonances at grazing incidence ( $\theta = 20^\circ$ ), and a strongest  $\sigma^*$  features at normal incidence ( $\theta = 90^\circ$ ). Moreover it is important to notice that the  $\pi^*$  orbitals are in majority oriented out of the molecular plane for  $\pi$ -conjugated molecules such as PTCDA. Therefore the angular dependence observed in Figures 1.17a,b, can be attributed to a nearly flat-lying adsorption geometry of the PTCDA molecules on the Au(111) surface.

Furthermore, the authors shown that a quantitative estimation of the molecule-substrate separation angle can be deduced from NEXAFS spectra [45]. The evolution of the  $\pi^*$  resonance intensity with the molecular plane tilt angle  $\alpha$ , for a specific x-ray incidence angle  $\theta$  is given by the following equation:

$$I_{\pi^*} = CP \left( \sin(\alpha)^2 \sin(\theta)^2 + 2 \cos(\alpha)^2 \cos(\theta)^2 \right) + C(1 - P) \sin(\alpha)^2, \quad (1.3)$$

Where  $I_{\pi^*}$  is the  $\pi^*$  resonance intensity, C is the normalization constant and P is the linear polarization of the X-ray beam. The molecular plane tilt angle  $\alpha$ , is measured with respect to the substrate surface plane. Figure 1.18 shows the intensity of the strongest  $\pi^*$  resonance (peak 2) depending on the incident angle of the X-ray beam ( $\theta$ ). The curve which corresponds to the PTCDA monolayer film is drawn with open circle signs, while the curve corresponding to the PTCDA multilayer film is drawn with cross signs. Finally, the theoretical curves obtained from equation 1.3 for various molecular tilt angles ( $\alpha$ ) are drawn in solid line. The normalization procedure introduced an error bar, which

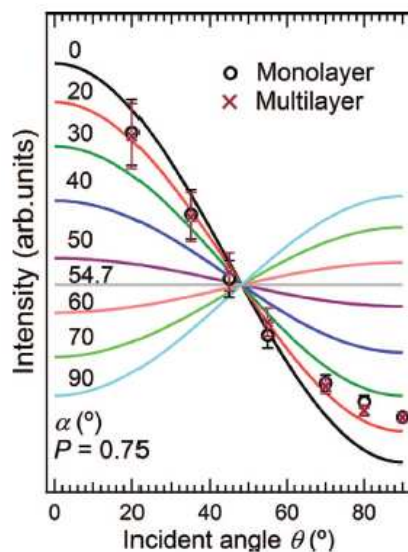


Figure 1.18: Intensity of the strongest  $\pi^*$  resonance of the NEXAFS spectrum of PTCDA on Au(111) surface (peak 2 in Figure 1.17) in function of the incident angle of the X-ray beam ( $\theta$ ), for monolayer coverage (open circle) and multilayer coverage (cross). In contrast, the solid-line represent the theoretical results of the angular dependence of  $\pi^*$  resonances for various molecular tilt angles [45].

is estimated to be 10% of the resonance intensity. The authors estimate the molecular angle tilt  $\theta$  to be  $21 \pm 10^\circ$  for both monolayer and multilayer [45]. It is important to notice that the PTCDA tilt angle estimation with NEXAFS spectroscopy is greatly overestimated. In fact STM measurements show that the PTCDA adsorption geometry is totally flat ( $\alpha = 0^\circ$ ) at monolayer coverage [46, 47]. The difference obtained between NEXAFS and STM measurements for the determination of  $\alpha$  can be partially explained by the fact that, there are some tilted PTCDA molecules adsorbed at step-edges or at surface defect sites. Moreover there are some thermal vibrations and distortions of the molecular plane which can affect the peak intensities observed in the NEXAFS spectrum [45].

To summarize, the angular NEXAFS spectroscopy is a useful tool, in order to determine the adsorption geometry of molecules on metal surface. In contrast to STM, the angular NEXAFS spectroscopy is not limited by the insulating molecular film thickness, i.e. the molecular adsorption geometry can be determined even at multilayer coverage. The knowledge of the adsorption geometry of molecules on surfaces is of prime importance, because it can give some information on the molecule-substrate interaction. Indeed the atomic species placed close to the surface are interacting stronger with the substrate than the atomic species placed far away. Additionally the comparison of the angular NEXAFS spectra obtained at monolayer and multilayer coverages can give some information about the molecule-molecule interactions. Both information are of prime importance to create self-assembled nanodevices. In addition to that it is also interesting to take a look on the charge transfer dynamics occurring at the metal-organic

interface, in order to determine the possibility to use a self-assembled architecture in organic photovoltaic devices.

### 1.3.3 Estimation of the Charge Transfer Time at the Metal-Organic Interface

The charge transfer time at the metal-organic interface can be estimated by using Resonant Photoemission Spectroscopy (RPES). A detail description of the resonant photoemission process is given in §2.2.1.5 of this document. A beautiful example of the use of the RPES to determine the charge transfer time is given by Aristov *et al.* [48, 49], for pristine CuPc<sup>16</sup> molecules deposited onto Au(100) at monolayer and multilayer coverages, Figure 1.19. The RPES spectra of figure 1.19, are taken for a photon energy

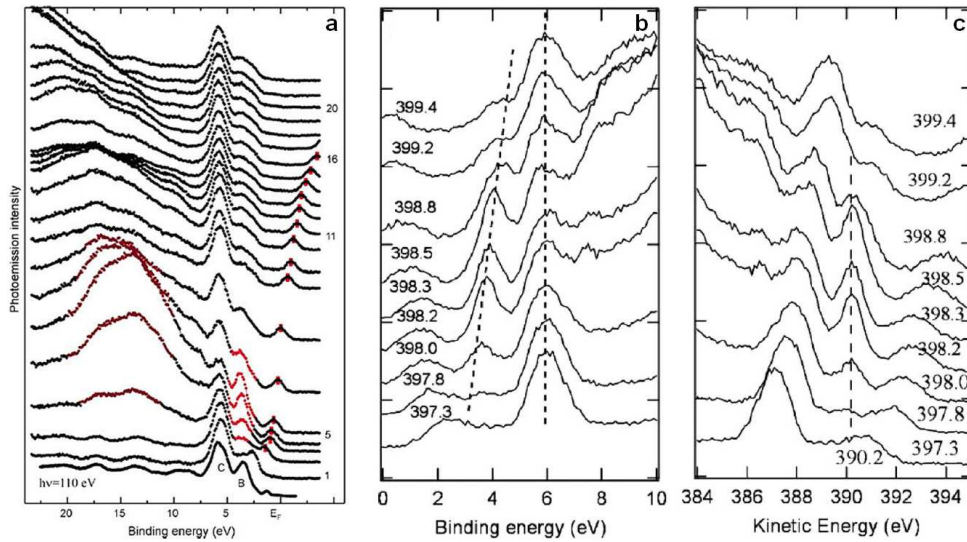


Figure 1.19: RPES spectra across the  $N_{1s} \rightarrow \pi^*$  resonance: a) for a pristine CuPc of 7nm thickness deposited on Au(100), b) for a multilayer of CuPc on Au(111), c) for a monolayer of CuPc on Au(111) [48, 49].

scanning across the  $N_{1s} \rightarrow \pi^*$  resonance. Figure 1.19a, shows the RPES spectrum of a CuPc multilayer grown on Au(100). In this Figure appears a sharp resonating feature at 3.7eV below the Fermi level. This feature is attributed to an autoionization decay process of the  $N_{1s}$  core-hole. Moreover Figure 1.19a shows a broad peak in the binding energy range of 10-20eV. The authors ascribe this broad feature to a spectator decay process. Theoretical calculations show that the strong resonant peak obtained at a binding energy of 3.7eV corresponds to an electronic state localized on the nitrogen atoms of the CuPc macrocycle. Finally, the appearance of the strong resonance peak at 3.7eV, and the presence of the spectator decay channel in the RPES spectrum of the CuPc/Au(100) interface, show that the charge transfer time is greater than the core-hole

<sup>16</sup>CuPc: Copper Phthalocyanine.

lifetime ( $6fs$ , [49, 50]). Figure 1.19b, shows the RPES spectrum of a CuPc multilayer grown on Au(111). This figure exhibits a strong attenuation of the peak resonance intensity obtained at  $3.7eV$ . This weak resonance shows that the excited electrons don't participate to the autoionization process, because of fast charge transfers occurring at the metal-organic interface. Therefore, in that case the charge transfer time is estimated to be smaller than the core-hole lifetime ( $6fs$ , [49, 50]). Finally it is possible to conclude that the charge transfer time observed at the metal-CuPc interface can be tuned by changing the metallic substrate used.

Another example of the qualitative determination of the charge-transfer time at the metal-organic interface is given by W. Chen *et al.* [51], for BBB<sup>17</sup> and BFF<sup>18</sup> molecules, Figure 1.20. Both molecules have been deposited on the cleaned Au(111) surface. DFT

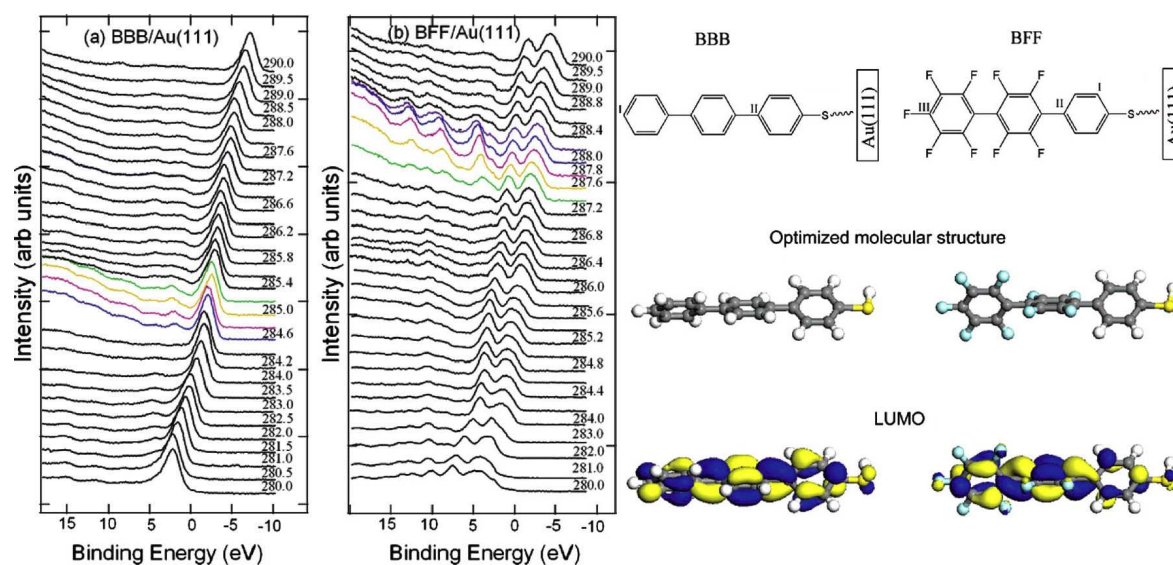


Figure 1.20: RPES spectra across the C K-edge of: a) BBB molecules on Au(111), b) BFF molecules on Au(111). Inset: DFT calculation of the optimized molecular structure, and LUMO states of the BBB and BFF molecules. The carbon atoms are represented in gray color, hydrogen in white, sulfur in yellow and fluorine in cyan [49, 51].

calculations show that the adsorption geometry of the BBB molecules is non-planar. The BBB molecules are linked to the Au(111) surface through the sulfur atom. The phenyl group attached to the sulfur atom is orthogonal to the Au(111) surface plane, whereas the two other phenyl groups are tilted with respect to the first one by the same angle. In this configuration the twist angles are small, resulting to a delocalization of the LUMO over the whole molecular skeleton. In the same way, the adsorption geometry of the BFF molecules consists of a phenyl ring orthogonal to the surface plane which is bound through the sulfur atom. However for BFF molecules, the second phenyl ring is almost perpendicular to the plane of the first and of the third phenyl rings. In this

<sup>17</sup>BBB: 1,1',4',1''-terphenyl-4''-thiol.

<sup>18</sup>BFF: p-thiophenyl-nonafluorobiphenyl. The BFF molecules can be obtained by substituting four hydrogen atoms of the BBB molecules with fluorine.

configuration the LUMO remains localized on the two fluorinated benzene rings. This explains the fact that the spectator decay intensity of the BBB photoemission spectrum is rather small, however it is stronger for the BFF molecules, Figures 1.20a,b. This finally reveals that the charge transfer is faster for the BBB molecules than for BFF, and may be placed below the 6fs range. In the case of the BFF molecules the fast charge transfer is inhibited by the weak overlapping between the phenyl rings. To conclude the molecular conformation and the molecular substituents used are key parameters, in order to control the charge transfer dynamics at the metal-organic interface [49, 51].

A last example of the use of resonant photoemission spectroscopy to determine the charge transfer time at the metal-organic interface is given by Vilmercati *et al.* for PTCDA molecules deposited onto Au(110) surface [49]. Figure 1.21a shows the two-

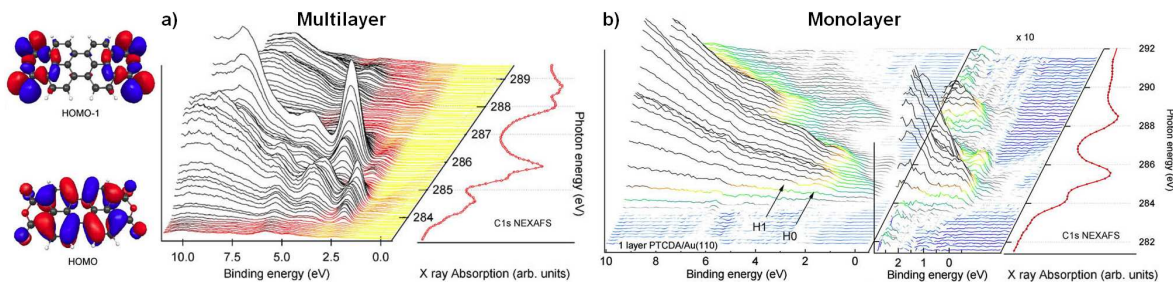


Figure 1.21: Two-dimensional RPES map at a constant binding energy across the C K-edge of a PTCDA film grown on Au(110): a) At a monolayer coverage, b) at a multilayer coverage [49].

dimensional RPES map obtained for a PTCDA multilayer film grown on Au(110) surface. Strong peaks are observed at 2.5, 4.1 and 6eV, which are attributed respectively to the HOMO and lower states (H-1, H-2) of the PTCDA molecule [49]. Sometime the strong photoemission resonances observed, are in correspondence with the NEXAFS absorption peaks. In that case the resonance peak can be assigned to an autoionization process (participator or spectator decay), which requires spatial overlapping between the involved wavefunctions [49]. For example, the HOMO (H-0) resonates strongly with the  $C_{perylene}1s \rightarrow LUMO$  transition, whereas the H-1 peak resonates preferentially with the  $C_{perylene}1s \rightarrow LUMO + 1$  transition obtained for a photon energy of 286eV. Moreover Figure 1.21a shows that the H-0 and H-1 resonance lines disappear completely with the  $C_{anhydride}1s \rightarrow LUMO$  transition at 288eV. This shows that the H-0 and H-1 wavefunctions are strongly located at the molecular end-group [49]. Furthermore, the resonances observed lie at a fixed binding energy revealing that the participator decay takes part in the autoionization process. Therefore, the excited electron in the LUMO+1 state remains localized on the molecules long enough for the participator decay to occur. Finally, the charge transfer time is qualitatively estimated to be in the order or longer than the  $C_{1s}$  core-hole lifetime (6fs, [49]). Figure 1.21b shows the two-dimensional RPES map for a PTCDA monolayer film grown on Au(110) surface. The H-0 and H-1 resonance peaks are strongly attenuated compared to the RPES multilayer spectra. This indicated that the excited electrons in the LUMO (L0), L1, L2, and L3 must be delocalized in

the metallic surface states, fast enough to prevent the autoionization decay process. Therefore the charge transfer time is estimated to be shorter than the  $C_{1s}$  core-hole lifetime ( $6fs$ , [49]). To conclude the precise control of the molecular film thickness is a key parameter to master the charge transfer time at the metal-organic interface.

To summarize these results show that the resonant photoemission spectroscopy is a useful tool to characterize the charge transfer dynamics at the metal-organic interface. Moreover these examples show that the charge transfer dynamics at the metal-organic interface is strongly influenced by the metallic surface and molecular substituents used, as well as by the molecular conformation and film thickness. The understanding of the modifications of the charge transfer time at the metal-organic interface through these parameters is of prime importance in order to develop new organic devices.

## Chapter Conclusions

In this chapter I described some results taken from the literature on the structures and electronic properties of organic self-assembled monolayers. These results show that a useful manner to build organic nanodevices is to take advantage of a self-assembly process which comes from a complex balance between the molecule-molecule and molecule-substrate interactions. Moreover the molecular organization of the resulting self-assembled nanoarchitectures can be controlled through a precise choice of the substrate and molecular substituents used. The final molecular arrangement can also be tuned by using host-guest systems and by adjusting the sample's temperature and surface coverage. In addition to that, to create useful organic devices it is also needed to determine the electronic properties of the self-assembled monolayer in order to understand the relation between the molecular structure and the resulting electronic properties. The final objective of that is to design devices at the nanometer-scale which possess well defined electronic properties. This is of prime importance in the field of nanoelectronics. Scanning Tunneling Microscopy (STM) combine with X-ray Photoemission Spectroscopy (XPS) are the appropriate techniques to get information about the structural and electronic properties of the self-assembled organic films. In fact STM allows to characterize, the molecular organization on metallic surfaces with an atomic resolution, as well as to operate single molecule manipulation with the STM tip. In addition to that XPS can give information about the occupancy and the energy position of the electronic states of the sample of interest. Moreover XPS and related techniques like RPES can be used to determine the charge transfer dynamics at the metal-organic interface. Finally, angular NEXAFS spectroscopy can be used to determine the molecular adsorption geometry even at a multilayer coverage. These information are of prime importance to develop organic devices for electronic and photovoltaic applications. It is the reason why in my PhD I have used STM and XPS techniques. Both techniques are widely described in the following chapter.

# Chapter 2

## Experimental Setups

As shown in the previous chapter, to develop the new generation of organic devices it is crucial to understand and control the relation between the structure and the electronic properties of the self-assembled organic films. An appropriate way to do that is to combine Scanning Tunneling Microscopy (STM) with photoemission spectroscopy techniques (XPS, NEXAFS and RPES). It is the reason why in this chapter I will describe the theoretical background, as well as the working principle of the STM and photoemission spectroscopy techniques used during my PhD.

### 2.1 Scanning Tunneling Microscopy

Here I will expose first, a simplified model of the tunneling effect, and tunneling current which appear in a STM experiment. Secondly I will describe the UHV system, the vibration isolation system, and the piezoelectric tube used in our STM experimental setup.

#### 2.1.1 The Tunneling Effect and Tunneling Current

##### 2.1.1.1 Simplified Model of the Tunneling Effect

The work of C.J. Davisson and L.H. Germer in 1927, is the first to show the wave nature of electrons [52]. In fact, they observed that an electron beam diffracts on the periodic array of atoms in a crystal. The quantum mechanics takes into account this wave nature by describing the electrons with a wave-function  $\Psi(\vec{r}, t)$ , satisfying to the Schrödinger equation:

$$i\hbar\frac{\partial}{\partial t}\Psi(\vec{r}, t) = -\frac{\hbar^2}{2m}\nabla^2\Psi(\vec{r}, t) + V(\vec{r}, t)\Psi(\vec{r}, t), \quad (2.1)$$

where an electron possesses a mass  $m$ , and was placed in the potential  $V(\vec{r}, t)$ . The Laplacian operator is  $\nabla^2 = \frac{\partial^2}{\partial x^2} + \frac{\partial^2}{\partial y^2} + \frac{\partial^2}{\partial z^2}$ . The Schrödinger equation replaces the equations of motions in classical mechanics, to describe the temporal and spatial evolution of electrons. The wave-function  $\Psi(\vec{r}, t)$ , represents a probability amplitude, whereas  $|\Psi(\vec{r}, t)|^2 d\vec{r} = \Psi^*\Psi d\vec{r}$ , represents the probability to found an electron in the volume

$d\vec{r}$ , with  $\Psi^*$  the complex conjugate of  $\Psi$ . By considering that the potential is time-independent  $V(\vec{r}, t) = V(\vec{r})$ , then the solution of equation 2.1 becomes:

$$\Psi(\vec{r}, t) = \psi(\vec{r})e^{-i\omega t}, \quad (2.2)$$

where  $\omega$  is a pulsation. By introducing this wave-function in the equation 2.1, it comes:

$$E\psi(\vec{r}) = -\frac{\hbar^2}{2m}\nabla^2\psi(\vec{r}) + V(\vec{r})\psi(\vec{r}), \quad (2.3)$$

where  $E = \hbar\omega$  is the electron energy. Equation 2.3 corresponds to the time-independent Schrödinger equation. In the case of free electron  $V(\vec{r}) = 0$ , the equation 2.3 has the solution:

$$\psi(\vec{r}) = Ae^{i\vec{k}\cdot\vec{r}}, \quad (2.4)$$

where  $A$  is a constant, and  $\vec{k}$  is the wave-vector, satisfying to the dispersion relation:

$$\omega = \frac{\hbar k^2}{2m}, \quad (2.5)$$

Finally, the free electron is described by the plane wave:

$$\Psi(\vec{r}, t) = Ae^{i(\vec{k}\cdot\vec{r}-\omega t)} \quad (2.6)$$

The wave nature of the electron gives it a purely quantum behavior, which cannot be explained by the classical mechanics. A perfect example of that is obtained for a one-dimensional square potential barrier, which can describe in a first approximation the electron behavior in a STM tunneling-junction.

Figure 2.1, shows the example of a one-dimensional square tunneling barrier with a height  $V_0$  and a width  $d$ . For this system the Schrödinger equation 2.3, becomes:

$$E\varphi(z) = -\frac{\hbar^2}{2m}\frac{d^2}{dz^2}\varphi(z) + V(z)\varphi(z), \quad (2.7)$$

Where  $\varphi(z)$  is the one-dimensional wave-function, and the potential  $V(z)$  is given by:

$$V(z) = 0, \text{ for } z < 0; \quad (2.8)$$

$$V(z) = V_0, \text{ for } 0 \leq z \leq d; \quad (2.9)$$

$$V(z) = 0, \text{ for } z > d; \quad (2.10)$$

Here it is considered that the electrons are coming from the left of the z-axis ( $z = -\infty$ ). The quantum problem can be divided in two different cases. A first case where the electron energy is smaller than the tunneling barrier height ( $E < V_0$ ), and a second case where the electron energy is higher than the tunneling barrier height ( $E > V_0$ ).

### ■ Case $E < V_0$ : Tunneling Effect

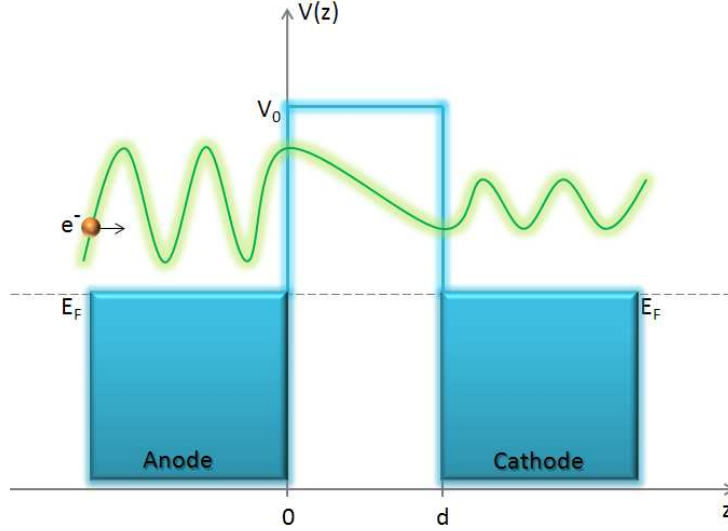


Figure 2.1: One-dimensional square tunneling barrier with a height  $V_0$  and a width  $d$ , for a bias voltage  $V_p = 0$ . The electrons are propagating from left to right of the  $z$ -axis, i.e. from the anode to the cathode of the STM tunneling-junction, with an energy  $E < V_0$ .

The solution of equation 2.7 in the potential 2.10 is given by:

$$\varphi(z) = e^{ikz} + \alpha e^{-ikz}, \text{ for } z < 0; \quad (2.11)$$

$$\varphi(z) = \delta e^{\kappa z} + \gamma e^{-\kappa z}, \text{ for } 0 \leq z \leq d; \quad (2.12)$$

$$\varphi(z) = \beta e^{ikz}, \text{ for } z \geq d; \quad (2.13)$$

with  $\kappa = \sqrt{2m(V_0 - E)/\hbar}$ . It is possible to determine the reflection coefficient  $\alpha$ , and the transmission coefficient  $\beta$ , by studying the continuities of the wave-function  $\varphi$  and of its derivative  $d\varphi/dz$  at  $z=0$  and  $z=d$ . First the continuity at  $z=0$ , gives:

$$\begin{cases} 1 + \alpha = \delta + \gamma \\ ik(1 - \alpha) = \kappa(\delta - \gamma) \end{cases}$$

Then the continuity at  $z=d$ , gives:

$$\begin{cases} \delta e^{\kappa d} + \gamma e^{-\kappa d} = \beta e^{ikd} \\ \kappa(\delta e^{\kappa d} - \gamma e^{-\kappa d}) = ik\beta e^{ikd} \end{cases}$$

Both continuities form a set of four linear equations with four unknown values. Solving this system, allows to determine the coefficient  $\alpha$ , corresponding to the wave fraction which is reflected by the tunneling barrier at  $z=0$ , such as:

$$\alpha = \frac{(\kappa^2 + k^2)(e^{\kappa d} - e^{-\kappa d})}{(k + i\kappa)^2 e^{\kappa d} - (k - i\kappa)^2 e^{-\kappa d}} \quad (2.14)$$

In the same way, the coefficient  $\beta$  corresponding to the wave fraction which is transmitted through the tunneling barrier (at  $z=d$ ) can be determined, such as:

$$\beta = \frac{4ik\kappa e^{-ikd}}{(k + i\kappa)^2 e^{\kappa d} - (k - i\kappa)^2 e^{-\kappa d}} \quad (2.15)$$

From equation 2.15, it is possible to deduce the square of the modulus of the transmitted wave  $|\beta|^2$ , corresponding to the probability to find an electron in the region  $z > d$ . Obviously this probability of presence corresponds to the transmission coefficient ( $T(E)$ ) through the tunneling barrier.

$$|\beta|^2 = T(E) = \frac{4E(V_0 - E)}{4E(V_0 - E) + V_0^2 \sinh^2(\kappa d)}, \quad (2.16)$$

where the hyperbolic sine is given by:

$$\sinh(u) = \frac{e^u - e^{-u}}{2} \quad (2.17)$$

If the tunneling barrier width is well above the spatial range of the electron wave ( $d \gg 1/\kappa$ ), then the equation 2.16 can be simplified as follows:

$$|\beta|^2 = T(E) = \frac{16E(V_0 - E)}{V_0^2} e^{-2\kappa d} \quad (2.18)$$

Thus, even if the electron energy is smaller to the tunneling barrier height ( $E < V_0$ ), the quantum mechanics shows that there is a non-zero probability for the electrons to pass through the potential barrier. This phenomenon is the tunneling effect occurring in the metal-vacuum-metal junction of an STM. The probability to pass through the tunneling barrier, decays exponentially with the barrier width  $d$ . This exponential decay of the transfer probability with the barrier width  $d$ , explains why STM possesses a very high spatial resolution ( $\pm 1\text{\AA}$ ).

#### ■ Case $E > V_0$ :

For an energy higher than the tunneling barrier, the electrons' behavior is again described by the one-dimensional time-independent Schrödinger equation 2.7. The resolution of this equation shows that the electron will not necessarily cross the potential barrier, in contrast to prediction of classical mechanics. Indeed the electron's wave is, at the same time partially transmitted and partially reflected. This uncommon behavior is a purely quantum effect. Here I will not go further in the description of this phenomenon, because it does not correspond to the main effect observed in a STM junction.

#### 2.1.1.2 The Tunneling Barrier Shape

Until now, it has been considered that the tunneling barrier of a STM apparatus can be approximated by a one-dimensional square potential. In reality the barrier shape can be modified through different external parameters like the bias-voltage or the interactions between electrons. It is the reason why, in this paragraph I will describe the influence of the tunneling barrier shape on the charge transfer process.

The probability  $P$  for an electron of the  $\mathbf{n}$ -th state of the sample, to be present at the surface of the tip at a distance  $Z$  of the sample, can be expressed as follows:

$$P \propto |\psi_n(0)|^2 e^{-2\kappa Z}, \quad (2.19)$$

where the coefficient  $\kappa$ , is defined such as:

$$\kappa = \sqrt{\frac{2m}{\hbar^2} (V_0 - E)} \simeq \sqrt{\frac{2m \langle W \rangle}{\hbar^2}} \quad (2.20)$$

The constant  $W$  (Figure 2.1) represents the mean workfunction ( $W = \langle W \rangle = \frac{W_{tip} + W_{sample}}{2}$ ) which is typically 5 eV for metals. The tunneling regime [53], is established for a typical distance  $Z \simeq 1/2\kappa = 5 \text{ \AA}$ .

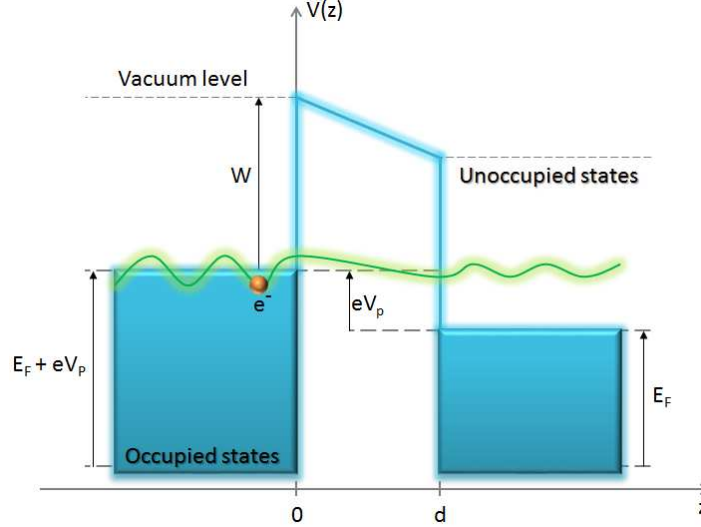


Figure 2.2: The trapezoidal tunneling barrier obtained for a non-zero bias-voltage  $V_p$ .  $W$  is the anode workfunction. The electrons which participates to the tunneling effect have an energy between  $E_F$  and  $E_F + eV_p$ .

To express the tunneling current it is needed to consider the Pauli Exclusion Principle, which says that two electrons cannot be placed in the same quantum state. Thereby, electrons from the occupied states of the tip, can be transferred only in unoccupied states of the sample. In most cases, the Fermi levels of the tip and sample are the same, implying a few number of available states for electron transfer. It is the reason why, it is helpful to apply a bias-voltage  $V_p \neq 0$  which shifts the Fermi level of the tip by an energy  $eV_p$  compared to the Fermi level of the sample, (where  $e = 1.602 \times 10^{-19} \text{ C}$  is the elementary charge). Then the electrons which participate to the tunneling current possess an energy between  $E_F$  and  $E_F + eV_p$ , Figure 2.2. In order to conserve the tunneling regime, the bias voltage applied is chosen in the limit  $eV_p \ll W$ , with  $W$  the tunneling barrier height (in the referential where  $E_F$  is taken as the origin). Therefore the tunneling current is given by summing elementary contributions  $e$  of each incoming electron with an energy  $E_n$ , weighted by their probability of presence  $|\psi_n(z=0)|^2$ , and their transmission probability  $T(E_n)$ , as follows:

$$I \propto \sum_{E_n=E_F}^{E_F+eV_p} e \times T(E_n) \times |\psi_n(Z=0)|^2 \quad (2.21)$$

However according to equation 2.18, the transmission coefficient is proportional to  $e^{-2\kappa Z}$ , then the equation 2.21 can be expressed as:

$$I \propto \sum_{E_n=E_F}^{E_F+eV_p} |\psi_n(Z=0)|^2 e^{-2\kappa Z} \quad (2.22)$$

Therefore, the tunneling current exponentially decays with the distance  $Z$  separating the tip to the sample. A better approximation of the tunneling current is obtained by considering the "Tersoff and Hamann" model, as shown in the next paragraph.

### 2.1.1.3 The Tunneling Current

As shown before, the tunneling current exponentially decays when increasing the tip-sample distance [54], i.e. when increasing the tunneling barrier width. In order to create this tunneling current it is necessary to use a metallic sample and a metallic tip, or other conducting materials. In fact, by using non-conducting materials, there is no charge transfer through the potential barrier. In previous paragraphs the calculations of the transmission coefficient and tunneling current were performed by considering that the electron wave-function can be decomposed in two parts, a transmitted and a reflected part. By doing that, a free electron gas was implicitly assumed to describe the electrons' behavior, i.e. without any interaction between the particles. In reality the tunneling current depends on the density of states of the anode's occupied states which provide the electrons, and of the cathode's unoccupied states which receive the electrons. Then it appears necessary to take into account the electron-electron interactions in order to evaluate more precisely the tunneling current. It is with this objective that the "Tersoff and Hamann" model was born. This model shows that the tunneling transfer process in the potential barrier region can be described by the superposition of the electronic wave-functions of the tip and of the sample (Figure 2.3). The Tersoff and Hamann model assumes that the electronic wave-function of the tip is dominated by the tip apex shape. In order to obtain STM images with atomic resolution, the tip apex must be composed of a single atom. It is the reason why in the Tersoff and Hamann model, the tip wave-function is described by a spherical wave, with an angular momentum  $l = 0$  (s-wave) as follows:

$$\Psi_t(\vec{r}) = \Omega_t^{-1/2} c_t \kappa_0 R \exp(\kappa_0 R) \frac{\exp(-\kappa_0 |\vec{r} - \vec{r}_t|)}{\kappa_0 |\vec{r} - \vec{r}_t|}, \quad (2.23)$$

with  $\Omega_t$  the tip volume,  $R$  its radius of curvature,  $\vec{r}_t$  the position of the curvature center of the spherical waves (Figure 2.3),  $\kappa_0$  their decay coefficient in vacuum, and  $c_t$  the wave amplitude ( $c_t \simeq 1$ ). Furthermore the Tersoff and Hamann model says that the electronic wave-function of the sample can be described by Bloch functions, which are a sum of the reciprocal lattice vectors  $\vec{G}$ , such as:

$$\Psi_s(\vec{r}) = \Omega_s^{-1/2} \sum_G c_G \exp \left[ - \left( \kappa_0^2 + |\vec{k}_G|^2 \right)^{1/2} z \right] \exp \left( i \vec{k}_G \cdot \vec{r}_{\parallel} \right), \quad (2.24)$$

with  $\vec{k}_G$  a wave vector parallel to the surface. Here we can distinguish also the Fourier transform, which allows to describe the sample in real space through its periodicity in

the reciprocal space. It can be noticed that the electron wave behavior is different if they are placed parallel or perpendicular to the surface plane. The first exponential factor of equation 2.24 describes the orthogonal component of the electron wave function, corresponding to the exponential decay of waves in vacuum ( $\kappa_0$  term). The second exponential factor describes the electron wave behavior in the surface plane.

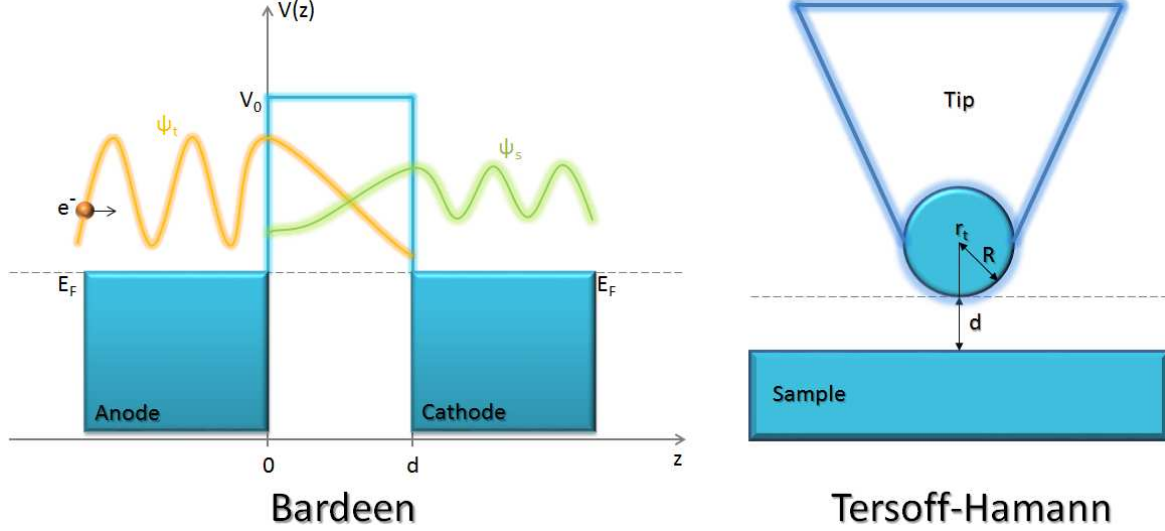


Figure 2.3: Scheme of the Bardeen formalism (left side), and of the Tersoff and Hamann model (right side).

Equations 2.23 and 2.24, derived from results of the Bardeen formalism, which will not be described in details here. The Bardeen formalism is used in the Tersoff and Hamann model to describe the tunneling effect as a superposition of the wave functions of the tip and the sample in the barrier region (Figure 2.3). By using this Bardeen formalism and by considering a quasi-trapezoidal tunneling barrier describes with a BKW<sup>1</sup> model, Tersoff and Hamann have obtained the following expressions for the tunneling current:

$$I(V_p, z) \propto \int_{-\infty}^{+\infty} [f(E - eV_p) - f(E)] \rho_t(E - eV_p) \rho_s(E) T(E, z, eV_p) dE, \quad (2.25)$$

where  $\rho_t$  and  $\rho_s$  are the local density of states of the tip and sample respectively.  $f(E)$  corresponds to the Fermi-Dirac distribution function. This equation 2.25 shows that STM is sensitive to the local density of states of the tip and sample, as well as to the  $z$ -distance separating the tip and the surface. Here the Fermi-Dirac distribution function  $f$  can be neglected because it is assumed that  $k_B T$  is small compared to the energy resolution of the experiment. Consequently the Fermi-Dirac distribution function can be approximated by a Heaviside function, which is equal to 1 in the interval  $[0, eV_p]$ ,

<sup>1</sup>The BKW approximation: The Brillouin, Kramers, Wentzel approximation. See Ref. [55].

and 0 outside. Moreover the vacuum level is taken as reference for the energy scale. Therefore the tunneling current can be written as follows:

$$I(V_p, z) \propto \int_{E_F}^{E_F + eV_p} \rho_t(E - eV_p) \rho_s(E) T(E, z, eV_p) dE, \quad (2.26)$$

where  $T(E, z, eV_p)$  is the transmission factor, as follows:

$$T(E, z, eV_p) \propto \exp[-2\kappa(E, eV_p)z]; \quad (2.27)$$

The transmission factor takes into account the exponential decays of the tunneling current with the  $Z$  distance, by including the  $\kappa$  decay factor:

$$\kappa(E, eV_p) = \sqrt{\frac{2m}{\hbar^2} \left[ \langle W \rangle + \frac{eV_p}{2} - (E - E_F) \right]}, \quad (2.28)$$

where  $\langle W \rangle = \frac{W_t + W_s}{2}$  is the mean workfunction, and  $V_p$  the bias voltage. The expression of  $\kappa$  is different to that obtained for a square potential barrier (see equation 2.20). In fact when the bias voltage is not negligible compared to the tunneling barrier height ( $eV_p \simeq W$ ), then a trapezoidal tunneling barrier is formed which modify the  $\kappa$  decay factor (Figure 2.2). From equation 2.25, it can be seen that the trajectory followed by the tip at a constant tunneling current ( $I_t = \text{constant}$ ), comes from a convolution of the local density of states of the tip and the sample, with the transmission coefficient of the tunneling barrier  $T(E, z, eV_p)$ . When  $eV_p < 0$ , the metallic surface corresponds to the negative electrode (anode), and the tunneling transfer coefficient  $T(E, z, eV_p)$  is maximum for an energy equal to the sample's Fermi level ( $E = E_F$ ). In contrast when  $eV_p > 0$ , the tip corresponds to the anode, and the transmission coefficient is maximum for an energy equal to the Fermi level of the tip ( $E = E_F + eV_p$ ). Then, the transmission coefficient is maximum when the electron energy is equal to the Fermi level of the negatively charged electrode (anode).

To conclude the scanning tunneling microscope (STM), is based on a quantum phenomenon called the tunneling effect. It has been designed in 1981 by Gerd Binnig, and Heinrich Rohrer two German physicists working at IBM, who obtained the Nobel prize in 1986 for this capital discovery in the world of nano-sciences. The STM offers the possibility to observe and to manipulate molecules and atoms at the nanometer-scale. In fact STM gives the possibility to observe in real space the sample's topography with a spatial resolution below 1Å. To explain the tunneling effect which arises between two metallic electrodes, it is possible to consider that it describes the electrons as quantum particles allowing their transfer through a potential barrier. In contrast the electron transfer through a potential barrier is forbidden by considering the classical mechanics description. In the case of STM, the electrons have a non-zero probability to pass through the potential barrier represented by the vacuum separating the tip and the sample. The electron transfer can occur from the tip toward the sample, or from the sample toward the tip depending on the bias voltage applied between the two electrodes. In

the end, the basic principle of the STM is to scan the surface of a conducting sample by using a conducting tip. The sample topography is retraced by measuring the tunneling current intensity which depends on the tip-sample distance, i.e. the width of the tunneling barrier (constant-height mode). Additionally a feedback loop can be used to keep constant the tunneling current. In that way the corrugation of the substrate at a precise location  $(x,y)$  of the surface can be measured by only considering the  $z$  position of the STM tip, compared to its initial position  $z_0$  (constant-current mode). This feedback loop is applied on a piezoelectric scanner which sustain the STM tip, as described in the following paragraph.

## 2.1.2 The STM experimental setup

In this section I will describe the working system of the STM apparatus used during my PhD. First I describe the mechanism of the piezoelectric scanner. Secondly I will describe the vibration isolation system. In a third part I describe the ultrahigh vacuum system used. Finally, in the last part I show the molecular evaporation system used.

### 2.1.2.1 The Piezoelectric Scanner

The piezoelectric scanner is one of the most important parts of a scanning tunneling microscope, because it is used to move the STM tip in all directions of the space  $(x,y,z)$ . The STM tip being fixed on the piezoelectric tube. The piezoelectric scanner allows

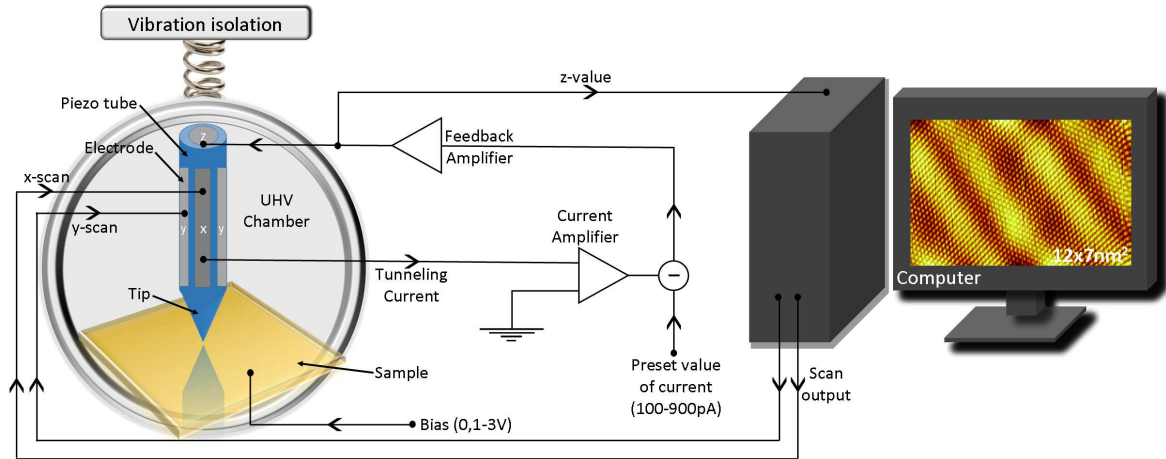


Figure 2.4: Principle of the feedback system used to control the piezoelectric tube, i.e. to control the motion of the STM tip [53].

to move the tip in the sub-nanometer range. This motion is produced by using a piezoelectric material which can be expanded or contracted when applying a voltage on it ( $\approx 10\text{\AA}$ , pour 1V). Therefore, it is possible to adjust the voltage applied on the piezoelectric scanner to conserve the same tunneling current during a lateral motion, i.e. to conserve the same tip-sample distance. By comparing the position  $z$  of the tip

at any time  $t$ , with respect to its initial position  $z_0$  at  $t = t_0$ , it is then possible to retrace the sample surface topography. In order to keep constant the tunneling current, a feedback loop is used (Figure 2.4). This feedback loop consists to sequentially execute the following procedures:

- The tip is approached to the sample surface at a distance of few angstroms, in order to establish the tunneling current. Then, the value of the tunneling current  $I_0$ , and the position of the tip  $z_0$  are taken as references.
- Subsequently, the tip is laterally displaced for a distance corresponding to the size of one pixel of the STM image. The size of the pixel depends on image size and image resolution, i.e. the number of pixels which constitute each image.
- After this lateral motion, the tunneling current ( $I$ ) is measured and it is compared with the reference value  $I_0$ . If  $I$  is different to  $I_0$ , then the voltage applied to the piezoelectric scanner is automatically adjusted in order to obtain  $I = I_0$ , i.e. to maintain constant the tip-sample distance. This is called the constant-current mode. In this mode the vertical position of the tip can change compared to its initial position ( $z \neq z_0$ ). Another mode called the constant-height mode exists, where  $z = z_0$  and where the tip-sample distance can vary. The constant-height mode will not be described here.
- Once found  $I = I_0$ , then the tip position  $z$  is measured and is compared to the reference value  $z_0$ . The distance  $z - z_0$  is a direct measurement of the surface corrugation at a precise position (x,y), and for a constant tunneling current  $I = I_0$ .
- Thereafter, the feedback loop goes back to the second step in order to measure the  $z - z_0$  distance for the next pixel of the STM image. In the end, the measured  $z - z_0$  distances are represented in the STM image by using a color scale. After many loops, a 2D topographic map of the sample can be retraced.

The piezoelectric scanner is generally constituted of different kinds of ceramics, which are composed of different alloys like the  $\text{PbZrO}_3$  or the  $\text{PbTiO}_3$ . These alloys are preferentially used, because their piezoelectric effect is much more important than quartz. With these ceramics different types of piezoelectric scanner were developed, like the piezoelectric tripods or the piezoelectric tubes, which are the most used today (Figures 2.4 and 2.5).

In the case of the piezoelectric tube, five electrodes (X,X', Y,Y', Z) are fixed on it, as shown in the Figure 2.5a. By applying a voltage on these electrodes it is possible to move the tip at the subnanometer distance range in all the directions of space. The application of a voltage on the Z electrode, allows to approach or retract the tip from the surface of the sample. In contrast the X,X',Y, and Y' electrodes allow to move the tip in the plane of the sample surface. Moreover the X and X' electrodes are diametrically opposite and are working together. When applying a voltage  $V$  on X, then a voltage  $-V$  is automatically applied on X'. This allows to contract a precise point of the piezoelectric tube, and in a same time to extend the diametrically opposite point in order to facilitate

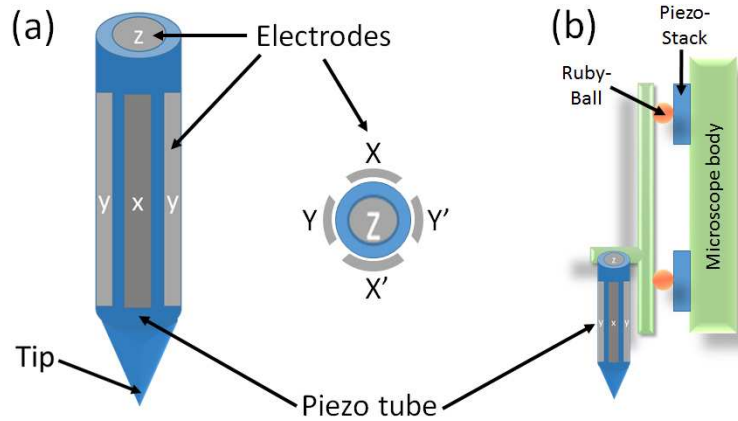


Figure 2.5: The piezoelectric tube: (a) The X,X', Y,Y' and Z electrodes used to control the subnanometer motion of the STM tip; (b) The piezo-stack and ruby-ball used for the macroscopic motion of the STM tip during the approach.

the lateral motion of the tip. In the same way the Y and Y' electrodes are diametrically opposite and are working together. Finally there is also the presence of piezoelectric stacks and ruby balls between the microscope body and the piezoelectric tube in order to approach macroscopically the tip from the sample surface, Figure 2.5b. To conclude a map of the sample's topography is obtained by scanning the substrate with a metallic tip. The motion of this tip is controlled at the nanometer scale by using a feedback-loop on a piezoelectric tube. In order to obtain accurate and reproducible map of the sample's topography, the motion of the tip need to be unperturbed by external vibration which coming from the human activities. It is the reason why a vibration isolation system is in most cases added to the STM experimental setup, as shown in the next paragraph.

### 2.1.2.2 The Vibration Isolation System

Another essential part of a STM is the vibration isolation system, which allows to minimize the mechanical noise [53]. The minimization of the mechanical noise is crucial in order to obtain well-resolved STM images. The vibration isolation of STM can be assured by two isolation systems which are working together. The first isolation system is present in the majority of STM apparatus, it is an internal system using vertical springs in order to suspend the STM head, i.e. the tip-sample system. These vertical springs allow to suppress the vertical vibrations of the machine. The second isolation system is an Eddy current system which suppresses the horizontal vibrations of the machine. The Eddy current system is constituted of copper plates intercalated with permanent magnets which are placed periodically around the STM head, Figure 2.6. Finally the internal isolation system allows to decoupling the whole tip-sample system to the rest of the experimental set-up. To conclude the combination of these two vibration isolation systems is useful to obtain STM images with a high resolution. Since each tip motion of an amplitude greater than  $0.04\text{\AA}$  (the maximal resolution in Z), can induce important deformations of the STM image. Another modification of the STM image can originate

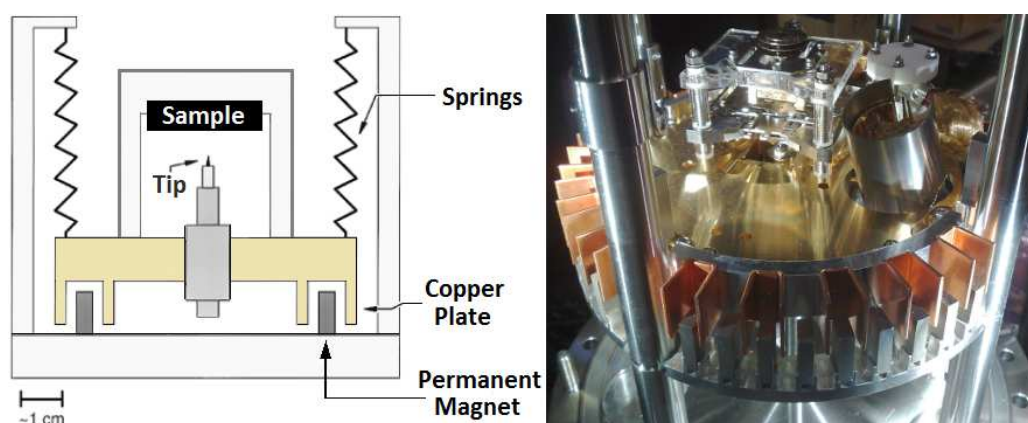


Figure 2.6: The STM vibration isolation system: On the left, a scheme of the vibration isolation system. On the right, a picture of the vibration isolation system of the VT-STM used during my PhD.

from pollution involved by the water or other molecules present in the atmosphere. To prevent this kind of pollution the STM experimental setup can be placed in ultra-high vacuum (UHV) environment, as described in the following paragraph.

### 2.1.2.3 The Ultrahigh Vacuum System

A scanning tunneling microscope can be placed in ultrahigh vacuum environment (UHV) in order to preserve the cleanliness of the sample, i.e. to prevent surface contamination by adsorption of oxygen atoms or  $\text{CO}_2$  molecules. This is of prime importance in order to prevent undesirable modifications of the physical properties of the sample. During my PhD, I have used a VT-STM<sup>2</sup> apparatus placed in an UHV chamber, running at a base pressure of  $10^{-10}$  mbar. The ultrahigh vacuum system used is composed of three chambers. A preparation chamber which is dedicated to the preparation of the tip and the sample, Figure 2.7. The preparation chamber is constituted of an ionic Ar gun, projecting ions  $\text{Ar}^+$  in order to rip out the first layers of a metallic crystal. In this way, all the impurities and pollution present at the surface of the tip or of the sample can be eliminated (this technique is called sputtering). Furthermore this preparation chamber is constituted of a filament which is used to heat a metallic surface at a temperature around  $\simeq 490^\circ\text{C}$ , in order to smooth the sample or the tip (this technique is called annealing). Finally the preparation chamber possesses some evaporation system (see §2.1.2.4), in order to deposit molecules and metallic entities on the surface of the sample of interest. Thereafter, the ultrahigh vacuum system is also composed of a STM chamber, which is dedicated to measurements, Figure 2.7. A load-lock chamber is also used to introduce sample and tip from ambient pressure to UHV environment without breaking the vacuum in all chambers, and without necessitating to bake-out the experimental system. The STM chamber is isolated to the other chambers by the pres-

<sup>2</sup>VT-STM: Variable Temperature Scanning Tunneling Microscope.

ence of valves. These valves allow to prevent the pollution of the STM chamber during the sample or tip preparation, i.e. to preserve a very low pressure ( $\simeq 4.0 \times 10^{-10}$  mbar). In order to reach this base pressure in all the chambers, the ultrahigh vacuum system is composed of three different types of pumps (Figure 2.7). A rotary vane pump allows to reduce the pressure from the ambient until  $10^{-3}$  mbar. This rotary vane pump is connected to a turbomolecular pump, which allows to lower the pressure from  $10^{-2}$  mbar, until  $10^{-10}$  mbar. Finally an ionic pump allows to keep the pressure around  $10^{-10}$  mbar, during STM measurements, without inducing mechanical noise. The pri-

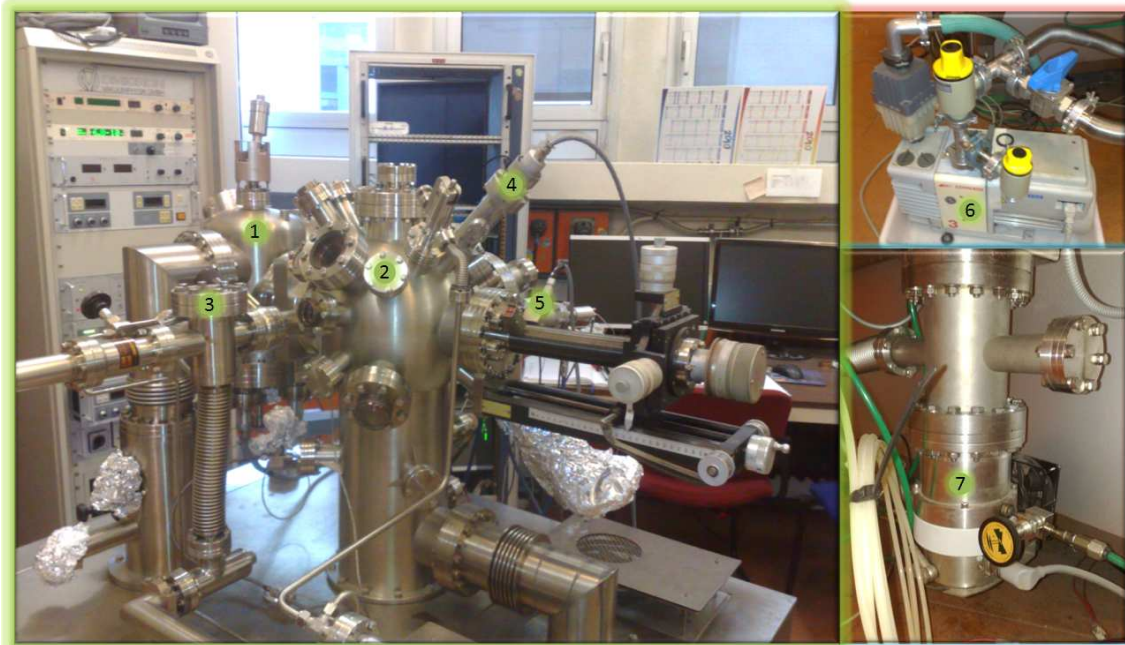


Figure 2.7: The ultrahigh vacuum system of the VT-STM apparatus: (1) The STM chamber. (2) The preparation chamber. (3) The Load-Lock chamber. (4) The electron gun used for sputtering the sample. (5) The Power supply used for annealing the sample. (6) The rotary vane pump. (7) The turbomolecular pump.

mary and turbomolecular pumps have approximately the same working principle. Both can be considered as huge turbines which eject outwards the air and particles present in the chambers. The main difference between these two pumps is the pressure range where they work. The rotary vane pump has a working range pressure between 1 bar to  $10^{-3}$  mbar. In contrast the turbomolecular pump needed a starting pressure around  $10^{-2}$  mbar, before that it works. It is the reason why the turbomolecular pump cannot work without the rotary vane pump. The rotation speed of the turbomolecular pump is greater than the rotary vane pump. Then the primary and turbomolecular pumps together, allow to reach a pressure of  $10^{-10}$  mbar. Thereafter, it can be noticed that the rotation frequency of the turbomolecular pump is around 10kHz [53]. Therefore the turbomolecular pump can create mechanical perturbations of the STM measurements. It is the reason why, it is needed to turn off the turbomolecular pump during STM

measurements, and to keep the low pressure by using a third type of pump called the ionic pump. The ionic pump consists of two metallic electrodes, one positively charged and one electronegatively charged. A voltage in the range of 5kV is applied between the two electrodes, in order to create an electric current. The electrons which leave the anode to reach the cathode, are used to ionize the particles presents in the chambers. Thereafter, the ionized particles are attracted by one of the two electrodes, according to their electrical charge. When the electrically charged particles reach the electrode they will be glued on it, involving a reduction of the pressure in the chamber. Moreover a magnetic field is also applied between the two electrodes, providing a helical trajectory to the electrons in order to maximize the number of collisions with the particles. To summarize the UHV system creates a vacuum in the range of  $10^{-10}$  mbar by combining three types of pumps, a rotary vane pump, a turbomolecular pump and an ionic pump. This UHV system is used to prevent undesirable modifications of the structures and electronic properties of the sample by minimizing the adsorption of polluting molecules. More precisely the use of UHV system in STM experiment allows to prevent some problem which habitually occurs at the liquid-solid and air-solid interface, where solvent and water can interact with the sample and then makes more difficult to build organized self-assembly in a predictable way. Thereafter to build the molecular self-assembly it is needed to use an evaporation system working in UHV environments in order to deposit the molecules on the surface, as it is shown in the next paragraph.

#### 2.1.2.4 The Evaporation System

In order to deposit molecules on the sample surface in UHV environment, an evaporation system has been used during my PhD, Figure 2.8. The molecules are placed in a

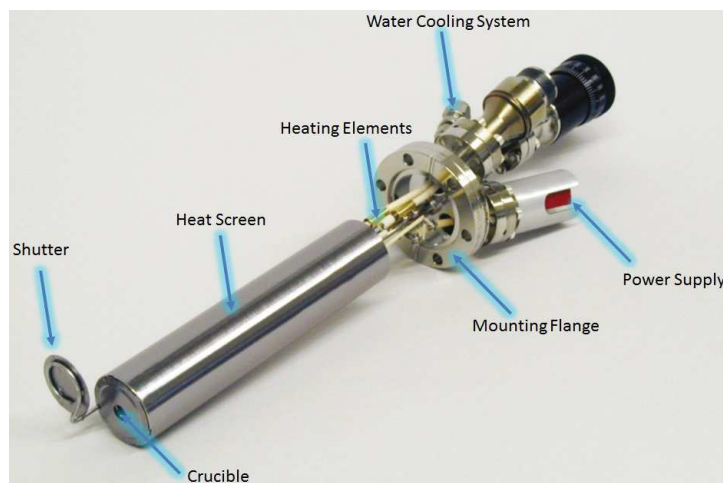


Figure 2.8: The thin film molecular deposition effusion-cell system.

crucible surrounded by a filament. A current of few amperes is applied to the filament in order to heat molecules above their evaporation temperature. In addition to that a water cooling system is used to prevent any overheating. This evaporation system allows

to deposit the molecules on a sample with a surface coverage ranging from submonolayer to continuous film. This well controlled molecular deposition is assured by the presence of a shutter which allows to precisely master the deposition time (Figure 2.8). In fact the shutter is habitually closed, and it is open only during molecular deposition. Finally a thermocouple is used to control the temperature of molecular deposition. This technique allows to homogeneously deposit molecules on surfaces with a high reproducibility. Therefore with this technique it is possible to create organized self-assembled molecular films, and then to characterize their structures by using a STM placed in a UHV chamber.

To summarize, the STM experimental setup used during my PhD is composed of UHV system (§2.1.2.3), a vibration isolation system (§2.1.2.2) and a evaporation system (§2.1.2.4). This experimental setup is well adapted to study the structures of the supramolecular self-assembled films at the nanometer scale with a high efficiency and high reproducibility. The use of UHV system allows to suppress the influence of water or solvent on the physical properties of the organic films. In addition to the STM experimental setup, X-ray photoemission spectroscopy (XPS) can be used to determine the electronic properties of the sample, as shown in the following section.

## 2.2 Photoemission Spectroscopy

Here I will describe first the basic principle of the photoemission spectroscopy. Thereafter I will describe the near-edge X-ray absorption fine structure and resonant photoemission spectroscopy, as well as the core-level spectroscopy. Finally I will give a brief description of the synchrotron SOLEIL and TEMPO beamline used during my PhD.

### 2.2.1 Photoemission Spectroscopy and Related Techniques

Photoemission Spectroscopy and related techniques are widely used for their outstanding ability to get information about the electronic structure and chemical environment of the atomic species constituting the sample of interest. The use of an adjustable energy source, like synchrotron radiation combined with photoemission spectroscopy allows to produce high surface sensitive measurements.

#### 2.2.1.1 Photoemission spectroscopy: basic principle

The photoemission spectroscopy consists to irradiate a sample with photon, in order to extract an electron by the absorption of a quantum of light. This phenomenon corresponds to a photoelectric process which has been discovered in 1887 by Frank and Hertz, and explained in 1905 by Einstein. The choice of X-ray sources as excitation beams comes from their ability to probe the core-level electrons, as well as the valence electrons. In comparison the use of less powerful sources like ultraviolet sources allows to probe only the valence electrons. The photoemission spectroscopy measurements are based on the analysis of the kinetic energy of the extracted photoelectron (Figure 2.9). In fact the measurement of the kinetic energy of the photo-emitted electron allows to

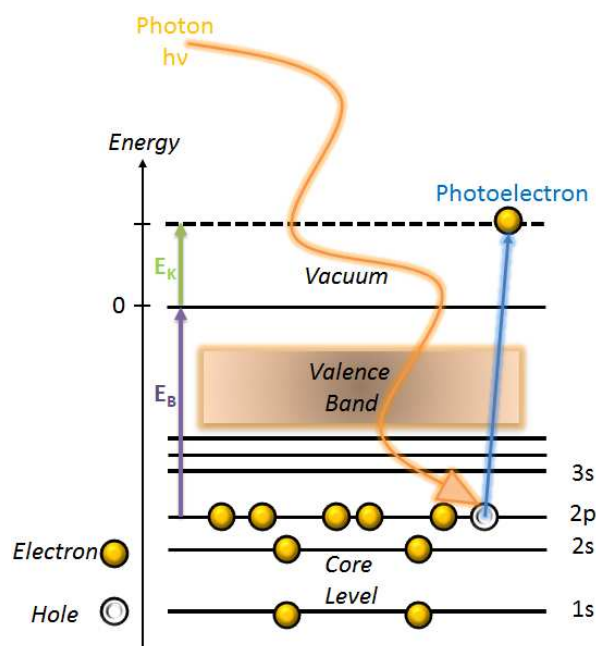


Figure 2.9: Principle of the photoemission spectroscopy. Electrons from the sample are extracted by the absorption of high energy photons. The determination of the kinetic and binding energies of the photo-emitted electron allows to characterize the electronic states of the sample of interest.

determine the binding energy of the electronic state where it comes from, by using the following energy conservation law (2.29).

$$h\nu = E_B + E_K, \quad (2.29)$$

where  $E_B$  corresponds to the binding energy of the photoelectron,  $E_K$  its kinetic energy,  $h$  the Planck constant and  $\nu$  the frequency of the excitation beam. The binding energy  $E_B$  is related to the chemical nature and chemical environment of the ionized atomic species. It is the reason why, the photoemission spectroscopy is sometimes called the "Electron Spectroscopy for Chemical Analysis" (ESCA).

### 2.2.1.2 Photoemission spectroscopy in solid: the three step model

The photoemission spectroscopy used in material science can be greatly explained by the following three step model.

#### **First step: ionization of an atomic species through photon absorption:**

After absorption of a photon, an electron of the sample can be extracted with a given kinetic energy. This extraction creates a hole in the atomic core-level. The photon excitation must have an energy higher than the electron binding energies, for the atomic ionization to occur.

**Second step: Travel of the photo-excited electron toward the surface:**

During travel toward the surface, the electron can be affected by some interactions with other particles that compose the solid, giving rise to distinct photoemission peaks. The origin of these distinct photoemission peaks can be explained by considering the following cases, Figure 2.10.

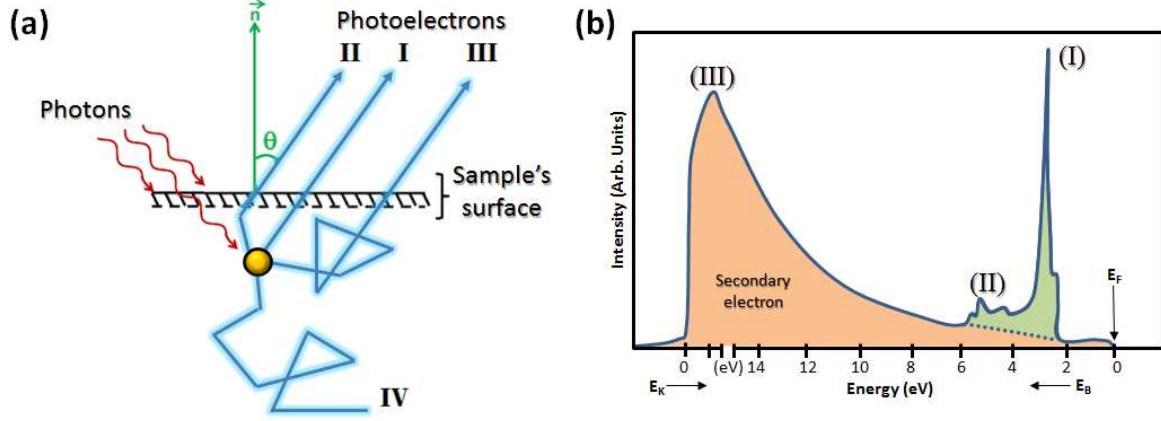


Figure 2.10: a) Scattering processes occurring in a solid after irradiation with a X-ray or UV excitation beam. b) Schematic view of a typical photoemission spectrum [56].

- Case I: The electron travel toward the surface without losing energy, i.e. without producing inelastic collisions. This gives rise to the main photoemission peak observed in the photoemission spectrum (I in Figure 2.10).
- Case II: The photo-excited electron is involved in a few number of inelastic collisions during its travel toward the surface. In that way the electron loses some part of its kinetic energy, leading to the appearance of satellite peaks at higher binding energy in the photoemission spectrum (II in Figure 2.10).
- Case III: The photo-excited electron is involved in many inelastic collisions during its travel toward the surface. In that way the electron loses a great part of its kinetic energy, leading to the appearance of secondary electron peaks at higher binding energy in the photoemission spectrum (III in Figure 2.10).
- Case IV: The photo-excited electron cannot reach the surface because it has lost too much kinetic energy in the inelastic collisions (IV in Figure 2.10).

Therefore the electron transport through a solid material is related to the mean distance traveled between two inelastic collisions, i.e. the mean free path  $\lambda$ . In fact the maximum depth probed with photoemission spectroscopy is restricted by the mean free path, as it is described in the following attenuation law:

$$I = I_0 \left( -\frac{z}{\lambda \cos(\theta)} \right), \quad (2.30)$$



### 2.2.1.3 X-ray Photoemission spectroscopy: Core-Level measurements

The use of X-ray sources allows to probe the core-level states of the sample of interest which are not accessible with less-powerful ultraviolet sources. X-ray Photoemission spectroscopy (XPS) was employed in many experiments to characterize the core-level electronic states of organic thin films [59, 60].

#### Electrical connection of the spectrometer with the sample:

The establishment of an electrical connection between the spectrometer and the sample of interest has the consequence to align their Fermi levels, Figure 2.12. Therefore the

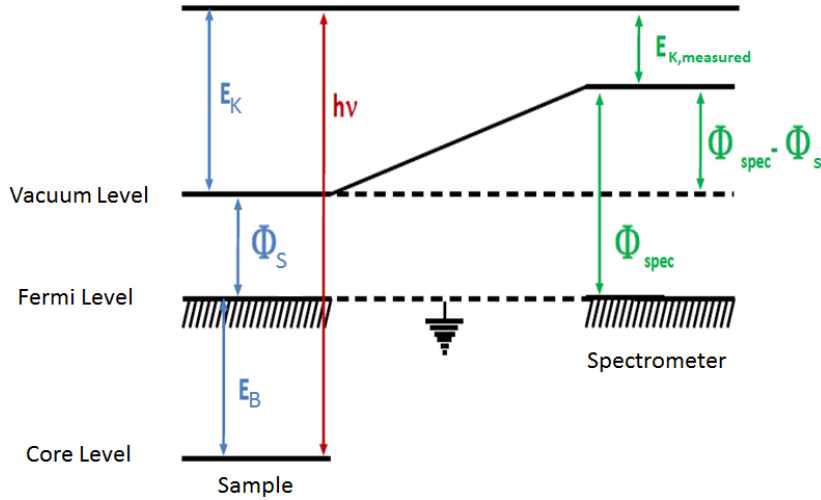


Figure 2.12: Scheme of the energy configuration taking place in a photoemission experiment where the spectrometer is electrically connected to the solid sample [56].

kinetic energy of the electron can be expressed such as:

$$E_K = E_{K,measured} + \Phi_{spec} - \Phi_s, \quad (2.32)$$

where  $\Phi_{spec}$  is the work function of the spectrometer. Additionally the energy conservation law (2.31) can be expressed in function of  $\Phi_{spec}$  in the following way:

$$h\nu = E_B + E_{K,measured} + \Phi_{spec} \quad (2.33)$$

The last equation (2.33) allows to determine the binding energy of the photo-emitted electron without considering  $\Phi_s$  the work function of the sample. Consequently for a given spectrometer with a well-defined  $\Phi_{spec}$  work function, it becomes possible to determine the binding energy of the electronic states of any sample. In contrast by considering equation (2.31) the evaluation of the  $\Phi_s$  work function is needed for each sample used.

#### The hemispherical spectrometer:

The determination of the photoelectron kinetic energy is essential to characterize the

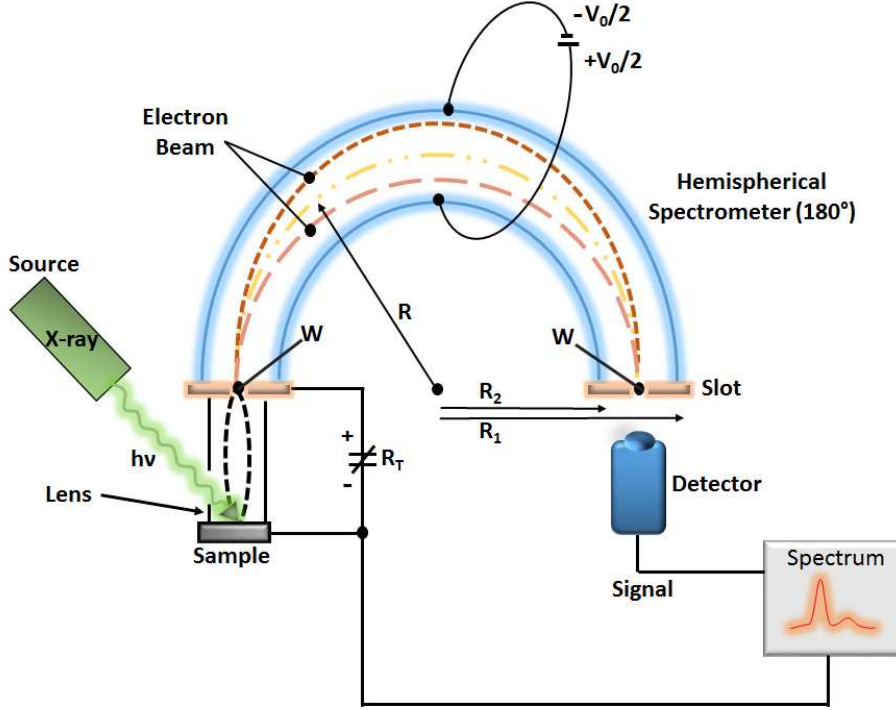


Figure 2.13: Scheme of the hemispherical spectrometer used in photoemission spectroscopy [61].

sample's energy levels. The spectrometer used in photoemission spectroscopy is a hemispherical photoelectrons detector which counts the number of photoelectrons emitted by the sample with a given kinetic energy. The photoelectron's kinetic energy is selected by applying a potential  $V_0$  between the two hemispheric walls of the detector, Figure 2.13. The potential  $V_0$  deflects the photoelectrons which possess a kinetic energy different to the selected one. In this way the photoelectrons which have a no-desired kinetic energy cannot reach the detector. In fact the trajectory of the photoelectrons depends on two parameters, the external potential applied  $V_0$ , and the curvature radius ( $R_1$ ,  $R_2$ ) of the internal and external hemispherical walls of the detector. Finally, the photoelectrons trajectory depends on their kinetic energy ( $E_K$ ), as shown in the following equation:

$$E_K = \frac{V_0}{\left(\frac{R_2}{R_1} - \frac{R_1}{R_2}\right)} \quad (2.34)$$

A typical photoemission spectrum consists to plot the number of photoelectrons which reach the detector in function of their kinetic energy, as it is depicted in Figure 2.14. This photoemission spectrum is obtained by changing the external potential  $V_0$  applied between the two electrodes. Figure 2.14 shows the relative energy positions of the 4d, 4f tungsten core-level peaks, the valence band and photoemission threshold, as well as the secondary electron (SE) peaks and SE background are shown. Additionally Figure 2.14 shows that the valence band appears at high kinetic energy just below the Fermi level

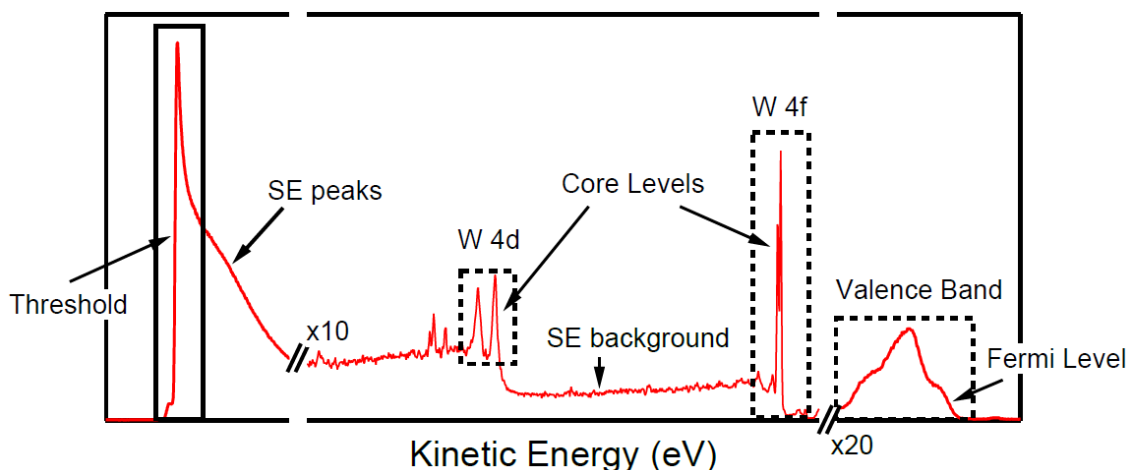


Figure 2.14: Example of a photoemission spectrum. In this photoemission spectrum the 4d and 4f tungsten core-level peaks, as well as the valence band and photoemission threshold are shown. Additionally the secondary electron (SE) peaks and SE background are also indicated [58].

(on the right of the photoemission spectrum). In comparison the 4f and 4d core-level are placed at the lower kinetic energies (at the center of the photoemission spectrum). Finally the photoemission threshold appears at the minimum kinetic energy which can be reached in the experiment (on the left of the photoemission spectrum). In some cases a close inspection of the energy positions of the core-level peaks can reveal binding energy shifts originating from a modification of the chemical environment of the emitting atomic species. In addition to that the photoemission peak intensity is proportional to the number of atoms involved in the photoemission process [56, 58, 61]. Consequently, the analysis of the photoemission peak intensities can give information about the stoichiometry of the sample.

### Shape of the Photoemission peaks:

The shape of a photoemission peak can be described by a convolution of Lorentzian and Gaussian functions. The Gaussian function width corresponds to the experimental broadening (X-ray core-level line-shape, Doppler and thermal broadening, and resolution of the detector). However the Lorentzian function width corresponds to the lifetime broadening (lifetime of the excited state).

To summarize the photoemission spectrum can give information about the modifications of the chemical environment of an emitting element by measuring the core-level binding energy shifts. Additionally the measurement of the peak intensities can give quantitative information about the sample's stoichiometry. Finally the shape of the core-level peaks allows to obtain an assessment of the core-hole lifetime of the associated element. The sample and the spectrometer are placed in UHV environments in order to prevent inelastic scattering of the photoelectron during their travel from the sample's surface to the detector. This allows to get a precise measurement of the kinetic

energy of the photo-excited electrons.

#### 2.2.1.4 Near-Edge X-ray Absorption Fine Structure: basic principle

The Near-Edge X-ray Absorption Fine Structure (NEXAFS) [62] is based on the photoemission process depicted in Figure 2.15. First a photoelectron is emitted by the absorption of a photon radiation in the energy range of X-ray, Figure 2.15a. The emission of the photoelectron created a hole in the core-level where it comes from. Thereafter, the hole will be filled by an electron which comes from a higher energy level, Figure 2.15b,c. This electron will lose some energy through two competing decay processes, corresponding to the emission of fluorescent photons or Auger electron (Figures 2.15b,c respectively). The occurrence probability of these two decay processes is mainly related to the atomic number  $Z$  of the chemical elements probed. In our case the NEXAFS spectroscopy is used to study molecules on surfaces possessing atomic species with relatively low  $Z$  (like N, C, O atoms), implying that the Auger decay process is the predominantly favored decay channel [56]. In contrast to XPS which probes the occupied electronic states, the

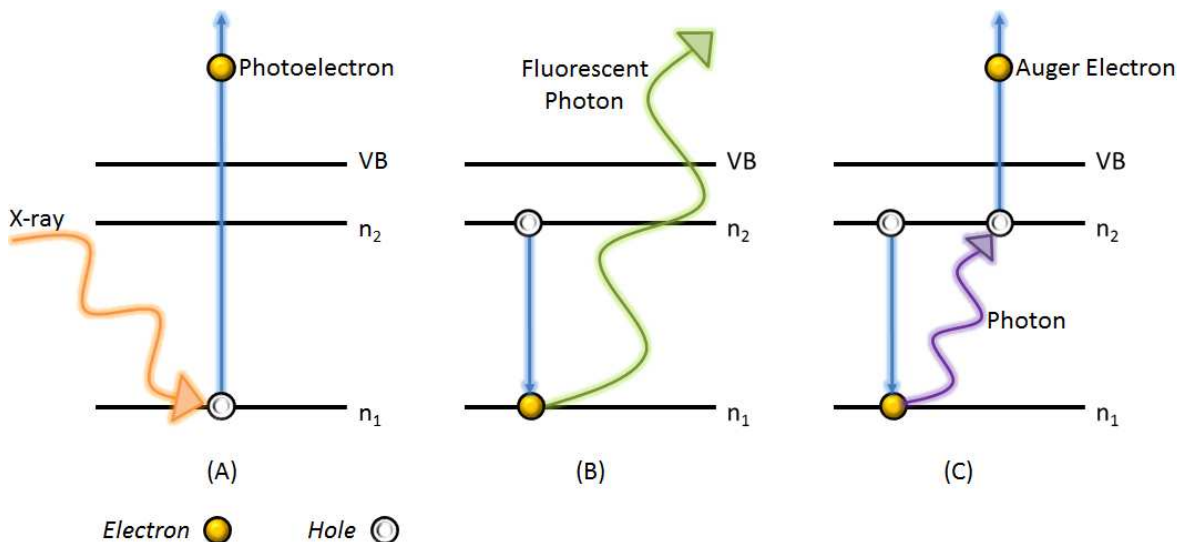


Figure 2.15: The basic principle of NEXAFS spectroscopy: (a) The X-ray absorption followed by the emission of a photoelectron; (b) The fluorescence decay process; (c) The Auger decay process.

NEXAFS spectroscopy gives information about the unoccupied states of the sample of interest. The use of a polarized excitation beam in NEXAFS spectroscopy allows to obtain information about the orientation of the molecular orbitals, and then enables to deduce the molecular adsorption geometry on surfaces. Additionally the NEXAFS spectroscopy is also sensitive to the chemical environment of the photo-excited element (as previously described for XPS spectroscopy).

Figure 2.16 shows a scheme of a typical NEXAFS spectrum. The NEXAFS spectrum is obtained by varying the photon energy of the excitation beam and by recording

the corresponding number of photo-emitted Auger electrons (in contrast to the XPS spectrum where the photon energy is fixed). Two different regions can be distinguished

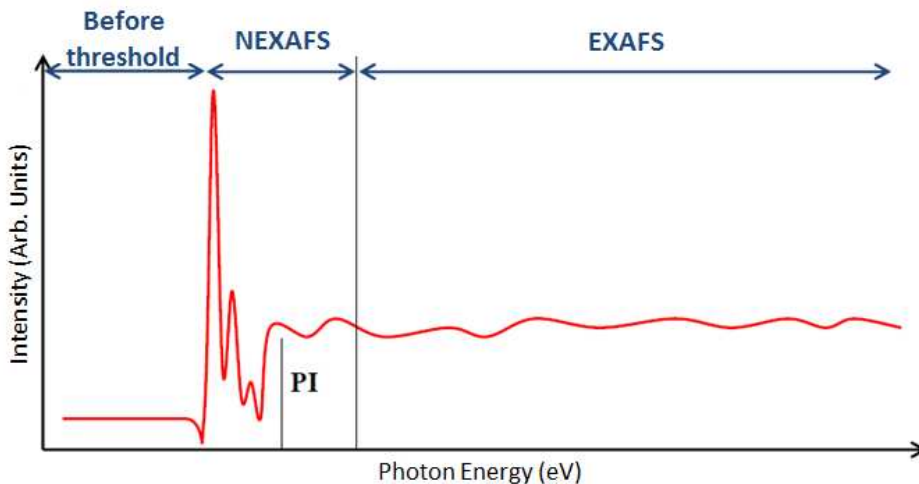


Figure 2.16: Scheme of a typical NEXAFS spectrum. The photo-ionization threshold is marked as PI, the NEXAFS and EXAFS regime are also indicated [56].

on the spectrum depicted in Figure 2.16. The first region corresponds to the NEXAFS domain which is obtained for photon energy close to the photo-ionization threshold (labeled PI). However the second region corresponds to the EXAFS (Extended X-ray Absorption Fine Structure) domain which is obtained for an excitation photon energy far above PI, the photo-ionization threshold. The peaks observed in the NEXAFS region can be attributed to the LUMOs (Lowest Unoccupied Molecular Orbitals) states of the atomic element considered.

Three different acquisition modes can be used in NEXAFS spectroscopy as it is described below (Figure 2.17):

- TEY (Total Electron Yield): All the photo-emitted electrons are integrated in the NEXAFS spectrum. The photoemission signal is constituted of two contributions, one from the molecular film and the other one from the substrate. This acquisition mode is well-adapted for the study of thick molecular films, where the contribution of the substrate is negligible.
- PEY (Partial Electron Yield): In this acquisition mode a negative voltage is applied in front of the photo-multiplier in order to minimize the contribution of the secondary electrons coming from the inelastic scattering.
- AEY (Auger Electron Yield): In this acquisition mode the energy window is centered on the Auger peak of a considered element. However the energy of the excitation beam varies during the acquisition of NEXAFS spectra. Therefore, in order to prevent undesired contributions to the NEXAFS spectrum like another photoemission process than the Auger peaks, an analyzer is used to select the kinetic energy of the detected Auger electrons.

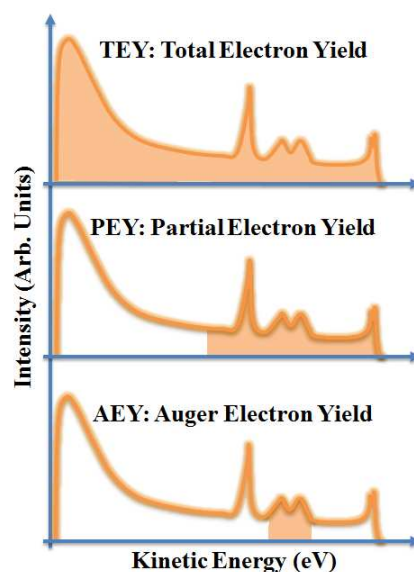


Figure 2.17: Scheme of the kinetic energy windows used in the three acquisition modes of the NEXAFS spectroscopy (TEY, PEY, AEY) [56].

### 2.2.1.5 Resonant Photoemission Spectroscopy: basic principle

The resonant photoemission spectroscopy (RPES) corresponds to the use of a core-hole lifetime as a temporal reference to probe the charge transfer dynamics arising at the metal-organic interface in the femto-second timescale (Core-hole clock spectroscopy) [45, 63, 64]. The resonant photoemission spectroscopy is based on a two-step process, Figure 2.18. The first step corresponds to the excitation of a core electron by the absorption of X-ray radiation, Figure 2.18a. This excitation involves the formation of a core-hole. The excited electron is placed in a higher energy level which corresponds to the Lowest Unoccupied Molecular Orbital (LUMOs). The second step corresponds to the decay process, for which many scenarios can be envisaged (Figures 2.18b-e). The auto-ionization decay process is represented in Figures 2.18b and 2.18c, while the charge transfer and de-excitation decay process is depicted in Figures 2.18d and 2.18e. The auto-ionization decay is composed of two competing processes called the participative and spectator decay channels. On the one hand there is the participative decay (Figure 2.18b), where the excited electron refilled the core-hole (i.e. goes back to its initial state) by emitting a photon which will in turn extracts an electron from the HOMOs<sup>3</sup> level. On the other hand there is the spectator decay process, where an electron from the HOMOs refilled the core-hole by emitting a photon which will in turn extracts another electron of the HOMO level. During the spectator decay process, the photo-excited electron remain localized at the LUMO level, Figure 2.18c.

Furthermore the auto-ionization process is itself in competition with the charge transfer and de-excitation process. Figure 2.18d, shows that the excited electron placed in

<sup>3</sup>HOMOs: The Highest Occupied Molecular Orbital.

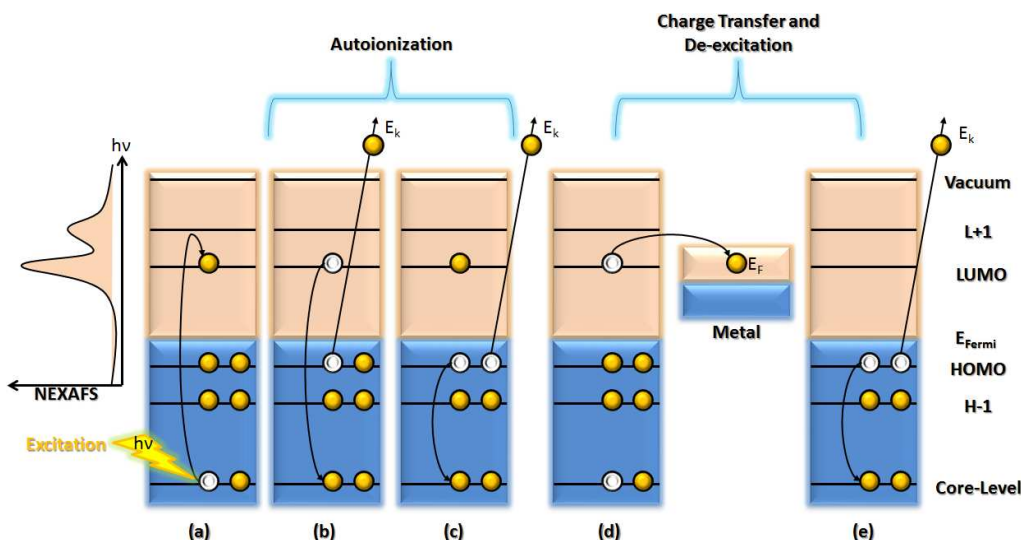


Figure 2.18: The basic principle of the resonant photoemission spectroscopy: (a) the photoemission process induced by X-ray excitation; (b-e) the competitive decaying processes.

the molecular LUMO level can be transferred into the Fermi level of the metallic surface (charge transfer process). Thereafter, an electron from the molecular HOMO level can fill the core-hole by emitting a photon which will in turn extract another electron of the HOMO level (de-excitation process), Figure 2.18e. Additionally, it is always the faster decay process which is the predominant one. When the charge transfer is faster than the auto-ionization process, a decrease in the RPES peak intensity can be observed.

A scheme of a typical RPES spectrum is given in Figure 2.19. A core-hole clock spectrum is obtained by recording the number of the photo-emitted electrons through the auto-ionization decay processes (peak intensity), in function of the incoming photon energy and outgoing kinetic energy. In that way the RPES spectrum corresponds to a three-dimensional map, as depicted in Figure 2.19. In this Figure two different dispersive behaviors labeled (l) and (d) can be observed in the RPES spectrum. The channel (l) corresponds to the case where a linear relation is established between the incoming photon energy and outgoing kinetic energy. This linear behavior is obtained when the excited core electron remains localized in the resonant state at a constant binding energy. The channel (l) is also called the Raman auto-ionization channel [50]. In contrast the channel (d) corresponds to the case where the excited state is coupled to a continuum (substrate for example) implying that the core electron is no longer localized to the resonant state. In that case, the channel (d) is observed at constant kinetic energy independently to the incoming photon energy, Figure 2.19. The channel (d) corresponds to the charge transfer channel of the auto-ionization process [50], Figure 2.18d. Additional Figure 2.19 shows that a correspondence exists between the NEXAFS absorption spectrum (§2.2.1.4) and the peak intensities of the RPES spectrum.

An estimation of the charge transfer time can be obtained by comparing the peak intensities of the Raman and charge transfer channels of the RPES spectrum as it is shown

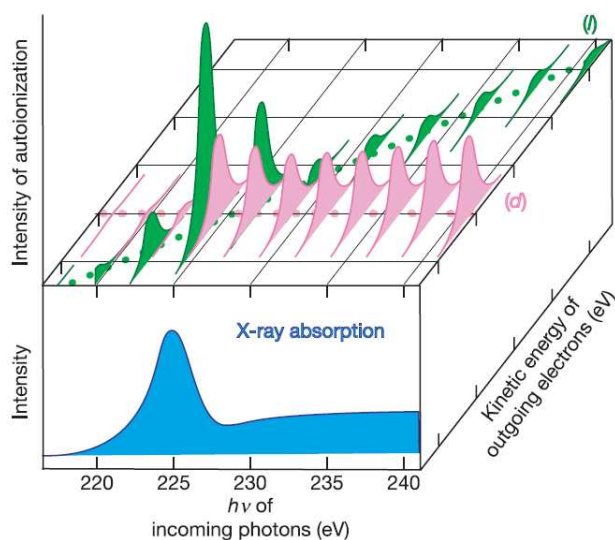


Figure 2.19: Schematic representation of the typical spectrum obtained in Resonant Photoemission Spectroscopy (RPES), i.e. core-hole clock spectroscopy. The correspondence between the RPES peak intensity with the typical absorption spectrum obtained in NEXAFS spectroscopy is shown. The channel labeled (l) corresponds to the case where the auto-ionization decay process leads to a localized final state with linear dispersion. In contrast the channel named (d) corresponds to the case where the auto-ionization decay process leads to a delocalized final state at constant kinetic energy [50].

in the literature [49, 50]. The choice of core-hole clock spectroscopy to determine the charge transfer dynamics at the metal-organic interface in the Femto-second timescale is related to its ability to determine simultaneously the charge transfer time needed to transfer an electron and the location of this electron before that the charge transfer occurs. For example, this cannot be achieved with classical pump-probe experiments.

## 2.2.2 The SOLEIL Synchrotron

### 2.2.2.1 General Description

To perform measurements with a high sensitivity to the surface, photoemission spectroscopy can be coupled to an excitation source possessing tunable photon energy like in synchrotron radiation facilities (see §2.2.1.2). It is the reason why during my PhD, I have done photoemission spectroscopy measurements at the TEMPO beamline of the SOLEIL synchrotron, Figure 2.20. The SOLEIL synchrotron is a circular accelerator of particles providing a photon excitation beam with a wide energy range, from hard X-ray to far infrared. The photon excitation beam is obtained by accelerating electrons close to the speed of light with a kinetic energy up to 2.75 GeV [65]. To achieve that, the synchrotron is composed of a succession of highly efficient experimental setups. The first experimental setup is an electron gun (Figure 2.21 A), which consists to heat a metal at a relatively high temperature in order to extract its electrons. The electrons are then



Figure 2.20: Picture of the SOLEIL synchrotron [65].

injected in the LINAC (Figure 2.21 B), which is a linear accelerator of 16m length [65]. By applying a strong magnetic field the LINAC gives a 100MeV energy to the electrons and a speed close to the speed of light. Thereafter, the electrons are transferred in a circular accelerator of 157m circumference which is named the Booster (Figure 2.21 C). The electrons get an energy of 2.75GeV after completing 150000 revolutions in the Booster [65]. When the energy of 2.75GeV is reached the electrons are injected in a storage ring (Figure 2.21 D), of 354m circumference. The electrons are accumulated in the storage ring until a current of 490mA is reached. In the end, the accelerated electrons are at the origin of the emission of a high energy photon radiation, which will be focused on a precise beamline (Figure 2.21 E). This high energy photon radiation will be then used to probe the electronic states, and physical properties of the sample of interest. The SOLEIL synchrotron is constituted of 26 beamlines (Figure 2.21). Each beamline is

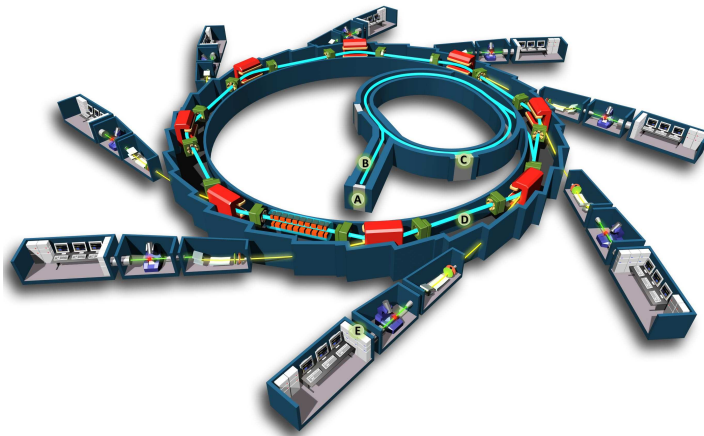


Figure 2.21: Scheme of the synchrotron SOLEIL: A) Electron gun; B) Linear accelerator (LINAC); C) Circular accelerator (Booster); D) Storage ring; E) The beamlines which use the photon excitation beam produced by the accelerated electrons in order to probe the physical properties of the sample [65].

characterized by an energy range and by the analytic technique that it uses. During my PhD, I used the TEMPO beamline (§2.2.2.2) which allows to carry out measurements by using X-ray photoemission spectroscopy (XPS, §2.2.1.3), near edge X-ray absorption fine structure (NEXAFS, §2.2.1.4), and resonant photoemission spectroscopy (RPES, §2.2.1.5).

### 2.2.2.2 The TEMPO Beamline

The TEMPO<sup>4</sup> beamline, is composed of two undulators HU80 and HU44, for an energy range between 50 and 1500 eV. Additionally the TEMPO beamline is constituted of a SCIENTA SES 2002 analyzer, and it is coupled with two ultrahigh vacuum chambers (Figure 2.22). The first chamber is the preparation chamber which allows to clean the

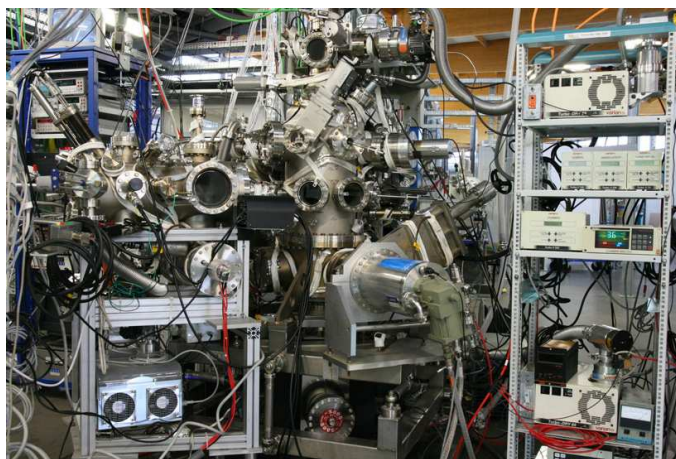


Figure 2.22: The UHV chambers of the TEMPO beamline.

sample surface by repeated cycles of sputtering and annealing. An evaporation system can be mounted on this UHV chamber in order to prepare molecular thin films. The photon excitation beam generated by the synchrotron arrives in the second chamber which is dedicated to measurements and which is equipped with a XPS spectrometer. A cryostat can be used in order to cool down the sample at a temperature of 50K by using liquid helium. The hemispherical XPS spectrometer allows to select the kinetic energy of the electrons arriving on the photomultiplier.

In the end, the TEMPO beamline has unique facilities in order to probe the electronic properties of a molecular film. In fact X-ray photoemission spectroscopy coupled with the synchrotron radiation excitation beam allows to get information on the electronic states of the sample with a high energetic resolution and a high sensitivity to the surface. The TEMPO beamline offers the possibility to excite a molecular film with a laser, and to record at the same time the core-level modifications with XPS. Finally, photoemission spectroscopy can be used to obtain information on the chemical and electronic properties

---

<sup>4</sup>TEMPO: Time resolved Experiments on Materials with PhOtoelectron spectroscopy.

of the sample, as well as on the charge transfer dynamics occurring at the molecule-substrate interface.

## Chapter Conclusions

In this chapter I have given a brief introduction of the tunneling effect and the resulting tunneling current occurring in a STM junction (§2.1.1). Thereafter I described the STM experimental setup used during my PhD. More precisely I showed that an ultra-high vacuum system can be used to preserve the cleanliness of the sample (§2.1.2.3). This is crucial to prevent undesirable modifications of the sample's properties. Additionally I showed the working principle of the piezoelectric scanner used in our STM experimental setup (§2.1.2.1). Moreover I showed the advantage of using a vibration isolation system to reduce the noise in the STM images, i.e. to increase the resolution (§2.1.2.2). Finally I showed that scanning tunneling microscopy is the appropriate technique to get topographic information of the sample at the atomic scale. In the second part of this chapter I have described the basic principle of the photoemission spectroscopy and related techniques (XPS, NEXAFS, RPES). Thereafter I showed that photoemission spectroscopy coupled with synchrotron radiation facilities is an ideal tool to probe the electronic properties of the sample with a high sensitivity to the surface and with a high energy resolution (§2.2.1.2). Furthermore I showed that X-ray photoemission spectroscopy can be used to get information about the occupied core-level states of the sample (§2.2.1.3). In contrast the NEXAFS spectroscopy gives information about the unoccupied states of the sample (§2.2.1.4). Finally I showed that the core-hole clock (RPES) spectroscopy can be used to characterize the charge transfer dynamics occurring at the molecule-substrate interface (§2.2.1.5). In the end I have described briefly the SOLEIL synchrotron facilities and TEMPO beamline used during my PhD. To conclude scanning tunneling microscopy and photoemission spectroscopy are useful tools to probe the structures and the electronic properties of organic thin film, as shown in the next chapter.

## Chapter 3

# Structure and Electronic properties of PTCDI films grown on Au(111) surface, investigated by STM and XPS

Perylene diimide derivatives are fascinating molecular building blocks for developing organic devices due to their outstanding chemical and thermal stability as well as their long-lasting photostability [66]. Intense research effort is focused on functionalizing a perylene diimide skeleton to optimize or to tune the packing and electronic properties of this molecular building block [66–75]. Perylene derivatives sublimated under vacuum have the ability to self-assemble on flat metal surfaces and to form two-dimensional hydrogen-bonded nanoarchitectures [76–80]. These molecules can also form multi-component organic structures when mixed with complementary building blocks [81–83]. Perylene derivatives are thus very attractive to fabricate new devices as new organic flat-heterojunction solar cells for example. Annealing is often used to reduce disorder in organic films and to improve the performance of devices based on organic building blocks [84,85]. Improvement of charge carrier mobility is often attributed to a higher degree of order in the solid state, but molecular organization can also be a key parameter. For example molecular cofacial orientation is expected to promote vertical electronic coupling through  $\pi$ - $\pi^*$  molecular interactions. This cofacial packing is presumed to enhance electronic communication between neighboring molecules in a column-type stacking, enabling efficient charge transport [86,87], through the molecular skeleton. However little is known about how the electronic properties of organic layers can be locally affected by lateral intermolecular electronic coupling.

Assessing the charge transfer arising at the molecule-metal interface is a key issue in molecular electronics. One issue is to master organic-metal interface to promote an efficient charge collection in the organic photovoltaic solar-cell and increase the performance of the device. In the field of spintronics, spin injection into organic semiconducting layer on ferromagnetic metal appears to be governed by the nature of the chemical bonds between the organic molecules and the magnetic electrodes at the interface [88].

These examples show that controlling the energy level alignment as well as the electronic processes at the interface between the metal electrode and the organic layer is of crucial importance for the injection of charges from the organic layer to the metal substrate. This is why the understanding of the organic/inorganic interface electronic properties is the focus of considerable research interest. Molecular chemical nature, molecular structure and shape, molecular packing [89–96] and the complex interplay of molecular adsorption-induced charge redistribution are key parameters driving energy level alignment at organic/metal interfaces as well as the efficiency and dynamics of charge transport across the contact. Resonant photo-emission electron spectroscopy is a powerful tool to assess charge transfer in organic thin film and at the organic/metal interface down to the sub-femtosecond range [45, 49, 50, 63, 97–100]. It is the reason why, in this chapter I will describe first how the molecular organization of a perylene diimide compound called PTCDI<sup>1</sup> can be control through sample’s temperature. After annealing, a new molecular structure is obtained with strong intermolecular electronic coupling between PTCDI molecules (§3.2.1). Thereafter I will describe the energy levels alignment of a PTCDI/Au(111) interface depending on the molecular film thickness by using XPS (§3.3, §3.4 and §3.5). Finally core-hole clock spectroscopy (i.e. RPES: Resonant Photoemission Spectroscopy) was used to demonstrate that a sub-femtosecond charge transfer can arise at the PTCDI/Au(111) interface for submonolayer coverage (§3.6). But before that I will give a brief description of the Au(111) substrate used, characterized by using STM (§3.1).

## 3.1 The Au(111) substrate: STM characterization

### 3.1.1 The gold single crystal

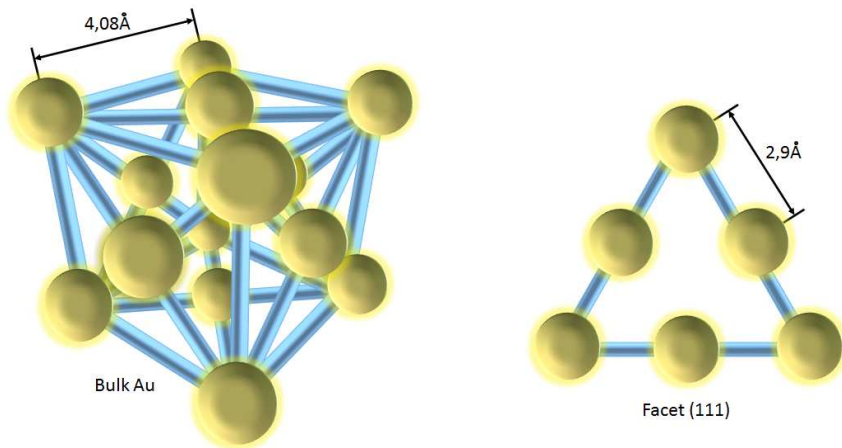


Figure 3.1: The Face-Centered Cubic (fcc) structure unit-cell of the Au bulk substrate.

<sup>1</sup>PTCDI: 3,4,9,10-perylenetetracarboxylic diimide.

To perform STM measurements, a conductive surface must be used. The gold substrate is one of the most commonly used substrates in STM experiment for its low reactivity and because it is easy to prepare. The bulk gold has a fcc (face-centered cubic) structure with a lattice parameter around  $4.08\text{\AA}$ , Figure 3.1. The distance between two nearby gold atoms is  $2.9\text{\AA}$ , [101]. In the work presented here, crystalline Au(111) substrates grown on mica were used (Figure 3.1).

### 3.1.2 The Au(111) herringbone reconstruction

The Au(111) herringbone reconstruction is a modification of the atomic packing at the surface in order to minimize the surface energy. This change of the atomic packing creates an atomic overdensity at the surface. The atomic overdensity involves a uniaxial

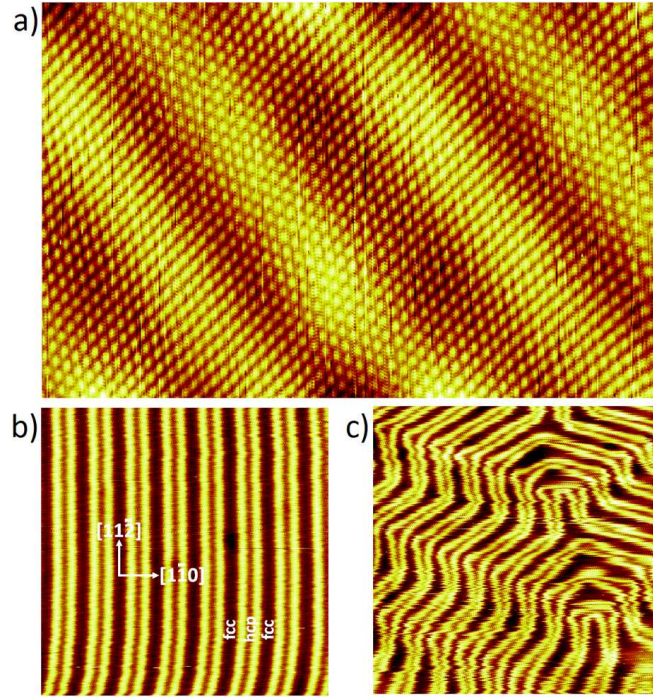


Figure 3.2: STM images of the  $[(22 \pm 1) \times \sqrt{3}]$  Au(111) reconstruction: (a) small range with atomic resolution,  $12 \times 7.2 \text{ nm}^2$ ,  $V_s = 0.3 \text{ V}$ ,  $I_t = 0.1 \text{ nA}$ ; (b) medium range  $48 \times 48 \text{ nm}^2$ ,  $V_s = 0.8 \text{ V}$ ,  $I_t = 0.2 \text{ nA}$ ; (c) wide range  $72 \times 72 \text{ nm}^2$ ;  $V_s = 0.9 \text{ V}$ ,  $I_t = 0.3 \text{ nA}$ .

contraction of the Au(111) topmost layer in the  $[\bar{1}\bar{1}0]$  direction [32]. The fcc packing of the gold bulk is modified at the surface, leading to a rectangular unit-cell with lattice vectors  $22a$  and  $\sqrt{3}a$ , where  $a = \frac{\sqrt{2}}{2}b$  and  $b \simeq 4.08\text{\AA}$  the lattice parameter of the gold fcc bulk structure. The resulting superstructure consists of alternating fcc and hcp (hexagonal close-packed) domains with in between a transition region. In the STM images the fcc and hcp domains appear dark, while the transition region appears bright, Figure 3.2b. The fcc domains correspond to the largest dark regions [32], while the hcp domains correspond to the smallest dark regions, Figure 3.2. Consequently the Au(111)

herringbone reconstruction exhibits a periodic pattern of pairwise parallel corrugation lines, running in the  $[11\bar{2}]$  direction, Figure 3.2b. The distance measured between neighbor pairs in the  $[1\bar{1}0]$  direction is 6.2nm, Figure 3.2b. The distance measured between two nearest Au atoms is around 2.8Å, Figure 3.2a. These values are really close to those obtained in the literature [32,101]. In addition to that, a long-range periodicity is observed in the reconstructed topmost layer consisting of a modification of the corrugation lines direction by  $\pm 120^\circ$  forming a herringbone pattern, Figure 3.2c.

## 3.2 Temperature-dependent PTCDI self-assembly on Au(111) substrate

### 3.2.1 Tailoring the intermolecular electronic coupling in PTCDI self-assembled monolayer by controlling the substrate temperature

Here we investigate the structure and electronic properties of PTCDI self-assembled nanoarchitectures grown on Au(111) substrate. Scanning tunneling microscopy (STM) in ultrahigh vacuum reveals structure dependent lateral intermolecular electronic coupling in a PTCDI layer after annealing.

Experiments were performed in an ultrahigh vacuum (UHV) chamber at a pressure of  $10^{-8}$  Pa. The Au(111) surfaces were sputtered with  $\text{Ar}^+$  ions and then annealed in UHV at  $600^\circ\text{C}$  during 1h. PTCDI molecules, Figure 3.3a, were evaporated at  $250^\circ\text{C}$  and then deposited on the gold surface kept at room temperature. Cut Pt/Ir tips were used to obtain constant current STM images at room temperature with a bias voltage applied to the sample. STM images were processed and analyzed using the home made FabViewer application [102].

Figure 3.3b shows the Au(111) surface after deposition of PTCDI molecules at room temperature. Self-assembled PTCDI domains are observed using STM. These domains are entirely covering the Au(111) surface at high concentration. Molecules are forming chains running parallel to each other. Molecules from neighboring chains are tilted in the opposite direction by the same angle of  $\pm 12^\circ$ . Analysis of the STM image shows that PTCDI chains are stabilized by double-hydrogen bonds ( $\text{N}-\text{H}\cdots\text{O}$ ) between imide groups of adjacent molecules, as it is confirmed by density functional theory calculations [104]. The model of this structure is presented in Figure 3.3c. The network unit cell of this canted structure is a parallelogram with  $\simeq 1.6\text{nm}$  and  $\simeq 1.5\text{nm}$  unit cell constants and an angle of  $\simeq 95^\circ$  between the axes.

Figure 3.3d shows the PTCDI network on Au(111) after 2 h postannealing at  $50^\circ\text{C}$ . Molecules are now forming a new two dimensional nanoarchitecture that has not been predicted by previous calculations [104]. The model of this structure is presented in Figure 3.3e. The network unit cell is a parallelogram with  $\simeq 2.4\text{nm}$  and  $\simeq 1.4\text{nm}$  unit cell constants and an angle of  $\simeq 105^\circ$  between the axes. Molecules are forming double-PTCDI chains separated by a single-PTCDI chain. PTCDI chains are stabilized by the double-hydrogen bonds between imide groups previously observed in Figure 3.3b.

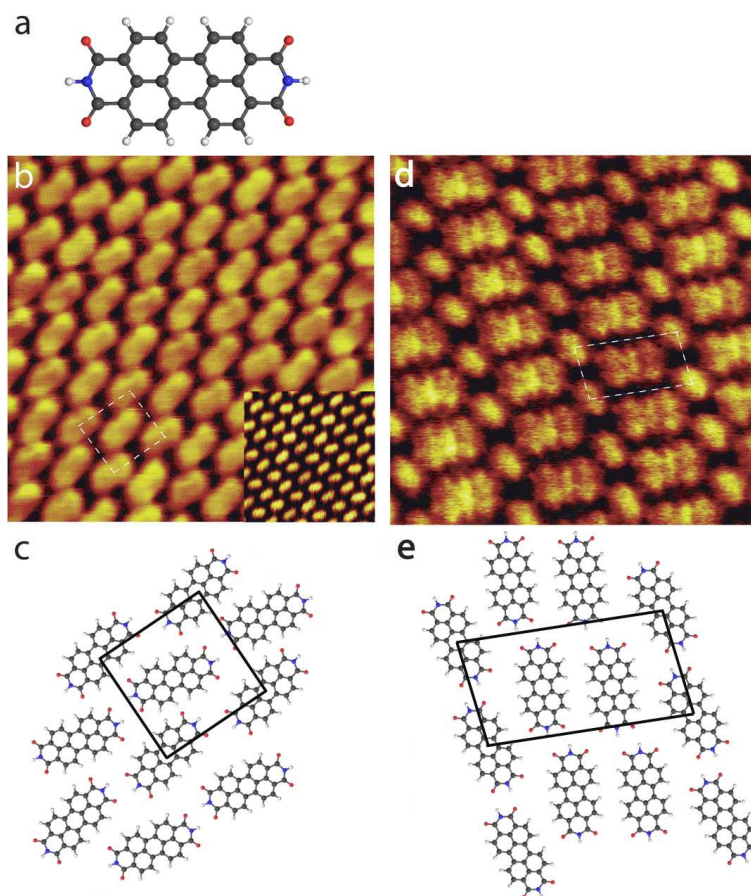


Figure 3.3: (a) Scheme of the PTCDI molecule. Blue, red, light gray and white balls correspond to nitrogen, oxygen, carbon and hydrogen atoms, respectively. (b) STM images of the PTCDI network on Au(111) at room temperature;  $7 \times 7 \text{ nm}^2$ ,  $V_s = -0.5 \text{ V}$ ,  $I_t = 0.8 \text{ nA}$ . Inset:  $7 \times 7 \text{ nm}^2$ ;  $V_s = -0.811 \text{ V}$ ,  $I_t = 0.211 \text{ nA}$ . (c) Model of the PTCDI canted network. (d) STM images of the PTCDI network on Au(111) after  $50^\circ\text{C}$  annealing;  $7 \times 7 \text{ nm}^2$ ,  $V_s = -0.811 \text{ V}$ ,  $I_t = 0.211 \text{ nA}$ . (e) Model of the PTCDI double chain nanoarchitecture. The PTCDI network unit cells are represented by white dotted lines in the STM images and by black lines in the molecular models [103].

The PTCDI double-chains are composed of two close-packed PTCDI chains, i.e. the molecules of neighboring chains are packed side-by-side. The molecules of each chain have the same orientation, i.e. molecules are rotated by an angle of  $+12^\circ$  in comparison with the chain direction. The molecules of the single-chain separating PTCDI double-chains are rotated in the opposite direction by an angle of  $-12^\circ$ .

Figure 3.4 reveals that the contrast of the PTCDI double-chains in the STM images is strongly affected by tunneling parameters. For a tunneling bias of  $-0.811 \text{ V}$ , the gap between two neighboring PTCDI molecules in the PTCDI double-row appears bright, Figure 3.4a. For a tunneling bias of  $-0.411 \text{ V}$ , the contrast of all PTCDI molecules is similar, Figure 3.4b. In contrast the gap between two neighboring PTCDI molecules in the PTCDI double-chain structure appears darker for a tunneling bias of  $-0.211 \text{ V}$ ,

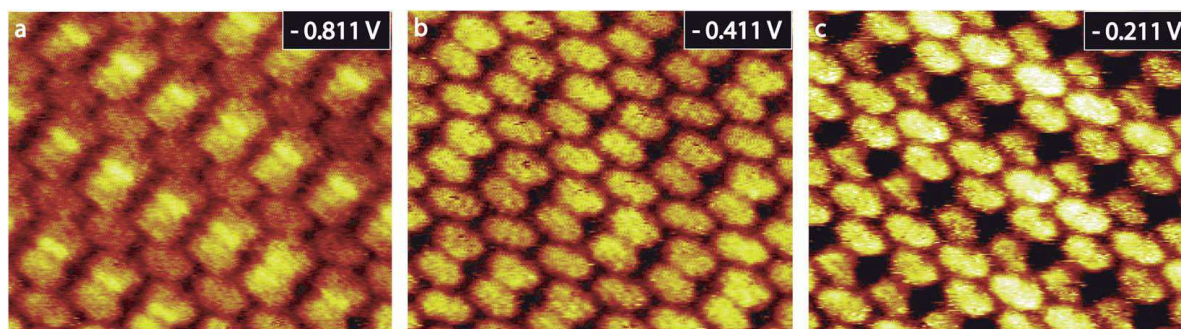


Figure 3.4: Influence of tunneling parameters on the contrast in STM images of the PTCDI network on Au(111) surface. The STM images in (a), (b), (c) have been recorded successively using the tunneling parameters: (a)  $V_s = -0.811$  V,  $I_t = 311$  pA, (b)  $V_s = -0.411$  V,  $I_t = 311$  pA, (c)  $V_s = -0.211$  V,  $I_t = 311$  pA, respectively. Image size:  $7 \times 5.8 \text{ nm}^2$ , [103].

Figure 3.4c. In addition the darkest area in the STM image is located in the center of the double-chain, in the gap separating two paired-molecular building blocks, Figure 3.4c. It should be noticed that the PTCDI molecules of the single-chains appear slightly brighter than the molecules of the double-chains, Figure 3.4c. To that extent molecular contrast in the STM image at  $-0.811$  V is reversed in comparison to the STM features observed at  $-0.211$  V.

PTCDI molecules can also locally form a triple-chain structure on Au(111) upon annealing, Figures 3.5a,b. The PTCDI triple-chain is composed of three side-by-side close-packed PTCDI chains. For a tunneling bias of  $-0.111$  V, the gap between side-by-side PTCDI molecules of neighboring chains appears bright in the triple-chain structure, Figure 3.5a. In comparison, for a tunneling bias of  $-0.211$  V the molecules of the central chain appear brighter, Figure 3.5c. The cross section shown in Figure 3.5d reveals that the height of the PTCDI molecules in the side-chain of the triple-chain structure appears  $\simeq 0.5 \text{ \AA}$  smaller than the PTCDI height in the central chain and appears  $\simeq 0.5 \text{ \AA}$  higher than the PTCDI height in the canted structure. In addition intramolecular features are visible on the high resolution STM image in Figure 3.5c. Molecules of the central-chain are composed of twelve bright spots. In contrast molecules of the side-chain are composed of ten bright spots, and molecules of the canted PTCDI structure are composed of two bright stripes.

STM images demonstrate that the electronic properties of the PTCDI film are strongly modified by the organic layer structure. Tunneling parameters are drastically affecting molecular contrast in the STM images when molecules are arranged in a side-by-side arrangement in the double and triple chain structures. STM especially shows that new electronic states appear in the gap separating side-by-side molecules at  $-0.811$  V (Figures 3.3d and 3.4a), i.e. new electronic states induced by lateral inter-molecular coupling are created by the side-by-side molecular arrangement. Surprisingly these electronic states are also delocalized onto the whole molecular skeleton at specific tunneling parameters. The contrast of the molecules in the double and triple-chain thus differs from the contrast of the molecules in the canted structure (Figures 3.4c and 3.5c).

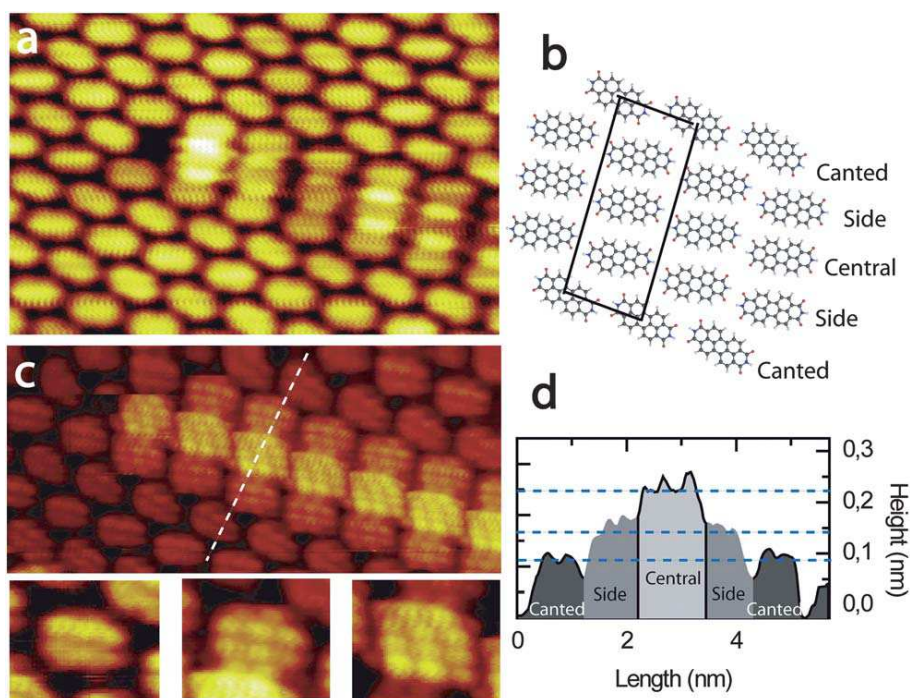


Figure 3.5: STM image of the PTCDI triple-chain structure on Au(111), (a)  $10 \times 7 \text{ nm}^2$ ,  $V_s = -0.111 \text{ V}$ ,  $I_t = 411 \text{ pA}$  (model of the triple-chain PTCDI structure in (b)); (c)  $12 \times 5 \text{ nm}^2$ ,  $V_s = -0.211 \text{ V}$ ,  $I_t = 411 \text{ pA}$ . Inset: canted PTCDI molecule (left), side-chain molecule (center) and central-chain molecule (right),  $3 \times 2 \text{ nm}^2$ . (d) Profile taken along the dotted line in (c). The profile of the canted PTCDI molecule is represented in dark gray, the profile of the side-chain PTCDI molecule is represented in gray and the profile of the central-chain PTCDI molecule is represented in light gray, [103].

For example the molecules of the central chain in the triple-chain structure appear the brightest at  $-0.211 \text{ V}$ , followed by the molecules of the side rows. In comparison the molecules of the canted structure are the darkest, Figure 3.5c. In addition STM images also show that intramolecular features are strongly affected by molecular location in the triple-chain structure. Particularly the number and the position of bright spots constituting the molecule in the STM image are different for the molecules located in the central and in the side chains of the triple chain structure, Figure 3.5c. It therefore appears that the thermally activated side-by-side molecular packing drastically affects the electronic properties of the whole molecular skeleton. Interestingly molecules having only one side-by-side neighbor have a symmetrical shape in the STM images; i.e. the molecules are composed of two parallel rows of three bright spots and two external rows of two bright spots at  $-0.211 \text{ V}$ , Figure 3.5c. In comparison molecules having two side-by-side neighbors have a parallelogram shape in the STM images. These molecules are composed of four rows of three bright spots. These rows are slightly shifted in comparison to each other leading to a molecular parallelogram shape despite PTCDI having a rectangular-like skeleton, Figure 3.3a. This shows that intermolecular binding affects molecular electronic properties so strongly that the molecular integrated density

of states recorded in the STM images differs from molecular geometric shape.

The STM measurements therefore reveal that charge transport across the perylene derivative layer would not only depend on the electronic properties of individual organic building blocks but also could be greatly enhanced or reduced by the structure of the organic layer. The side-by-side molecular arrangement is opening new electronic channels through the PTCDI layer. Electron transport from the gold surface to the STM tip is favored at  $-0.811$  V in the gap between side-by-side molecules in the double-row structure. This channel disappears at  $-0.411$  V. At a voltage of  $-0.211$  V, electron transport from the surface to the STM tip is locally reduced; side-by-side molecules appear darker in the double chain structure. The position of these electronic channels is shifted in energy in the triple-chain structure. For example the favored electronic channel localized in the gap between side-by-side molecules appears at  $-0.111$  V in the triple-chain structure whereas it appears at  $-0.811$  V in the double-chain structure. These observations are of prime importance in the field of organic photovoltaic for example, where perylene derivatives are widely used as building blocks. This opens new possibilities for improving charge transport in organic devices. In order to understand the appearance of these new electronic states induced by the side-by-side packing of the molecules on Au(111), one would have to compare high resolution scanning tunneling spectroscopy spectra [105] or synchrotron valence band spectra [42] with a local density of states calculation for these monolayers adsorbed on the gold surface. Since these structures are incommensurable and the PTCDI monolayer unit cells are quite large, this kind of calculation would be difficult to achieve at present.

### 3.2.2 PTCDI self-assembled architecture formed on Au(111) surface after a post-annealing at 200°C

After a post-annealing of the sample at 200°C during 1 hour, a closed-packed side-by-side structure was obtained, Figure 3.6. In contrast to the double-chains and triple-chains structures (§3.2.1), all the PTCDI molecules are placed in a side-by-side configuration after annealing at 200°C, i.e. no molecule remains in the typical PTCDI canted structure. Large domains of this side-by-side structure up to  $50 \times 50$  nm<sup>2</sup> were observed. Figure 3.6a, shows that the Au(111) herringbone reconstruction is unperturbed by the PTCDI molecular film, indicating a relatively weak molecule-substrate interaction. The PTCDI side-by-side network unit-cell is parallelogram with  $A \simeq 1.22$  nm and  $B \simeq 0.91$  nm, the lattice vector lengths which are separated by an angle of  $\simeq 75^\circ$ , Figure 3.6b. A molecular model of this PTCDI side-by-side structure is given in Figure 3.6c. The motif of the PTCDI side-by-side network unit-cell is composed of one PTCDI molecule. The side-by-side structure consists of PTCDI chains which running parallel to each other. The PTCDI molecules of a same chain are linked together through N–H $\cdots$ O hydrogen bonds. The distance between two electronically coupled neighboring PTCDI chains is equal to 0.91 nm, while the distance between two PTCDI molecules of a same chain is around 1.22 nm.

To summarize, in this section I investigated temperature-dependent PTCDI two-dimensional self-assembly on Au(111) surface in ultrahigh vacuum using scanning tun-

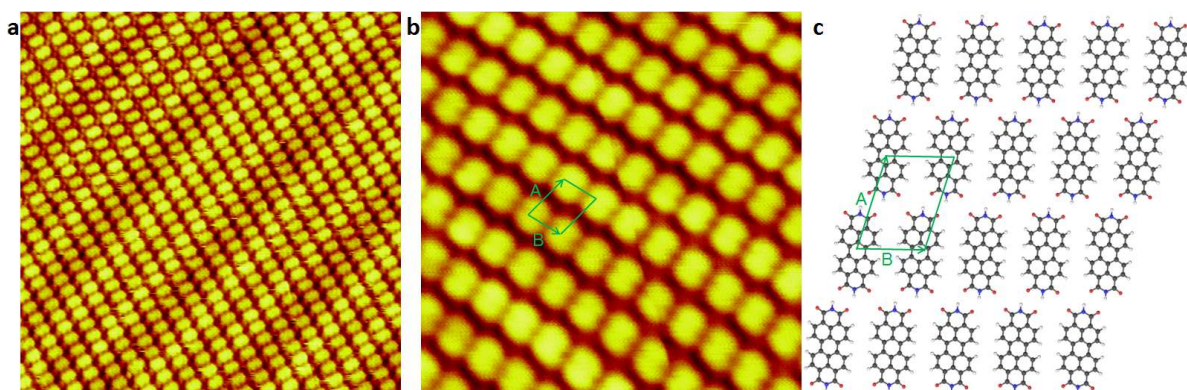


Figure 3.6: STM image of the PTCDI side-by-side structure formed on Au(111) surface after annealing at 200°C: (a) wide range STM image 24×24 nm<sup>2</sup>, V<sub>s</sub>= +1.6 V, I<sub>t</sub>=201 pA; (b) small range STM image 10×10nm<sup>2</sup>, V<sub>s</sub>= +1.9 V, I<sub>t</sub>=201 pA; (c) molecular model of the side-by-side structure: Blue, red, gray and white balls correspond to nitrogen, oxygen, carbon and hydrogen atoms, respectively.

neling microscopy. STM images show that molecules self-assemble into a hydrogen-bonded canted structure at room temperature (§3.2.1). After 50°C post-annealing, PTCDI molecules self-assemble into new double and triple-chain structures. STM images recorded at different bias reveal strong electronic coupling between molecules packed side-by-side. This electronic coupling strongly affects molecular contrast and molecular shape in the STM images (§3.2.1). Additionally, after annealing the sample at 200°C, the PTCDI canted structure was no longer observed, i.e. all the PTCDI molecules are packed side-by-side (§3.2.2). In that way, large domains of the side-by-side structure were obtained (up to 50×50 nm<sup>2</sup>). Therefore in this section I showed that post-annealing can be used not only to modify the structure of the perylene-based film as it is usually expected but also to create new electronic states. This is of huge interest to engineer new perylene diimide-based nanoarchitectures having specific electronic properties for organic devices. In addition to that, the energy level alignment at the organic/metal interface is also a relevant quantity in order to understand and control the electronic properties of organic nano-devices. It is the reason why in the three following sections I will successively describe the lineshape and energy position of the core-level, NEXAFS and valence band spectra of the PTCDI/Au(111) interface according to molecular film thickness.

### 3.3 Evolution of the PTCDI core-level spectra with surface coverage

The XPS measurements were performed at the TEMPO<sup>2</sup> beamline of the French synchrotron SOLEIL. The beamline is equipped with SCIENTA SES 2002 analyzer, and two undulators HU80 and HU44 for an energy range of 50 to 1500eV. The C<sub>1s</sub>, N<sub>1s</sub> and

<sup>2</sup>TEMPO: Time resolved Experiments on Materials with PhOtoelectron spectroscopy.

$O_{1s}$  core-level spectra of a PTCDI film grown on Au(111) surface have been successively recorded at sub-monolayer, monolayer and multilayer coverage.

### 3.3.1 $C_{1s}$ core-level spectra of PTCDI films

First, the  $C_{1s}$  core-level photoemission spectrum was recorded for each coverage with a beamline photon energy fixed at 385 eV. The  $C_{1s}$  core-level spectra were fitted using a Voigt Area G/L function with a constant Lorentzian width of 0.07eV. Figures 3.7a,b,c

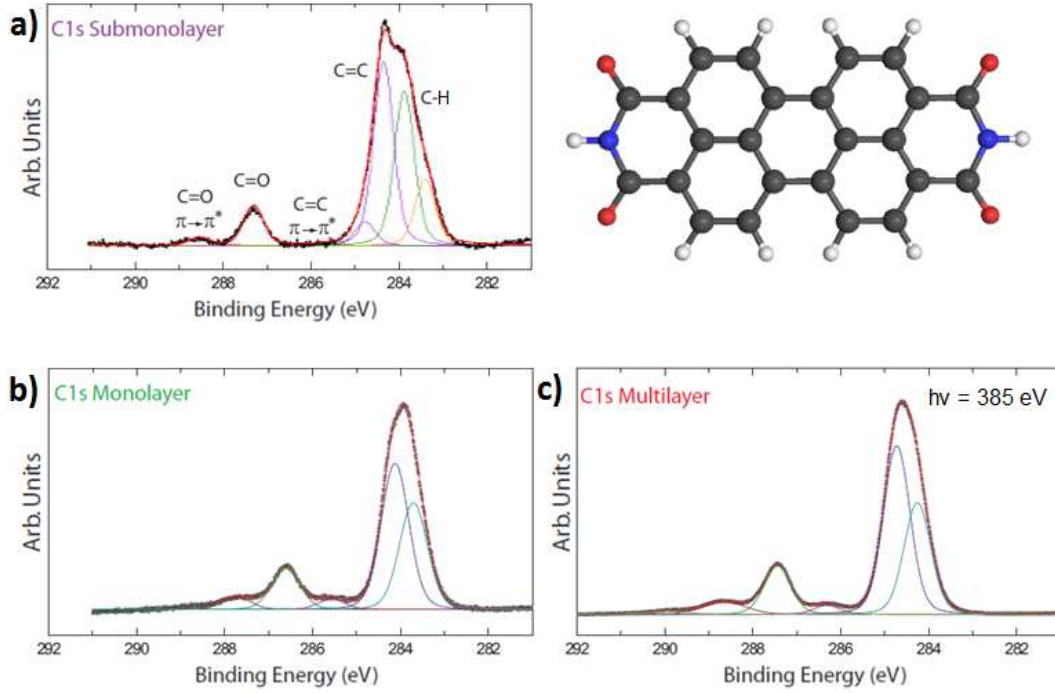


Figure 3.7: PTCDI  $C_{1s}$  core level photoemission spectra measured by using a photon energy  $h\nu = 385$  eV. The PTCDI films were grown on the Au(111) surface with three different coverages: (a) sub-monolayer, (b) monolayer, and (c) multilayer.

display the peak fit analysis of the PTCDI  $C_{1s}$  core-level spectra at sub-monolayer, monolayer and multilayer coverage respectively. All characteristics of the peak fit analysis are shown in table 3.1, such as the energies positions, the peak areas, and the Gaussian widths. At multilayer coverage the PTCDI  $C_{1s}$  core-level spectrum is composed of five main peaks (Figure 3.7c), similar to those previously obtained by Zahn *et al* [42] for PTCDA, i.e. with approximately the same lineshape and same energy positions (with a maximum offset about 1.32eV). These five main peaks ( $C-H$ ,  $C-C$ ,  $\pi \rightarrow \pi_{C=C}^*$ ,  $C=O$ ,  $\pi \rightarrow \pi_{C=O}^*$ ) are also observed for PTCDI submonolayer and monolayer coverage with binding energy offsets smaller than 1eV. As demonstrated in previous work [42], the first peak of the PTCDI  $C_{1s}$  spectrum observed at 284.14eV binding energy can be assigned to the  $C-H$  bonds of the PTCDI molecule. The second and the fourth peaks correspond respectively to  $C-C$  and  $C=O$  bonds, with binding energies around 284.40

and 287.10eV. The C=O bond has a higher binding energy than the C–C bond, due to the higher electronegativity of oxygen compared to that of carbon atom. The third and fifth peaks correspond to the  $\pi \rightarrow \pi^*$  electronic transitions of the C–C and C=O components respectively, with binding energies around 295.96 and 288.32eV. Furthermore, two additional peaks are observed in the PTCDI submonolayer film at binding energies of 283.41 and 284.77eV. The origin of these additional features is not well-understood at present.

Each PTCDI molecule possess 24 carbon atoms, as depicted in Figure 3.3a. By determining the area of each peak divided by the total area of the  $C_{1s}$  curve it is therefore possible to calculate the number of atoms of the PTCDI molecule which are involved in the photoemission process of each peak. As depicted in table 3.1 the relative area of the C–H peak for PTCDI monolayer is calculated around 33.6%, corresponding to a number of 8 carbon atoms. This corresponds to the number of C–H bonds of a single PTCDI molecule, Figure 3.3a. In the same way, it is possible to calculate the number of the C–C bonds of a PTCDI molecule by considering the areas of the C–C and  $\pi \rightarrow \pi^*_{C-C}$  peaks. This calculation leads to a relative area of 49.2%, which corresponds to 12 carbon atoms (i.e. 12 C–C bonds). Finally a value of 17.2% is obtained by considering the areas of the C=O and  $\pi \rightarrow \pi^*_{C=O}$  peaks, corresponding to a number of 4 carbon atoms involved in the formation of C=O bonds. The same procedure was applied for the PTCDI submonolayer and multilayer films, and leads to similar results. These calculations support the idea that the five main features obtained by fitting the  $C_{1s}$  spectrum can be assigned to the chemical bonds of the PTCDI molecule (C–H, C–C,  $\pi \rightarrow \pi^*_{C=C}$ , C=O,  $\pi \rightarrow \pi^*_{C=O}$ ).

Thickness	Submonolayer				Monolayer				Multilayer			
	Energy (eV)	Rel. Area(%)	$W_G$ (eV)	$W_L$ (eV)	Energy (eV)	Rel. Area(%)	$W_G$ (eV)	$W_L$ (eV)	Energy (eV)	Rel. Area(%)	$W_G$ (eV)	$W_L$ (eV)
$C_{1s}$												
C-H	283.87	32.40	0.1912	0.07	284.24	33.6	0.3481	0.07	284.50	31.13	0.2944	0.07
C-C	284.35	38.67	0.1912	0.07	284.74	46.03	0.3481	0.07	285.01	46.85	0.2944	0.07
$\pi \rightarrow \pi^*_{C-C}$	285.89	0.03	0.1912	0.07	286.48	3.17	0.3481	0.07	286.71	2.82	0.2944	0.07
C=O	287.26	8.28	0.1912	0.07	287.72	13.13	0.3481	0.07	287.94	13.64	0.2944	0.07
$\pi \rightarrow \pi^*_{C=O}$	288.49	1.64	0.1912	0.07	289.06	4.07	0.3481	0.07	289.25	5.56	0.4964	0.07
Add. feature 1	283.41	14	0.1912	0.07	$\emptyset$	$\emptyset$	$\emptyset$	$\emptyset$	$\emptyset$	$\emptyset$	$\emptyset$	$\emptyset$
Add. feature 2	284.77	4.98	0.1912	0.07	$\emptyset$	$\emptyset$	$\emptyset$	$\emptyset$	$\emptyset$	$\emptyset$	$\emptyset$	$\emptyset$

Table 3.1: Results of the peak fit analysis of the PTCDI  $C_{1s}$  spectrum of Figure 3.7.

### 3.3.2 $N_{1s}$ core-level spectra of PTCDI films

Thereafter, the PTCDI  $N_{1s}$  core-level photoemission spectra were recorded at submonolayer, monolayer and multilayer coverages with a beamline photon energy fixed at  $h\nu = 500$  eV, Figure 3.8. The  $N_{1s}$  core-level spectra were fitted using a Voigt Area G/L function with a constant Lorentzian width of 0.1658 eV. All the characteristics of the peak fit analysis are given in Table 3.2. For PTCDI submonolayer and monolayer coverage, the  $N_{1s}$  core-level photoemission spectra are composed of only one peak at binding energies of 399.01 and 399.52eV respectively. This peak can be attributed to the C–N bonds of the PTCDI molecule [42]. In contrast for the PTCDI multilayer

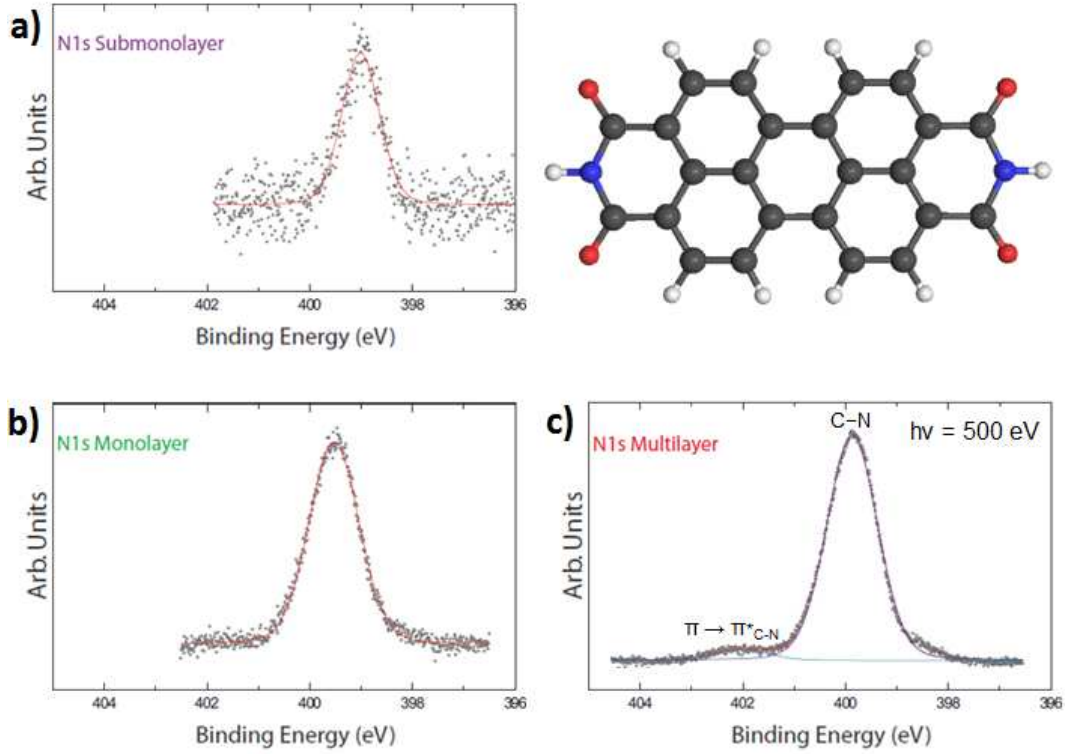


Figure 3.8: PTCDI  $N_{1s}$  core level photoemission spectra measured by using a photon energy  $h\nu = 500$  eV. The PTCDI films were grown on the Au(111) surface with three different coverages: (a) sub-monolayer, (b) monolayer, and (c) multilayer.

film, two peaks were obtained in the  $N_{1s}$  core-level spectrum. The first peak at 399.86 eV binding energy is attributed to the C–N bond, while the second peak at 401.96 eV corresponds to the  $\pi \rightarrow \pi^*$  electronic transitions of the C–N bond. The lineshape and energy positions of these peaks are similar to those obtained by Zahn *et al* for DiMe-PTCDI [42]. The  $\pi \rightarrow \pi^*$  shake-up processes are suppressed at monolayer and submonolayer coverage due to stronger molecule-substrate interactions compared to the PTCDI multilayer film. This phenomenon was previously observed by O’Shea *et al* [106] for PTCDI  $C_{1s}$  core-level, but not for the  $N_{1s}$  core-level spectra.

Thickness	Submonolayer				Monolayer				Multilayer			
	Energy (eV)	Rel. Area(%)	$W_G$ (eV)	$W_L$ (eV)	Energy (eV)	Rel. Area(%)	$W_G$ (eV)	$W_L$ (eV)	Energy (eV)	Rel. Area(%)	$W_G$ (eV)	$W_L$ (eV)
$N_{1s}$												
C-N	399.01	100	0.2818	0.1658	399.52	100	0.4038	0.1658	399.86	95.5	0.4108	0.1658
$\pi \rightarrow \pi^*_{C-N}$	$\emptyset$	$\emptyset$	$\emptyset$	$\emptyset$	$\emptyset$	$\emptyset$	$\emptyset$	$\emptyset$	401.96	4.5	0.4108	0.1658

Table 3.2: Results of the peak fit analysis of the PTCDI  $N_{1s}$  spectrum of Figure 3.8.

### 3.3.3 O<sub>1s</sub> core-level spectra of PTCDI films

In the same way the PTCDI O<sub>1s</sub> core-level photoemission spectra were recorded at sub-monolayer, monolayer and multilayer coverage with a beamline photon energy fixed at  $h\nu = 632$  eV, Figure 3.9. The O<sub>1s</sub> core-level spectra were fitted using a Voigt Area G/L

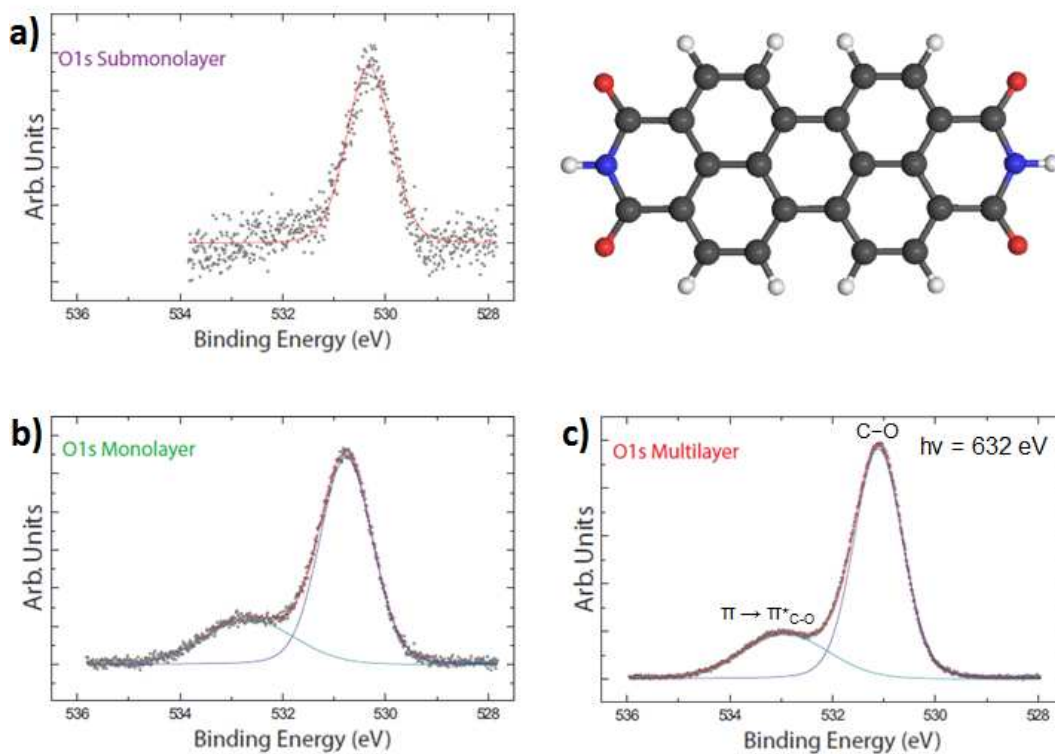


Figure 3.9: PTCDI O<sub>1s</sub> core level photoemission spectra measured by using a photon energy  $h\nu = 632$  eV. The PTCDI films were grown on the Au(111) surface with three different coverages: (a) sub-monolayer, (b) monolayer, and (c) multilayer.

function with a constant Lorentzian width of 0.16 eV. All the characteristics of the peak fit analysis are recorded in Table 3.3. At sub-monolayer coverage a single peak was observed at 530.32 eV binding energy, that can be attributed to the C–O bonds of the PTCDI molecule. At monolayer coverage two peaks were observed in the O<sub>1s</sub> core-level spectrum. The first peak at a binding energy of 530.78 eV can be attributed to C–O bonds, while the second peak at 532.68 eV corresponds to the  $\pi \rightarrow \pi^*_{C-O}$  electronics transitions. Similarly at multilayer coverage two peaks were obtained at binding energies of 531.11 and 532.92 eV corresponding to the C–O bonds and  $\pi \rightarrow \pi^*_{C-O}$  electronics transitions respectively. Again the lineshape and energy positions of these peaks are similar to those previously obtained by Zahn *et al* for DiMe-PTCDI [42]. Finally the  $\pi \rightarrow \pi^*$  shake-up processes are observed at monolayer and multilayer coverages but not at the sub-monolayer range. In fact for the PTCDI sub-monolayer film, the interactions with the gold surface are too strong and suppress the  $\pi \rightarrow \pi^*$  electronic transitions.

This phenomenon was previously observed for PTCDI  $C_{1s}$  core-level, but not for the  $O_{1s}$  core-level spectra [106].

Thickness	Submonolayer					Monolayer					Multilayer				
	Energy (eV)	Rel. Area(%)	nbr. atom	$W_G$ (eV)	$W_L$ (eV)	Energy (eV)	Rel. Area(%)	nbr. atom	$W_G$ (eV)	$W_L$ (eV)	Energy (eV)	Rel. Area(%)	nbr. atom	$W_G$ (eV)	$W_L$ (eV)
$O_{1s}$															
C-O	530.32	100	4	0.3649	0.16	530.78	74.1	3	0.4343	0.16	531.11	74.79	3	0.4026	0.16
$\pi \rightarrow \pi_{C-O}^*$	$\emptyset$	$\emptyset$	$\emptyset$	$\emptyset$	$\emptyset$	532.68	25.9	1	0.8279	0.16	532.92	25.21	1	0.5994	0.16

Table 3.3: Results of the peak fit analysis of the PTCDI  $O_{1s}$  spectrum of Figure 3.9.

### 3.3.4 PTCDI core-level spectra: Comparison with other perylene derivatives

In this section I will compare the core-levels of a PTCDI molecule with those obtained by Zahn *et al* for two other perylene derivatives called DiMe-PTCDI and PTCDA [42]. On the one hand, PTCDI multilayer has the same  $C_{1s}$  core level spectrum than PTCDA with the same lineshape and the same number of peaks (excluding the C–C–O peak), but with a 1eV shift to the lower binding energies. Additionally the C–N component of the DiMe-PTCDI core-level spectrum is not observed for PTCDI molecule which does not possess any methyl group ( $-N-CH_3$ ) attached to its nitrogen atoms. On the other hand, PTCDI multilayer has the same  $O_{1s}$  core level spectrum than DiMe-PTCDI with the same lineshape and the same peaks (C=O and  $\pi \rightarrow \pi_{C-O}^*$ ), but with a 0.4eV shift to the lower binding energies. In contrast to PTCDI, an additional C–O–C feature is observed in the  $O_{1s}$  core level spectrum of PTCDA due to the oxygen atoms that substitute the N–H groups of PTCDI.

Another characteristic of the  $C_{1s}$  core level spectra is the energy splitting between the aromatic part (the C–C peak), and the functional group (the C=O peak). For PTCDI an energy splitting of 2.7eV was measured, in comparison the energy splitting obtained in previous works [42] is 3.3eV for PTCDA, and 2.7eV for DiMe-PTCDI. This is quite surprising because the energy splitting is related to the electronegativity of the substituent (R) attached to the terminal end-group (R–C=O). Therefore a larger energy splitting is expected for PTCDI compared to DiMe-PTCDI, due to the smaller electronegativity of the  $H_3C-N-$  group compared to  $H-N-$ . But in reality the same energy splitting was obtained for both PTCDI and DiMe-PTCDI.

The electronic transition  $\pi \rightarrow \pi_{C-O}^*$ , corresponds to a shake-up process, i.e. an intramolecular charge-transfer depending on the substituent electronegativity. It was demonstrated by Zahn *et al* [42], that the amplitude of the  $C_{1s}$  core level  $\pi \rightarrow \pi_{C-O}^*$  peak is larger for PTCDA than for DiMe-PTCDI due to a greater electronegativity of the PTCDA functional end-groups compared to DiMe-PTCDI. For the  $\pi \rightarrow \pi_{C-O}^*$  peak of the PTCDI  $C_{1s}$  core-level, we found an intensity of 28% of the corresponding main line (C=O peak intensity). This intensity is lower than the one obtained for PTCDA (50%) molecule, but it is equivalent to the  $\pi \rightarrow \pi_{C-O}^*$  peak intensity observed for DiMe-PTCDI molecule. Similarly we can compare the  $\pi \rightarrow \pi_{C-O}^*$  peak intensity of the  $O_{1s}$  core level spectra for PTCDI, PTCDA and DiMe-PTCDI. An intensity of 18.77% of the corresponding main line (C=O) was measured for PTCDI, which must be compared to

the intensity of 20% obtained in previous work [42] for PTCDA, and 16% for DiMe-PTCDI. Therefore, the  $\pi \rightarrow \pi_{C-O}^*$  peak intensity of the PTCDI  $O_{1s}$  core level spectrum is between those obtained for PTCDA and DiMe-PTCDI. This is coherent with the fact that the intensity of the shake-up  $\pi \rightarrow \pi_{C-O}^*$  process, is related to the electronegativity of the functional end group of the considered perylene derivative.

A displacement of the C–C peak to higher binding energies was observed by comparing the energy positions of the core-level peaks obtained for the PTCDI sub-monolayer and multilayer films. This energy shift is about 0.8 eV for the  $O_{1s}$  and  $N_{1s}$  core level, and around 0.4 eV for the  $C_{1s}$  core level. The modification of the energy positions of PTCDI core-levels with the film thickness can be explained by a greater charging effect in multilayer compared to sub-monolayer film. The charging effect is observed for insulating materials. During the photoemission process there are creation and accumulation of positive charges in the insulating film. These positive charges imply a decrease of the photoelectrons kinetic energy (speed), i.e. an increase of the measured binding energy ( $E = E_k + E_b$ ).

The disappearance of the  $\pi \rightarrow \pi_{C-O}^*$  peak in the  $O_{1s}$  and  $N_{1s}$  core level spectra can be attributed to an enhanced molecule-substrate interaction occurring at low coverage [106]. In contrast to the previous results of O’Shea *et al* [106], the  $\pi \rightarrow \pi_{C-O}^*$  peak of PTCDI  $C_{1s}$  core-level spectra is always observed even at sub-monolayer coverage.

To summarize, significant modifications of the line-shape and energy positions of the PTCDI electronic states depending on the molecular film thickness were observed by measuring the  $C_{1s}$ ,  $N_{1s}$  and  $O_{1s}$  core-level spectra of PTCDI films grown on Au(111) surface. Additionally, by comparing our results on PTCDI molecules with those obtained for PTCDA and DiMe-PTCDI [42] it appears that molecular substituents play an important role in the electronic properties of perylene derivatives, i.e. on the energy level alignment. This information is crucial to design organic nano-devices with desired properties. Moreover to build organic nano-devices it is also needed to learn more about the growth of molecular multilayer films. It is what I show in the next section for a PTCDI multilayer film, by using angular NEXAFS spectroscopy.

### 3.4 Angular NEXAFS spectra of a PTCDI multilayer Film

Figure 3.10 shows the NEXAFS (Near Edge X-ray Absorption Fine Structure) spectra of the PTCDI multilayer film taken at the C K-edge. In this Figure the absorption spectra are taken for different incidence angles of the excitation beam. The angles are measured with respect to the normal of the substrate ( $r = 0^\circ$ ). At normal incidence the absorption spectrum is really flat. However by increasing the incidence angle until  $r = 75^\circ$  (grazing incidence), the growth of five peaks can be observed at binding energies of 284.1, 285.6, 287.2, 288.0 and 289.0eV. In a previous work, Taborski *et al.* have identified the NEXAFS peaks of a PTCDI multilayer film [62]. The peak 1 (284.1eV) is attributed to transitions from the carbon 1s level of the perylene core to the LUMO ( $L_0$ ). The most intense peak 2 is measured at 285.6 eV binding energy, Figure 3.10. It is

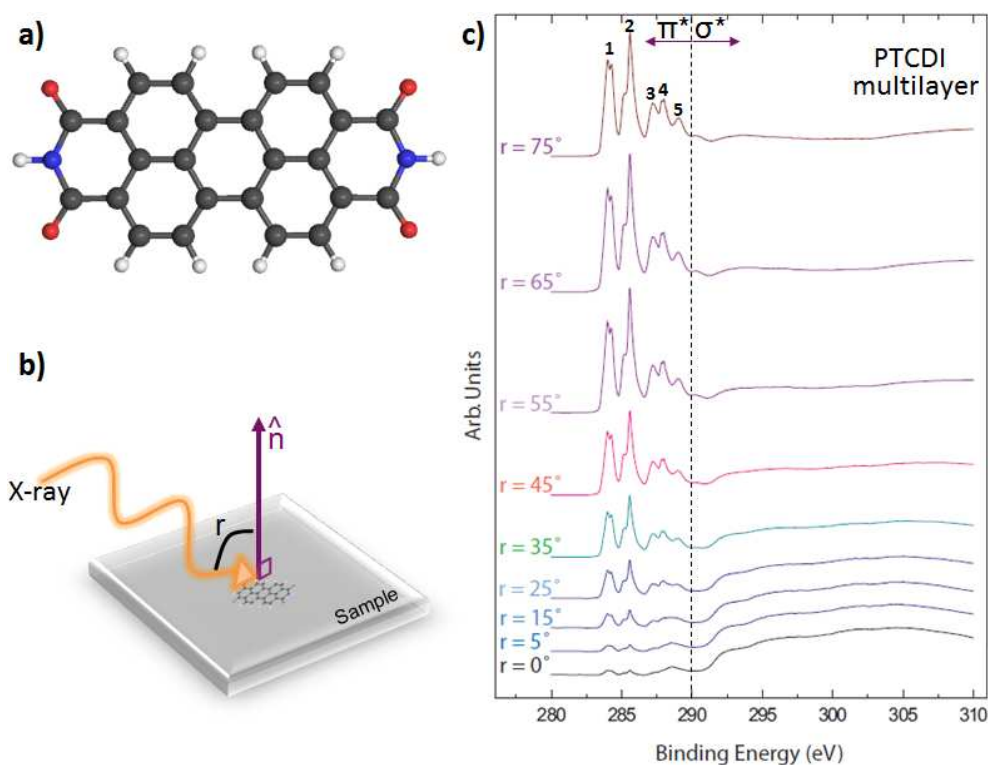


Figure 3.10: Angular dependence of the NEXAFS measurements of a PTCDI multilayer film grown on Au(111) taken at the C K-edge: a) PTCDI molecule. Blue, red, gray and white balls correspond to nitrogen, oxygen, carbon and hydrogen atoms, respectively. b) Reference used to measure the incident angle  $r$  of the excitation beam. c) The NEXAFS spectra obtained for different incident angles  $r$  of the excitation beam.

attributed to transitions from the carbon  $1s$  level of the perylene core to higher LUMO,  $L_1$ ,  $L_2$ ,  $L_3$ . The triple peak feature (3,4,5) measured at 287.2, 288.0, 289.0 eV binding energies can be attributed to transitions involving the PTCDI imide group because it strongly differs from those observed for perylene and PTCDA molecules [45, 49, 62]. Peaks 3 and 4 are assigned to transitions from the imide carbon atom into  $L_0$  and  $L_1 + L_2 + L_3$ . The peak 5 is attributed to transitions into  $L_5$  and  $L_7$  final states [62].

Furthermore, the sharp peaks below 290eV correspond to  $C_{1s} \rightarrow \pi^*$  electronic transitions, while the broad components above 290eV correspond to  $C_{1s} \rightarrow \sigma^*$  electronic transitions [45]. The  $C_{1s} \rightarrow \pi^*$  transitions are maximized at grazing incidence ( $r = 75^\circ$ ), whereas the  $C_{1s} \rightarrow \sigma^*$  transitions are maximized at normal incidence ( $r = 0^\circ$ ), Figure 3.10. The  $\pi^*$  orbitals of the PTCDI molecules are essentially oriented out of the molecular plane. Therefore the drastic change of the shape of the absorption spectrum with the angle of the excitation beam shows that PTCDI molecules are always lying flat on Au(111) surface, even at a multilayer coverage range. This information is crucial to design devices based on the PTCDI molecule. In addition to that, the assessment of the relative positions of the valence band and conduction band of the PTCDI/Au(111) interface is essential in order to determine the electronic properties of the sample, as shown in the following paragraph (§3.5).

### 3.5 Evolution of the PTCDI NEXAFS and Valence Band spectra with the molecular film thickness

Figure 3.11 shows the valence band (VB) and NEXAFS spectra for PTCDI multilayer, monolayer and submonolayer films grown on Au(111). The VB spectrum of the bare

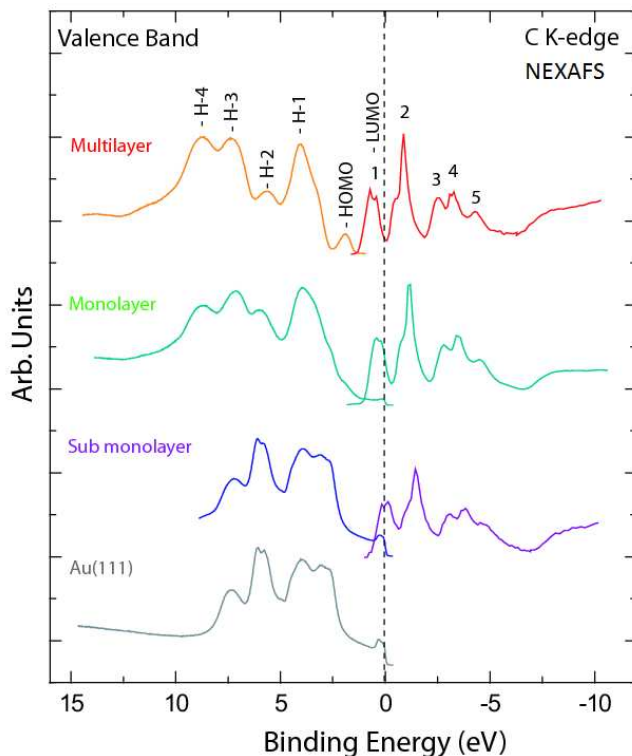


Figure 3.11: Valence band and C *K*-edge NEXAFS spectra for PTCDI sub-monolayer, monolayer and multilayer films grown on Au(111). The gray spectrum corresponds to the Valence Band (VB) of a bare Au(111) surface. The binding energy of the perylene  $C_{1s}$  core level is used as a reference to place on a common energy scale the VB and NEXAFS spectra of the PTCDI films.

Au(111) surface is shown as a reference. The NEXAFS and VB spectra were placed on a common scale using the binding energy of the perylene  $C_{1s}$  core level as a reference [45, 107]. The vertical dashed black line highlights the position of the Fermi level ( $E_F$ ). The photon energy was chosen to probe the C *K*-edge and the PTCDI  $\pi^*$  transitions. The PTCDI thin film occupied states and unoccupied states are revealed by the valence band and NEXAFS spectra, respectively. Additionally, Figure 3.11 shows that the bare Au(111) surface contributes significantly to the valence band of the sub-monolayer and monolayer PTCDI films. In comparison distinct frontiers of the molecular orbitals are resolved for the VB spectrum of the PTCDI multilayer film. The positions of the highest occupied molecular orbitals (HOMOs), HOMO-1, HOMO-2, and HOMO-3 deduced from the VB spectra of PTCDI films are listed in Table 3.4. The strongest feature (HOMO-1) in the PTCDI VB spectra was observed at -3.91 and -4.00 eV for monolayer and

multilayer coverage respectively, Figure 3.11. The strongest  $\pi^*$  feature in the PTCDI NEXAFS spectra was observed at 2.53, 2.79 and 3.04 eV for sub-monolayer, monolayer and multilayer coverage respectively, Figure 3.11. The energy positions of the NEXAFS spectra peaks are listed in Table 3.4 for the three PTCDI films. Figure 3.11 reveals that the PTCDI LUMO is located at the Fermi level for the PTCDI submonolayer film grown on Au(111). In comparison the PTCDI LUMO of the PTCDI monolayer and multilayer films lies below  $E_F$ . This shift below the Fermi level obtained at high molecular coverage is usually attributed to Coulomb interaction between the C core-holes and the photoexcited electrons [108], i.e. to a charging effect.

To summarize, a strong modification of the energy level alignment of the HOMOs and LUMOs states is observed for PTCDI films grown on Au(111) surface, depending on the molecular film thickness. This information is crucial to develop nano-devices with desired properties based on PTCDI molecule. Additionally it is also of prime importance to determine how the charge transfer process arising at the metal-organic interface can be affected by the molecular film thickness, as shown in the next paragraph.

Thickness	Valence band states (eV)					NEXAFS states (eV)				
	HOMO-4	HOMO-3	HOMO-2	HOMO-1	HOMO	$C_{\text{perylene}} 1s \rightarrow \text{LUMOs}$ 1 (LUMO)	2	$C_{\text{imide}} 1s \rightarrow \text{LUMOs}$ 3	4	5
Multilayer	-8.60	-7.32	-5.63	-4.00	-1.88	-0.62	0.88	2.53	3.18	4.28
Monolayer	-8.70	-7.10	-5.60	-3.91	$\emptyset$	-0.31	1.14	2.79	3.49	4.5
Submonolayer	$\emptyset$	$\emptyset$	$\emptyset$	$\emptyset$	$\emptyset$	0.00	1.44	3.04	3.75	4.64

Table 3.4: Highest Occupied Molecular Orbitals (HOMOs) and Lowest Unoccupied Molecular Orbitals (LUMOs) of PTCDI sub-monolayer, monolayer and multilayer films grown on Au(111) surface.

### 3.6 Evolution of the PTCDI Resonant Photoemission Spectrum with the molecular film thickness

Figure 3.12 shows the experimental results obtained with Synchrotron-based resonant photoemission spectroscopy (RPES) for PTCDI multilayer, monolayer and submonolayer films grown on Au(111). The photon energy range was chosen to cross the  $C_{1s} \rightarrow \pi^*$  absorption threshold, i.e. from 280 eV to 295 eV. Figure 3.12a reveals that the resonance photon energies of PTCDI multilayer film are correlated with the five absorption peaks (1-5) of the NEXAFS spectrum. The HOMO peak preferentially resonates at photon energies corresponding to NEXAFS peak 1 followed by peak 2. In comparison HOMO-1 peak preferentially resonates at photon energies corresponding to NEXAFS peak 2 followed by peak 1. HOMO-2 peak resonances associated with NEXAFS peak 1 and 2 have similar intensity. HOMO, HOMO-1 and HOMO-2 resonances are therefore essentially connected with  $C_{\text{perylene}} 1s \rightarrow \text{LUMOs}$  transitions, i.e. the intensity of H-0, H-1 and H-2 resonances related to  $C_{\text{imide}} 1s \rightarrow \text{LUMOs}$  transitions are negligible in that case. However, resonances associated with  $C_{\text{imide}} 1s \rightarrow \text{LUMOs}$  transitions are noticeable for H-3 and H-4 peaks. This indicates that the H-0, H-1 and H-2 wave functions are preferentially located on the molecule perylene skeleton and weakly extended to the

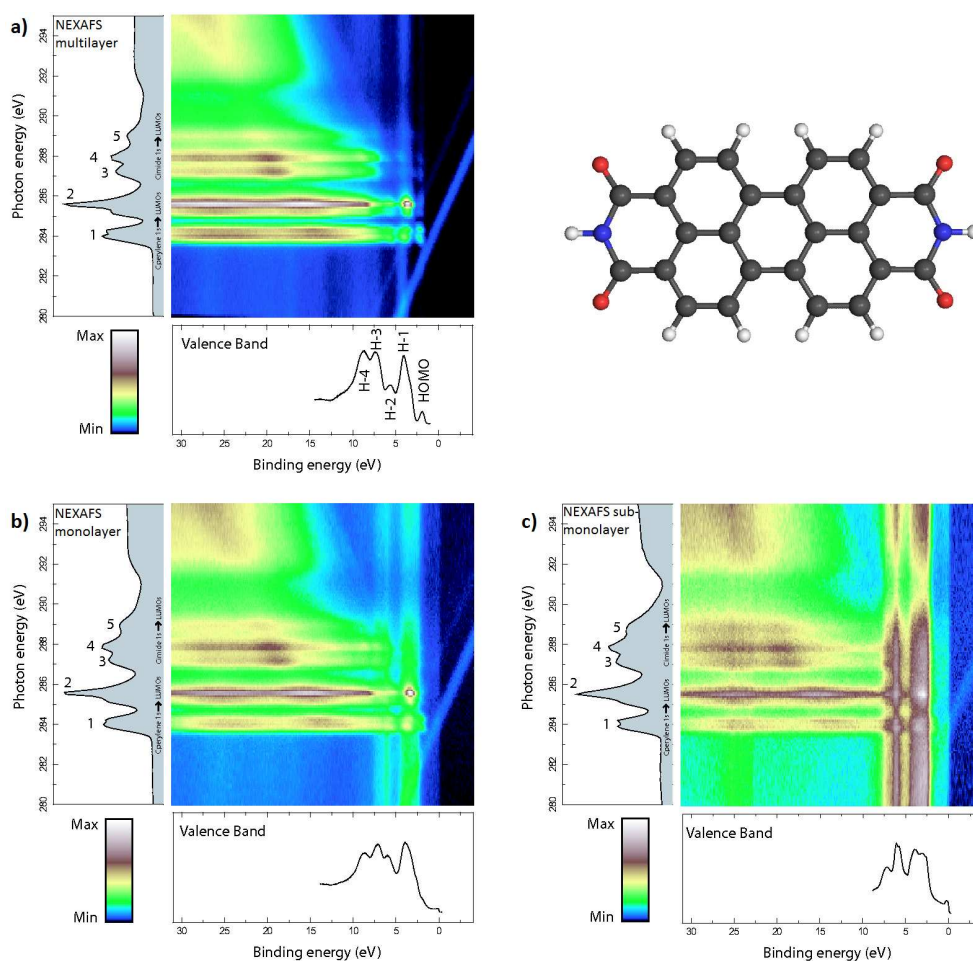


Figure 3.12: RPES map of PTCDI films grown on Au(111) surface for three different coverages: (a) multilayer, (b) monolayer, and (c) sub-monolayer. The bottom curves are corresponding to the VB spectra measured with photon energy of 60 eV, whereas the curves on the left side are their respective NEXAFS spectra.

molecular end-groups where N atoms are localized. The two linear dispersion channels, that can be observed to the right of Figure 3.12a, correspond to Raman auto-ionization channels.

The features of the PTCDI monolayer RPES spectrum (Figure 3.12b) are similar to those of the multilayer spectrum (Figure 3.12a). However the features of the PTCDI sub-monolayer RPES spectrum (Figure 3.12c) appear drastically different. The resonances involving the L0, L1, L2, L3 states are strongly attenuated, i.e. electrons are delocalized fast enough to prevent resonant auto-ionization. This suggests that the charge transfer process involving the L0, L1, L2, L3 states take place in a time-range smaller than the  $C_{1s}$  core-hole lifetime (6 fs, see [49]). It therefore appears that fast electron delocalization combined with electronic transfer occur at the PTCDI/Au(111) single layer interface. These results show that the charge transfer process occurring at the metal-organic interface strongly depends on the molecular film thickness. This information is crucial to design new electronic nano-devices.

## Chapter Conclusions

In this chapter, scanning tunneling microscopy and synchrotron photoemission spectroscopy were used to investigate the morphology and the electronic properties of PTCDI thin films grown on Au(111) surface. STM measurements show that PTCDI molecules are forming a canted structure on the Au(111) surface kept at room temperature. This canted network is transformed into a double-chain and triple-chain structures after post-annealing the sample at 50° during 1 hour. STM image contrast modifications reveal the appearance of a strong electronic coupling between the PTCDI molecules packed side-by-side (§3.2.1). In addition to that after post-annealing the sample at 200° during 1 hour, a new side-by-side structure was formed without any PTCDI "canted" chain (§3.2.2). XPS measurements show a strong modification of the C<sub>1s</sub>, O<sub>1s</sub> and N<sub>1s</sub> core-level spectra with the PTCDI film thickness (§3.3). By comparing the core-level spectra obtained here for PTCDI with those of another perylene derivative called PTCDA [49], it appears that local modifications of molecular skeleton can drastically affect the electronic properties of a metal-organic interface (§3.3.4). Angular NEXAFS spectroscopy shows that PTCDI molecules are adsorbed in a flat-lying configuration on Au(111) surface, and PTCDI multilayer film consists in a succession of flat-lying molecule layers (§3.4). Core-hole clock spectroscopy (RPES) shows that the charge transfer arising at the PTCDI/Au(111) interface depends on the molecular film thickness (§3.6). In fact a fast charge transfer (below 6fs) involving the L0, L1, L2, L3 states take place in the PTCDI sub-monolayer film. This fast charge transfer is not observed for monolayer and multilayer coverages. Such information is crucial to design new systems and optimize organic film-metal electrode interface in order to develop the next generation of organic and hybrid materials for spintronics and photovoltaic applications. In the following Chapter 4, I will describe how the PTCDI molecular self-assembly can be modified and controlled through the subsequent adsorption of Sodium Chloride compounds followed by a post-annealing of the sample.

# Chapter 4

## Self-assembled nanoarchitectures based on NaCl and PTCDI molecules

Perfectly organized NaCl thin films are attracting considerable interest, because they promise to have many applications in nanotechnology [109–114]. In addition to that, the control of the nano-fabrication of organized semiconducting thin films is crucial in order to develop the new generation of organic devices. It is the reason why in this chapter I described first the NaCl multilayer island grown on the Au(111) surface. Thereafter I described the temperature dependence of the supramolecular self-assembly of NaCl with PTCDI molecules, characterized by using scanning tunneling microscopy. During this work it was observed that four different bi-molecular nano-architectures can be obtained by mixing NaCl with PTCDI on the Au(111) surface, depending on substrate temperature.

### 4.1 Sodium Chloride: NaCl

#### 4.1.1 NaCl bulk structure

First, it is crucial to notice that bulk sodium chloride is ionic crystal which possesses a Face Centered Cubic (fcc) structure, Figure 4.1. This NaCl bulk fcc structure consists of a mixture of sodium cation ( $\text{Na}^+$ ) and chloride anion ( $\text{Cl}^-$ ) in equal proportion. Each positively charged  $\text{Na}^+$  ion is surrounded by six negatively charged  $\text{Cl}^-$  ions. In that way the closest neighbors of a negatively charged  $\text{Cl}^-$  ion is always a positively charged  $\text{Na}^+$  ion. Reciprocally the closest neighbors of a positively charged  $\text{Na}^+$  ion is always a negatively charged  $\text{Cl}^-$  ion. This leads to the minimization of the NaCl bulk crystal structure energy. The NaCl(100), (010), and (001) facets are electronically neutral because they are constituted of a racemic mixture of sodium and chloride ions, Figure 4.1. However the NaCl(111) facet is polar, because it is constituted of only one type of ions. In addition to that, Roessler and Walker have shown in 1968, that the bulk single crystal NaCl is an insulating material which possesses an 8.97eV band-gap [115].

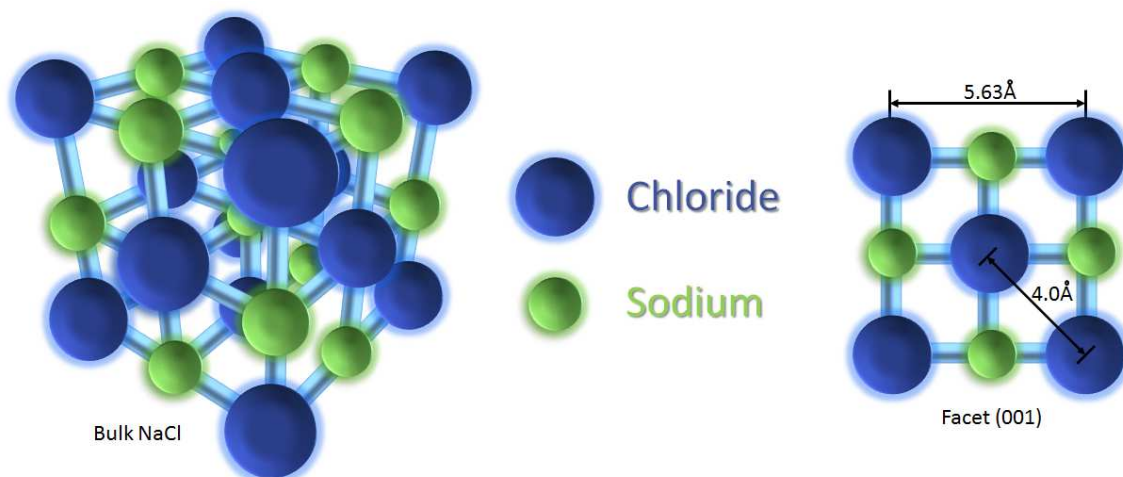


Figure 4.1: The Face Centered Cubic (fcc) structure unit-cell of the NaCl bulk.

However, some electronic couplings can appear between the electronic states of a NaCl thin film and those of a supporting metallic surface. These electronic couplings allow the tunneling effect to occur through the tip-vacuum-NaCl-metal junction, and then it becomes possible to record STM images of a NaCl thin film [101], as it is shown in the next paragraph for NaCl grown on a Au(111) surface.

#### 4.1.2 NaCl thin film grown on Au(111) surface

Sodium-chloride created square islands on the bare Au(111) surface, as it is shown in Figures 4.2a,b. The NaCl islands grow preferentially at the step edges. Moreover the square NaCl islands can cross the step edge of the Au(111) surface, without modifications of the NaCl packing and island's shape 4.2a. The Au(111)- $(22 \times \sqrt{3})$  herringbone reconstruction can be clearly observed underneath the NaCl islands, Figures 4.2a-c. This indicates that the interaction between the NaCl film and the Au(111) surface is rather small, because there is no modification of the herringbone reconstruction under NaCl deposition. Figures 4.2c,d show atomic resolution of a NaCl island. In these Figures, the bright protrusions can be attributed to the  $\text{Cl}^-$  anions [116–118]. The lattice distance is measured as  $5.6\text{\AA}$ , while the distance between two nearest neighbors Chloride atoms in the NaCl islands is measured as  $3.9\text{\AA}$ , Figures 4.1 & 4.2d. These values are really close to those reported in literature for a bare NaCl(001) surface [118], as well as for NaCl growth on bare Au(111) surface [119]. To develop the new generation of organic compounds, it may be also interesting to combine insulator with semiconducting material like PTCDI. It is the reason why in the following sections I will describe some results on the mixing of NaCl and PTCDI molecules on the Au(111) surface. Moreover I will show how the resulting bi-molecular self-assembly can be controlled by a precise adjustment of the sample's temperature.

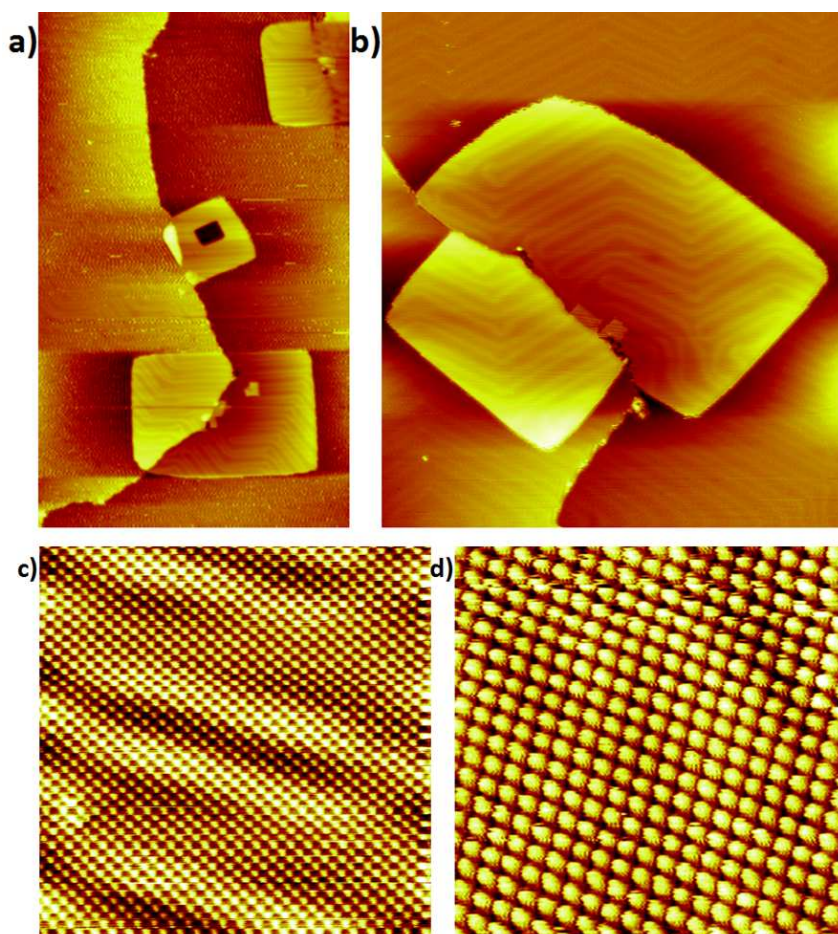


Figure 4.2: NaCl island's growth on Au(111) surface kept at room temperature (a) Wide-range STM image  $143 \times 239 \text{ nm}^2$ ,  $V_s = +1.80 \text{ V}$ ,  $I_t = 300 \text{ pA}$ ; (b)  $108 \times 120 \text{ nm}^2$ ,  $V_s = +1.80 \text{ V}$ ,  $I_t = 300 \text{ pA}$ ; (c) Atomic resolution of a NaCl island  $12 \times 12 \text{ nm}^2$ ,  $V_s = +1.83 \text{ V}$ ,  $I_t = 101 \text{ pA}$ ; (d)  $7.2 \times 7.2 \text{ nm}^2$ ,  $V_s = +0.51 \text{ V}$ ,  $I_t = 300 \text{ pA}$ .

## 4.2 Tailoring the NaCl-PTCDI bi-molecular nanoarchitectures by controlling the substrate temperature

### 4.2.1 NaCl-PTCDI bi-molecular nanoarchitectures formed at room temperature

First the NaCl and PTCDI molecules were evaporated at  $390^\circ \text{ C}$  and  $245^\circ \text{ C}$  respectively, on a Au(111) surface kept at room temperature. In that case the PTCDI molecules are located around small NaCl islands composed by a few number of NaCl monomers forming different kinds of PTCDI-NaCl structures with different sizes and shapes. In that way, a lot of PTCDI-NaCl structures can be formed with the same probability. Finally this does not lead to the appearance of a well-organized molecular film. The STM images

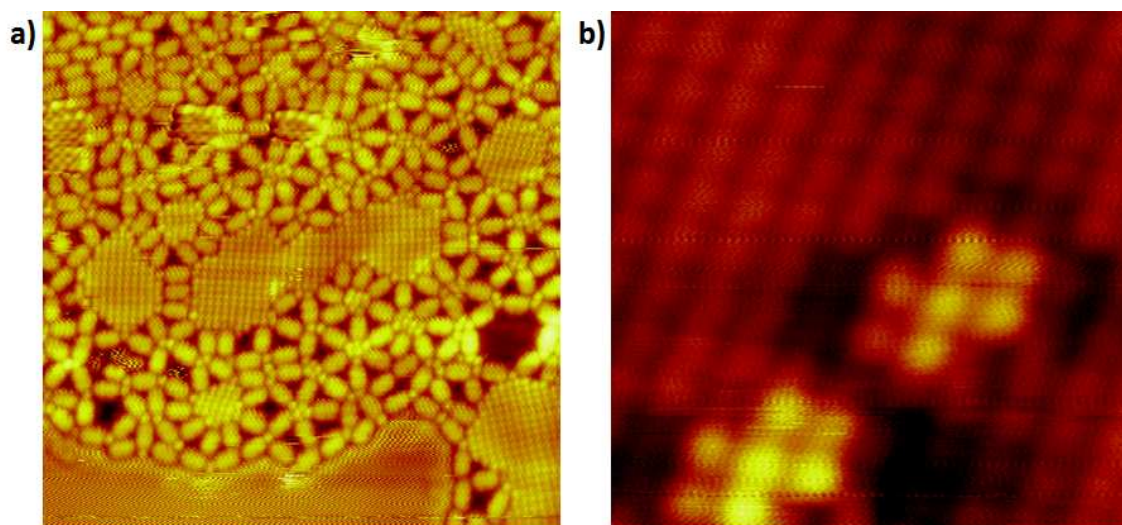


Figure 4.3: STM images of the NaCl-PTCDI structures formed on Au(111) surface kept at room temperature, (a)  $23.9 \times 23.9 \text{ nm}^2$ ,  $V_s = +1.23 \text{ V}$ ,  $I_t = 210 \text{ pA}$ ; (b)  $3.4 \times 3.3 \text{ nm}^2$ ,  $V_s = +1.83 \text{ V}$ ,  $I_t = 110 \text{ pA}$ .

show that deposition of NaCl on PTCDI film, breaks the typical canted structure formed at room temperature by PTCDI molecules on the Au(111) surface. Only small domains of pure NaCl can be observed in our STM images (i.e. up to  $10 \times 10 \text{ nm}^2$ ). Table 4.1 and Table 4.2 give an overview of the most common PTCDI-NaCl structures formed on the Au(111) surface at room temperature.

Each line of Table 4.1 corresponds to a precise number of NaCl monomers involved in the formation of the PTCDI-NaCl structures (from 1 to 5 NaCl monomers). Each column of Table 4.1 corresponds to a precise number of PTCDI molecules involved in the PTCDI-NaCl structures, i.e. from 3 to 8 PTCDI molecules. When the NaCl core is constituted of only one NaCl monomer, then three PTCDI-NaCl structures can be built by attaching 3, 4 or 5 PTCDI molecules to the single NaCl monomer. In that case the PTCDI molecules seem to be linked to the NaCl monomer through their amino groups. In the same way when the NaCl core is constituted of two NaCl monomers, then three PTCDI-NaCl structures can be built. These three structures are constituted of 4, 5 or 6 PTCDI molecules linked to the NaCl core. In addition to that there is the formation of  $\text{O} \cdots \text{H}-\text{C}$  and  $\text{O} \cdots \text{H}-\text{N}$  hydrogen bonds between neighboring PTCDI molecules which are placed perpendicular to each other. In the case where three NaCl monomers constitute the NaCl island core, then three different PTCDI-NaCl structures can be built. As it is shown in the third line of Table 4.1, these three PTCDI-NaCl structures are constituted of 4, 5 or 6 PTCDI molecules which surround the NaCl island core. In the same way, when the NaCl island core is constituted of 4 or 5 NaCl monomers then the NaCl-PTCDI structures can be constituted of 5 up to 8 PTCDI molecules surrounding the NaCl core. In Table 4.1, it is observed that larger is the size of the NaCl island core, higher is the number of PTCDI molecules which can be involved in the formation of the PTCDI-NaCl structures. Likewise, Table 4.2 depicts the most common PTCDI-NaCl structures formed on the Au(111) surface when the NaCl island cores are composed of 6

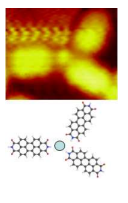
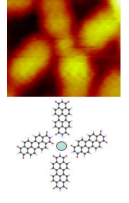
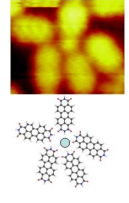
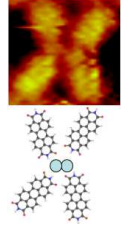
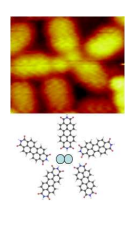
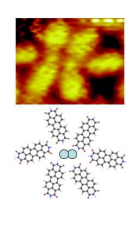
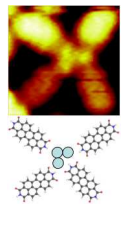
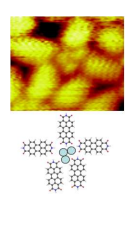
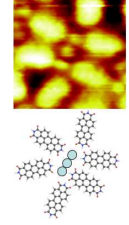
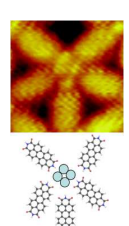
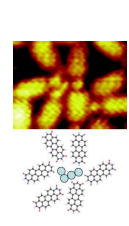
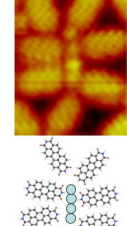
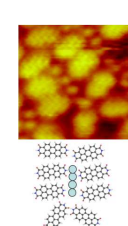
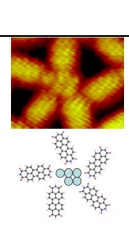
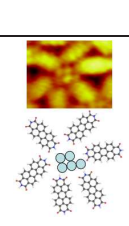
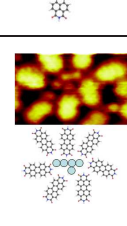
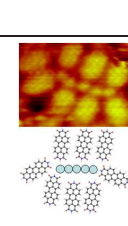
Numbers	3 PTCDI	4 PTCDI	5 PTCDI	6 PTCDI	7 PTCDI	8 PTCDI
1 NaCl				∅	∅	∅
2 NaCl	∅				∅	∅
3 NaCl	∅				∅	∅
4 NaCl	∅	∅				
5 NaCl	∅	∅				

Table 4.1: Overview of the most common PTCDI-NaCl structures formed on the Au(111) surface kept at room temperature. Each column corresponds to a defined number of PTCDI molecules (from 3 to 8), involved in the formation of the PTCDI-NaCl structures. In the same way, each line of the table corresponds to a precise number of NaCl monomers (from 1 to 5), involved in the formation of the PTCDI-NaCl structures. Blue, red, gray and white balls correspond to nitrogen, oxygen, carbon and hydrogen atoms respectively, while NaCl monomers are represented with cyan balls.

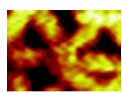
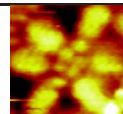
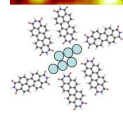
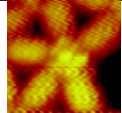
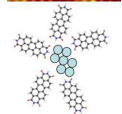
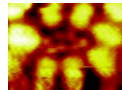
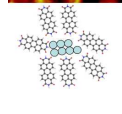
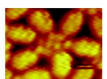
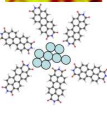
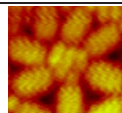
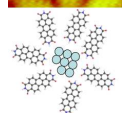
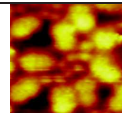
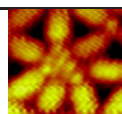
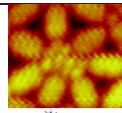
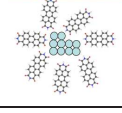
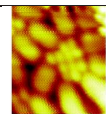
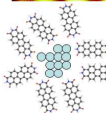
Numbers	5 PTCDI	6 PTCDI	7 PTCDI	8 PTCDI
6 NaCl	 	 	∅	∅
7 NaCl	 	∅	 	∅
8 NaCl	∅	 	 	 
9 NaCl	∅	∅	 	∅
10 NaCl	∅	∅	 	∅
11 NaCl	∅	∅	∅	 

Table 4.2: Overview of the most common PTCDI-NaCl structures formed on the Au(111) surface kept at room temperature. Each column corresponds to a defined number of PTCDI molecules (from 5 to 8), involved in the formation of the PTCDI-NaCl structures. In the same way, each line of the table corresponds to a precise number of NaCl monomers (from 6 to 11), involved in the formation of the PTCDI-NaCl structures. Blue, red, gray and white balls correspond to nitrogen, oxygen, carbon and hydrogen atoms respectively, while NaCl monomers are represented with cyan balls.

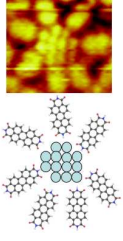
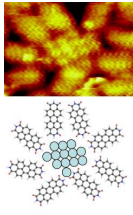
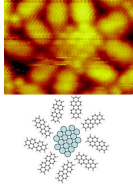
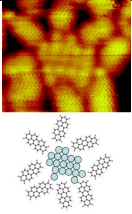
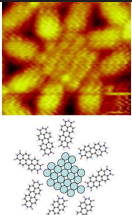
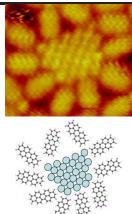
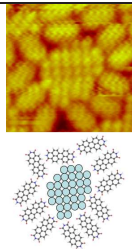
Numbers	7 PTCDI	8 PTCDI	9 PTCDI	10 PTCDI	11 PTCDI
13 NaCl		∅		∅	∅
17 NaCl	∅	∅		∅	∅
19 NaCl	∅		∅	∅	∅
21 NaCl	∅		∅	∅	∅
28 NaCl	∅	∅	∅		∅
31 NaCl	∅	∅	∅	∅	

Table 4.3: Overview of the less common PTCDI-NaCl structures formed on the Au(111) surface kept at room temperature. Each column corresponds to a defined number of PTCDI molecules (from 7 to 11), involved in the formation of the PTCDI-NaCl structures. In the same way, each line of the table corresponds to a precise number of NaCl monomers (from 13 to 31), involved in the formation of the PTCDI-NaCl structures. Blue, red, gray and white balls correspond to nitrogen, oxygen, carbon and hydrogen atoms respectively, while NaCl monomers are represented with cyan balls.

up to 11 NaCl monomers. In the same way, Table 4.3 shows some less common PTCDI-NaCl structures formed on the Au(111) surface kept at room temperature. These less common structures are composed of 13 up to 31 NaCl monomers.

Figure 4.3b, shows that the NaCl islands can also grow over single PTCDI molecule. In this case, few PTCDI molecules remain trapped underneath the NaCl film. When this arises a distortion of the NaCl film appears, consisting of seven bright spots in the atomically resolved STM image. The length of this bright distortion is around 1.24nm, while its width is measured as 0.71nm. These distances are equal to the typical length and width of a PTCDI molecule in the Figure 4.3a. The seven brighter features can be presumably attributed to chloride atoms which are located in the center of the seven aromatic rings of a single PTCDI molecule. The presence of the underlying PTCDI molecules does not change the lattice parameter of the NaCl islands, i.e. around 5.6Å.

Successive scans of the same area with the STM tip lead to slight modifications of the shape of the PTCDI-NaCl structures, Figures 4.4a-f. For easier reading, the modifications of the PTCDI-NaCl structures are shown in the corresponding molecular models, where the purple and white balls indicate the NaCl monomers which are respectively added or removed during the scans. Initially the biggest NaCl-PTCDI structure depicted in Figure 4.4a is composed of 77 NaCl monomers and 14 PTCDI molecules. However after several scans, a NaCl monomer is added at the bottom left border of the biggest NaCl-PTCDI structure, Figure 4.4b. At the same time two NaCl monomers are removed at the left and right border of the biggest NaCl-PTCDI structure, Figure 4.4b. Further scans of the same area lead to the formation of a new PTCDI-NaCl structure composed of 5 NaCl monomers and 5 PTCDI molecules at the top left corner of Figure 4.4c. Simultaneously, two NaCl monomers are removed at the left border of the biggest PTCDI-NaCl structure, Figure 4.4c. Thereafter, a new PTCDI-NaCl structure is formed at the top of Figure 4.4d, consisting of 1 NaCl monomer surrounded by 3 PTCDI molecules. Additionally, a NaCl monomer is removed at the right border of the biggest PTCDI-NaCl structure, Figure 4.4d. Figure 4.4e shows that a PTCDI molecule is removed at the left border of the biggest PTCDI-NaCl structure after successive scans of the same area with the STM tip. At the same time, a NaCl monomer is removed at the left border of the biggest PTCDI-NaCl structure, Figure 4.4e. In addition to that, two NaCl monomers are added at the top right border of the biggest PTCDI-NaCl structure. Finally, Figure 4.4f shows that a NaCl monomer is transferred from the left border to the right border of the biggest PTCDI-NaCl structure. The final PTCDI-NaCl structure is composed of 74 NaCl monomers and 13 PTCDI molecules. The interaction between the molecular film and the STM tip is responsible of the shape modification observed after several scans of the PTCDI-NaCl structures of Figure 4.4. This kind of modification is mostly observed at the border of large PTCDI-NaCl structures, possessing more than 11 NaCl monomers. The shape modifications obtained here after several scans of the same area, was not observed for the PTCDI-NaCl structures formed at higher temperature (§4.2.2, §4.2.3, and §4.2.4).

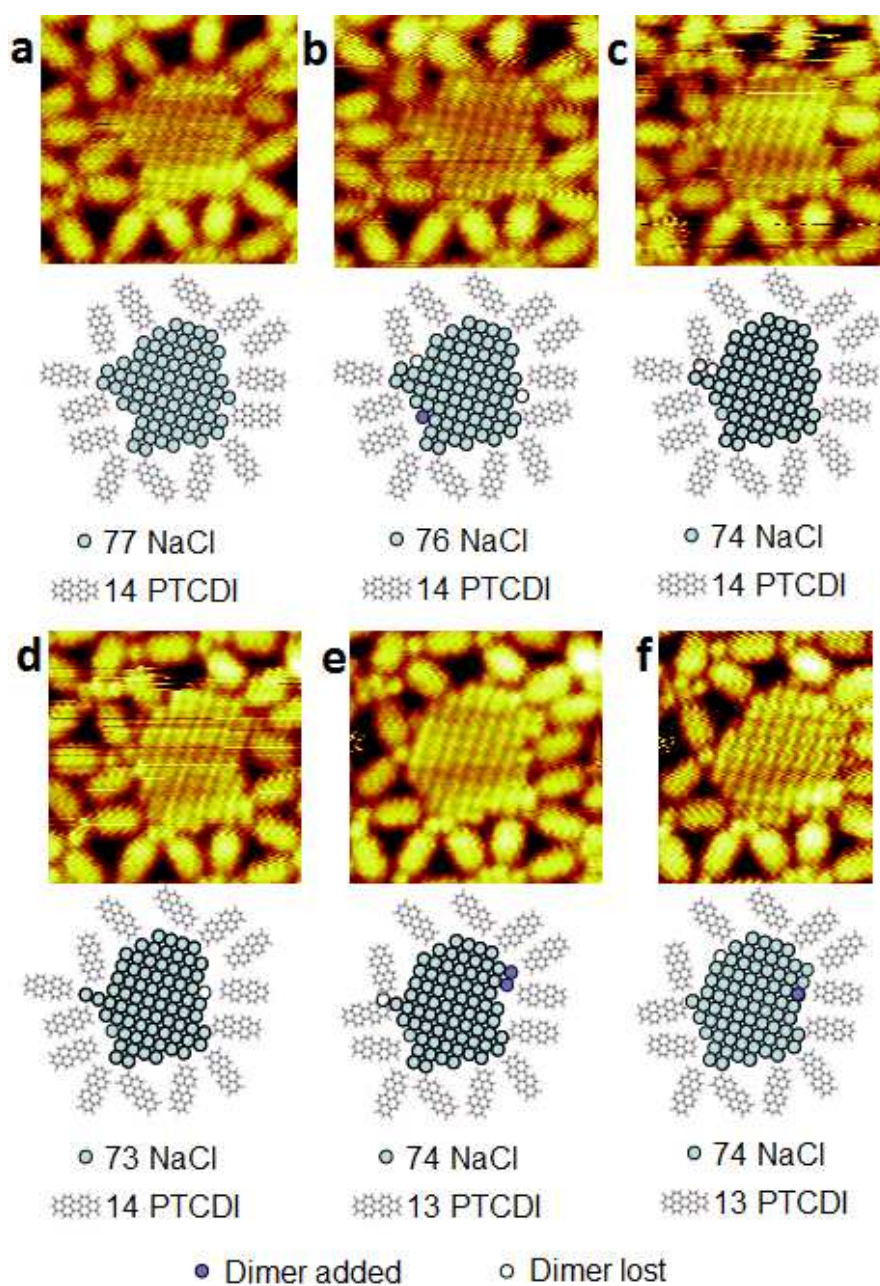


Figure 4.4: Evolution of the shape of a PTCDI-NaCl structure obtained at room temperature on Au(111), after successive scans with the STM tip on the same area: (a)  $6.2 \times 6.2 \text{ nm}^2$ ;  $V_s = +1.43\text{V}$ ,  $I_t = 310\text{pA}$ ; (b)  $6.2 \times 6.2 \text{ nm}^2$ ;  $V_s = +1.63\text{V}$ ,  $I_t = 310\text{pA}$ ; (c)  $6.2 \times 6.2 \text{ nm}^2$ ;  $V_s = +1.13\text{V}$ ,  $I_t = 210\text{pA}$ ; (d-e)  $6.2 \times 6.2 \text{ nm}^2$ ;  $V_s = +1.23\text{V}$ ,  $I_t = 210\text{pA}$ ; (f)  $4.9 \times 6.2 \text{ nm}^2$ ;  $V_s = +1.23\text{V}$ ,  $I_t = 610\text{pA}$ . Blue, red, gray and white balls correspond to nitrogen, oxygen, carbon and hydrogen atoms respectively, while NaCl monomers are represented with cyan balls. The purple and white balls in the molecular model correspond respectively to the NaCl monomers which are added or removed compared to the previous STM image.

To summarize, the deposition of PTCDI molecules on the Au(111) surface kept at room temperature subsequently followed by NaCl deposition leads to the formation of PTCDI-NaCl structures which consist of small NaCl islands surrounded by some PTCDI molecules. Surprisingly when NaCl is deposited before PTCDI, it is not possible to observe any domains of mixed PTCDI-NaCl structures. This suggests that PTCDI deposition cannot break the NaCl islands, while NaCl deposition can break the PTCDI canted structure formed at room temperature (see §3.2.1, Figure 3.3). The most common PTCDI-NaCl structures formed on the Au(111) surface are constituted of 1 up to 11 NaCl monomers, surrounded by 3 up to 8 PTCDI molecules (see Tables 4.1 and 4.2). The less common PTCDI-NaCl structures formed on the Au(111) surface are constituted of 13 up to 31 NaCl monomers, surrounded by 7 up to 11 PTCDI molecules (see Table 4.3). Sometimes larger NaCl domains are formed with a size up to  $10 \times 10 \text{ nm}^2$ , where few PTCDI molecules can be trapped underneath the NaCl film and then appear in the STM image as seven bright spots. Slight modifications of the shape of the PTCDI-NaCl structures can be observed after successive scans with the STM tip of the same area. Finally with these growth conditions, no extended organized bi-molecular architectures can be formed by mixing PTCDI with NaCl. But in order to create useful organic devices with specific properties, it is needed to control the molecular organization in a predictable way. It is the reason why, we have changed the growth conditions in order to control the molecular organization of the PTCDI-NaCl mixture. The results of these change are shown in the following sections, where the sample was subsequently annealing at temperatures of  $100^\circ\text{C}$ ,  $150^\circ\text{C}$ , and  $200^\circ\text{C}$ .

#### 4.2.2 NaCl-PTCDI bi-molecular nanoarchitectures formed after a post-annealing at $100^\circ\text{C}$

A porous PTCDI-NaCl nano-architecture was formed on the Au(111) surface after post-annealing the sample at a temperature around  $100^\circ\text{C}$  during twelve hours, Figure 4.5a. In that structure, four PTCDI molecules are placed around a NaCl monomer forming a cross-like pattern. In this cross-like pattern there are two opposite PTCDI molecules which are linked to the NaCl monomer through their amino groups, leading to a perfect linear arrangement of these two molecules, Figure 4.5b,c. However the two other PTCDI molecules are not bonded to the NaCl monomer, but they are linked to the two perfectly aligned PTCDI molecules through the establishment of a  $\text{N}-\text{H}\cdots\text{O}$  and a  $\text{C}-\text{H}\cdots\text{O}$  hydrogen bonds, leading to the perpendicular arrangement observed for neighboring molecules. This involves a slight shift between the two PTCDI molecules which are not bonded to the NaCl monomer, i.e. they are not perfectly aligned one compared to the other. The PTCDI-NaCl porous network unit-cell is rectangular with  $A \simeq 2.3 \text{ nm}$  and  $B \simeq 2.0 \text{ nm}$  the unit cell constants and an angle of  $\simeq 90^\circ$  between the axes, Figure 4.5c. In fact there is one NaCl monomer placed at the center of the unit-cell, which is surrounded by four PTCDI molecules leading to a cross-like pattern. In addition to that there is one NaCl monomer placed at each corner of the unit-cell. Therefore, the cross-like molecular pattern of this porous structure is constituted of four PTCDI molecules and two NaCl monomers in each unit-cell (i.e. with the molecular ratio 2:1). The

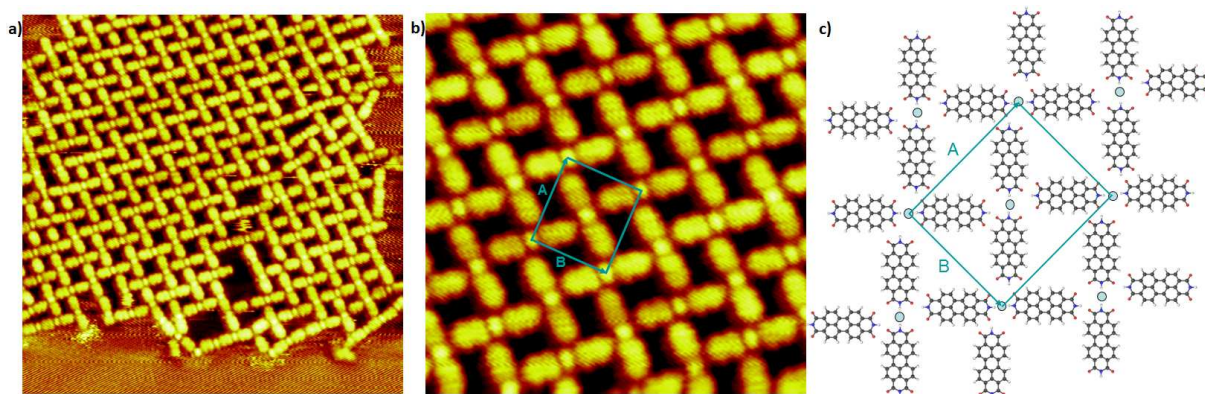


Figure 4.5: The NaCl-PTCDI porous structure formed on Au(111) after twelve hours annealing at  $100^{\circ}\text{C}$ : (a) Wide-range STM image  $28.7\times 28.7\text{nm}^2$ ,  $V_s = +1.98\text{V}$ ,  $I_t = 206\text{pA}$ ; (b) Short-range STM image  $10.8\times 10.8\text{nm}^2$ ,  $V_s = +1.98\text{V}$ ,  $I_t = 206\text{pA}$ ; (c) Molecular model of the PTCDI-NaCl porous network. Blue, red, gray and white balls correspond to nitrogen, oxygen, carbon and hydrogen atoms respectively, whereas NaCl monomers are represented with cyan balls.

pores of this PTCDI-NaCl structure are rectangular with a typical size of  $1.2\times 0.74\text{nm}^2$ . Moreover some molecular defects in the PTCDI-NaCl porous network can be clearly observed at the bottom right corner of Figure 4.5a, where some PTCDI molecules are missing. These molecular defects lead to an increase of the pores size. When only one PTCDI molecule is missing the pore size becomes  $2.0\times 1.55\text{nm}^2$ . However, when a cross-like pattern is missing (i.e. a NaCl monomer which is surrounded by four PTCDI molecules), then the pore size becomes  $2.6\times 2.3\text{nm}^2$ , Figure 4.5a. Figure 4.5b, shows that two orientations are observed for the perfectly aligned axis of the cross-like patterns (i.e. for the two PTCDI molecules linked to the NaCl monomer, forming a PTCDI-NaCl-PTCDI linear structure). These two possible orientations have the same occurrence probability and are turned by an angle of  $90^{\circ}$  one compared to the other. Each PTCDI molecule participates only one time to the formation of a PTCDI-NaCl-PTCDI linear structure. In that way, the four nearest neighbors of a PTCDI-NaCl-PTCDI linear structure correspond to four PTCDI-NaCl-PTCDI linear structures which are linked to the first one by the establishment of  $\text{N}-\text{H}\cdots\text{O}$  and  $\text{C}-\text{H}\cdots\text{O}$  hydrogen bonds, and are turned by the same angle of  $90^{\circ}$  with respect to the first one, Figure 4.5c. Therefore, a porous PTCDI-NaCl bi-molecular structure can be formed on the Au(111) surface after annealing at  $100^{\circ}\text{C}$  during twelve hours. The sample's post-annealing favor the formation of a cross-like pattern composed of 1 NaCl monomer center surrounded by 4 PTCDI molecules. This cross-like pattern, is one of the most common PTCDI-NaCl complexes observed at room temperature before annealing (see the first line of Table 4.1). Finally this porous PTCDI-NaCl structure can be transformed into a closely-packed structure by annealing the sample at higher temperature; as it is show in the next paragraph.

### 4.2.3 NaCl-PTCDI bi-molecular nanoarchitectures formed after a post-annealing at 150° C

In the same way, the sample was post-annealed at a temperature around 150° C during twelve hours, leading to the formation of a PTCDI-NaCl "Wave Networks", Figure 4.6a. This "Wave Network" is more compact than the PTCDI-NaCl porous network obtained

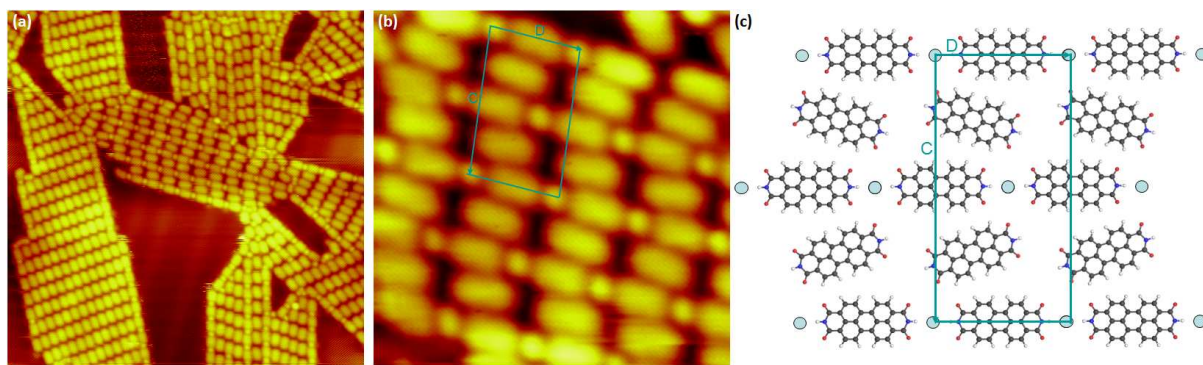


Figure 4.6: The NaCl-PTCDI "Wave Network" structure formed on Au(111) after twelve hours annealing at 150° C: (a) Wide-range STM image,  $31.8 \times 31.8 \text{ nm}^2$ ,  $V_s = +1.68 \text{ V}$ ,  $I_t = 210 \text{ pA}$ ; (b) Short-range STM image of the "Wave Network",  $6 \times 6 \text{ nm}^2$ ,  $V_s = +1.68 \text{ V}$ ,  $I_t = 210 \text{ pA}$ ; (c) Molecular model of the "Wave Network". Blue, red, gray and white balls correspond to nitrogen, oxygen, carbon and hydrogen atoms respectively, whereas NaCl monomers are represented with cyan balls.

after annealing at 100° C, (see §4.2.2). The "Wave network" is composed of two types of molecular chains. The first type of chains consists of PTCDI molecule alternated with NaCl monomer. Each PTCDI molecule seems to be linked to two NaCl monomers through its amino end-groups in a "pearl necklace" pattern, Figure 4.6b. All the PTCDI molecules of this type of molecular chain are aligned with the chain direction. The second type of chain is only constituted of PTCDI molecules which are turned by an angle of  $\pm 5^\circ$  compared to the chain direction. All the PTCDI molecules of a same chain have the same orientation. Two neighboring PTCDI molecules of the single-component chain are separated by a distance of 1.5 nm. For comparison, the distance separating two PTCDI molecules of the canted structure within a same chain is around 1.2 nm (§3.2.1). Each PTCDI molecule of the single-component chains is bonded to two NaCl monomers of neighboring "pearl necklace" chains through their oxygen atoms. As a consequence the PTCDI-NaCl "Wave network" consists of alternating "pearl necklace" chains with the single-component PTCDI chains. The PTCDI molecules of the two single-component chains which surround a PTCDI-NaCl "pearl necklace" chain are turned in opposite directions, i.e.  $+5^\circ$  and  $-5^\circ$  respectively. The unit-cell of the "Wave Network" is almost rectangular with  $C \simeq 2.6 \text{ nm}$  and  $B \simeq 1.5 \text{ nm}$  the unit-cell constants and an angle of  $\simeq 85^\circ$  between the axes, Figure 4.6c. The molecular pattern of the "Wave Network" is composed of 4 PTCDI molecules and 2 NaCl monomers in each unit-cell. The arrangement of the four PTCDI molecules which compose the molecular pattern looks like a wave. Figure 4.6a, shows a large scale image of the "Wave Network". It

appears clearly on this STM image that the "Wave Network" remains localized on the surface, i.e. it was not possible to observe domains larger than  $12 \times 6 \text{ nm}^2$ . A PTCDI side-by-side structure can be observed on the left of the same image (see §3.2.2 on the PTCDI side-by-side structure). Some NaCl monomers are observed between PTCDI molecules of the side-by-side structure. In most cases the NaCl monomers remain localized at the borders of the side-by-side structure, where they form PTCDI-NaCl "pearl necklace" chains. This can be carefully explained by the fact that it is not energetically favorable to break the PTCDI side-by-side structure in order to replace it by the PTCDI-NaCl "Wave Network". Therefore the appearance of the "Wave Network" can be understood as a reorganization of the less stable PTCDI canted structure (see §3.2.1), induced by the incorporation of NaCl monomers and activated by a precise control of the sample temperature (i.e. annealing at  $150^\circ \text{ C}$  during 12 hours). Therefore, a PTCDI-NaCl "Wave Network" is formed after annealing the sample at a temperature of  $150^\circ \text{ C}$  during 12 hours. After this post-annealing it is no longer possible to observe any domains of the PTCDI-NaCl porous structure, or pure NaCl domains. Moreover, only few domains of the PTCDI canted structure were observed. In fact after this annealing the predominantly observed structures are the PTCDI side-by-side network followed by the PTCDI-NaCl "Wave Network" structure. Both structures are the most stable networks formed at a temperature of  $150^\circ \text{ C}$ . However, only small domains of the PTCDI-NaCl "Wave Network" can be formed (i.e.  $12 \times 6 \text{ nm}^2$ ). These information are of prime importance to develop nano-devices based on NaCl and PTCDI molecules. Finally, another modification of molecular organization can be obtained by annealing the sample at a temperature of  $200^\circ \text{ C}$ , as it is shown in the next section.

#### 4.2.4 NaCl-PTCDI bi-molecular nanoarchitectures formed after a post-annealing at $200^\circ \text{ C}$

Likewise, the sample was post-annealed at a temperature around  $200^\circ \text{ C}$  during twelve hours, leading to the formation of a PTCDI-NaCl "Ladder Network" on the Au(111) surface, Figures 4.7a,b. In these Figures it is observed that both PTCDI molecules and NaCl monomers form linear chains. The "Ladder Network" is formed by alternating PTCDI chains with NaCl chains. The PTCDI molecules within a chain are running parallel to each other. The NaCl monomers are arranged in pairs in the NaCl chains. All the NaCl pairs are aligned in the same direction. The distance between the two NaCl monomers of a pair is measured around  $4.3 \text{ \AA}$ , this value is slightly higher than the typical distance measured between two nearest chloride atoms in a NaCl island, i.e.  $3.9 \text{ \AA}$  (see §4.1.2). Two neighboring NaCl pairs of a same chain are slightly shifted in the direction perpendicular to the NaCl chain. The "Ladder Network" unit-cell is parallelogram with  $E \simeq 0.7 \text{ nm}$  and  $F \simeq 1.8 \text{ nm}$  the unit-cell constants and an angle of  $\simeq 73^\circ$  between the axes, Figure 4.7c. The molecular pattern of this "Ladder Network" is constituted of one PTCDI molecule and two NaCl monomers in each unit-cell. Each PTCDI molecule is linked to six NaCl monomers through its two amino groups and its four oxygen atoms. However, each NaCl monomer is only bonded to three PTCDI molecules. Figure 4.7c shows that the PTCDI molecules of a same chain are placed in a side-by-side configura-

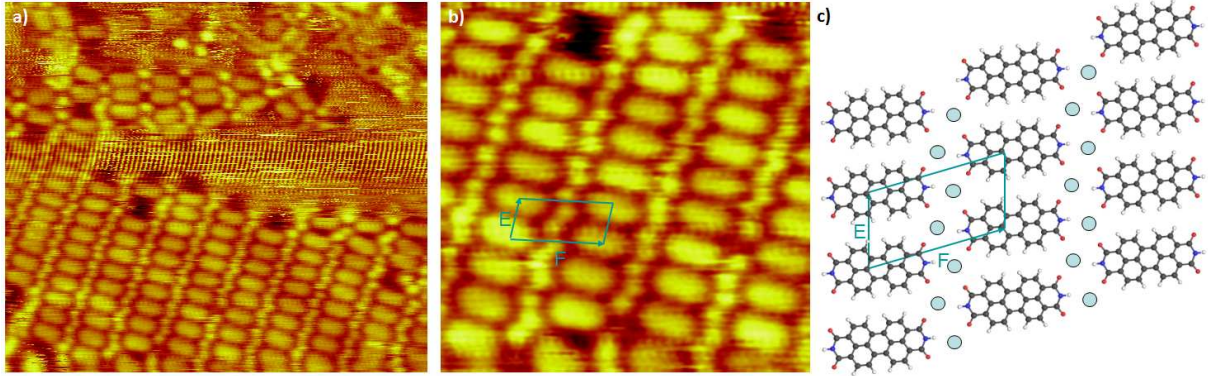


Figure 4.7: The NaCl-PTCDI "Ladder Network" structure formed on Au(111) after twelve hours annealing at 200° C: (a) Wide-range STM image,  $16.7 \times 14.3 \text{ nm}^2$ ,  $V_s = +1.92 \text{ V}$ ,  $I_t = 211 \text{ pA}$ ; (b) Short-range STM image of this "Ladder Network" structure  $7.2 \times 7.2 \text{ nm}^2$ ,  $V_s = +1.92 \text{ V}$ ,  $I_t = 211 \text{ pA}$ ; (c) Molecular model of the PTCDI-NaCl compact "Ladder Network" structure. Blue, red, gray and white balls correspond to nitrogen, oxygen, carbon and hydrogen atoms respectively, whereas NaCl monomers are represented with cyan balls.

tion. Therefore it is possible to say that the "Ladder Network" is presumably formed by the incorporation of NaCl monomers in the PTCDI side-by-side structure. Furthermore the incorporation of the NaCl monomers does not affect the side-by-side packing of the PTCDI molecules; i.e. the distances between neighboring PTCDI molecules within a chain are rather the same ( $\simeq 0.7 \text{ nm}$ ). However the distance between neighboring PTCDI chains is slightly increased from  $1.4 \text{ nm}$  for the pure PTCDI side-by-side structure; to  $1.8 \text{ nm}$  for the PTCDI-NaCl "Ladder Network". The increase of the PTCDI chain-to-chain distance followed by the incorporation of NaCl monomers is only possible when the sample is post-annealed at a temperature around  $200^\circ \text{C}$ . The large scale STM image depicted in Figure 4.7a, shows that the "Ladder Network" is really localized on the surface, i.e. with a domain size up to  $10 \times 14 \text{ nm}^2$ . After this post-annealing it is no longer possible to observe any domains of the PTCDI "Canted" structure and PTCDI-NaCl "Wave Network". In fact the majority of the Au(111) surface is covered by the PTCDI side-by-side structure, and only few domains of the "Ladder Network" can be observed. Some molecular defects can appear in the PTCDI-NaCl "Ladder Network", as shown at the top of Figure 4.7b. These molecular defects correspond to some PTCDI molecules and/or NaCl monomers which are missing. Therefore, after a post-annealing of the sample at  $200^\circ \text{C}$  during 12 hours a closely-packed PTCDI-NaCl "Ladder Network" was formed. The incorporation of the NaCl monomers in the PTCDI side-by-side structure involves an increase of the PTCDI chain-to-chain distance. In addition to that the formation of the PTCDI-NaCl "Ladder Network" also implies an increase of the Chlorine-to-Chlorine distance in the NaCl pairs. The small size of the "Ladder Network" domains ( $\simeq 10 \times 14 \text{ nm}^2$ ) is correlated with the partial desorption of the NaCl monomers observed under annealing. This indicates that a possible way to increased the size of the "Ladder Network" domains, is to continuously deposit NaCl during the sample annealing

at 200°C. This information is of prime importance to develop devices based on PTCDI and NaCl compounds.

## Chapter Conclusions

In this chapter I showed that NaCl grows as square islands on the Au (111) surface, with a lattice distance equivalent to that one measured with AFM<sup>1</sup> by G. Meyer *et al* for a bare NaCl(001) surface [118], i.e. around 5.6Å (§4.1.2). Thereafter I showed the temperature dependence of the bi-molecular self-assembly formed by mixing PTCDI with NaCl on Au(111) surface. At room temperature the NaCl deposition onto the PTCDI/Au(111) substrate leads to the reorganization of the PTCDI sub-monolayer film. The PTCDI molecules surround small NaCl islands, and then form PTCDI-NaCl structures of different shapes and sizes (§4.2.1). A modification of the shape of the PTCDI-NaCl structures obtained at room temperature was observed after successive scans with the STM tip on the same area. After annealing of the sample at 100°C during twelve hours, a porous PTCDI-NaCl architecture is formed (§4.2.2). In the same way by annealing the sample at 150°C during 12 hours, PTCDI and NaCl monomers form a compact "Wave Network" structure (§4.2.3). Finally, after annealing the sample at 200°C during twelve hours, a more compact "Ladder Network" is formed (§4.2.4). Subsequent annealing of the sample above 200°C, leads to the complete NaCl desorption from the Au(111) substrate. In that case, large domains of the PTCDI side-by-side structure were formed. All the STM images were taken at room temperature showing that the modification of the molecular self-assembly obtained after post-annealing is an irreversible process. In the end, these results show that the sample's temperature is a key parameter driving the PTCDI-NaCl bi-components self-assembly on the Au(111) surface. This information is of prime importance in order to develop nano-devices based on PTCDI and Sodium Chloride compounds. Another useful manner to control the molecular organization is to change the molecular substituents used, as well as the molecular skeleton used. It is what I showed in the next chapter.

---

<sup>1</sup>AFM: Atomic Force Microscopy.

# Chapter 5

## Self-Assembled Molecular Architectures Investigated by STM

Engineering organic nano-architectures on surfaces is the focus of recent research interest [76, 120–129]. Controlling the self-assembly of molecules on surfaces offers the possibility to build two-dimensional (2D) supramolecular nano-structures. The resulting organic architectures can be tailored at the nanometer scale by exploiting molecule-substrate and molecule-molecule interactions [11, 130–132]. The chemical structure of molecules, as well as the molecular shape, size, and nature of molecular substituents are key parameters governing the formation of self-assembled organic films (see §1.2.1.3). In that way, intense research have been focused on the synthesis of new molecules and on developing new procedures to engineer organic self-assembled nano-structures. The main objective is to understand the factors governing the molecular self-assembly process [133, 134] in order to create useful organic nano-devices. In fact, the formation of large self-organized films is of prime importance in order to design and to optimize nano-materials that can be used in spintronic applications [135] and in photovoltaic devices [136]. It is the reason why in this chapter I will exposed some results on the formation of organized self-assembled molecular thin film, based on different molecules. These molecules have been chosen for their particular shape (i.e. molecular skeleton) and their molecular substituents. The molecular substituents have been chosen in order to create strong and directional hydrogen bonds from which self-assembled monolayers can be build in a predictable way (see §1.1.2.4). First of all, I will describe some self-assembled nano-architectures based on single molecule that I obtained during my PhD. In that way I will show that the choice of the molecular skeleton and molecular substituents used is crucial to control the self-assembly. Secondly, I will demonstrate how it is possible to control the self-assembly by mixing different types of molecular species. Finally, I will describe the formation and the use of host-guest molecular systems in order to modify and control the organization of additional molecular entities.

## 5.1 Single-component supramolecular self-assemblies

### 5.1.1 Compact Self-Assemblies of Ni(II)-Salen Derivative on HOPG

Metal-salen-based complexes (see Figure 5.1a) are among the most fascinating metallo-organic systems because of their chemical versatility and flexibility [137]. A variety of metal ions (dia and/or paramagnetic) can be introduced in the coordination pocket leading in most cases to almost flat structures particularly adapted to enhance molecule/substrate interactions. In addition, numerous substituents can be placed on the phenol rings and the diamine bridge allowing to tune the size and the shape of the complexes in order to control their self-assembly on surfaces. To date, hydrophobic [138–140] or weak dipolar [141, 142] interactions have been previously exploited for this purpose with this type of complexes. However, hydrogen-bond interactions have not

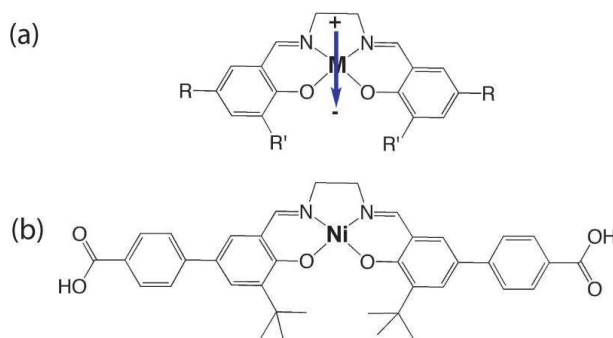


Figure 5.1: (a) Scheme of metal-salen skeleton. Negative and positive molecular poles are indicated by (–) and (+), respectively. The arrow reflects the resulting molecular dipole. (b) Scheme of  $[\text{Ni}(\text{H}_2\text{L})]$  complex (**1**), [143].

yet been explored. The strength and directionality of these interactions have been exploited to generate predictable organic architectures [23, 46, 144, 145]. Placing carboxylic groups in the para-position of the phenol rings of a metal-salen-based complex is, for example, expected to lead to the formation of H-bond one-dimensional (1D) chains on the surface. In comparison the 2D molecular ordering is obviously less predictable. In addition carboxylic groups can be directly linked to the phenol or can be spaced using benzyl rings to tune the length of the complex. This will influence the structure of the 1D organic chain as well as the molecular 2D assembly.

In this section, I investigate the self-assembly of a Ni(II)-R,R'-salen complex where R' is tert-butyl and R is benzoic acid (Figure 5.1b). Scanning tunneling microscopy images reveal that molecules self-assemble into a close-packed two-dimensional nanoarchitecture at the solid/liquid interface on a highly oriented pyrolytic graphite (HOPG) substrate. This structure consists of a stack of H-bonded molecular chains. Complex **1** of formula  $[\text{Ni}(\text{H}_2\text{L})]$  [ $\text{H}_4\text{L}$  is diaminoethane-*N,N'*-bis(tert-butyl-5-(4'-benzoic acid)salicylidene)] is obtained by the reaction of hydrated nickel(II) acetate and the salen derived ligand  $\text{H}_4\text{L}$  in a mixture of methanol and dimethylformamide. A solution of complex **1** in 1-

octanol [146] (98%, Acros) was prepared. A droplet of this solution was then deposited on a freshly cleaved HOPG substrate. STM imaging of the sample was performed at the liquid/solid interface using a Pico-STM scanning tunneling microscope (Molecular Imaging, Agilent Technology). Mechanically etched Pt/Ir wires were used to obtain constant current images at room temperature with a bias voltage applied to the sample. STM images were processed and analyzed using the application FabViewer [102].

The large-scale STM image (Figure 5.2a) shows that molecules of complex **1** self-assemble at the liquid/graphite interface into close-packed 2D networks. Molecular domains are typically  $500\text{nm}^2$  large. Molecules lie flat on the surface (Figure 5.2b). Red and green-colored molecules represent the network unit cell. It is a parallelogram with  $\simeq 2.6$  and  $\simeq 1.6$  nm unit cell edges forming an angle of  $\simeq 83^\circ$  between them. The

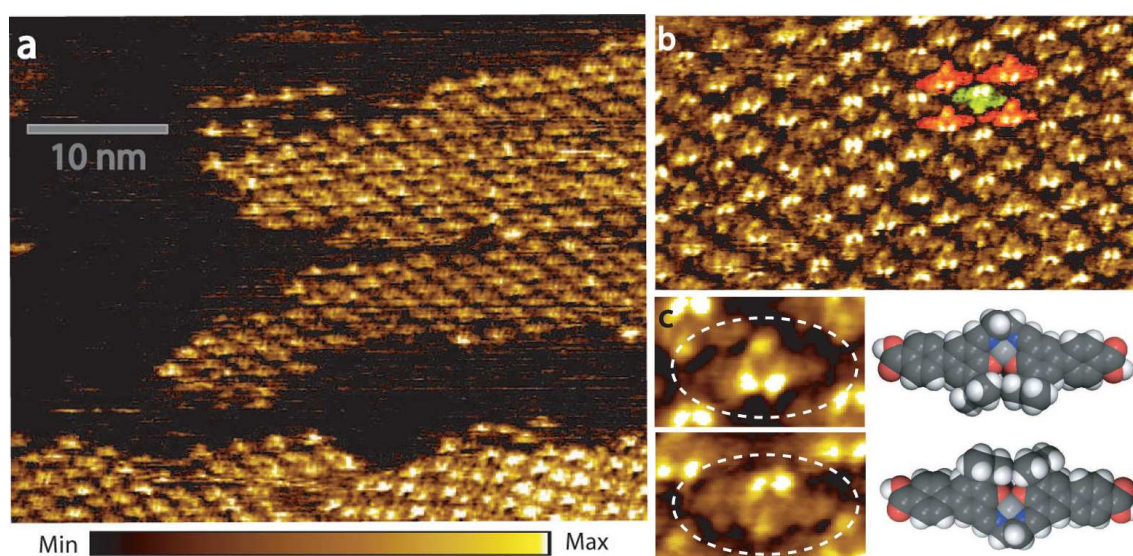


Figure 5.2: (a) Large-scale STM image of the self-assembled structure of molecule **1** on graphite,  $45 \times 38\text{nm}^2$ ;  $V_s = 0.8$  V,  $I_t = 25$  pA. Bottom: color scale bar. (b) High resolution STM image  $20 \times 11\text{nm}^2$ ;  $V_s = 0.8$  V,  $I_t = 35$  pA. Red and green colored molecules show the two orientations of the molecular building block in the organic layer. (c) Observed molecular orientation. Left: STM images of complex **1** (surrounded by white dotted ellipse). Right: Model of complex **1**. Carbon atoms are dark gray, hydrogen atoms are white, oxygen atoms are red, nitrogen atoms are blue, and nickel atom is light gray, respectively [143].

assembly of complex **1** is composed of close-packed chains. Neighboring molecular chains are shifted along their axis by a distance equal to half-molecule length. This leads to a close-packed paving of the 2D space. As shown in Figure 5.2c, two molecular orientations are observed. They are related by a  $180^\circ$  rotation angle along the molecular chain axis. High-resolution STM images reveal intramolecular features, Figure 5.2c. Complex **1** is not a perfectly flat molecule due to the tert-butyl and ethylene-diamine groups. Tert-butyl groups appear as bright spots in the STM image of the molecule (Figure 5.2c) indeed. In comparison, ethylene-diamine substituents appear as weaker protrusions.

Molecules have been colored in red and green in the STM image, Figure 5.3a. The

colors highlight the two molecular orientations observed in the organic network in Figure 5.2c. Molecular chains are stabilized along their axis (blue arrows in Figure 5.3a, b) by hydrogen bonds between the carboxylic groups of neighboring molecules. This is

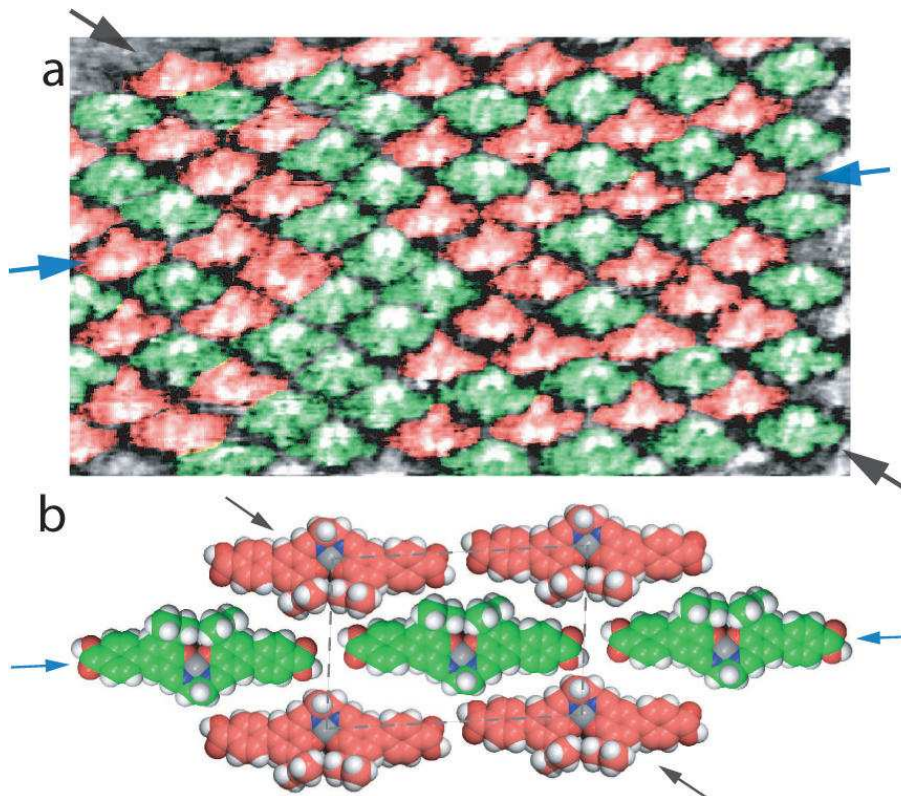


Figure 5.3: (a) STM image of the self-assembled complex **1** nanoarchitecture,  $20 \times 11 \text{ nm}^2$ ;  $V_s = 0.8 \text{ V}$ ,  $I_t = 35 \text{ pA}$ . Molecules are colored in red or green false color according to their respective orientation. Blue arrows indicate the direction of complex **1** H-bonded chains. Black arrows indicate complex **1** closest-neighbor separation, [143].

expected since carboxylic acids are known to form dimers in the vapor phase [147–149]. Within a chain, molecules of **1** adopt preferentially the same orientation (blue arrows in Figure 5.3). STM images show that the nanoarchitecture of complex **1** consists of a stack of chains having opposite orientation. A quasi-ordered 2D organization is thus observed. In this 2D structure (Figure 5.3b), each molecule is surrounded by four neighbors having the opposite orientation ( $180^\circ$ ). Analysis of STM images suggests that the interchain interactions are governed by van der Waals (vdw) forces (along the black arrow direction in Figure 5.3).

The adequate molecular chain interpenetration appears to be at the origin of the excellent close-packing of the organic nanoarchitecture. However,  $\approx 30\%$  of the molecules adopt a different orientation from the majority in the 2D molecular network. Figure 5.3a shows that local misorientation ( $180^\circ$  rotation) of individual molecules does not affect the close-packing of the structure. These observations lead to the conclusions that (i) intrachain H-bonds and interchain vdw forces together with the molecule shape are

stabilizing the 2D compact molecular structure and (ii) the H-bonds and vdw interactions are not directly responsible for the alternate molecular orientation of neighboring chains. In fact, complexes have a twofold symmetry axis along the direction bisecting the OMO and the NMN angles displaying a dipolar moment along this direction [141], as depicted in Figure 5.1a. Since most of the closest-neighboring molecules have opposite orientation, molecular dipolar interactions are minimized in this arrangement (Figure 5.3b). Consequently, molecules belonging to the same chain have larger dipole-dipole distance than those belonging to adjacent chains. As a result, the molecules are thus preferentially oriented in the same direction along the salen chain. In comparison, molecules belonging to adjacent chains adopt preferentially an opposite orientation. Indeed among the 90 molecules in Figure 5.3a, 46 have their electric dipolar moment in one direction and 44 in the other direction thus leading to a zero net moment, despite the few molecular orientation "errors" observed in the 2D salen self-assembly.

In summary, a new nickel(II) salen complex with carboxylic acid groups has been studied using STM. STM images reveal that complex **1** self-assembles into a close-packed structure at the solid-liquid interface on graphite surface. Future work will be focused on changing the nature of the metal ions. Paramagnetic metal ions will be introduced to create a magnetic molecule. Two-dimensional nanometer-scale networks of magnetic building blocks [150–153] based on salen molecules are new model systems to explore nano-magnetism at the atomic scale. Spin-polarized scanning tunneling spectroscopy can be, for example, used to reveal local magnetic coupling between molecular metal atoms [154] as well as spin-electron coupling of the metal ion inside the organic assembly [155]. Exploring these phenomena at atomic scale is essential for developing new concepts in organic spintronics and nano-magnetism for applications in high-density data storage technology. Future work will be also focused on changing the nature of the substituents of the salen ligand. In this way, more insight will be gained into their roles to build new organic nanoarchitectures. To create nano-devices based on the nickel(II) salen complex **1**, a profound understanding of the intermolecular interactions governing the self-assembly is of prime importance. One example of the influence of the molecular substituents on the self-assembly of two DNA<sup>1</sup> bases is given in the following paragraphs.

### 5.1.2 DNA bases Self-Assemblies on Au(111)

In this section I described some results on the supramolecular self-assembly of two DNA bases, called guanine and adenine. These two DNA bases possess the same molecular skeleton but have different kinds of molecular substituents. The first paragraph depicted the molecular nano-architectures formed by the guanine molecules on Au(111) surface. The second paragraph described the self-assembled structures formed by the adenine molecules on Au(111) surface. Finally the effect of molecular substituents on the self-assembly of these two DNA bases will be determined by comparing the results obtained for both molecules. As substrate, we used Au(111) films grown on mica. The samples were introduced into the ultra-high vacuum (UHV) chamber of an STM apparatus (Omicron VT-STM with Nanonis controller) operating at a pressure of  $10^{-10}$  mbar. The

---

<sup>1</sup>DNA: desoxyribonucleic acid.

Au(111) surfaces were sputtered with  $\text{Ar}^+$  ions, typically for 15 min and then annealed in UHV at temperatures between 460 and 500 °C, during 1 hour. Guanine and adenine molecules were evaporated at 160 °C and 60 °C respectively, and then deposited on the gold surface. Cut Pt/Ir tips were used to obtain constant current STM images at room temperature with a bias voltage applied to the sample. STM images were processed and analyzed using the home made FabViewer application [102].

### 5.1.2.1 Guanine Self-Assemblies on Au(111)

The guanine molecule is composed of one oxygen atom, five nitrogen atoms, five hydrogen and five carbon atoms, as depicted in Figure 5.4a. It has been previously demonstrated that a weak molecule-substrate interaction is obtained for guanine thin films grown on gold surfaces [156]. This is confirmed by the fact that no isolated guanine molecule was observed even at room temperature. After deposition of the guanine molecules on the Au(111) surface, large terraces covered with the assemblies of the molecules were seen. The guanine molecules appear as triangular protrusions in the high resolution STM images, Figure 5.4. Figure 5.4b shows the irregular phase formed by the

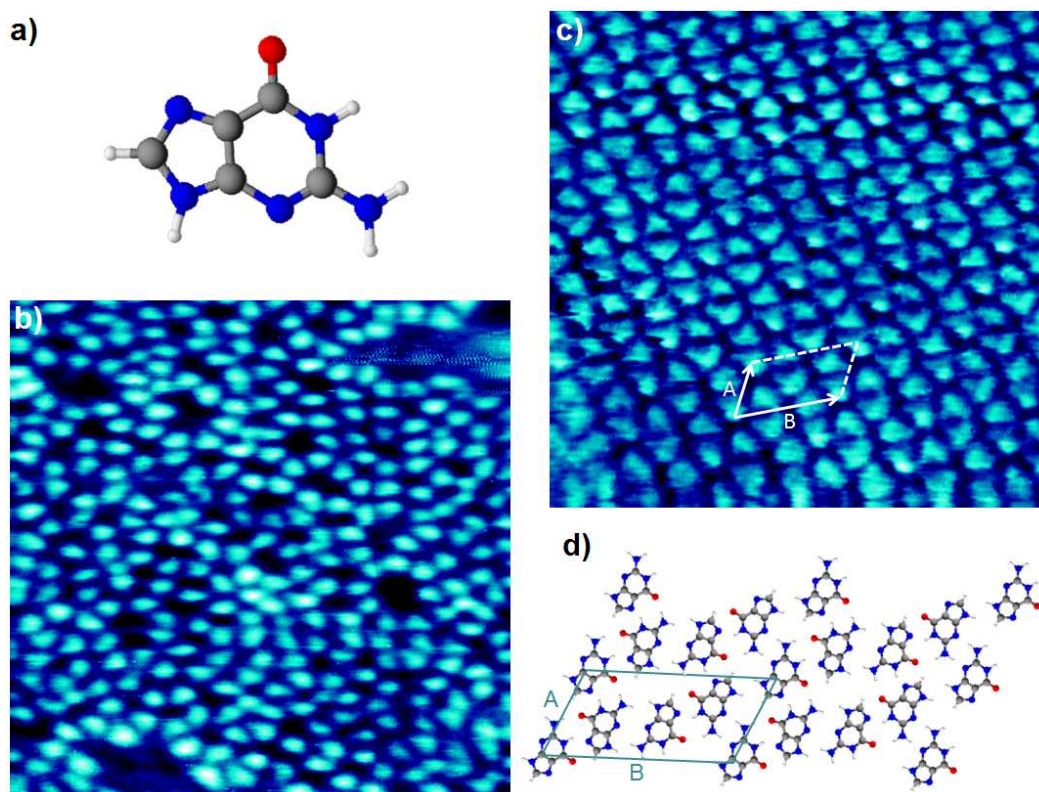


Figure 5.4: (a) Scheme of the guanine molecule. Carbon atoms are gray, oxygen atoms red, nitrogen atoms blue, hydrogen atoms white, respectively. STM images of the guanine structures formed on Au(111) surface: (b)  $9.6 \times 9.6 \text{ nm}^2$ ;  $V_s = -0.7 \text{ V}$ ,  $I_t = 0.6 \text{ nA}$ ; (c)  $9.6 \times 9.6 \text{ nm}^2$ ;  $V_s = 0.32 \text{ V}$ ,  $I_t = 0.8 \text{ nA}$ ; (d) Molecular model of the guanine self-assembled network in c.

Number of molecules in the guanine circles	5	6	7	8	9	10
Number of guanine circles in 10 images	118	90	36	18	5	1
Proportion of the guanine circles	44%	33.6%	13.4%	6.7%	1.9%	0.4%

Table 5.1: Proportions of the guanine circles in the disordered phase, with respect to their sizes (Figure 5.4b).

guanine molecules on the Au(111) surface kept at a temperature between 25 and 70°C. This disordered phase consists of guanine circles of different shapes and sizes, reminding the molecular circles formed by another guanosine derivative called xanthine [157]. The guanine circles can be composed of 5 up to 10 molecules. As it is shown in Table 5.1, the irregular phase is composed of a majority of circles possessing 5 guanine molecules (44%), and a minority of circles composed of 10 molecules (0.4%). A possible explanation for this consists to say that the guanine circles of small sizes possessing five, six or seven molecules are more stable energetically than the big guanine circles constituted of eight, nine or ten molecules. However this interpretation must be confirmed by DFT calculations. This porous guanine disordered phase has never been reported previously.

By increasing the sample temperature above 70°C during molecular deposition, the disordered phase completely disappears. A close-packed ordered structure also present at room temperature become preponderant above this temperature, Figure 5.4c. A scheme of the guanine self-assembled structure unit-cell is depicted in Figure 5.4d. The molecular pattern of this close-packed network is composed of four guanine molecules in each unit-cell. Each guanine molecule is doubly bonded with three of its nearest neighbors. Moreover this close-packed structure is composed of molecular ribbons, which are typical motifs for the supramolecular self-assembly of guanosine derivatives [158, 159]. The close-packed network unit-cell is parallelogram with  $A \simeq 0.89$  nm and  $B \simeq 1.72$  nm the unit-cell parameters and an angle of  $\simeq 65^\circ$  between them, Figure 5.4d. This close-packed structure has been already observed on HOPG (Highly Oriented Pyrolytic Graphite) and on gold surface after a post-annealing at 400K [156, 160], but it had never been observed at room temperature.

To summarize, we demonstrated that guanine molecules can form two phases at room temperature, one disordered phase with typical guanosine circles and one close-packed structure. Moreover when the temperature of the gold surface is increased above 70°C during molecular deposition, then the disordered guanine circles phase disappears while the close-packed phase becomes preponderant. To pursue this study it will be interesting to investigate the self-assembled nano-architectures formed on gold surface by a molecule which possesses the same molecular skeleton than guanine but has different kinds of molecular substituents. In that way, it will be possible to determine the effect of the molecular substituents on the self-assembly process. It is the reason why, in the next section I describe some results on the supramolecular nanostructures built on the Au(111) surface by using a molecule similar to guanine which is called adenine.

### 5.1.2.2 Adenine Self-Assemblies on Au(111)

The adenine molecule is composed of five nitrogen atoms, five carbon atoms, and five hydrogen atoms, as depicted in Figures 5.5b,d. After deposition of the adenine molecules on the Au(111) surface, large terraces covered with the assemblies of the molecules were seen. The adenine molecules form two different organic nano-structures on Au(111) surface kept at room temperature, Figures 5.5a,c. Figure 5.5a, shows that adenine

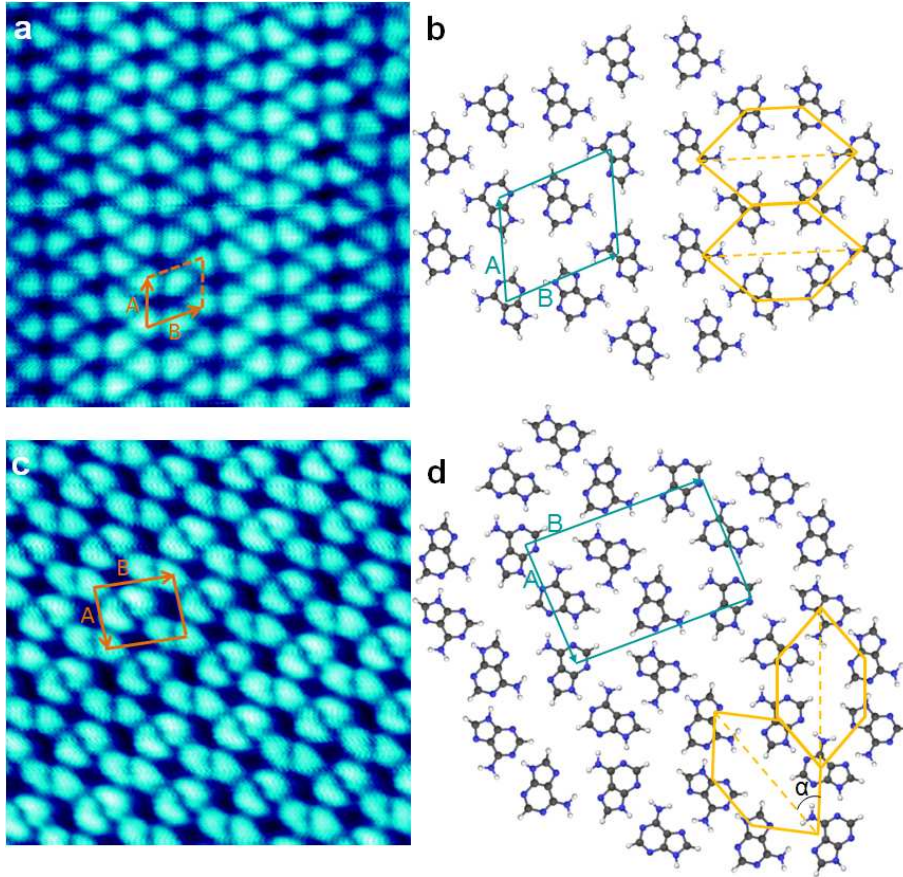


Figure 5.5: (a) STM image of the adenine honeycomb network formed on Au(111) surface,  $7.2 \times 7.2 \text{ nm}^2$ ;  $V_s = -300 \text{ mV}$ ,  $I_t = 220 \text{ pA}$ . (b) Scheme of the honeycomb self-assembled structure unit-cell. Carbon atoms are gray, nitrogen atoms blue, and hydrogen atoms white, respectively. (c) STM image of the adenine slanting network formed on Au(111) surface,  $7.2 \times 7.2 \text{ nm}^2$ ;  $V_s = +511 \text{ mV}$ ,  $I_t = 311 \text{ pA}$ . (d) Scheme of the slanting self-assembled structure unit-cell.

forms a honeycomb phase, where a molecule is placed at each corner of a hexagon. Each adenine molecule is rotated by an angle of  $\pm 180^\circ$  compared to its nearest neighbors, Figure 5.5b. The molecular pattern of this honeycomb structure is composed of two adenine molecules per unit-cell, which are rotated by an angle of  $180^\circ$  one compared to the other. In this structure all the hexagons are equivalent, and are placed in the same orientation. The lattice vector lengths of the unit-cell are  $A \simeq 0.73 \text{ nm}$  and  $B \simeq 1.1 \text{ nm}$ , with an angle of  $72^\circ$  between them. These values are really close to those obtained

in previous works [161]. A scheme of the adenine honeycomb self-assembled structure unit-cell is depicted in Figure 5.5b.

Another coexisting adenine network can be observed on the Au(111) surface kept at room temperature, Figure 5.5c. This network is formed by two periodically repeated hexagons which are not equivalent to each other. Each hexagon is composed of six adenine molecules. All the equivalent hexagons are placed in the same direction. However, two adjacent nonequivalent hexagons are turned by an angle of  $\alpha = 37^\circ$  one compared to the other, Figure 5.5d. The molecular pattern of this "slanting" structure is composed of four adenine molecules per unit-cell. The adenine molecules can be adsorbed in two different enantiomeric configurations, left- or right-handed. The unit-cell is composed of two molecules in a left-handed configuration, and two molecules in a right-handed configuration. The lattice vector lengths of the "slanting" network unit-cell are  $A \simeq 1.0\text{nm}$  and  $B \simeq 1.4\text{nm}$ , with an angle of  $85^\circ$  between them. These values are really close to those obtained in previous works [161]. A scheme of the adenine slanting self-assembled structure unit-cell is depicted in the Figure 5.5d.

To summarize, the adenine molecules form two coexisting molecular architectures on the Au(111) surface kept at room temperature, a "honeycomb" structure and a "slanting" structure. By comparing the results obtained here for adenine with those previously obtained for guanine, it appears that the self-assembly of two similar molecules possessing the same molecular skeleton deposited on the same substrate can be strongly affected by their molecular substituents. Indeed guanine molecules are forming a close-packed ribbon-like network and a disordered circles phase (Figures 5.4c, 5.4b respectively), whereas adenine molecules are forming a "honeycomb" network and a "slanting" structure (Figures 5.5a, 5.5c respectively). Therefore, this example shows that molecular substituents can be chosen to drive the self-assembled nano-architectures based on DNA materials. Furthermore the effect of molecular substituents on the self-assembly process is not limited to DNA bases. In reality, the molecular substituents can take part in the self-assembly process through intermolecular interactions and thus affect the molecular organization. For example the effect of molecular substituents on molecular organization can be also observed for two perylene derivatives called PTCDI and PTCDA, as it is shown in the next paragraph.

### 5.1.3 PTCDA self-assembly on Au(111)

The PTCDA<sup>2</sup> molecule is composed of six oxygen atoms, eight hydrogens and twenty four carbon atoms, as depicted in Figure 5.6a. PTCDA molecules were evaporated at  $195^\circ\text{C}$ , onto a clean Au(111) surface in UHV environment. After deposition of the PTCDA molecules on the gold surface kept at room temperature, large terraces covered with the assemblies of the molecules were seen, Figure 5.6b. Figure 5.6c shows that PTCDA can form a herringbone phase with two molecules per unit-cell which are separated by an angle of  $76^\circ$ . A scheme of the PTCDA herringbone self-assembled structure unit-cell is depicted in Figure 5.6d. The lattice vector lengths of the herringbone network unit-cell are  $A \simeq 1.1\text{nm}$  and  $B \simeq 1.8\text{nm}$ , with an angle of  $78^\circ$  between them. These

---

<sup>2</sup>PTCDA: 3,4,9,10-perylenetetracarboxylic dianhydride.

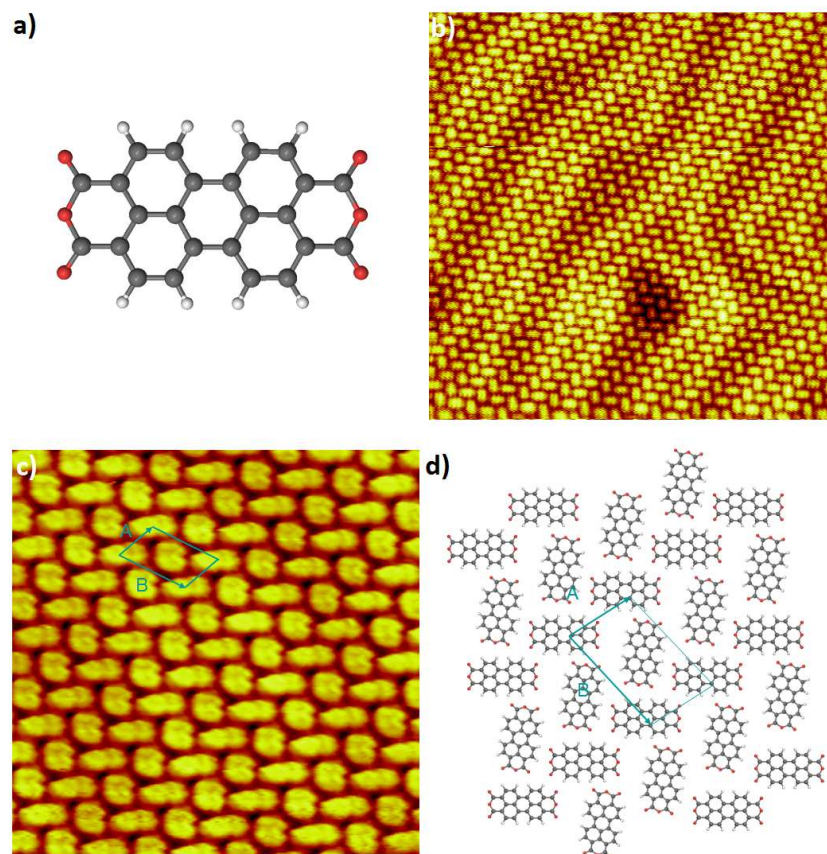


Figure 5.6: (a) 3,4,9,10-perylenetetracarboxylic dianhydride (PTCDA) molecule. Carbon atoms are gray, oxygen atoms red, hydrogen atoms white, respectively. (b) Wide-range STM image of the PTCDA herringbone network formed on the Au(111) surface,  $28.7 \times 28.7 \text{ nm}^2$ ;  $V_s = +811 \text{ mV}$ ,  $I_t = 412 \text{ pA}$ ; (c) Small-range STM image of the same structure,  $9.6 \times 9.6 \text{ nm}^2$ ;  $V_s = +711 \text{ mV}$ ,  $I_t = 211 \text{ pA}$ ; (d) Scheme of the PTCDA herringbone self-assembled structure uni-cell.

values are really close to those obtained in previous works [46]. The molecular model in Figure 5.6d shows that the PTCDA herringbone structure is stabilized through the establishment of eight C–H $\cdots$ O hydrogen bonds in each unit-cell. This interpretation is supported by the results obtained from DFT<sup>3</sup> calculations [46]. Finally Figure 5.6b shows that the Au(111)- $(22 \times \sqrt{3})$  herringbone reconstruction can be clearly seen underneath the PTCDA molecular film, indicating a weak molecule-substrate interaction.

During this work we have shown that the PTCDA molecules can form on gold surface at room temperature a herringbone phase which is stabilized through hydrogen bonds. By comparing the results obtained here for PTCDA with those previously obtained for another perylene derivative called PTCDI (see chapter 3), it appears that the change of only two molecular substituents can strongly affect the molecular self-assembly. In fact, after deposition of the PTCDI molecules on the Au(111) surface kept at room temperature, a canted structure was formed where the molecules of neighboring chains

<sup>3</sup>DFT: Density Functional Theory.

are almost parallel to each other ( $\pm 12^\circ$ ). In contrast, after deposition of the PTCDA molecules on the Au(111) surface kept at room temperature, a herringbone structure was formed where the molecules of neighboring chains are rotated by an angle of  $76^\circ$  one compared to the other. This modification of the resulting molecular nano-architecture is obtained by substituting the two amino groups of the PTCDI molecule, by two oxygen atoms in the PTCDA molecule. To conclude, the choice of the molecular substituents used is crucial in order to control and design new organic nanoarchitectures. In addition to that, another useful manner to control the molecular organization on surfaces is to mix different kinds of molecular species. It is what I will show in the next paragraph, where PTCDA and PTCDI molecules have been successively mixed with adenine molecules on the Au(111) surface.

## 5.2 Multi-component supramolecular self-assemblies

### 5.2.1 Compact PTCDA-Adenine supramolecular self-assemblies

Here I describe the molecular nano-architectures formed on Au(111) surface after co-deposition of the PTCDA and adenine molecules in UHV environment, subsequently followed by a post-annealing at  $50^\circ\text{C}$  during 1 hour. Figures 5.7a,b show that the semiconducting PTCDA molecule and adenine DNA base self-assemble into a complex bi-molecular architecture which drastically differs from the pure PTCDA self-assembled structure (Figure 5.6), and pure adenine networks (Figure 5.5). The PTCDA molecules have a rectangular shape, while the adenine molecules have a triangular shape in the STM images, Figures 5.7a,b. In addition to that PTCDA molecules appear brighter than adenine molecules in the STM images. The PTCDA-Adenine network unit-cell is parallelogram with  $A \simeq 3.5 \text{ nm}$  and  $B \simeq 3.2 \text{ nm}$ , the lattice vectors lengths which are separated by an angle of  $\simeq 77^\circ$ , Figure 5.7c. The unit-cell of this multi-component two-dimensional nanoarchitecture is composed of 10 PTCDA molecules and 4 Adenine molecules. A detail analysis of the molecular model depicted in Figure 5.7c, reveals that the PTCDA-Adenine self-assembled network is composed of some PTCDA "zigzag" patterns which are identical to those observed in the pure PTCDA herringbone structure of Figure 5.6d. These PTCDA "zigzag" patterns are placed at each side of the parallelogram unit-cell of the bi-molecular structure, Figure 5.7c. In contrast, 4 PTCDA molecules are placed in a square configuration at each corner of the PTCDA-Adenine unit-cell. This square configuration is identical to that obtained in the pure PTCDA "domino" [46] structure. The unit-cell center consists of 4 PTCDA molecules in a square configuration which is turned by an angle of approximately  $45^\circ$  compared to the PTCDA square structures placed at the corners. Finally, 4 adenine molecules bind the central PTCDA square structure to the external PTCDA square and "zigzag pattern" structures, Figure 5.7c. The molecules in the PTCDA "zigzag" patterns are connected to each other through two  $\text{O} \cdots \text{H}-\text{C}$  hydrogen bonds. In contrast the four PTCDA molecules in the square structures are linked to each other through three  $\text{O} \cdots \text{H}-\text{C}$  hydrogen bonds. Finally the adenine molecules are bonded to PTCDA molecules through  $\text{O} \cdots \text{H}-\text{N}$ ,  $\text{O} \cdots \text{H}-\text{C}$ , and  $\text{N} \cdots \text{H}-\text{C}$  hydrogen bonds.

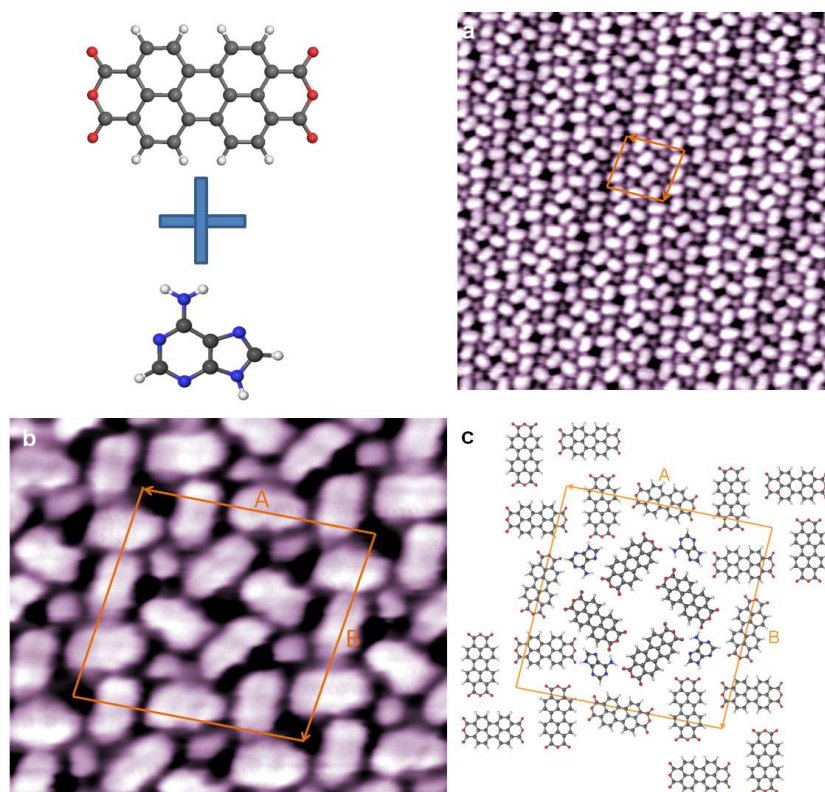


Figure 5.7: (a) Large-scale STM image of the PTCDA-Adenine bi-molecular network formed on Au(111) surface,  $21.5 \times 21.5 \text{ nm}^2$ ;  $V_s = +511 \text{ mV}$ ,  $I_t = 500 \text{ pA}$ . (b) Small-range STM image of the same structure,  $7.2 \times 6.3 \text{ nm}^2$ ;  $V_s = +811 \text{ mV}$ ,  $I_t = 600 \text{ pA}$ . (c) Scheme of the PTCDA-Adenine bi-molecular self-assembled structure unit-cell. Carbon atoms are gray, oxygen atoms red, nitrogen atoms blue, and hydrogen atoms white, respectively.

In the end, these results show that mixing symmetrical and non-symmetrical molecules could be a useful method to increase the complexity and sophistication of hydrogen bonded supramolecular architectures. Another example of that, is obtained by mixing PTCDI with adenine molecules, as it will be shown in the next paragraph.

### 5.2.2 Compact PTCDI-Adenine supramolecular self-assemblies

In this paragraph, I describe the molecular nano-architecture formed on Au(111) surface after co-deposition of the PTCDI and adenine molecules in UHV environment, subsequently followed by a post-annealing at  $50^\circ\text{C}$  during 1 hour, Figure 5.8. In this Figure the PTCDI molecules appear with a rectangular shape, while adenine molecules appear with an asymmetric ball shape. The one-dimensional (1D) bi-molecular network formed is composed of two PTCDI chains which are separated by one adenine row, Figure 5.8a. The molecules in the PTCDI chains are turned by an angle of  $12^\circ$  compared to the row's direction, as previously observed in the PTCDI canted structure (Figure 3.3). To prevent molecular defects, the PTCDI molecules of the bi-components network adopt

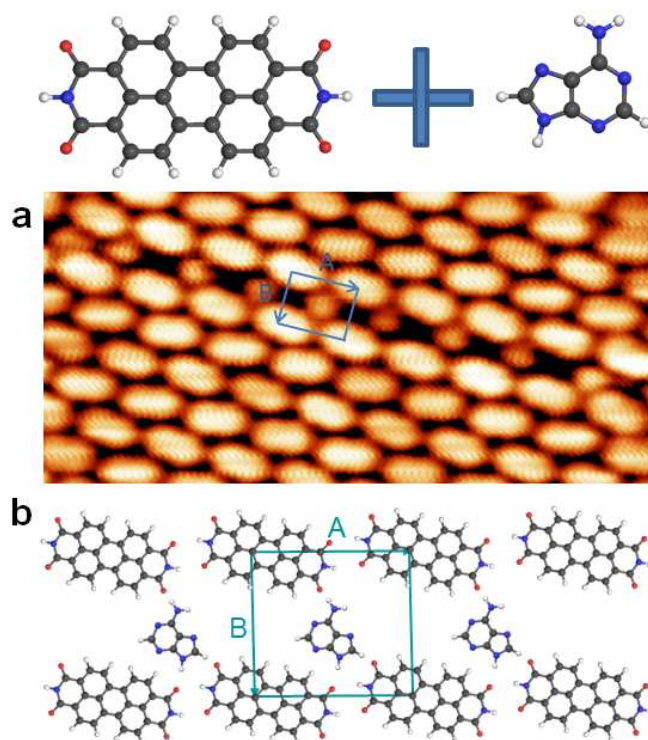


Figure 5.8: (a) STM image of the PTCDI-Adenine bi-molecular network formed on Au(111) surface,  $12 \times 4.8 \text{ nm}^2$ ;  $V_s = -111 \text{ mV}$ ,  $I_t = 411 \text{ pA}$ . (b) Scheme of the bi-molecular self-assembled structure unit-cell. Carbon atoms are gray, oxygen atoms red, nitrogen atoms blue, and hydrogen atoms white, respectively.

the configuration of the surrounding PTCDI canted structure. A molecular model of the PTCDI-Adenine structure is given in Figure 5.8b, suggesting that the adenine molecules act as a "glue" between the two PTCDI rows. In fact, adenine molecules are probably linked with PTCDI molecules through  $\text{N}-\text{H} \cdots \text{O}$ ,  $\text{N} \cdots \text{H}-\text{C}$  and  $\text{C}-\text{H} \cdots \text{O}$  hydrogen bonds. Furthermore, the molecules within a PTCDI chain are attached to each other by the establishment of two  $\text{N}-\text{H} \cdots \text{O}$  hydrogen bonds. The resulting PTCDI-Adenine network unit-cell is parallelogram with  $A \approx 1.2 \text{ nm}$  and  $B \approx 1.1 \text{ nm}$ , the vector lengths which are separated by an angle of  $\approx 90^\circ$ , Figure 5.8b. The molecular pattern of this bi-components nanoarchitecture is composed of one PTCDI molecule and one adenine molecule in each unit-cell.

After successive scans of the same area with the STM tip, the PTCDI-Adenine bi-molecular network can be transformed into a PTCDI zigzag pattern, Figure 5.9a-f. First the adenine molecules of the PTCDI-Adenine network are removed after 10 scans of the same area (top left corner in Figures 5.9d,e). Further scans of the same area with the STM tip (where now the adenine molecules are missing), leads to the rotation of the PTCDI molecules. This involves the formation of a new PTCDI zigzag chain, Figure 5.9f. In addition to that, a PTCDI side-by-side structure is present at the bottom right corner of Figure 5.9a. A molecular defect can be observed in this side-by-side structure

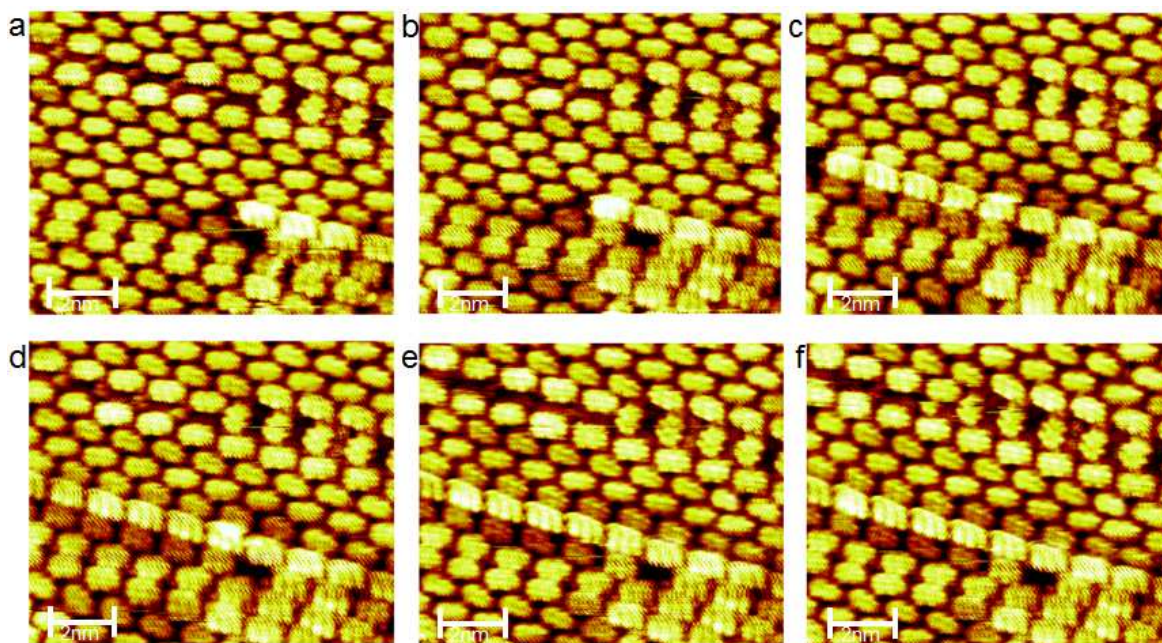


Figure 5.9: (a-f) Evolution of the PTCDI-Adenine network and PTCDI side-by-side structure on Au(111) surface after successive scans with the STM tip on the same area:  $11.4 \times 9.4 \text{ nm}^2$ ;  $V_s = -211 \text{ mV}$ ,  $I_t = 411 \text{ pA}$ .

("big" hole), where a PTCDI molecule is missing. Additionally, there is a "small" hole between the central chain of the PTCDI side-by-side structure and the molecule of the surrounding canted structure. After successive scans of this area, a PTCDI molecule of the canted structure moves to the right by refilling the small hole, Figures 5.9a,b. This implies the expansion of the PTCDI triple-chains structure. When this happens, a new small hole is created in front of the side-by-side structure, i.e. at the interface of the PTCDI canted and triple-chain structures, Figure 5.9b. Again after successive scans, when this new small hole is refilled with a PTCDI molecule of the canted structure, there is an expansion of the PTCDI side-by-side structure. Therefore the PTCDI triple-chain structure can be expanded through an iterative process involving the creation and the refilling of a small hole with a PTCDI molecule of the surrounding canted structure, Figures 5.9a-f. This iterative process originates from the interaction between the molecular film and the STM tip. However, the relation between the number of successive scans and the number of PTCDI molecules added to the side-by-side structure is not linear and cannot be predicted.

In conclusion, the co-deposition of PTCDI with adenine molecules on Au(111) surface in UHV environment allows to form a one-dimensional supramolecular architecture (Figure 5.8). In contrast when adenine molecules are mixed with PTCDA, a two-dimensional nanostructure is formed (Figure 5.7). Therefore the molecular substituents are key factors governing the bi-molecular self-assembly of adenine with the perylene derivatives. Additionally I have shown that adenine molecules form two different phases on Au(111) surface, a honeycomb phase and a slanting network, Figures 5.5a,c respectively. These

pure adenine structures cannot be recognized in the bi-molecular self-assembled architectures formed with the two perylene derivatives (Figures 5.8, and 5.7). However, the pure PTCDI canted structure depicted in Figure 3.3a, can be easily recognized at the sides of the PTCDI-Adenine bi-molecular structure, Figure 5.8. In the same way, the "zigzag" patterns of the pure PTCDA herringbone phase (Figure 5.6c), can be found at the sides of the PTCDA-Adenine network unit-cell (Figure 5.7b). In the end, the results shown here demonstrate that the use of multi-components systems is a useful tool to create sophisticated molecular architectures. In addition to that, multi-components architectures can be used to build host-guest systems in order to control the self-organization of additional molecules, as shown in the following paragraphs (see §5.2.3, and §5.3.2).

### 5.2.3 Host-guest supramolecular self-assembly formed by the PTCDI and truncated TAPB molecules

Here I described the formation of a new host-guest supramolecular system by mixing a truncated TAPB<sup>4</sup> molecule with PTCDI on Au(111) surface. The undamaged TAPB molecule is represented in Figure 5.10a. The truncated TAPB molecule (named BAPB<sup>5</sup>) is obtained after evaporation of the undamaged TAPB molecule at relatively high temperature in UHV, i.e. around 260-280° C (Figure 5.10b). These evaporation parameters allow to remove an amino-phenyl group from the TAPB molecule, resulting in the appearance of Aniline and 1,3-Bis(4-AminoPhenyl)Benzene (BAPB) molecules, Figure 5.10b. The BAPB molecule consists of two amino-phenyl groups attached to a benzene core, Figure 5.10b. The Aniline molecule appears in the STM images as a

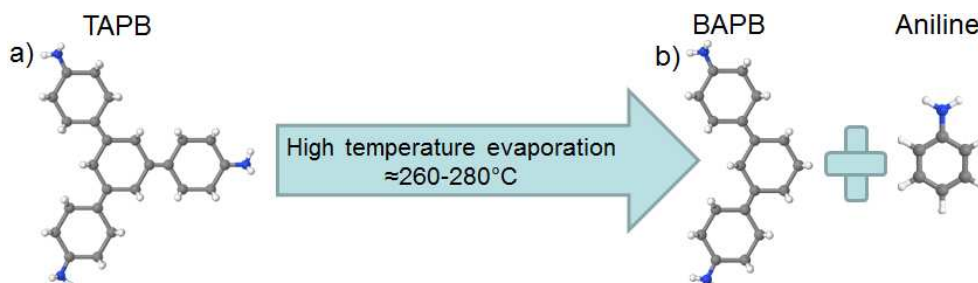


Figure 5.10: Thermal decomposition of the TAPB molecule: (a) 1,3,5-Tris(4-AminoPhenyl)Benzene (TAPB) molecule; (b) 1,3-Bis(4-AminoPhenyl)Benzene (BAPB) and Aniline molecules, obtained after evaporation of the TAPB molecules at relatively high temperature around 260-280° C in UHV.

single bright spot (Figure 5.11b), while the BAPB molecule appears in the STM images as a bright arc (Figures 5.11a-c). Finally PTCDI molecule appears with a rectangular shape, Figures 5.11a-c. A porous molecular structure is obtained after evaporation of the PTCDI molecules at 245° C onto the Au(111) surface with the pre-adsorbed BAPB molecules, Figure 5.11a. A molecular model of this porous PTCDI-BAPB structure

<sup>4</sup>TAPB: 1,3,5-Tris(4-AminoPhenyl)Benzene.

<sup>5</sup>BAPB: 1,3-Bis(4-AminoPhenyl)Benzene.

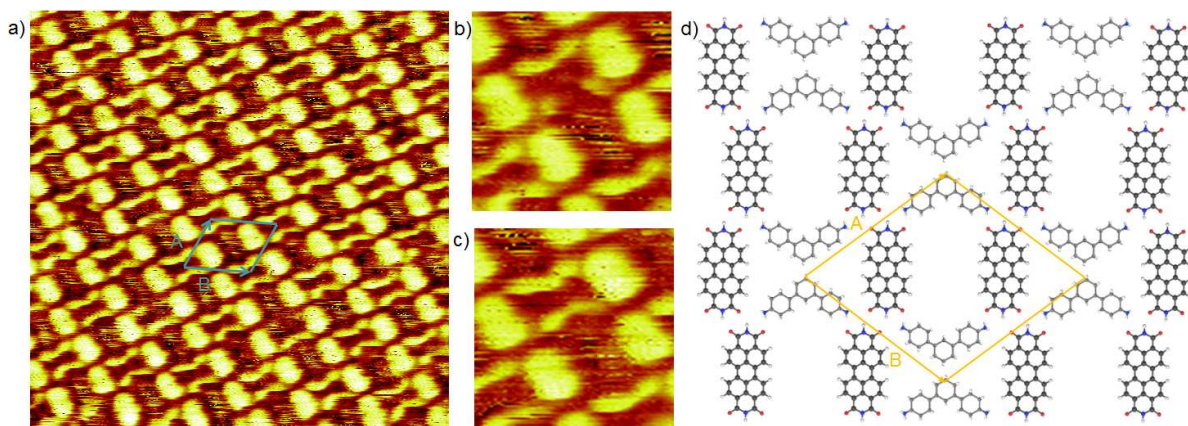


Figure 5.11: Bi-molecular nano-architecture formed on the Au(111) surface after deposition of the PTCDI and BAPB molecules: (a) wide-range STM image of the porous network formed by the BAPB and PTCDI molecules on Au(111) surface,  $14.3 \times 14.3 \text{ nm}^2$ ,  $V_s = +911 \text{ mV}$ ,  $I_t = 684 \text{ pA}$ ; (b) small-range STM image of two Aniline molecules inserted in the PTCDI-BAPB porous network by replacing a single BAPB molecule,  $3.1 \times 3.1 \text{ nm}^2$ ;  $V_s = +911 \text{ mV}$ ,  $I_t = 684 \text{ pA}$ ; (c) small-range STM image of the PTCDI-BAPB porous network,  $3.1 \times 3.1 \text{ nm}^2$ ;  $V_s = +911 \text{ mV}$ ,  $I_t = 684 \text{ pA}$ ; (d) Molecular model of the PTCDI-BAPB porous self-assembled structure. Carbon atoms are gray, nitrogen atoms blue, hydrogen atoms white, and oxygen atoms red, respectively.

is given in Figure 5.11d. The network unit-cell is parallelogram with  $A \simeq 2.0 \text{ nm}$  and  $B \simeq 2.3 \text{ nm}$ , the unit-cell parameters and an angle of  $\simeq 65^\circ$  between them. The molecular pattern of the PTCDI-BAPB porous structure is composed of two PTCDI and two BAPB molecules in the network unit-cell. The two BAPB molecules are placed at two opposite corners of the parallelogram network unit-cell, and are pointing in opposite directions. Each BAPB molecule is linked to two PTCDI molecules through two  $\text{N}-\text{H} \cdots \text{O}$  hydrogen bonds. In that way the BAPB molecules are placed perpendicular to the PTCDI molecules. The PTCDI molecules are forming chains which running parallel to each other. Two neighboring PTCDI molecules of a same chain are linked together through two  $\text{N}-\text{H} \cdots \text{O}$  hydrogen bonds. The PTCDI molecules are alternatively shifted to the left and to the right of their chain direction, leading to a "zigzag" pattern. This zigzag pattern is formed in order to accommodate the presence of the BAPB molecules. In addition to that, two closest BAPB molecules are pointing in opposite directions (i.e. up and down), leading to a "butterfly" pattern placed at each corner of the PTCDI-BAPB network unit-cell, Figure 5.11d. Therefore, the BAPB butterfly patterns are alternatively placed to the left and to the right of a PTCDI zigzag chain. Finally the resulting pore size of the PTCDI-BAPB structure is measured as  $1.6 \times 0.9 \text{ nm}^2$ .

Thereafter, additional PTCDI molecules can be trapped in the PTCDI-BAPB porous network forming a host-guest supramolecular system. Figures 5.12a,c show that each PTCDI molecule trapped in a pore of the PTCDI-BAPB structure is placed parallel to two other PTCDI molecules, forming like a side-by-side structure (§3.2.1). Moreover

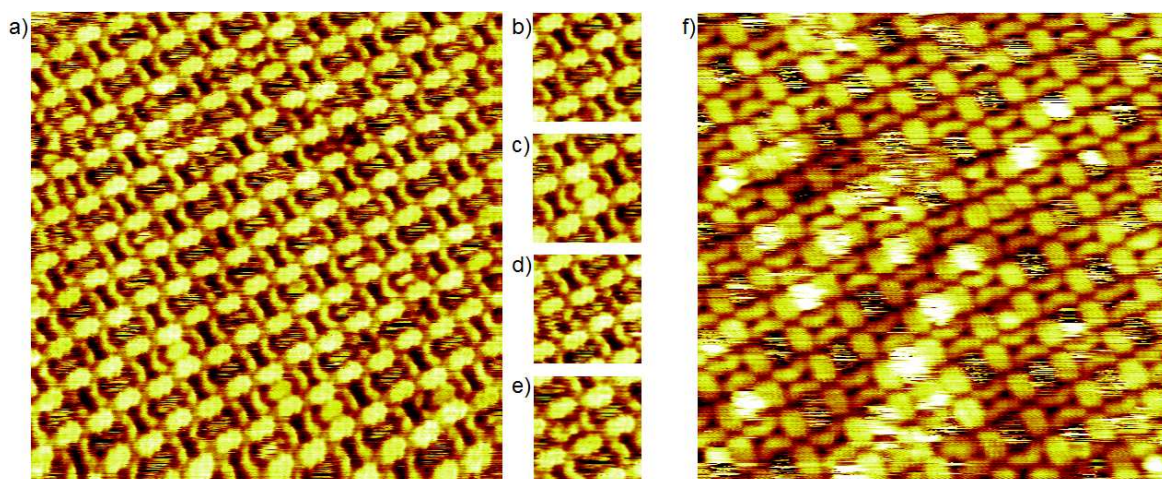


Figure 5.12: Host-guest supramolecular system formed by the BAPB molecules (i.e. truncated TAPB) with PTCDI on the Au(111) surface: (a) Wide-range STM image  $19.1 \times 19.1 \text{ nm}^2$ ;  $V_s = -311 \text{ mV}$ ,  $I_t = 374 \text{ pA}$ ; (b) Small-range STM image of the porous PTCDI-BAPB structure,  $4.3 \times 4.3 \text{ nm}^2$ ;  $V_s = -311 \text{ mV}$ ,  $I_t = 374 \text{ pA}$ ; (c) Small-range STM image of a PTCDI molecule trapped in the PTCDI-BAPB porous structure,  $4.3 \times 4.3 \text{ nm}^2$ ;  $V_s = -311 \text{ mV}$ ,  $I_t = 374 \text{ pA}$ ; (d) Small-range STM image of a BAPB molecule trapped in the PTCDI-BAPB network,  $4.3 \times 4.3 \text{ nm}^2$ ;  $V_s = -311 \text{ mV}$ ,  $I_t = 374 \text{ pA}$ ; (e) Small-range STM image of a undamaged TAPB molecule trapped in the PTCDI-BAPB porous structure  $3.8 \times 3.8 \text{ nm}^2$ ;  $V_s = -311 \text{ mV}$ ,  $I_t = 374 \text{ pA}$ ; (f) Wide-range STM image of the host-guest PTCDI-BAPB system,  $16.7 \times 16.7 \text{ nm}^2$ ;  $V_s = +911 \text{ mV}$ ,  $I_t = 984 \text{ pA}$ .

additional molecules (presumably aniline) can be trapped into the pores of the PTCDI-BAPB structure but cannot be imaged clearly at room temperature due to thermal motion, i.e. appear extremely fuzzy (Figure 5.12f). In order to unambiguously attribute the extremely fuzzy features observed in Figure 5.12f to the motion of aniline molecules trapped in the pores of the PTCDI-BAPB structure, it is needed to make further investigations at lower temperature in order to reduce the molecular motion, as it is done in many others studies [162]. Furthermore Figure 5.12d, shows that a BAPB molecule can also be trapped in a pore of the PTCDI-BAPB bi-molecular structure. Finally undamaged TAPB molecules can also be observed on the Au(111) surface as bright star-shape molecules, Figure 5.12e.

Therefore the thermally activated decomposition of the TAPB molecules into Aniline and BAPB molecules followed by the adsorption of PTCDI molecules leads to the formation of a porous molecular structure on Au(111) surface. This porous molecular architecture is stabilized through  $\text{N-H} \cdots \text{O}$  hydrogen bonds. The resulting PTCDI-BAPB porous structure acts as a template for the organization of additional molecules. Finally the results presented here show that host-guest supramolecular systems are useful tools to control the organization of additional organic molecules on metallic surfaces. As discussed before (Chapter 1), the control of molecular organization on surfaces is crucial to develop the new generation of organic nano-devices. It is the reason why in the next section I will describe some results on the control of the molecular organization

of another star-shape molecule named TCPB, which leads to the formation of another host-guest supramolecular system.

### 5.3 Single and multi-component self-assemblies based on 1,3,5-Tris (4-CarboxyPhenyl) Benzene (TCPB) molecule

Here the supramolecular self-assembly of 1,3,5-Tris(4-carboxyphenyl)benzene (TCPB) molecule on the Au(111) surface was investigated. The special flat star-shape of this molecule is particularly adapted to create two-dimensional architectures, Figure 5.14. In this section I will describe first the new close-packed molecular structures obtained after deposition of the TCPB molecules on the Au(111) surface. Secondly, I will describe the porous molecular nano-architectures formed by the TCPB molecules after annealing. Finally, I will demonstrate that the porous TCPB structure can be used as a template for the organization of additional sodium chloride compounds, and then leads to the formation of a host-guest supramolecular system.

#### 5.3.1 Compact networks of TCPB molecules on Au(111)

The chemical structure of 1,3,5-tris(4-carboxyphenyl)benzene (TCPB) molecule consists of three carboxyphenyl groups attached to a central benzene ring, Figure 5.13b. After deposition of the TCPB molecules at a temperature of 300°C during 1min, the molecules entirely cover the Au(111) surface. The star shape of the TCPB molecule is well resolved in the high resolution STM image, Figure 5.13a. The TCPB molecules oriented to the right direction are falsely colored in orange while the molecules oriented to the left direction are colored in green. Figure 5.13a shows that the TCPB molecules are forming a complex closely packed network on the gold surface kept at room temperature. The network unit-cell is parallelogram with  $A \simeq 3.8$  nm and  $B \simeq 2.9$  nm, the unit-cell parameters and an angle of  $\simeq 70^\circ$  between them. This unit-cell is drawn in white dashed line in Figure 5.13a. A scheme of the molecular network unit-cell is given in Figure 5.13b. The motif of the network unit-cell is composed of 5 molecules pointing to the right (orange color), and 5 molecules pointing to the left (green color). The TCPB molecules oriented to the right are forming a "chair" pattern in the center of the unit-cell, with the seat-back pointing upwards. In contrast the TCPB molecules oriented to the left are forming two inverted "chair" patterns on the left and right sides of the unit-cell, with the seat-back pointing down. Henceforth, this new structure will be called the "chair network". The scheme of the supramolecular structure unit-cell of Figure 5.13b, is built by considering only three different dimers stabilized through hydrogen bonds which are illustrated in Figure 5.14. The two TCPB molecules in the dimers (a) and (b) are placed in opposite directions (schematically represented by green and orange color). In the case of the dimer (a), the molecule oriented down (orange color) is slightly shifted to the right compared to the oriented up molecule (green color). In contrast for dimer (b), the molecule oriented down is slightly shifted to the left compared to the oriented

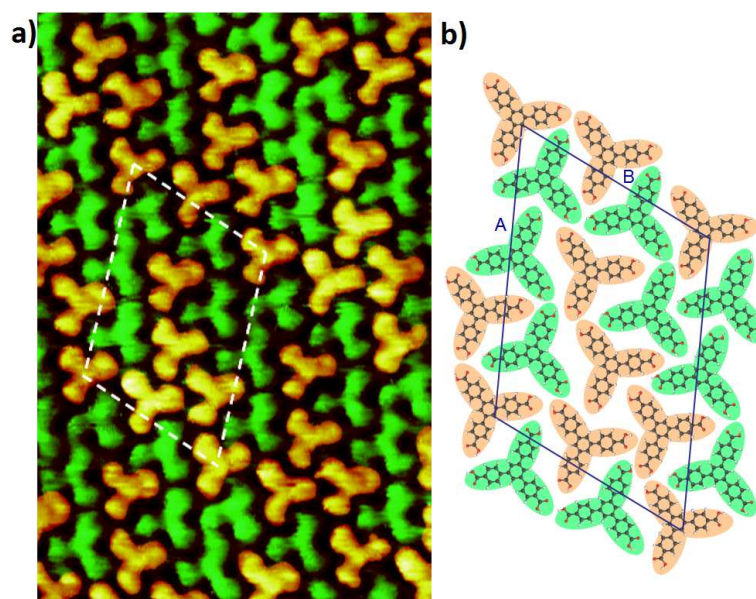


Figure 5.13: (a) STM image of the 1,3,5-Tris(4-carboxyphenyl)benzene (TCPB) "chair network" formed on Au(111) surface,  $10.8 \times 7.2 \text{ nm}^2$ ;  $V_s = +90 \text{ mV}$ ,  $I_t = 40 \text{ pA}$ . Molecules are falsely colored in orange or green according to their respective orientation (right or left). (b) Scheme of the chair network unit-cell. Carbon atoms are gray, oxygen atoms are red, and hydrogen atoms are white, respectively.

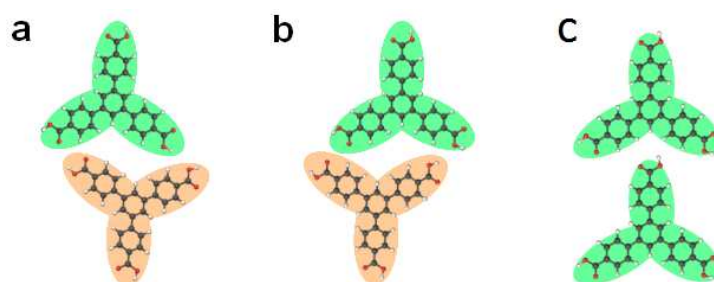


Figure 5.14: Chemical structure of the 1,3,5-tris(4-carboxyphenyl)benzene (TCPB) dimers. The dimers are built by the establishment of hydrogen bonds between carboxyl groups and hydrogen atoms of the phenyl rings. The two TCPB molecules in the dimers (a) and (b) are placed in opposite directions (represented in green and orange color respectively), while in the case of the dimer (c) these two molecules are placed in the same direction.

up molecule, Figure 5.14. These dimers are built by the establishment of  $\text{O}-\text{H} \cdots \text{O}$  and  $\text{C}-\text{H} \cdots \text{O}$  hydrogen bonds between the carboxyphenyl groups of neighboring molecules. Finally the dimer (c) is composed of two TCPB molecules oriented in the same direction. The dimer (c) is built by the formation of  $\text{C}-\text{H} \cdots \text{O}$  hydrogen bonds between the carboxyl end-group of the first molecule and hydrogen atoms of the phenyl rings of the second molecule. These three different dimers stabilized through hydrogen bonds are at the origin of the new close-packed networks observed in the work presented here.

The three TCPB molecules placed at the junction of the seat-back and leg of a "chair" pattern are linked together through dimers of type (c). However, the others TCPB molecules of the "chair network" are linked to each other by the formation of dimers of type (a) or (b). Figure 5.15 shows a large scale STM image of the supramolecular

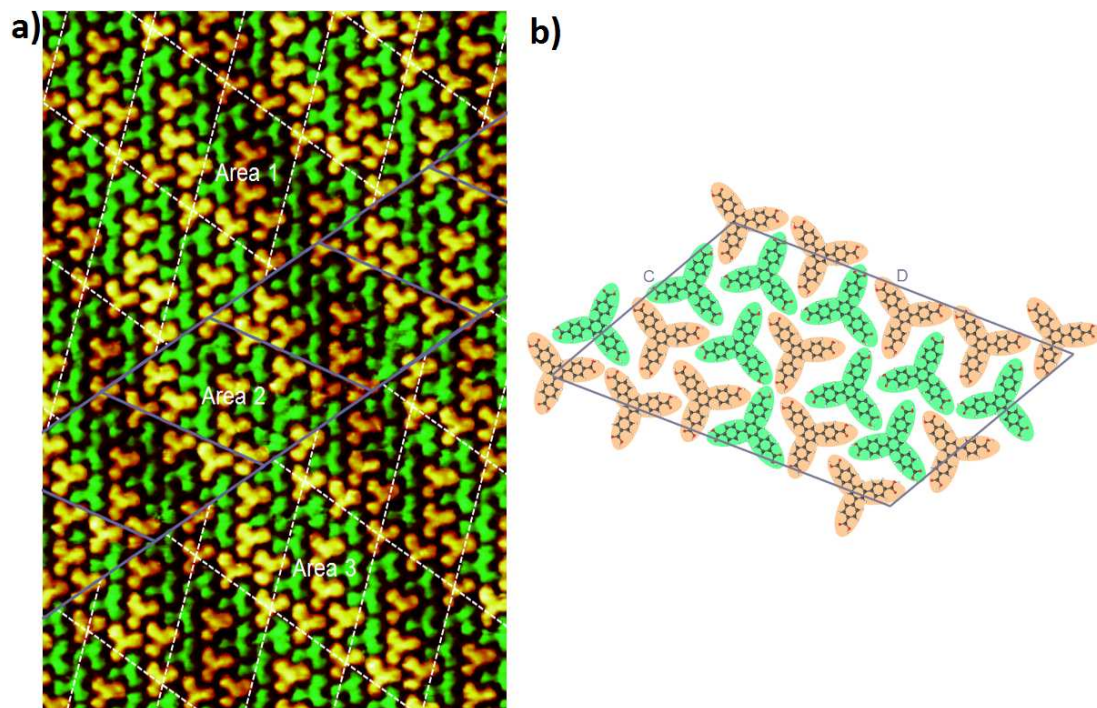


Figure 5.15: (a) Large scale STM image of the 1,3,5-Tris(4-carboxyphenyl)benzene (TCPB) network formed on Au(111) surface,  $21.6 \times 14.3 \text{ nm}^2$ ;  $V_s = +90 \text{ mV}$ ,  $I_t = 40 \text{ pA}$ . Three different phases can be distinguished on this image. The first and the third phases correspond to two chair network domains, which are slightly shifted one compared to the other. This shift is accommodated by the formation of a transition domain, which correspond to the phase 2. Molecules are colored in orange or green false color according to their respective orientation (right or left). (b) Scheme of the transition domain unit-cell. Carbon atoms are gray, oxygen atoms are red, and hydrogen atoms are white, respectively.

structure formed by the TCPB molecules on Au(111) surface kept at room temperature. Three different areas can be clearly seen on Figure 5.15a. The Area 1 and Area 3 placed at the top left corner and bottom right corner of Figure 5.15a respectively, correspond to two "chair networks" which are slightly shifted one compared to the other. The unit-cell vectors of the "chair networks" of Area 1 and Area 3 are running parallel to each other. The unit-cell of the "chair network" of Area 3 is shifted by 0.8nm along the longer axis of the "chair network" unit-cell of Area 1, i.e. the "A" axis in Figure 5.13b. A new molecular structure is observed in Area 2 at the interface of the two "chair network" of Areas 1 and 3, in order to accommodate the slight shift which exists between them. Henceforth, this new structure will be called the "transition network". A scheme of the molecular organization of this "transition network" is given in Figure 5.15b. The

"transition network" has a periodicity in only one direction which is turned by an angle of  $43^\circ$  compared to the "A" axis of the "Chair networks". The "transition network" unit-cell is parallelogram with  $C \simeq 4.0$  nm and  $D \simeq 5.5$  nm, the unit-cell parameters with an angle of  $\simeq 57^\circ$  in between, Figure 5.15b. The "transition network" unit-cell is composed of 10 molecules pointing to the right (orange color), and 10 molecules pointing to the left (green color). The unit-cell of the "transition network" is composed of two "chair patterns" formed by the TCPB molecules oriented to the right. These "chair patterns" are placed at the center and at the left border of the "transition network" unit-cell, Figure 5.15a. In addition to that the "transition network" unit-cell is composed of two inverted "chair patterns" formed by the TCPB molecules which pointing to the left (green color). These two inverted "green chair" patterns are placed around the "orange chair" pattern at the center of the network unit-cell. The "chair" pattern at the left border of the "transition network" is connected to a "chair" pattern of Area 1 through the top of its seat. However the "chair" pattern at the center of the "transition network" is connected to a "chair" pattern of Area 3 through the leg of its chair. Furthermore, the inverted "chair" pattern at the left of the "transition network" unit-cell is connected to an inverted "chair" pattern of Area 1 through the leg of its chair. In contrast the inverted "chair" pattern at the right of the "transition network" unit-cell (Area 2) is connected to an inverted "chair" pattern of Area 3 through the top of its seat.

Additionally the TCPB molecules can also form a rectangular close-packed network on the Au(111) surface kept at room temperature, Figure 5.16. A scheme of the molecu-

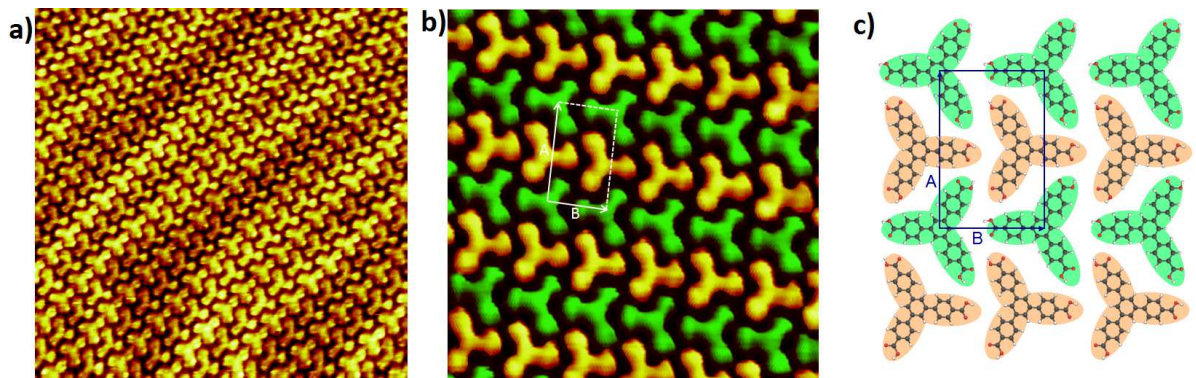


Figure 5.16: (a) STM image of the 1,3,5-Tris(4-carboxyphenyl)benzene (TCPB) rectangular network formed on Au(111) surface,  $16.7 \times 16.7$  nm<sup>2</sup>;  $V_s = +120$  mV,  $I_t = 100$  pA. (b) Zoom of the rectangular network formed on Au(111) surface,  $7.2 \times 7.2$  nm<sup>2</sup>;  $V_s = +500$  mV,  $I_t = 500$  pA. Molecules are colored in orange or green false color according to their respective orientation (right or left). (c) Scheme of the rectangular self-assembled structure unit-cell. Carbon atoms are gray, oxygen atoms are red, and hydrogen atoms are white, respectively.

lar organization of this "rectangular network" is given in Figure 5.16c. The "rectangular network" unit-cell parameters are  $E \simeq 1.9$  nm and  $F \simeq 1.1$  nm with an angle of  $\simeq 90^\circ$  between them, Figures 5.16b,c. The motif of the "rectangular network" unit-cell is composed of one TCPB molecule oriented to the right and one TCPB molecule oriented to

the left. The "rectangular network" pattern can be built by only considering the dimers (a), (b) and (c) of Figure 5.14. The TCPB molecules are forming chains which running parallel to each other. Molecules from neighboring chains are oriented in opposite directions. To distinguish these two opposite directions, the TCPB molecules are falsely colored in green and orange color according to the left and right directions respectively. The "orange" chain placed at the center of the rectangular network unit-cell is connected to the "green" chain placed at the top side of the unit-cell through the formation of dimers (a), Figure 5.14. Moreover this "orange" chain is connected to the "green" chain placed at the down side of the unit-cell through the formation of dimers (b), Figure 5.14. Each TCPB molecule of the "orange" chains are involved in a dimer (a) and in a dimer (b). These two dimers are turned by an angle of  $120^\circ$  one compared to the other, Figure 5.16b,c. Therefore the neighboring chains of the rectangular network are bond to each other by alternating dimers of types (a) and (b), Figure 5.14. Finally the TCPB molecules placed in the same chain are linked together through dimers of type (c) depicted in Figure 5.14. Furthermore, the Au(111) herringbone reconstruction remains present after molecular deposition (Figure 5.16a), suggesting weak molecules-substrate interactions.

All the structures formed by the 1,3,5-tris(4-carboxyphenyl)benzene (TCPB) molecules observed in this study (Figures 5.13, 5.15, 5.16) are stabilized by the three dimers depicted in Figure 5.14. These dimers have been observed in previous experiments for the TCPB molecules placed at the 1-phenyloctane/graphite interface [148]. However the close-packed networks obtained for the TCPB molecules at the 1-phenyloctane/graphite interface [148], are different to those observed here.

To summarize, the TCPB molecules form large scale close-packed networks at saturation coverage on the Au(111) surface kept at room temperature. The "chair network" and "rectangular network" depicted in Figures 5.13 and 5.16 respectively, totally cover the Au(111) surface without any pores. In addition to that a "transition network" is formed at the interface of two "chair network" domains, as it is shown in Figure 5.15. All the molecular architectures observed here can be built by only considering the three different dimers (a), (b) and (c) depicted in Figure 5.14. The dimers (a) and (b) are composed of two TCPB molecules placed in opposite directions, while dimers (c) is composed of two TCPB molecules placed in the same direction. These dimers are built by the establishment of hydrogen bonds between the carboxyphenyl groups of TCPB molecules. In the next paragraph I will show that a post-annealing of the sample leads to the formation of a TCPB porous molecular structure. This porous TCPB nanoarchitecture is at the origin of a host-guest supramolecular system involving sodium chloride compounds.

### 5.3.2 Host-guest supramolecular system formed by the TCPB molecules with NaCl on Au(111)

Here I have reported some results on the formation of a host-guest supramolecular system based on TCPB molecules and sodium chloride compounds. First, the 1,3,5-tris(4-carboxyphenyl)benzene molecules were evaporated at a temperature of  $390^\circ\text{C}$ ,

onto a gold surface. The sample was subsequently post-annealed at 200 °C during 1 hour. In that case TCPB molecules form a porous molecular architecture consisting of polygons of different sizes and shapes, Figure 5.17. It was observed that seven differ-

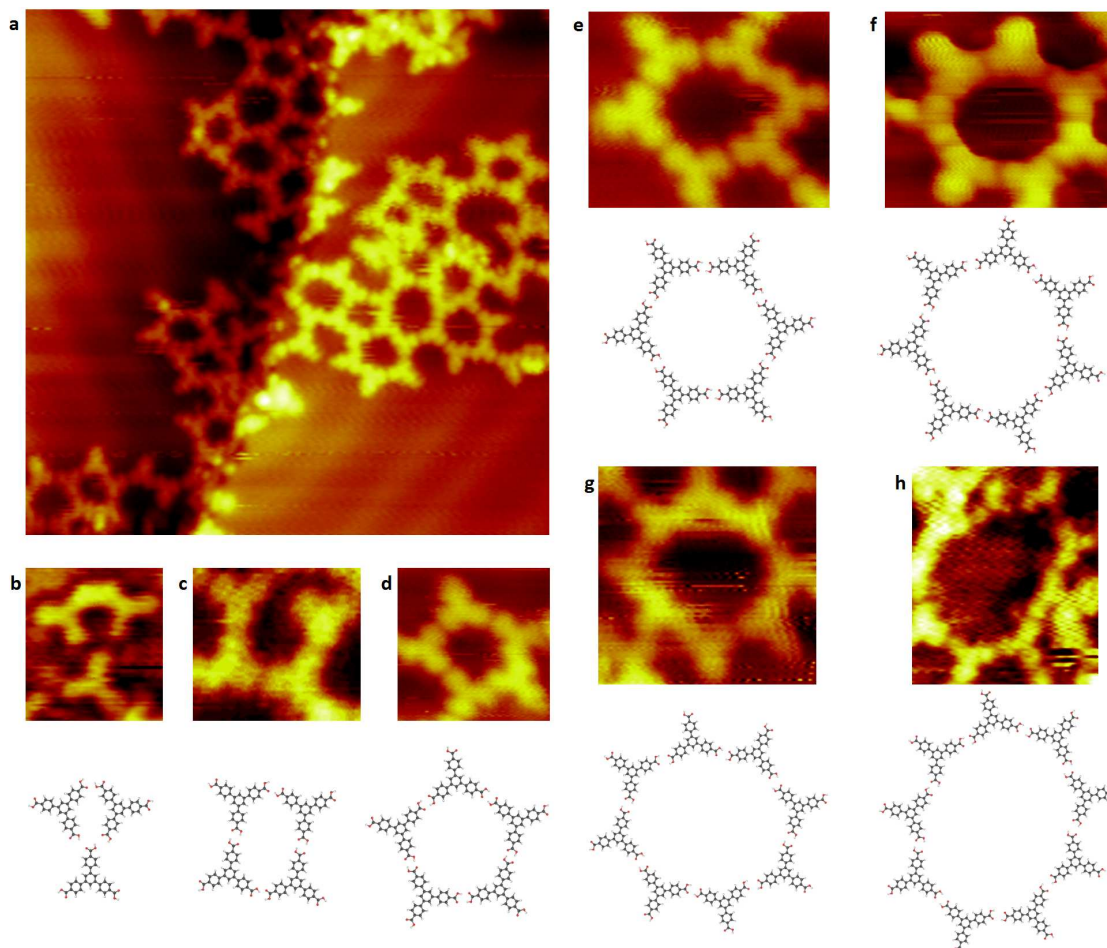


Figure 5.17: STM images and molecular models of the polygonal architectures formed by the 1,3,5-tris(4-carboxyphenyl)benzene (TCPB) molecules on the Au(111) surface: (a) Wide-range STM image,  $24 \times 24 \text{ nm}^2$ ,  $V_s = +1.90 \text{ V}$ ,  $I_t = 201 \text{ pA}$ ; (b) Small-range STM image of the TCPB triangular structure:  $2.4 \times 2.6 \text{ nm}^2$ ,  $V_s = +1.02 \text{ V}$ ,  $I_t = 511 \text{ pA}$ ; (c) The TCPB square structure:  $3.8 \times 3.3 \text{ nm}^2$ ,  $V_s = +1.61 \text{ V}$ ,  $I_t = 201 \text{ pA}$ ; (d) The TCPB pentagonal structure:  $3.8 \times 3.8 \text{ nm}^2$ ,  $V_s = +1.90 \text{ V}$ ,  $I_t = 201 \text{ pA}$ ; (e) The TCPB hexagonal structure:  $4.3 \times 3.6 \text{ nm}^2$ ,  $V_s = +1.90 \text{ V}$ ,  $I_t = 201 \text{ pA}$ ; (f) The TCPB heptagonal structure:  $4.8 \times 4.1 \text{ nm}^2$ ,  $V_s = +1.20 \text{ V}$ ,  $I_t = 401 \text{ pA}$ ; (g) The TCPB octagonal structure:  $4.8 \times 4.8 \text{ nm}^2$ ,  $V_s = +1.40 \text{ V}$ ,  $I_t = 301 \text{ pA}$ ; (h) The TCPB nonagonal structure:  $4.8 \times 5.5 \text{ nm}^2$ ,  $V_s = +1.81 \text{ V}$ ,  $I_t = 111 \text{ pA}$ .

ent kinds of polygons can be obtained from TCPB molecules. A triangular structure is formed when three TCPB molecules are linked together. A molecular model of this structure is depicted in Figure 5.17b. The triangular structure is stabilized by the formation of four  $\text{O}-\text{H} \cdots \text{O}$  hydrogen bonds between the carboxyl groups of the TCPB

molecules. The pore diameter size of the triangular structure is approximately 0.7nm. A square structure can be obtained when four TCPB molecules are linked together, Figure 5.17c. In that structure there are two TCPB molecules which are pointing upwards, and two TCPB molecules which are pointing downwards. The square structure is formed by the establishment of six O–H···O hydrogen bonds between the carboxyl groups of the TCPB molecules. Four O–H···O hydrogen bonds are formed between the TCPB molecules placed in opposite directions. However only two O–H···O hydrogen bonds are established between the TCPB molecules placed in the same direction. The pore diameter size of the TCPB square structure is around 1.3nm. A pentagonal structure is formed when five TCPB molecules are linked together, Figure 5.17d. In that case all the TCPB molecules are linked to their two nearest neighbors through four O–H···O hydrogen bonds established between their carboxyl groups. The neighboring TCPB molecules are placed in opposite directions. The pore diameter size of the pentagonal structure is around 1.7nm. In the same way, hexagonal, heptagonal, octagonal and nonagonal structures can be formed respectively when six, seven, eight, and nine TCPB molecules are linked together through their carboxyl end-groups (Figures 5.17 e,f,g,h). The pores shape of the hexagonal, heptagonal, and octagonal TCPB structures can be considered as rings possessing a pore diameter size of 1.8nm, 2.1nm and 2.4nm respectively. However the pore of the nonagonal structure can be considered as an ellipse with a major axis length of 3.5nm, and a minor axis length of 2.7nm. The TCPB polygons predominantly observed on the Au(111) surface are in descending order the hexagons and pentagons, followed by the heptagons and octagons. The less common TCPB structures observed on the gold surface are the nonagonal structures, the triangular and the square structures. Figure 5.17a shows a large scale image of the TCPB polygonal structures formed on the Au(111) surface after annealing at 200 °C. This STM image illustrates the fact that the TCPB polygonal structures are mostly observed at the step-edge. This indicates that the growth process is preferentially initiated at the step-edges. Moreover the polygonal structures formed by the TCPB molecules are crossing the step-edge without modification of their organizations. Figure 5.17a also shows that the underneath Au(111) herringbone reconstruction is undisturbed by the molecular TCPB film, indicating a weak molecule-substrate interaction.

Thereafter NaCl monomers were evaporated at a temperature of 390 °C, onto the pre-existing TCPB polygonal structures. In Figure 5.18 the TCPB molecule appears as a star-shape molecule with three bright lobes corresponding to the carboxyphenyl end-groups which cannot be differentiated of the benzene core. However, the bright protrusions which appear in the pore of the polygonal structure can be attributed to the Cl<sup>-</sup> anions of NaCl islands [116–118]. The wide-range STM image depicted in Figure 5.18a taken across a step-edge shows that almost 50% of the TCPB polygonal structures are filled by the NaCl monomers. Figures 5.18b, 5.18c, 5.18d show the molecular structures formed when 7, 9 and 12 NaCl monomers are respectively trapped in a TCPB pentagonal structure. In the same way Figures 5.18e, 5.18f, 5.18g show the host-guest systems formed when 4, 6, and 7 NaCl monomers are respectively adsorbed in the pore of a TCPB hexagonal structures. These images show that for a low NaCl:TCPB molecular ratio, the NaCl monomers are preferentially adsorbed on the internal pore side

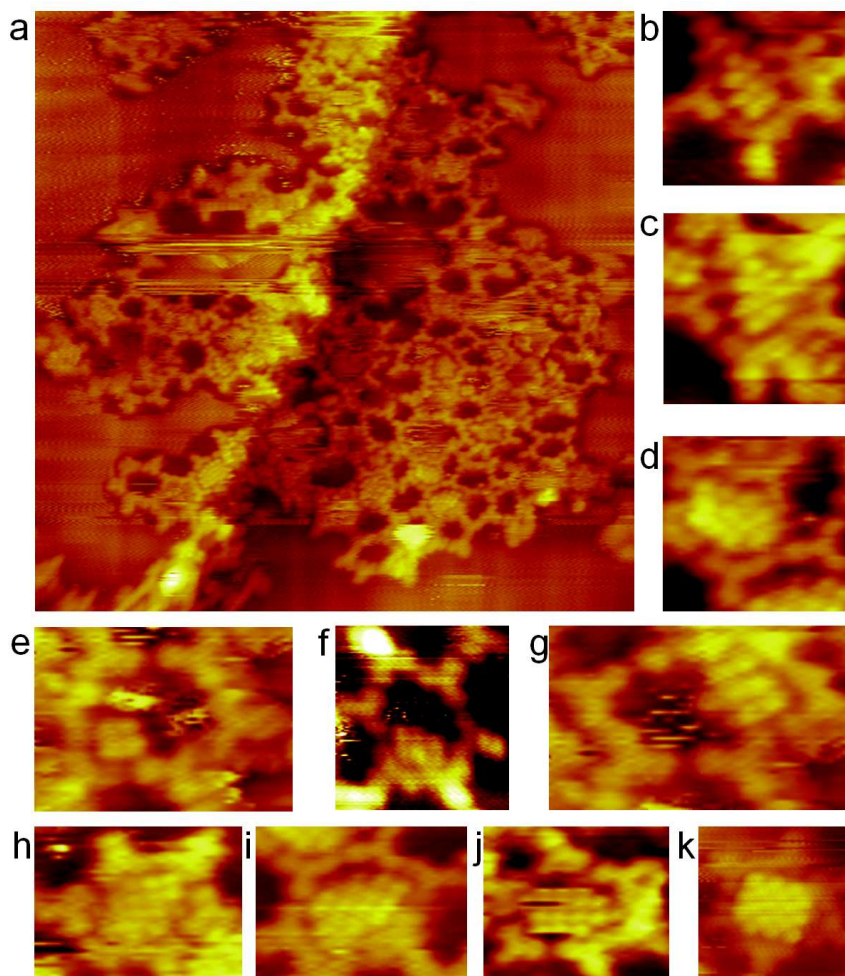


Figure 5.18: STM images of the host-guest systems formed by the TCPB polygonal structures with the sodium chloride dimers (NaCl) on the Au(111) surface: (a) Wide-range STM image,  $33.5 \times 33.5 \text{ nm}^2$ ,  $V_s = +1.40 \text{ V}$ ,  $I_t = 201 \text{ pA}$ ; (b) Architecture formed by 5 TCPB molecules and 7 NaCl monomers,  $3.1 \times 2.9 \text{ nm}^2$ ,  $V_s = +1.40 \text{ V}$ ,  $I_t = 201 \text{ pA}$ ; (c) Architecture formed by 5 TCPB molecules and 9 NaCl monomers,  $2.9 \times 2.9 \text{ nm}^2$ ,  $V_s = +1.40 \text{ V}$ ,  $I_t = 201 \text{ pA}$ ; (d) Architecture formed by 5 TCPB molecules and 12 NaCl monomers,  $2.9 \times 2.6 \text{ nm}^2$ ,  $V_s = +1.40 \text{ V}$ ,  $I_t = 201 \text{ pA}$ ; (e) Architecture formed by 6 TCPB molecules and 4 NaCl monomers,  $4.3 \times 3.3 \text{ nm}^2$ ,  $V_s = +1.40 \text{ V}$ ,  $I_t = 201 \text{ pA}$ ; (f) Architecture formed by 6 TCPB molecules and 6 NaCl monomers,  $3.8 \times 4.1 \text{ nm}^2$ ,  $V_s = +1.00 \text{ V}$ ,  $I_t = 201 \text{ pA}$ ; (g) Architecture formed by 6 TCPB molecules and 7 NaCl monomers,  $4.3 \times 2.9 \text{ nm}^2$ ,  $V_s = +1.40 \text{ V}$ ,  $I_t = 201 \text{ pA}$ ; (h) Architecture formed by 6 TCPB molecules and 14 NaCl monomers,  $3.8 \times 2.9 \text{ nm}^2$ ,  $V_s = +1.40 \text{ V}$ ,  $I_t = 201 \text{ pA}$ ; (i) Architecture formed by 6 TCPB molecules and 15 NaCl monomers,  $3.3 \times 2.9 \text{ nm}^2$ ,  $V_s = +1.40 \text{ V}$ ,  $I_t = 201 \text{ pA}$ ; (j) Architecture formed by 6 TCPB molecules and 16 NaCl monomers,  $3.3 \times 2.9 \text{ nm}^2$ ,  $V_s = +1.40 \text{ V}$ ,  $I_t = 201 \text{ pA}$ ; (k) Architecture formed by 6 TCPB molecules and 18 NaCl monomers,  $3.8 \times 3.8 \text{ nm}^2$ ,  $V_s = +1.20 \text{ V}$ ,  $I_t = 811 \text{ pA}$ .

of the TCPB polygonal structure. This indicates that the interactions between NaCl monomers and the sides of the TCPB molecules are attractive. Moreover after successive scans of the same area with the STM tip, it was not possible to observe any motion of the NaCl islands inside the pores of the TCPB polygonal structures. Figures 5.18h, 5.18i, 5.18j, and 5.18k, show the molecular structures formed when 14, 15, 16, and 18 NaCl monomers are respectively trapped in the pore of a TCPB hexagonal structure. No NaCl monomer was observed on top of the TCPB molecules, indicating that NaCl monomers are preferentially adsorbed in the pores of the TCPB molecular film.

The lattice parameter of the NaCl islands as well as the distance measured between two nearby chloride atoms trapped in TCPB polygons, are equivalent to those obtained for isolated NaCl islands grown on bare Au(111) surface, i.e. around 5.6Å and 3.9Å respectively (see §4.1.2). This means that the stacking of the NaCl islands is undisturbed by the presence of the TCPB molecules. However, the NaCl islands cannot cross the TCPB polygonal structures. It means that the NaCl islands remain trapped in the pores formed by the TCPB polygons. Therefore the porous TCPB nano-architectures act as templates for the NaCl islands growth by creating preferential adsorption sites on the substrate. Finally, the deposition of NaCl monomers does not affect the organization of the pre-existing TCPB molecular film. This indicates that the O–H···O hydrogen bonds established between the carboxyl end-groups of the TCPB molecules are strong enough to prevent reorganization of the TCPB polygonal structures after NaCl deposition.

The distance between two TCPB molecules, was measured by considering the central benzene core of the molecules. In that way, the center-to-center distance obtained is around 1.5nm. Rico Gutzler *et al.*, have deposited the 1,3,5-tris(4-bromophenyl)benzene molecules on the Cu(111) surface and then annealed the sample at 300° in order to dissociate the bromine atoms from the molecular core, leading to the formation of radicals at the terminal end-groups. This finally resulting in the formation of covalently bound polygonal structures, which look like similar to the polygonal structure observed in our system (depicted in Figure 5.17). But the center-to-center distance between two molecules, obtained for this covalently bound structure is equal to 1.24nm; which is relatively small compared to the value of 1.5nm observed in our case (Figure 5.17). This difference can be explained by the fact that the dissociation of the carboxyl end-groups from the triphenylbenzene core will not occur in our experiment, even after a post-annealing at 200° C.

To summarize, after annealing at 200 °C the TCPB molecules can form many polygonal structures on the Au(111) surface leading to a porous supramolecular architecture. The most commonly observed polygons are the hexagons and pentagons which are respectively constituted of 6 and 5 TCPB molecules linked through their carboxyphenyl end-groups. I have shown that the porous nano-architectures formed by the TCPB molecules can be used as templates for the organization of additional sodium chloride compounds on the Au(111) surface. Indeed the presence of the underlying TCPB molecular structure creates preferential adsorption sites where small NaCl islands grow and remain localized in the pores of the polygonal structures. This opens new possibilities in the field of nano-electronics where the growth of perfectly organized insulating thin

films is of prime importance.

## Chapter Conclusions

In this chapter I have shown that molecular organization can be controlled through many parameters, like the molecular skeleton and substituents used, as well as the sample's temperature (§5.3). First of all, I have shown that the molecular organization of DNA bases and perylene derivatives can be controlled by a precise choice of the molecular substituents used (§5.1.2, and §5.1.3). Thereafter I have shown that the molecular organization can be controlled by mixing different kinds of molecular species, like in the case of PTCDA-Adenine and PTCDI-Adenine bi-molecular nano-architectures (§5.2.1, and §5.2.2 respectively). Moreover I have shown that the host-guest supramolecular systems, are useful tools to control the organization of molecular entities on surfaces. In fact TCPB porous polygonal structures can be used to control the shape and the size of additional NaCl islands (§5.3.2). In the same way, porous PTCDI-BAPB structure can be used to control the organization of additional PTCDI molecules on the Au(111) surface (§5.2.3). Finally the interaction between the STM tip and the molecular film can be used to transform the PTCDI-Adenine network into a PTCDI zigzag structure (§5.2.2). In the same way the tip-molecule interaction can be used to expand a PTCDI triple-chain structure by reducing the typical canted structure (§5.2.2). Therefore, the results shown in this chapter constitute a first step in the understanding of the key parameters driving the molecular organization on surfaces. In the end, this is of prime importance in order to develop useful and low-cost organic and electronic self-assembled nano-devices.

# General Conclusions

During my PhD thesis, I have investigated the structure and electronic properties of organic self-assembled nano-architectures by using Scanning Tunneling Microscopy and X-ray Photoemission Spectroscopy (see Chapter 2). These experiments allowed to show that a strong relation exists between the structure and the electronic properties of the organic thin films. For example in chapter 3, we have demonstrated that the intermolecular electronic coupling between PTCDI molecules can be modified by controlling molecular organization. Indeed, strong intermolecular electronic coupling appears between PTCDI molecules packed side-by-side. This strong intermolecular electronic coupling is not observed in the typical PTCDI canted structure obtained at room temperature on the Au(111) surface. In addition to that, by using X-ray photoemission spectroscopy I showed that the line-shape and energy levels alignment of the valence-band, NEXAFS, core-level and RPES spectra of a PTCDI film grown on Au(111) depend strongly of the molecular film thickness. The strong modification of the resonance peak intensity of the PTCDI RPES spectra with molecular coverage demonstrate that a fast charge transfer (below 6fs) occurs at the PTCDI/Au(111) interface at the sub-monolayer range (§3.6). Moreover, by comparing our results on PTCDI with previous works [42] on other perylene derivatives, it clearly appears that the molecular substituents play an important role in the sample's electronic properties, i.e. line-shape and energy levels alignment. Thereafter, I described how the molecular organization can be controlled through a few number of key parameters forming like a toolbox. For example, a useful tool to control molecular organization is the host-guest supramolecular system which can be used as a template for the adsorption of additional molecules. It is what I showed in §5.2.3 and §5.3.2, where the PTCDI-BAPB and TCPB porous structures have been employed to create preferential adsorption sites for additional PTCDI molecules and NaCl monomers respectively. Another possibility to control molecular organization is to mix different kinds of molecular species, as shown in Chapter 4 and §5.1.2 where new PTCDI-NaCl, PTCDI-Adenine and PTCDA-Adenine multi-components nano-architectures have been constructed. Furthermore, the control of the sample's temperature is also a useful tool to tuned molecular organization at the nanometer scale. It is what I showed in Chapter 4, where four bi-molecular nano-architectures based on PTCDI and NaCl compounds were obtained by post-annealing the sample at several temperatures. Finally by comparing the molecular structure obtained with two DNA bases called adenine and guanine, it is possible to deduce that the replacement of molecular substituents can strongly modify the resulting self-assembly, even if the molecular skeleton remains the same (see §5.1.2). In the same way, by comparing the structure of the self-assembled network obtained with

two perylene derivative called PTCDI and PTCDA, it clearly appears that the change of only one functional group can strongly affect molecular organization (see §3.2.1 and §5.1.3). Additionally, the interaction between the STM tip and the molecular film can be used to modify the molecular organization on surfaces. Indeed, successive scans with the STM tip on the same sample area, can lead to a shape modification of the PTCDI-NaCl structures formed at room temperature on the gold substrate (§4.2.1). In the same way, the tip-molecule interaction can be used to transform a PTCDI-Adenine bimolecular structure into a single-component PTCDI zigzag structure (§5.2.2). Similarly, after successive scans a PTCDI triple-chains structure can be expanded by displacing some PTCDI molecules of the surrounding canted structure (§5.2.2). To conclude, I showed some particular cases where the molecular organization on surfaces can be controlled by choosing the molecular skeleton and substituents used, as well as by adjusting the sample's temperature or by using host-guest and multi-components systems. Moreover I showed that the electronic properties of a PTCDI thin film strongly depends on molecular organization. These results constitute a first step in the understanding and control of the formation of organic self-assembled monolayers (SAMs). The creation of perfectly organized SAMs with desired structure and physical properties is one of the most interesting ways to develop the new generation of organic devices (Chapter 1). Indeed SAMs promise to have many industrial applications like in organic photovoltaic devices, as well as in high density magnetic data storage devices, or in flexible screen and luminescent wallpaper.

# Acknowledgements

First, I would like to acknowledge François Daviaud, Patrice Roche, Serge Palacin, and Luc Barbier for the organisation of the scientific activity of the SPEC and SPCSI departments, where I had the chance to work. I would like to acknowledge my PhD supervisor, Fabien Silly to give me the opportunity to do my PhD in his team. I would like also to acknowledge Mathieu Silly for its hard work and the great help that he gave me during the synchrotron experiments. Additionally I would like to thank, all the members of the jury for taking the time to evaluate my work. More broadly, I would like to thank all the people who help me during my PhD. In particular I would like to acknowledge Yannick Dappe and Claire Mathieu for their fruitful scientific discussions. I would like also to thank Silvain Latil and Ludovic Tortech who give me the opportunity to teach quantum mechanics and polymeric materials at the Ecole Centrale of Paris, and Paris-Sud University. Teaching become a real passion for me, I think that the transmission of knowledge is one of the most beautiful things in the world. It is the reason why I would like to thank them warmly to give me this chance and to give me this real breath of fresh air which is so important for making a successful PhD. Likewise, I would like to acknowledge Jean-Baptiste Moussy for his valuable advice on molecular growth, as well as for the great enthusiasm and interest he showed for my STM work. In addition I would like to thank all the technical staff of the department: Christophe Lubin, Frédéric Merlet, Silvain Fouquart, Thierry Bernard, Bruno Delomez, Dominique Martinotti, and Bruno Lectar. Thereafter I would like to express gratitude to Catherine Julien and Christine Prigian for their administrative work. In addition to that I would like to thank all the PhD students for their friendship and support, especially Jonathan Bares, Marina Barlet, Sara Gonzales, Dongzhe Li, David Peyrot, Maxime Rioult, Vincent Barth. . .

Finally I would like to thank all my family, and particularly my parents and my brother, who help me during all my studies, and without whom this would not have been possible. To everyone I have not mentioned or accidentally forget, I want to say: THANK YOU.

# Remerciements

Je voudrais tout d'abord remercier François Daviaud, Patrice Roche, Serge Palacin, et Luc Barbier pour avoir si bien organisé la vie scientifique et administrative des services du SPEC et du SPCSI dans lesquels j'ai eu la chance de travailler. Je voudrais remercier mon directeur de thèse, Fabien Silly de m'avoir permis d'effectuer une thèse au CEA Saclay. Je veux aussi remercier l'énorme travail et la très grande aide que m'a apportée Mathieu Silly en ce qui concerne les expériences synchrotrons que nous avons menées durant ma thèse. Je voudrais remercier tous les membres du jury qui ont accepté de prendre de leur temps afin d'évaluer mon travail de thèse. Je voudrais également remercier toutes les personnes qui m'ont aidé durant ma thèse. Je pense notamment à Yannick Dappe et Claire Mathieu qui m'ont apporté de bons conseils scientifiques et qui sont également devenu pour moi des amis. Je voudrais également remercier Silvain Latil et Ludovic Tortech qui m'ont permis de délivrer des enseignements de mécanique quantique et de matériaux polymères à l'école centrale de Paris ainsi qu'à l'Université Paris-Sud. Enseignements pour lesquels je me suis vraiment pris de passion, j'estime que la transmission du savoir est une des plus belles choses qui soient. Je veux donc ici les remercier de m'avoir offert cette chance et cette réelle bouffée d'oxygène nécessaire à une thèse réussie. Je voudrais aussi remercier Jean-Baptiste Moussy pour ses précieux conseils d'expert en croissance, et pour la réalisation de certains de nos échantillons, ainsi que pour son grand enthousiasme et son intérêt porté sur mon travail d'imagerie STM. Je ne voudrais pas non plus oublier de remercier tout le support technique que m'ont apporté Christophe Lubin, Frédéric Merlet, Silvain Fouquart, Thierry Bernard, Bruno Delomez, Dominique Martinotti et Bruno Lectar. Je ne veux pas non plus oublier l'énorme et très important travail de secrétariat que m'ont apporté Catherine Julien et Christine Prigian. Mais aussi je voudrais remercier mes collègues doctorants pour leur amitié et leurs soutiens, notamment Jonathan Bares, Marina Barlet, Sara Gonzales, Dongzhe Li, David Peyrot, Maxime Rioult, Vincent Barth et tous les autres. . . Enfin je voudrais remercier toute ma famille et plus particulièrement mes parents et mon frère, qui m'ont soutenu pendant ces huit années d'études et sans qui tout cela n'aurait pas été possible. À tous ceux que je n'ai pas cités, ou malencontreusement oublié je voudrais vous dire: MERCI.

# Bibliography

- [1] M. Wautelet. *Les Nanotechnologies*. Dunod, 2003.
- [2] G. Schull. *Dynamique d'autoassemblages moléculaires bidimensionnels*. PhD thesis, Ecole normale supérieure de Cachan, 2006.
- [3] J-M. Lehn. *La chimie supramoléculaire*. De Boeck, 1997.
- [4] A. Rochefort, Y. Makoudi, A. Maillard, J. Jeannoutot, J. Blier, F. Chérioux, and F. Palmino. Anisotropic growth of the thiophene-based layer on Si(111)-B. *Chemical Communications*, 50:5484–5486, 2014.
- [5] S.V. Snegir, O.L. Kapitanchuk, E. Lacaze, and A. Marchenko. STM study of self-organization of 10CB molecules on Au(111) surface. *Molecular Crystals and Liquid Crystals*, 589:90–95, 2014.
- [6] N. Katsonis, E. Lacaze, and B.L. Feringa. Molecular chirality at fluid/solid interfaces: expression of asymmetry in self-organised monolayers. *Journal of Materials Chemistry*, 18:2065–2073, 2008.
- [7] S.V. Snegir, A.A. Marchenko, P. Yu, F. Maurel, O.L. Kapitanchuk, S. Mazerat, M. Lepeltier, A. Léaustic, and E. Lacaze. STM observation of open- and closed-ring forms of functionalized diarylethene molecules self-assembled on a Au(111) surface. *The Journal of Physical Chemistry Letters*, 2:2433–2436, 2011.
- [8] B. Zappone, E. Lacaze, H. Hayeb, M. Goldmann, N. Boudet, P. Barois, and M. Alba. Self-ordered arrays of linear defects and virtual singularities in thin smectic-A films. *Soft Matter*, 7:1161–1167, 2011.
- [9] M.G. Silly, S. Blanchandin, F. Sirotti, F. Lux, S. Chevreux, G. Lemercier, and F. Charra. Evidence of mixed-valence hydrated europium-chloride phase in vacuum by means of optical and electronic spectroscopies. *The Journal of Physical Chemistry C*, 117:9766–9771, 2013.
- [10] C. Pereira-Nabais, J. Światowska, A. Chagnes, A. Gohier, S. Zanna, A. Seyeux, P. Tran-Van, C-S. Cojocar, M. Cassir, and P. Marcus. Insight into the solid electrolyte interphase on Si nanowires in Lithium-Ion battery: Chemical and morphological modifications upon cycling. *The Journal of Physical Chemistry C*, 118:2919–2928, 2014.

- [11] J.V. Barth. Molecular architectonic on metal surfaces. *Annual Revue of Physical Chemistry*, 58:375–407, 2007.
- [12] J.V. Barth. Transport of adsorbates at metal surfaces: from thermal migration to hot precursors. *Surface Science Reports*, 40:75–149, 2000.
- [13] L.J. Lauhon and W. Ho. Single molecule thermal rotation and diffusion: Acetylene on Cu(001). *Journal of Chemical Physics*, 111:5633–5636, 1999.
- [14] N. Pottier. *Physique statistique hors d'équilibre*. EDP Sciences , CNRS Editions, 2007.
- [15] W. Xiao, X. Feng, P. Ruffieux, O. Groning, K. Mullen, and R. Fasel. Self-assembly of chiral molecular honeycomb networks on Au(111). *Journal of American Chemical Society*, 130:8910–8912, 2008.
- [16] H. Liang, Y. He, Y. Ye, X. Xu, F. Cheng, W. Sun, X. Shao, Y. Wang, J. Li, and K. Wu. Two-dimensional molecular porous networks constructed by surface assembling. *Coordination Chemistry Reviews*, 253:2959–2979, 2009.
- [17] L. Grill, M. Dyer, L. Lafferentz, M. Persson, M.V. Peters, and S. Hecht. Nano-architectures by covalent assembly of molecular building blocks. *Nature*, 2:687–691, 2007.
- [18] S. Stepanow, N. Lin, D. Payer, U. Schlickum, F. Klappenberger, G. Zoppellaro, M. Ruben, H. Brune, J.V. Barth, and K. Kern. Surface-assisted coordination chemistry: 2D metal organic assemblies exhibiting three-fold symmetry. *Angewandte Chemie International Edition*, 46:710–713, 2007.
- [19] M.A. Lingenfelder, H. Spillmann, A. Dmitriev, S. Stepanow, N. Lin, J.V. Barth, and K. Kern. Towards surface-supported supramolecular architectures: Tailored coordination assembly of 1,4-Benzenedicarboxylate and Fe on Cu(100). *Chemistry - A European Journal*, 10:1913–1919, 2004.
- [20] Y. Makoudi, F. Palmino, M. Arab, E. Duverger, and F. Chérioux. Complete supramolecular self-assembled adlayer on a silicon surface at room temperature. *Journal of the American Chemical Society*, 130:6670–6671, 2008.
- [21] G. Pawin, K.L. Wong, K-Y. Kwon, and L. Bartels. A homomolecular porous network at a Cu(111) surface. *Science*, 313:961–962, 2006.
- [22] C.R. van den Brom, I. Arfaoui, T. Cren, B. Hessen, T.T.M. Palstra, J.T.M. De Hosson, and P. Rudolf. Selective immobilization of nanoparticles on surfaces by molecular recognition using simple multiple H-bonding functionalities. *Advanced Functional Materials*, 17:2045–2052, 2007.
- [23] F. Silly, A.Q. Shaw, M.R. Castell, G.A.D. Briggs, M. Mura, N. Martsinovich, and L.N. Kantorovich. Melamine structures on the Au(111) surface. *The Journal of Physical Chemistry C*, 112:11476–11480, 2008.

- [24] A. Dmitriev, N. Lin, J. Weckesser, J.V. Barth, and K. Kern. Supramolecular assemblies of trimesic acid on a Cu(100) surface. *The Journal of Physical Chemistry B*, 106:6907–6912, 2002.
- [25] F. Silly, A.Q. Shaw, M.R. Castell, and G.A.D. Briggs. A chiral pinwheel supramolecular network driven by the assembly of PTCDI and melamine. *Chemical Communications*, 16:1907–1909, 2008.
- [26] M. Ruben, D. Payer, A. Landa, A. Comisso, C. Gattinoni, N. Lin, J-P. Collin, J-P. Sauvage, A. De Vita, and K. Kern. 2D supramolecular assemblies of benzene-1,3,5-triyl-tribenzoic acid: Temperature-induced phase transformations and hierarchical organization with macrocyclic molecules. *Journal of the American Chemical Society*, 128:15644–15651, 2006.
- [27] D. Payer, A. Comisso, A. Dmitriev, T. Strunskus, N. Lin, C. Wöll, A. DeVita, J.V. Barth, and K. Kern. Ionic hydrogen bonds controlling two-dimensional supramolecular systems at a metal surface. *Chemistry - A European Journal*, 13:3900–3906, 2007.
- [28] F. Silly, A.Q. Shaw, K. Porfyrakis, G.A.D. Brigg, and M.R. Castell. Pairs and heptamers of C<sub>70</sub> molecules ordered via PTCDI-melamine supramolecular networks. *Applied Physics Letters*, 91:1–3, 2007.
- [29] M. Stöhr, M. Wahl, C.H. Galka, T. Riehm, T.A. Jung, and L.H. Gade. Controlling molecular assembly in two dimensions: The concentration dependence of thermally induced 2D aggregation of molecules on a metal surface. *Angewandte Chemie International Edition*, 44:7394–7398, 2005.
- [30] Y. Wang, S. Fabris, T.W. White, F. Pagliuca, P. Moras, M. Papagno, D. Topwal, P. Sheverdyeva, C. Carbone, M. Lingenfelder, T. Classen, K. Kern, and G. Costantini. Varying molecular interactions by coverage in supramolecular surface chemistry. *Chemical Communications*, 48:534–536, 2012.
- [31] T. Yokoyama, S. Yokoyama, T. Kamikado, Y. Okuno, and S. Mashiko. Selective assembly on a surface of supramolecular aggregates with controlled size and shape. *Nature*, 413:619–621, 2001.
- [32] J.V. Barth, H. Brune, and G. Ertl. Scanning tunneling microscopy observations on the reconstructed Au(111) surface: Atomic structure, long-range superstructure, rotational domains, and surface defects. *Physical Review B*, 42:9307–9318, 1990.
- [33] U. Harten, A.M. Lahee, J. Peter Toennies, and C. Wöll. Observation of a soliton reconstruction of Au(111) by high-resolution helium-atom diffraction. *Physical Review Letters*, 54:2619–2622, 1985.
- [34] C. Wöll, S. Chiang, R.J. Wilson, and P.H. Lippel. Determination of atom positions at stacking-fault dislocations on Au(111) by scanning tunneling microscopy. *Physical Review B*, 39:7988–7991, 1988.

- [35] F. Silly, A.Q. Shaw, G.A.D. Briggs, and M.R. Castell. Epitaxial ordering of a perylenetetracarboxylic diimide-melamine supramolecular network driven by the Au(111)-(22x $\sqrt{3}$ ) reconstruction. *Applied Physics Letters*, 92:1–3, 2008.
- [36] J.A. Theobald, N.S. Oxtoby, M.A. Phillips, N.R. Champness, and P.H. Beton. Controlling molecular deposition and layer structure with supramolecular surface assemblies. *Nature*, 424:1029–1031, 2003.
- [37] B. Baris, J. Jeannoutot, V. Luzet, F. Palmino, A. Rochefort, and F. Chérioux. Noncovalent bicomponent self-assemblies on a silicon surface. *ACS Nano*, 6:6905–6911, 2012.
- [38] D. Bonifazi, H. Spillmann, A. Kiebele, M. de Wild, P. Seiler, F. Cheng, H-J. Guntherodt, T. Jung, and F. Diederich. Supramolecular patterned surfaces driven by cooperative assembly of C<sub>60</sub> and porphyrins on metal substrates. *Angewandte Chemie International Edition*, 43:4759–4763, 2004.
- [39] L. Sanchez, R. Otero, J.M. Gallego, R. Miranda, and N. Martin. Ordering fullerenes at the nanometer scale on solid surface. *Chemical Reviews*, 109:2081–2091, 2009.
- [40] M. Stöhr, M. Wahl, H. Spillmann, L.H. Gade, and T.A. Jung. Lateral manipulation for the positioning of molecular guests within the confinements of a highly stable self-assembled organic surface network. *Small*, 3:1336–1340, 2007.
- [41] E. Mena-Osteritz and P. Bäuerle. Complexation of C<sub>60</sub> on a cyclothiophene monolayer template. *Advanced Materials*, 18:447–451, 2006.
- [42] D.R.T. Zahn, G.N. Gavrilin, and G. Salvati. Electronic and vibrational spectroscopies applied to organic/inorganic interfaces. *Chemical Reviews*, 107:1161–1232, 2007.
- [43] J.B. Gustafsson, H.M. Zhang, E. Moons, and S.O. Johansson. Electron spectroscopy studies of PTCDA on Ag/Si(111). *Physical Review B*, 75:1–10, 2007.
- [44] A.P. Dementjev, A. de Graaf, M.C.M. van de Sanden, K.I. Maslakov, A.V. Naumkin, and A.A. Serov. X-ray photoelectron spectroscopy reference data for identification of the C<sub>3</sub>N<sub>4</sub> phase in carbon-nitrogen films. *Diamond and Related Materials*, 75:1904–1907, 2000.
- [45] L. Cao, Y-Z. Wang, T-X. Chen, W-H. Zhang, X-J. Yu, K. Ibrahim, J-O. Wang, H-J. Qian, F-Q. Xu, D-C. Qi, and A.T.S. Wee. Charge transfer dynamics of 3,4,9,10-perylene-tetracarboxylicdianhydride molecules on Au(111) probed by resonant photoemission spectroscopy. *Journal of Chemical Physics*, 135:1–7, 2011.
- [46] M. Mura, X. Sun, F. Silly, H.T. Jonkman, G.A.D. Briggs, M.R. Castell, and L.N. Kantorovich. Experimental and theoretical analysis of H-bonded supramolecular assemblies of PTCDA molecules. *Physical Review B*, 81:1–11, 2010.

- [47] K. Glockler, C. Seidel, A. Soukopp, M. Sokolowski, E. Umbach, M. Böhringer, R. Berndt, and W.D. Schneider. Highly ordered structures and submolecular scanning tunnelling microscopy contrast of PTCDA and DM-PBDCI monolayers on Ag(111) and Ag(110). *Surface Science*, 405:1–20, 1998.
- [48] V.Y. Aristov, O.V. Molodtsova, V. Maslyuk, D.V. Vyalikh, V.M. Zhilin, Y.A. Ossipyan, T. Bredow, I. Mertig, and M. Knupfer. Electronic structure of pristine CuPc: Experiment and calculations. *Applied Surface Science*, 254:20–25, 2007.
- [49] P. Vilmercati, D. Cvetko, A. Cossaro, and A. Morgante. Heterostructured organic interfaces probed by resonant photoemission. *Surface Science*, 603:1542–1556, 2009.
- [50] A. Föhlisch, P. Feulner, F. Hennies, A. Fink, D. Menzel, D. Sanchez-Portal, P.M. Echenique, and W. Wurth. Direct observation of electron dynamics in the attosecond domain. *Nature*, 436:373–376, 2005.
- [51] W. Chen, L. Wang, C. Huang, T.T. Lin, X.Y. Gao, K.P. Loh, Z.K. Chen, and A.T.S. Wee. Effect of functional group (fluorine) of aromatic thiols on electron transfer at the molecule-metal interface. *Journal of the American Chemical Society*, 128:935–939, 2006.
- [52] L. Aigouy, Y. De Wilde, and C. Frétigny. *Les nouvelles microscopies, à la découverte du nanomonde*. Belin, 2006.
- [53] C.J. Chen. *Introduction to Scanning Tunneling Microscopy*. Oxford university press, 1993.
- [54] B. Heinrich. *Tunneling spectroscopy of nanoscale objects: from metallic islands to single atoms and molecules*. PhD thesis, Université de Strasbourg, 2010.
- [55] J.A. Appelbaum, W.F. Brinkmann, E. Jouguelet, and C. Dennis. Theory of many-body effects in tunnelling. *Physical Review*, 186:464–470, 1969.
- [56] C. Mathieu. *Approche intégrée "Spectroscopies électroniques et Calculs ab-initio d'états de coeur excités" des modes d'adsorption de l'ammoniac et de diamines sur la surface Si(001)-2x1*. PhD thesis, Université Pierre et Marie Curie, 2009.
- [57] C.R. Brundle. Elucidation of surface structure and bonding by photoelectron spectroscopy? *Surface Science*, 48:99–136, 1975.
- [58] J. Rault. *Chemical and Electronic Structure of the Metal-Ferroelectric Interface as a Function of Ferroelectric Polarization*. PhD thesis, Université Pierre et Marie Curie, 2013.
- [59] L. Caillard, O. Seitz, P.M. Campbell, R.P. Doherty, A-F. Lamic-Humblot, E. Lacaze, Y.J. Chabal, and O. Pluchery. Gold nanoparticles on oxide-free silicon–molecule interface for single electron transport. *Langmuir*, 29:5066–5073, 2013.

- [60] M.R. Tchalala, H. Enriquez, A.J. Mayne, A. Kara, S. Roth, M.G. Silly, A. Bendounan, F. Sirotti, T. Greber, B. Aufray, G. Dujardin, M. Ait Ali, and H. Oughaddou. Formation of one-dimensional self-assembled silicon nanoribbons on Au(110)-(2x1). *Applied Physics Letters*, 102:1–5, 2013.
- [61] M. El Kazzi. *Etude par photoémission (XPS et XPD) d’heterostructure d’oxydes fonctionnels épitaxiés sur silicium*. PhD thesis, Ecole Centrale de Lyon, 2007.
- [62] J. Taborski, P. Väterlein, H. Dietz, U. Zimmermann, and E. Umbach. NEXAFS investigations on ordered adsorbate layers of large aromatic molecules. *Journal of Electron Spectroscopy and Related Phenomena*, 75:129–147, 1995.
- [63] J. Schnadt, P.A. Brühwiler, L. Patthey, J.N. O’Shea, S. Södergren, M. Odelius, R. Ahuja, O. Karis, M. Bässler, P. Persson, H. Siegbahn, S. Lunell, and N. Martensson. Experimental evidence for sub-3-fs charge transfer from an aromatic adsorbate to a semiconductor. *Nature*, 418:620–623, 2002.
- [64] S. Yu, S. Ahmadi, M. Zuleta, H. Tian, and K. Schulte. Adsorption geometry, molecular interaction, and charge transfer of triphenylamine-based dye on rutile TiO<sub>2</sub>(110). *Journal of Chemical Physics*, 133:1–11, 2010.
- [65] J-M. Filhol. Pleins feux sur la lumière synchrotron. DocSciences, 2010.
- [66] C. Li and H. Wonneberger. Perylene imides for organic photovoltaics: Yesterday, today, and tomorrow. *Advanced Materials*, 24:613–636, 2012.
- [67] H. Yang, A.J. Mayne, G. Comtet, G. Dujardin, Y. Kuk, P. Sonnet, L. Stauffer, S. Nagarajan, and A. Gourdon. STM imaging, spectroscopy and manipulation of a self-assembled PTCDI monolayer on epitaxial graphene. *Physical Chemistry Chemical Physics*, 15:4939–4946, 2013.
- [68] M. Yu, W. Xu, N. Kalashnyk, Y. Benjalal, S. Nagarajan, F. Masini, E. Laegsgaard, M. Hliwa, X. Bouju, A. Gourdon, C. Joachim, F. Besenbacher, and T.R. Linderoth. From zero to two dimensions: supramolecular nanostructures formed from perylene-3,4,9,10-tetracarboxylic diimide (PTCDI) and Ni on the Au(111) surface through the interplay between hydrogen-bonding and electrostatic metal-organic interactions. *Nano Research*, 5:903–916, 2012.
- [69] A. Herrmann and K. Müllen. From industrial colorants to single photon sources and biolabels: The fascination and function of rylene dyes. *Chemistry Letters*, 35:978–985, 2006.
- [70] Y. Avlasevich, C. Li, and K. Müllen. Synthesis and applications of core-enlarged perylene dyes. *Journal of Materials Chemistry*, 20:3814–3826, 2010.
- [71] S. Yagai, M. Usui, T. Seki, H. Murayama, Y. Kikkawa, S. Uemura, T. Karatsu, A. Kitamura, A. Asano, and S. Seki. Supramolecularly engineered perylene bisimide assemblies exhibiting thermal transition from columnar to multilamellar structures. *Journal of the American Chemical Society*, 134:7983–7994, 2012.

- [72] I. Willerich and F. Gröhn. Molecular structure encodes nanoscale assemblies: Understanding driving forces in electrostatic self-assembly. *Journal of the American Chemical Society*, 133:20341–20356, 2011.
- [73] N. Tasios, C. Grigoriadis, M.R. Hansen, H. Wonneberger, C. Li, H.W. Spiess, K. Müllen, and G. Floudas. Self-assembly, dynamics, and phase transformation kinetics of donor acceptor substituted perylene derivatives. *Journal of the American Chemical Society*, 132:7478–7487, 2010.
- [74] C-C. You and F. Würthner. Self assembly of ferrocene functionalized perylene bisimide bridging ligands with Pt(II) corner to electrochemically active molecular squares. *Journal of the American Chemical Society*, 125:9716–9725, 2003.
- [75] J. van Herrikhuyzen, A. Syamakumari, A.P.H.J. Schenning, and E.W. Meijer. Synthesis of n-type perylene bisimide derivatives and their orthogonal self-assembly with p-type oligo(p-phenylene vinylene)s. *Journal of the American Chemical Society*, 126:10021–10027, 2004.
- [76] Q.H. Wang and M.C. Hersam. Room-temperature molecular-resolution characterization of self-assembled organic monolayers on epitaxial graphene. *Nature Chemistry*, 1:206–211, 2009.
- [77] H. Huang, S. Chen, X. Gao, W. Chen, and A.T.S. Wee. Structural and electronic properties of PTCDA thin films on epitaxial graphene. *ACS Nano*, 3:3431–3436, 2009.
- [78] C. Weiss, C. Wagner, R. Temirov, and F.S. Tautz. Direct imaging of intermolecular bonds in scanning tunneling microscopy. *Journal of the American Chemical Society*, 132:11864–11865, 2010.
- [79] R. Temirov, S. Soubatch, O. Neucheva, A.C. Lassise, and F.S. Tautz. A novel method achieving ultra-high geometrical resolution in scanning tunnelling microscopy. *New Journal of Physics*, 10:1–11, 2008.
- [80] J. Lobo-Checa, M. Matena, K. Müller, J.H. Dil, F. Meier, L.H. Gade, T.A. Jung, and M. Stöhr. Band formation from coupled quantum dots formed by a nanoporous network on a copper surface. *Science*, 325:300–303, 2009.
- [81] R. Madueno, M.T. Raisanen, C. Silien, and M. Buck. Functionalizing hydrogen-bonded surface networks with self-assembled monolayers. *Nature*, 454:618–621, 2008.
- [82] M.E. Canas-Ventura, K. Ait-Mansour, P. Ruffieux, R. Rieger, K. Müllen, H. Brune, and R. Fasel. Complex interplay and hierarchy of interactions in two-dimensional supramolecular assemblies. *ACS Nano*, 5:457–469, 2011.
- [83] C. Silien, M.T. Räsänen, and M. Buck. A supramolecular network as sacrificial mask for the generation of a nanopatterned binary self-assembled monolayer. *Small*, 6:391–394, 2010.

- [84] P.E. Keivanidis, I.A. Howard, and R.H. Friend. Intermolecular interactions of perylene diimides in photovoltaic blends of fluorene copolymers: Disorder effects on photophysical properties, film morphology and device efficiency. *Advanced Functional Materials*, 18:3189–3202, 2008.
- [85] J.P. Schmidtke, R.H. Friend, M. Kastler, and K. Müllen. Control of morphology in efficient photovoltaic diodes from discotic liquid crystals. *The Journal of Chemical Physics*, 124:1–6, 2006.
- [86] J.E. Bullock, R. Carmieli, S.M. Mickley, J. Vura-Weis, and M.R. Wasielewski. Photoinitiated charge transport through  $\pi$ -stacked electron conduits in supramolecular ordered assemblies of donor acceptor triads. *Journal of the American Chemical Society*, 131:11919–11929, 2009.
- [87] M.J. Ahrens, L.E. Sinks, B. Rybtchinski, W. Liu, B.A. Jones, J.M. Giaimo, A.V. Gusev, A.J. Goshe, D.M. Tiede, and M.R. Wasielewski. Self-assembly of supramolecular light-harvesting arrays from covalent multi-chromophore perylene-3,4:9,10-bis(dicarboximide) building blocks. *Journal of the American Chemical Society*, 126:8284–8294, 2004.
- [88] C. Barraud, P. Seneor, R. Mattana, S. Fusil, K. Bouzehouane, C. Deranlot, P. Graziosi, L. Hueso, I. Bergenti, V. Dediu, F. Petroff, and A. Fert. Unraveling the role of the interface for spin injection into organic semiconductors. *Nature Physics*, 6:615–620, 2010.
- [89] D. Niedzialek, V. Lemaire, D. Dudenko, J. Shu, M.R. Hansen, J.W. Andreasen, W. Pisula, K. Müllen, J. Cornil, and D. Beljonne. Probing the relation between charge transport and supramolecular organization down to angstrom resolution in a benzothiadiazole-cyclopentadithiophene copolymer. *Advanced Materials*, 25:1939–1947, 2013.
- [90] P.J. Skabara, J-B. Arlin, and Y.H. Geerts. Close encounters of the 3D kind – exploiting high dimensionality in molecular semiconductors. *Advanced Materials*, 25:1948–1954, 2013.
- [91] M. Knupfer and H. Peisert. Electronic properties of interfaces between model organic semiconductors and metals. *Physica Status Solidi (a)*, 201:1055–1074, 2004.
- [92] J. Hwang, A. Wan, and A. Kahn. Energetics of metal–organic interfaces: New experiments and assessment of the field. *Materials Science and Engineering*, 64:1–31, 2009.
- [93] H. Ishii, K. Sugiyama, E. Ito, and K. Seki. Energy level alignment and interfacial electronic structures at organic/metal and organic/organic interfaces. *Advanced Materials*, 11:605–625, 1999.

- [94] X. Crispin. Interface dipole at organic/metal interfaces and organic solar cells. *Solar Energy Materials and Solar Cells*, 83:147–168, 2004.
- [95] S. Braun, W.R. Salaneck, and M. Fahlman. Energy-level alignment at organic/metal and organic/organic interfaces. *Advanced Materials*, 21:1450–1472, 2009.
- [96] M. Mura, A. Gulans, T. Thonhauser, and L.N. Kantorovich. Role of van der waals interaction in forming molecule metal junctions, flat organic molecules on the Au(111) surface. *Physical Chemistry Chemical Physics*, 12:4759–4767, 2010.
- [97] L. Wang, L. Liu, W. Chen, Y. Feng, and A.T.S. Wee. Configuration dependent interface charge transfer at a molecule metal junction. *Journal of the American Chemical Society*, 128:8003–8007, 2006.
- [98] L.C. Mayor, J.B. Taylor, G. Magnano, A. Rienzo, C.J. Satterley, J.N. O’Shea, and J. Schnadt. Photoemission, resonant photoemission, and x-ray absorption of a Ru(II) complex adsorbed on rutile TiO<sub>2</sub>(110) prepared by in situ electrospray deposition. *The Journal of Chemical Physics*, 129:1–9, 2008.
- [99] T.D. Märk and P. Scheier. Ionization dynamics, unexpected electrons. *Nature Physics*, 6:82–83, 2010.
- [100] W. Chen, L. Wang, D.C. Qi, S. Chen, X.Y. Gao, and A.T.S. Wee. Probing the ultrafast electron transfer at the CuPc/Au(111) interface. *Applied Physics Letters*, 88:1–3, 2006.
- [101] X. Sun. *Engineering supramolecular architectures on insulating or metal surfaces studied by scanning tunneling microscopy*. PhD thesis, University of Groningen, 2010.
- [102] F. Silly. A robust method for processing scanning probe microscopy images and determining nanoobject position and dimensions. *Journal of Microscopy*, 236:211–218, 2009.
- [103] J. Hieulle and F. Silly. Localized intermolecular electronic coupling in two-dimensional self-assembled 3,4,9,10-perylenetetracarboxylic diimide nanoarchitectures. *Journal of Materials Chemistry C*, 1:4536–4539, 2013.
- [104] M. Mura, F. Silly, G.A.D. Briggs, M.R. Castell, and L.N. Kantorovich. H-Bonding supramolecular assemblies of PTCDI molecules on the Au(111) surface. *The Journal of Physical Chemistry C*, 113:21840–21848, 2009.
- [105] X. Lu, M. Grobis, K.H. Khoo, S.G. Louie, and M.F. Crommie. Spatially mapping the spectral density of a single C<sub>60</sub> molecule. *Physical Review Letters*, 90:1–4, 2003.

- [106] J.N. O’Shea, A. Saywell, G. Magnano, L.M.A. Perdigo, C.J. Satterley, P.H. Beton, and V.R. Dhanak. Adsorption of PTCDI on Au(111): Photoemission and scanning tunnelling microscopy. *Surface Science*, 603:3094–3098, 2009.
- [107] J. Schnadt, J.N. O’Shea, L. Patthey, J. Krempaský, N. Mårtensson, and P.A. Brühwiler. Alignment of valence photoemission, x-ray absorption, and substrate density of states for an adsorbate on a semiconductor surface. *Physical Review B*, 67:1–7, 2003.
- [108] J. Schnadt, J. Schiessling, and P.A. Brühwiler. Comparison of the size of excitonic effects in molecular  $\pi$  systems as measured by core and valence spectroscopies. *Chemical Physics*, 312:39–45, 2005.
- [109] G. Cabailh, C.R. Henry, and C. Barth. Thin NaCl films on silver (001): island growth and work function. *New Journal of Physics*, 14:1–18, 2012.
- [110] C. Barth, M. Gingras, A.S. Foster, A. Gulans, G. Félix, T. Hynninen, R. Peresutti, and C.R. Henry. Two-dimensional nanostructured growth of nanoclusters and molecules on insulating surfaces. *Advanced Materials*, 24:3228–3232, 2012.
- [111] A.S. Foster, C. Barth, and C.R. Henry. Chemical identification of ions in doped NaCl by scanning force microscopy. *Physical Review Letters*, 102:1–4, 2009.
- [112] C. Barth and C.R. Henry. NaCl(001) surfaces nanostructured by Suzuki precipitates: a scanning force microscopy study. *New Journal of Physics*, 11:1–18, 2009.
- [113] C. Barth and C.R. Henry. Surface double layer on (001) surfaces of alkali halide crystals: A scanning force microscopy study. *Physical Review Letters*, 98:1–4, 2007.
- [114] C. Barth and C.R. Henry. Imaging Suzuki precipitates on NaCl:Mg<sup>2+</sup>(001) by scanning force microscopy. *Physical Review Letters*, 100:1–4, 2008.
- [115] D.M. Roessler and W.C. Walker. Electronic spectra of crystalline NaCl and KCl. *Physical Review*, 166:599–606, 1968.
- [116] K. Glöckler, M. Sokolowski, A. Soukopp, and E. Umbach. Initial growth of insulating overlayers of NaCl on Ge(100) observed by scanning tunneling microscopy with atomic resolution. *Physical Review B*, 54:7705–7708, 1996.
- [117] W. Hebenstreit, J. Redinger, Z. Horozova, M. Schmid, R. Podloucky, and P. Varga. Atomic resolution by STM on ultra-thin films of alkali halides: experiment and local density calculations. *Surface Science*, 424:L321–L328, 1999.
- [118] G. Meyer and N.M. Amer. Optical beam deflection atomic force microscopy: The NaCl(001) surface. *Applied Physics Letters*, 56:2100–2101, 1990.
- [119] X. Sun, M.P. Felicissimo, P. Rudolf, and F. Silly. NaCl multi-layer islands grown on Au(111)-(22 ×  $\sqrt{3}$ ) probed by scanning tunneling microscopy. *Nanotechnology*, 19:1–5, 2008.

- [120] J.V. Barth, G. Costantini, and K. Kern. Engineering atomic and molecular nanostructures at surfaces. *Nature*, 437:671–679, 2005.
- [121] Y. Pennec, W. Auwärter, A. Schiffrin, A. Weber-Bargioni, A. Riemann, and J.V. Barth. Supramolecular gratings for tuneable confinement of electrons on metal surfaces. *Nature Nanotechnology*, 2:99–103, 2007.
- [122] Y. Yang and C. Wang. Hierarchical construction of self-assembled low-dimensional molecular architectures observed by using scanning tunneling microscopy. *Chemical Society Reviews*, 38:2576–2589, 2009.
- [123] S. Jensen, J. Greenwood, H.A. Früchtl, and C.J. Baddeley. STM investigation on the formation of oligoamides on au111 by surface-confined reactions of melamine with trimesoyl chloride. *The Journal of Physical Chemistry C*, 115:8630–8636, 2011.
- [124] J. Greenwood, H.A. Früchtl, and C.J. Baddeley. Ordered growth of upright melamine species on Ni(111): A study with scanning tunnelling microscopy and reflection absorption infrared spectroscopy. *The Journal of Physical Chemistry C*, 116:6685–6690, 2012.
- [125] H. Walch, A-K. Maier, W.M. Heckl, and M. Lackinger. Isotopological supramolecular networks from melamine and fatty acids. *The Journal of Physical Chemistry C*, 113:1014–1019, 2009.
- [126] N. Martsinovich and A. Troisi. Modeling the self-assembly of benzenedicarboxylic acids using monte carlo and molecular dynamics simulations. *The Journal of Physical Chemistry C*, 114:4376–4388, 2010.
- [127] P. Szabelski and S. De Feyter. Chiral occlusion in two-dimensional binary supramolecular networks studied by the monte carlo method. *CrystEngComm*, 13:5542–5550, 2011.
- [128] Y. Wang, S. Fabris, G. Costantini, and K. Kern. Tertiary chiral domains assembled by achiral metal-organic complexes on Cu(110). *The Journal of Physical Chemistry C*, 114:13020–13025, 2010.
- [129] R. Gutzler, O. Ivasenko, C. Fu, J.L. Brusso, F. Rosei, and D.F. Perepichka. Halogen bonds as stabilizing interactions in a chiral self-assembled molecular monolayer. *Chemical Communications*, 47:9453–9455, 2011.
- [130] F. Rosei, M. Schunack, Y. Naitoh, P. Jiang, A. Gourdon, E. Laegsgaard, I. Stensgaard, C. Joachim, and F. Besenbacher. Properties of large organic molecules on metal surfaces. *Progress in Surface Science*, 71:95–146, 2003.
- [131] D.S. Deak, F. Silly, K. Porfyrakis, and M.R. Castell. Controlled surface ordering of endohedral fullerenes with a SrTiO<sub>3</sub> template. *Nanotechnology*, 18:1–6, 2007.

- [132] C. Lu, E. Zhu, Y. Liu, Z. Liu, Y. Lu, J. He, D. Yu, Y. Tian, and B. Xu. C<sub>60</sub> on nanostructured Nb-Doped SrTiO<sub>3</sub>(001) surfaces. *The Journal of Physical Chemistry C*, 114:3416–3421, 2010.
- [133] J. Wen and J. Ma. Modulating morphology of thiol-based monolayers in honeycomb hydrogen-bonded nanoporous templates on the Au(111) surface: Simulations with the modified force field. *The Journal of Physical Chemistry C*, 116:8523–8534, 2012.
- [134] L. Cao, Y. Wang, J. Zhong, Y. Han, W. Zhang, X. Yu, F. Xu, D-C. Qi, and A.T.S. Wee. Electronic structure, chemical interactions and molecular orientations of 3,4,9,10-perylene-tetracarboxylic-dianhydride on TiO<sub>2</sub>(110). *The Journal of Physical Chemistry C*, 115:24880–24887, 2011.
- [135] S. Sanvito. Molecular spintronics. *Chemical Society Reviews*, 40:3336–3355, 2011.
- [136] A. Hagfeldt and M. Grätzel. Molecular photovoltaics. *Accounts of Chemical Research*, 33:269–277, 2000.
- [137] C.J. Whiteoak, G. Salassa, and A.W. Kleij. Recent advances with  $\pi$ -conjugated salen systems. *Chemical Society Reviews*, 41:622–631, 2012.
- [138] M.T. Räsänen, F. Mögele, S. Feodorow, B. Rieger, U. Ziener, M. Leskelä, and T. Repo. Alkyl chain length defines 2D architecture of salophen complexes on liquid–graphite interface. *European Journal of Inorganic Chemistry*, 25:4028–4034, 2007.
- [139] L. Chen, J. Kim, T. Ishizuka, Y. Honsho, A. Saeki, S. Seki, H. Ihee, and D. Jiang. Noncovalently netted, photoconductive sheets with extremely high carrier mobility and conduction anisotropy from triphenylene-fused metal trigon conjugates. *Journal of the American Chemical Society*, 131:7287–7292, 2009.
- [140] G. Salassa, M.J.J. Coenen, S.J. Wezenberg, B.L.M. Hendriksen, S. Speller, J.A.A.W. Elemans, and A.W. Kleij. Extremely strong self-assembly of a bimetallic salen complex visualized at the single-molecule level. *Journal of the American Chemical Society*, 134:7186–7192, 2012.
- [141] S. Kuck, S-H. Chang, J-P. Klöckner, M.H. Prosenc, G. Hoffmann, and R. Wiesendanger. Steering two-dimensional molecular growth via dipolar interaction. *ChemPhysChem*, 10:2008–2011, 2009.
- [142] A. DiLullo, S-H. Chang, N. Baadji, K. Clark, J-P. Klöckner, M-H. Prosenc, S. Sanvito, R. Wiesendanger, G. Hoffmann, and S-W. Hla. Molecular kondo chain. *Nano Letters*, 12:3174–3179, 2012.
- [143] M. Viciano-Chumillas, J. Hieulle, T. Mallah, and F. Sully. Compact hydrogen-bonded self-assembly of Ni(II)–Salen derivative investigated using scanning tunneling microscopy. *The Journal of Physical Chemistry C*, 116:23404–23407, 2012.

- [144] G.R. Desiraju. Supramolecular synthons in crystal engineering-A new organic synthesis. *Angewandte Chemie International Edition*, 34:2311–2327, 1995.
- [145] S. Uemura, M. Aono, T. Komatsu, and M. Kunitake. Two-dimensional self-assembled structures of melamine and melem at the aqueous solution-Au(111) interface. *Langmuir*, 27:1336–1340, 2011.
- [146] F. Silly. Moiré pattern induced by the electronic coupling between 1-octanol self-assembled monolayers and graphite surface. *Nanotechnology*, 23:1–6, 2012.
- [147] Y. Ye, W. Sun, Y. Wang, X. Shao, X. Xu, F. Cheng, J. Li, and K. Wu. A unified model: Self-assembly of trimesic acid on gold. *The Journal of Physical Chemistry C*, 111:10138–10141, 2007.
- [148] F. Silly. Two-dimensional 1,3,5-tris(4-carboxyphenyl)benzene self-assembly at the 1-phenyloctane-graphite interface revisited. *The Journal of Physical Chemistry C*, 116:10029–10032, 2012.
- [149] M. Lackinger and W.M. Heckl. Carboxylic acids: Versatile building blocks and mediators for two-dimensional supramolecular self-assembly. *Langmuir*, 25:11307–11321, 2009.
- [150] C. Carbone, S. Gardonio, P. Moras, S. Lounis, M. Heide, G. Bihlmayer, N. Atodiresei, P.H. Dederichs, S. Blügel, S. Vlaic, A. Lehnert, S. Ouazi, S. Rusponi, H. Brune, J. Honolka, A. Enders, K. Kern, S. Stepanow, C. Krull, T. Balashov, A. Mugarza, and P. Gambardella. Self-assembled nanometer-scale magnetic networks on surfaces: Fundamental interactions and functional properties. *Advanced Functional Materials*, 21:1212–1228, 2011.
- [151] F. Silly, M. Pivetta, M. Ternes, F. Patthey, J.P. Pelz, and W-D. Schneider. Coverage-dependent self-organization: from individual adatoms to adatom superlattices. *New Journal of Physics*, 6:1–13, 2004.
- [152] F. Silly, M. Pivetta, M. Ternes, F. Patthey, J.P. Pelz, and W-D. Schneider. Creation of an atomic superlattice by immersing metallic adatoms in a two-dimensional electron sea. *Physical Review Letters*, 92:1–4, 2004.
- [153] N. Weiss, T. Cren, M. Epple, S. Rusponi, G. Baudot, S. Rohart, A. Tejada, V. Repain, S. Rousset, P. Ohresser, F. Scheurer, P. Bencok, and H. Brune. Uniform magnetic properties for an ultrahigh-density lattice of noninteracting Co nanostructures. *Physical Review Letters*, 95:1–4, 2005.
- [154] S. Loth, S. Baumann, C.P. Lutz, D.M. Eigler, and A.J. Heinrich. Bistability in atomic-scale antiferromagnets. *Science*, 335:196–199, 2012.
- [155] V. Iancu, A. Deshpande, and S-W. Hla. Manipulation of the kondo effect via two-dimensional molecular assembly. *Physical Review Letters*, 97:1–4, 2006.

- [156] R. Otero, M. Schöck, L.M. Molina, E. Laegsgaard, I. Stensgaard, B. Hammer, and F. Besenbacher. Guanine quartet networks stabilized by cooperative hydrogen bonds. *Angewandte Chemie International Edition*, 44:2270–2275, 2005.
- [157] M. Yu, J. Wang, M. Mura, Q-Q. Meng, W. Xu, H. Gersen, E. Lægsgaard, I. Stensgaard, R.E.A. Kelly, J. Kjems, T.R. Linderoth, L.N. Kantorovich, and F. Besenbacher. Homochiral xanthine quintet networks self-assembled on Au(111) surfaces. *ACS Nano*, 5:6651–6660, 2011.
- [158] J.T. Davis. G-Quartets 40 years later: From 5'-GMP to molecular biology and supramolecular chemistry. *Angewandte Chemie International Edition*, 116:684–716, 2004.
- [159] T. Giorgi, F. Grepioni, I. Manet, P. Mariani, S. Masiero, E. Mezzina, S. Pieraccini, L. Saturni, G.P. Spada, and G. Gottarelli. Gel-like lyomesophases formed in organic solvents by self-assembled guanine ribbons. *Chemistry - A European Journal*, 8:2143–2152, 2002.
- [160] S.J. Sowerby, M. Edelwirth, and W.M. Heckl. Self-assembly at the prebiotic solid-liquid interface: Structures of self-assembled monolayers of adenine and guanine bases formed on inorganic surfaces. *The Journal of Physical Chemistry B*, 102:5914–5922, 1998.
- [161] M. Lukas, R.E.A. Kelly, L.N. Kantorovich, R. Otero, W. Xu, E. Laegsgaard, I. Stensgaard, and F. Besenbacher. Adenine monolayers on the Au(111) surface: Structure identification by scanning tunneling microscopy experiment and ab initio calculations. *The Journal of Chemical Physics*, 130:1–9, 2009.
- [162] O. Guillermet, A. Mahmood, J. Yang, J. Echeverria, J. Jeannoutot, S. Gauthier, C. Joachim, F. Chérioux, and F. Palmino. Seeding molecular rotators on a passivated silicon surface. *ChemPhysChem*, 15:271–275, 2014.



**Abstract:** One of the most important scientific challenges for the next decades is to build and to control devices at the nanometer scale. These nano-devices promise to have many applications in physics, chemistry and medicine. For example the nano-devices may be used to go further in the miniaturization of electronic compounds in order to improve the processors efficiency and performances. A judicious manner to create nano-devices is to take advantage of inter-molecular interactions in order to obtain self-assembled structures using a small numbers of molecules ("bottom-up" approach). The objective of this thesis was to create new organic self-assembled monolayers (SAMs), and to investigate their structures and electronic properties. Scanning tunneling microscopy (STM) was used to determine molecular organization with an atomic resolution. It was observed that the molecular skeleton and substituents used are key parameters driving the molecular self-assembly. Additionally we have showed that a post-annealing of the sample can be used not only to change the structure of a perylene-based film as it is usually expected but also to modify its electronic states. Photoemission-based techniques combined with synchrotron radiation facilities were used to access to the chemical and electronic properties of SAMs. A strong modification of the line-shape and energy positions of the electronic states of SAMs with the molecular film thickness was observed. In the same way core-hole-clock spectroscopy shows that the charge transfer dynamics at the PTCDI/Au(111) interface is strongly affected by the film thickness.

**Keywords:** self-assembly, scanning tunneling microscope, photoemission spectroscopy, thin films, Au(111) surface, PTCDI molecule.

**Résumé:** L'un des défis scientifiques les plus importants pour les prochaines décennies est de construire des dispositifs à l'échelle nanométrique. Ces nano-dispositifs promettent d'avoir de nombreuses applications en physique, chimie et médecine. Par exemple, ils peuvent être utilisés pour aller plus loin dans la miniaturisation des composés électroniques afin d'améliorer les performances des processeurs. Une manière judicieuse de créer des nano-dispositifs est de profiter des interactions intermoléculaires afin d'obtenir des structures auto-assemblées à l'aide d'un petit nombre de molécules (approche "bottom-up"). L'objectif de cette thèse est de créer de nouvelles monocouches auto-assemblées (SAMs), et d'examiner leurs structures et leurs propriétés électroniques. Tout d'abord, la microscopie à effet tunnel (STM) a été utilisée pour déterminer l'organisation moléculaire avec une résolution atomique. On a observé que le squelette moléculaire et les substituants utilisés sont des paramètres clés pour contrôler l'auto-assemblage. En outre, nous avons montré qu'un post-recuit de l'échantillon peut être utilisé non seulement pour modifier la structure d'un film à base de pérylène comme généralement attendu, mais permet aussi de modifier ses états électroniques. Par la suite, nous avons utilisé des techniques de photoémissions combinés avec des installations de rayonnement synchrotron pour accéder aux propriétés chimiques et électroniques des SAMs. Une forte modification de la forme et des positions en énergie des états électroniques des SAMs avec l'épaisseur du film moléculaire a été observée. De la même manière nous avons montré que la dynamique de transfert de charge à l'interface PTCDI/Au(111) est fortement affectée par l'épaisseur du film.

**Mots clés:** auto-assemblage, microscope à effet tunnel, spectroscopie de photoémission, films minces, surface d'Au(111), molécule de PTCDI.